Functional and Regulatory Biomolecular Networks Organized by DNA Nanostructures

by

Minghui Liu

A Dissertation Presented in Partial Fulfillment
of the Requirements for the Degree
Doctor of Philosophy

Approved April 2013 by the
Graduate Supervisory Committee:

Hao Yan, Co-Chair
Yan Liu, Co-Chair
Julian Chen
Peiming Zhang

ARIZONA STATE UNIVERSITY

May 2013

ABSTRACT

DNA has recently emerged as an extremely promising material to organize molecules on nanoscale. The reliability of base recognition, self-assembling behavior, and attractive structural properties of DNA are of unparalleled value in systems of this size. DNA scaffolds have already been used to organize a variety of molecules including nanoparticles and proteins. New protein-DNA bio-conjugation chemistries make it possible to precisely position proteins and other biomolecules on underlying DNA scaffolds, generating multi-biomolecule pathways with the ability to modulate inter-molecular interactions and the local environment. This dissertation focuses on studying the application of using DNA nanostructure to direct the self-assembly of other biomolecular networks to translate biochemical pathways to non-cellular environments.

Presented here are a series of studies toward this application. First, a novel strategy utilized DNA origami as a scaffold to arrange spherical virus capsids into one-dimensional arrays with precise nanoscale positioning. This hierarchical self-assembly allows us to position the virus particles with unprecedented control and allows the future construction of integrated multi-component systems from biological scaffolds using the power of rationally engineered DNA nanostructures. Next, discrete glucose oxidase (GOx)/ horseradish peroxidase (HRP) enzyme pairs were organized on DNA origami tiles with controlled interenzyme spacing and position. This study revealed two different distance-dependent kinetic processes associated with the assembled enzyme pairs. Finally, a tweezer-like DNA nanodevice was designed and constructed to actuate the activity of an enzyme/cofactor pair. Using this approach, several cycles of externally controlled enzyme inhibition and activation were successfully demonstrated. This

principle of responsive enzyme nanodevices may be used to regulate other types of enzymes and to introduce feedback or feed-forward control loops.

ACKNOWLEDGEMENTS

First and foremost, I would like to thank my husband Haisi Yi, without whom I would not have accomplished all that I have. I feel deeply grateful for his endless support and love six-thousand miles away across the Pacific Ocean. I am also thankful for my parents, who are always supportive over these five years of my PhD pursuit overseas.

I want to acknowledge my mentors, Dr. Hao Yan and Dr. Yan Liu, who brought me into this amazing world of DNA nanotechnology. Their passion, dedication, and incredible drive are truly inspirational for my future career in the academic field. I am also grateful to the members of my committee, Dr. Julian Chen and Dr. Peiming Zhang, for their time and invaluable advice. I thank our collaborators, Dr. Neal Woodbury, Dr. Matthew Francis, Dr. Kurt Gothelf and Dr. Nicolas Stephanopoulos. Without their inspiring suggestions much of my work would not have been successful.

Finally, I want to thank all the past and present graduate students, postdocs, and lab researchers who I have interacted with within these five years. Their advice and support have been instrumental to my research. My special thanks go to Dr. Jinglin Fu, one of the most outstanding and brilliant scientists I have ever met, for our successful collaborations since the year of 2010. I would like to thank my colleagues, Dr. Yonggang Ke, Dr. Zhe Li, Xixi Wei, Yuhe Yang, Dr. Xiaowei Liu, Zhao Zhao and Shuoxing Jiang for stimulating discussions. I also specially thank Dr. Jeanette Nangreave and Angela Edwards for all their help on manuscripts and thesis proofreading.

TABLE OF CONTENTS

Page

CHAPTER Page

LIST OF TABLES

Table Page

LIST OF FIGURES

Figure Page

Figure Page

Chapter 1

DNA Nanotechnology and DNA Organized Biomolecular Networks

Adapted with permission from Fu, J.; Liu, M.; Liu, Y.; Yan, H., Spatially-Interactive Biomolecular Networks Organized by Nucleic Acid Nanostructures. *Acc. Chem. Res.* **2012**, *45*, 1215-1226.

1.1. Abstract

Living systems have evolved a variety of nanostructures to control the molecular interactions that mediate many functions including the recognition of targets by receptors, the binding of enzymes to substrates, and the regulation of enzymatic activity. Mimicking these structures outside of the cell requires methods that offer nanoscale control over the organization of individual network components. Advances in DNA nanotechnology have enabled the design and fabrication of sophisticated one-, two- and three-dimensional (1D, 2D, and 3D) nanostructures that utilize spontaneous and sequence-specific DNA hybridization. Compared with other self-assembling biopolymers, DNA nanostructures offer predictable and programmable interactions and surface features to which other nanoparticles and biomolecules can be precisely positioned. The ability to control the spatial arrangement of the components while constructing highly organized interactive networks will lead to various applications of these systems. In this chapter, we introduce the principle of structural DNA nanotechnology, summarize the most advances in the DNA nanostructure directed assembly of biomolecular networks and explore the possibility of applying this technology to other fields of study.

1.2. Introduction

Biological systems use complex macromolecular nanostructure networks to mediate a range of cellular functions such as biomolecular synthesis, signal transduction, and gene expression and regulation, all with high efficiency and specificity. Many of these macromolecular systems have evolved through the spontaneous self-assembly of components into highly organized spatial structures, where the position and orientation of molecules are precisely controlled to facilitate functionality. For example, the multienzyme cascades[1] found in biochemical synthesis pathways and the light harvesting system in photosynthetic reaction centers[2] both rely on very specific arrangements of components. Over the past few decades, molecular self-assembly processes have been exploited to construct various nanostructures including vesicles, nanofibers, and nanotubes from self-assembling lipids, peptides, nucleic acids, and polysaccharides.[3] However, current methods to assemble multienzyme pathways, including genetic fusion, chemical crosslinking, liposome compartmentalization, and surface co-immobilization, all lack the ability to precisely control inter-component distance and overall spatial organization without compromising functionality. Additional challenges include the development of novel assembly algorithms to increase structural complexity and improve the fidelity and yield of the assembly process.

Deoxyribonucleic acid (DNA) is among the most promising biomolecules for the construction of complex biomolecular networks.[4] As illustrated in Figure 1.1, DNA is a self-assembling biopolymer that is directed by canonical Watson-Crick base pairing[5] to form predictable, double helical secondary structures, which are stabilized by hydrogen-bonding, π-π stacking, and hydrophobic interactions. B-form DNA double helices have

well-defined structural characteristics, including a helical repeat of ~3.4 nm, helical diameter of ~2.0 nm, and ~34.3 °twist angle between base pairs in solution.

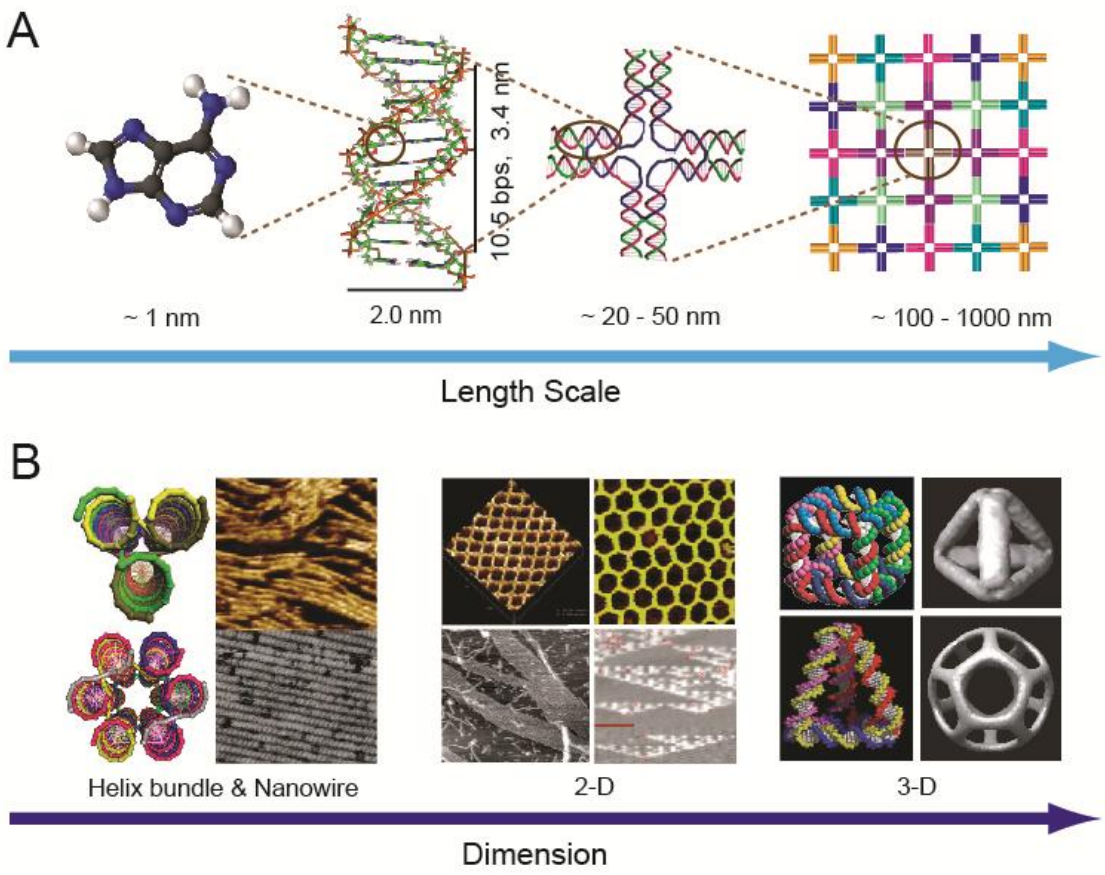

Figure 1.1. Introduction to structural DNA nanotechnology. (A) Self-assembly of nanostructures based on DNA base pairing. (B) Examples of DNA helix bundles (left), 2D arrays (middle) and small 3D cages (right).

In the early 1980's, Nadrian Seeman constructed artificial DNA tiles, where four rationally designed DNA strands self-assembled into an immobile four-way branched junction[6]. The creation of these junctions led nanotechnology to a new era with the engineering of double helical DNA molecules. Double-crossover (DX) DNA tiles,[7] with increased structural rigidity, were developed later and were suitable for assembling more

complex periodic nanostructures through sticky end interactions.[8] Tile-based DNA assembly has been demonstrated through the construction of a number of unique nanostructures, ranging from multi-helix bundles, nanotubes[9] and 2D lattice arrays[10] to 3D geometric cube,[11] tetrahedron,[12] and buckyball.[13]

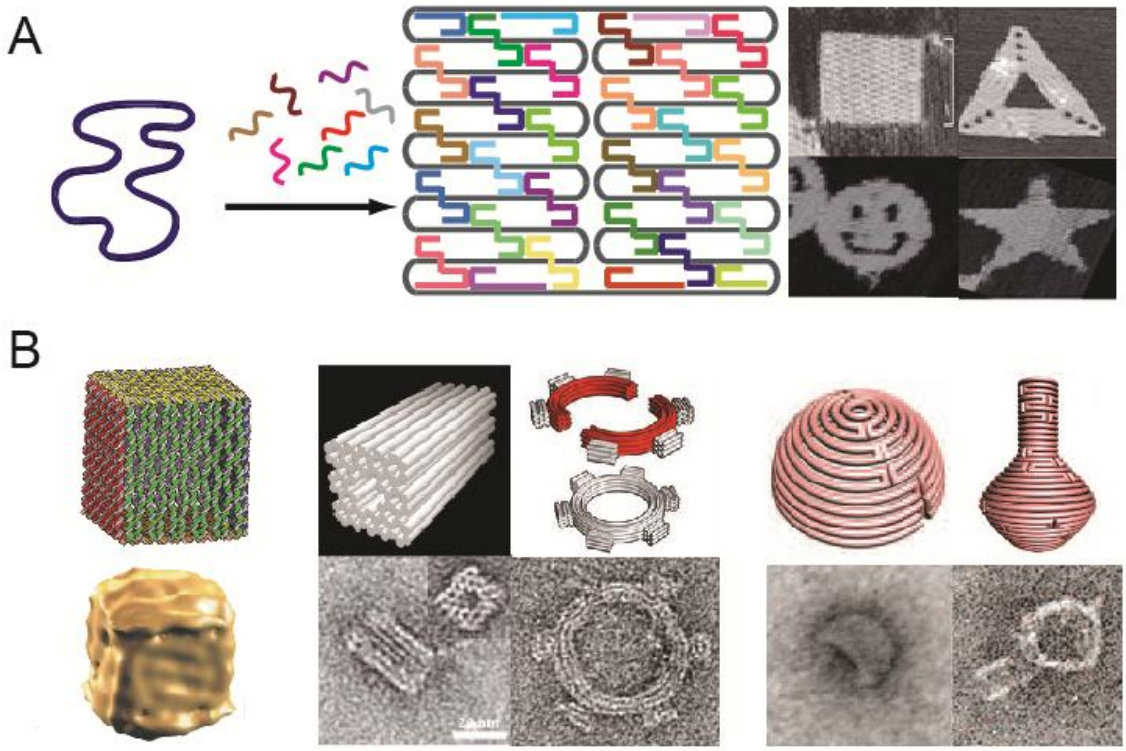

Figure 1.2. Introduction to DNA origami: arbitrary shapes can be created by folding DNA, such as (A) 2D DNA origami nanostrcutures, and (B) 3D DNA origami nanostructures.

An important milestone in structural DNA nanotechnology was the creation of aperiodic patterns using a scaffolding strategy. In 2006, Paul Rothemund made a breakthrough in scaffold-directed DNA nanostructure assembly; in the method he developed, referred to as DNA origami, a long single-stranded DNA scaffold (e.g., 7429-nt M13 bacteriophage genome DNA) is folded into arbitrary 2D shapes by following

predetermined folding paths that are specified by a collection of short oligonucleotide "staple" strands complementary to two or more regions of the scaffold that are not adjacent. (Figure 1.2A).[14] Many 2D origami examples including a square, rectangle, smiley face, triangle, and star have been demonstrated using the DNA origami method. One of the most attractive properties of DNA origami structures is the addressability of the surface, a result of the unique sequence at each oligonucleotide staple position. Thus, various patterns can be displayed by selectively modifying staple strands at desired locations with single-stranded probe extensions. The DNA-origami method has several advantages over "tile-based" assembly approaches: (1) scaffolded DNA can be folded into nearly any symmetric or asymmetric structure; (2) well-formed nanostructures are generated with high yield using unpurified staple strands, because the scaffold imposes the correct stoichiometry between strands; (3) spatially addressable assembly is achieved with a resolution of ~6 nm. The DNA origami approach was further developed for the construction of 3D nanostructures (Figure 1.2B). The Gothelf group assembled a hollow DNA box by joining six distinct (though connected by the scaffold) origami sheets through the action of staple strands bridging the edges.[15] The Shih group introduced a method to construct solid 3D shapes by packing scaffolded DNA double helices into pleated layers, constrained to a honeycomb or square lattice.[16-18] Twisted and curved 3D objects were further developed through insertion or deletion of base pairs at selected positions within the helical layers.[19] Our group also developed a strategy to construct DNA nanostructures with complex curvatures by nesting a collection of concentric DNA rings of decreasing circumference to generate the rounded contours of various 3D objects.[20]

In conclusion, as an information-encoding polymer, DNA can be programmed to assume a particular nanoscale shape. Cohesive, intermolecular interactions (sticky ends) can be used to link individual elements together and thus, it is possible to assemble intricate DNA networks in all three dimensions. They are reliable directors in the organization of heterogeneous nanoscale entities such as peptide, proteins, and nanoparticles. Molecular networks that are scaffolded by DNA nanostructures exhibit well-controlled inter-component distances and well-defined numbers. This characteristic presents exciting opportunities for fundamental studies of distance-dependent molecular interactions and for practical applications including biocatalysis and responsive nanodevices.

1.3. DNA-Directed Self Assembly

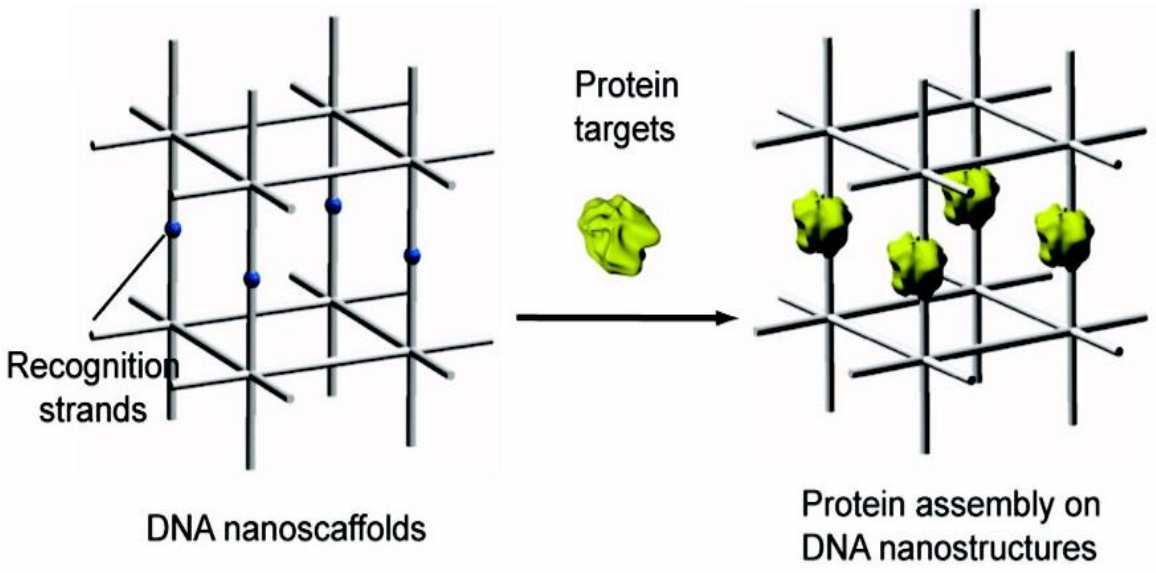

Figure 1.3. Seeman's proposal to organize macromolecules within a DNA nanoscaffold.

As shown in Figure 1.3, Seeman's original proposal suggested that a DNA nano-lattice could be used as a framework to organize proteins into 3D crystals, where the

position and orientation of each protein could be controlled by elements of the DNA lattice.[6]

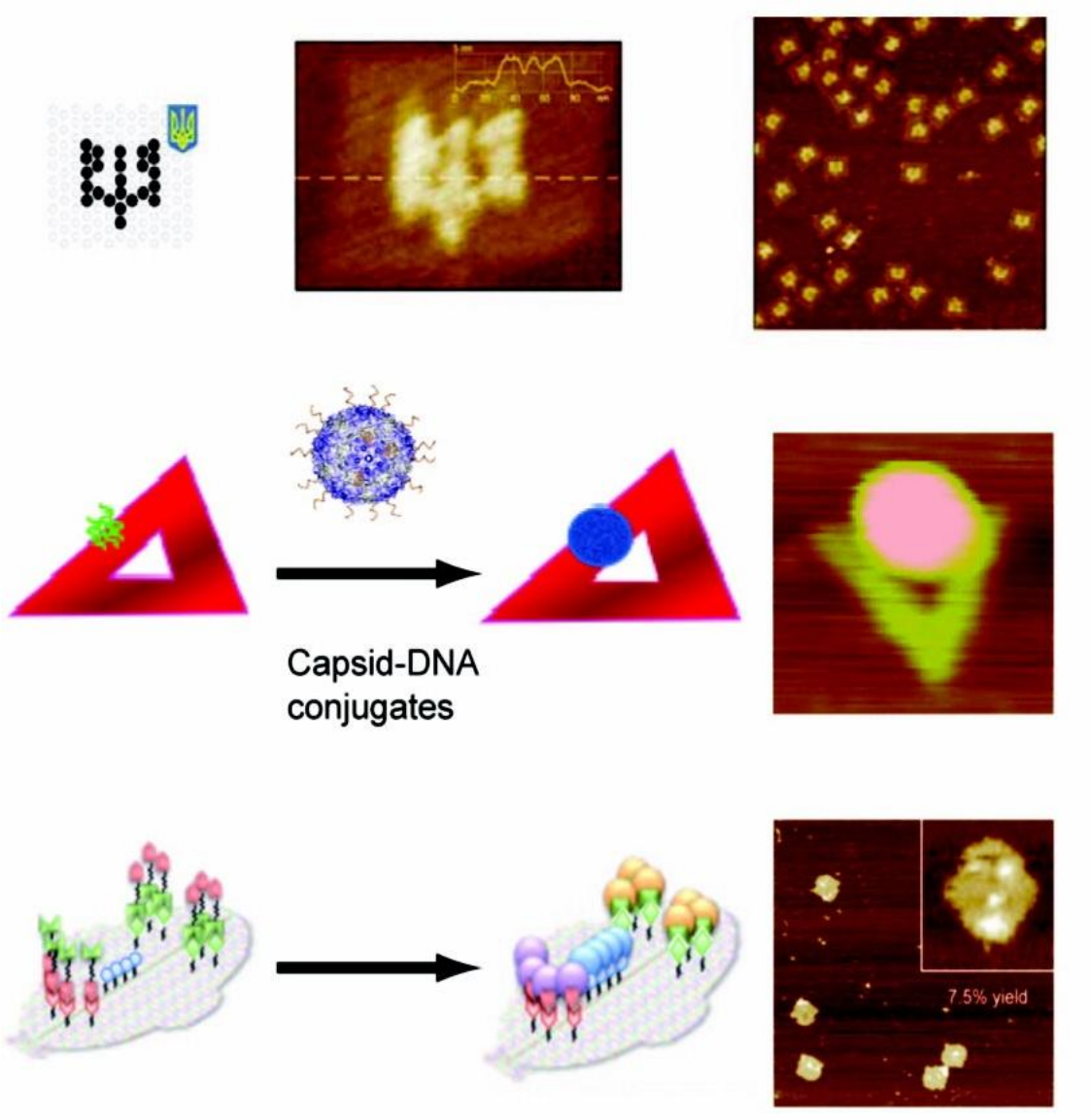

Figure 1.4. DNA origami directed assembly of macromolecules: streptavidin (top),[23] virus capsid (middle),[24] and orthogonal protein decoration (bottom).[25]

Since 1982, the sequence specificity of DNA hybridization has been exploited to assemble external biomolecules at specific positions on addressable DNA nanostructures.

Sequence-specific hybridization between the DNA functionalized biomolecules and single-stranded probe extensions of the DNA nanostructures generate networks of molecules with controlled intermolecular distances and ratios. This approach was demonstrated by organizing smaller biomolecules, including aptamers[21] and peptide,[22] as well as larger macromolecules, including proteins[23] and virus capsids,[24] on DNA nanostructures (Figure 1.4). DNA-directed assembly of virus capsids is described in chapter 2.

To guarantee highly efficient DNA-directed assembly yield, people have developed many oligonucleotide-biomolecule coupling methods. One of the attractive features of DNA scaffolds is that the constituent oligonucleotides can be modified with a variety of different functional groups for subsequent crosslinking reactions with other biomolecules;[26] amino and thiol modifications are among the most common. A widely used conjugation method is to use a bivalent coupling reagent, Succinimidyl-4-[N-maleimidomethyl] cyclohexane-1-carboxylate (SMCC) to attach to a lysine residue on a protein surface, for subsequence linkage to a thiol-modified oligonucleotide.[27] Figure 1.5 illustrates an alternative approach which is to modify a protein with an N-succinimidyl 3-(2-pyridyldithio) propionate (SPDP) crosslinker, followed by the activation of the pyridyl disulfide group to facilitate a disulfide bond exchange reaction with thiol-modified DNA. The leaving group pyridine 2-thione has specific absorbance at 343nm (extinction coefficient: 8.08×10^{3} $M^{-1}cm^{-1}$) and thus the coupling yield can be determined by measuring the absorbance change at this wavelength.

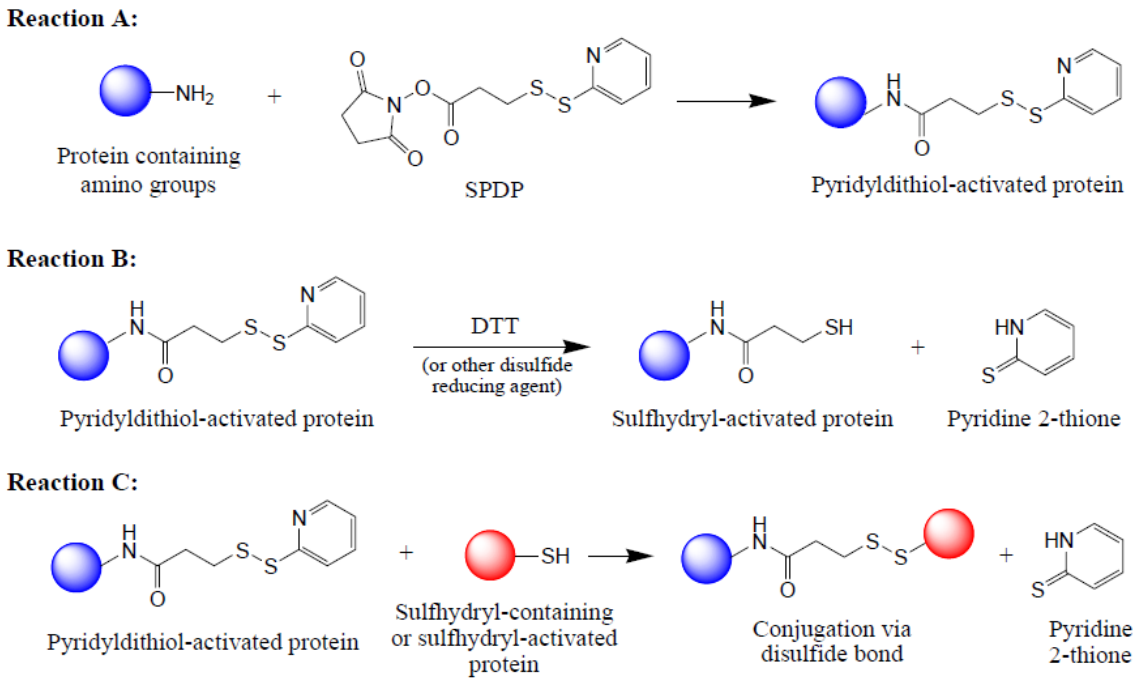

Figure 1.5. Chemistry of SPDP crosslinker reaction between amine and thiol functional groups.[28]

Despite their versatility, one of the drawbacks of conventional crosslinking methods is a lack of control over the conjugation site and stoichiometry of coupling. The presence of multiple lysine and cysteine residues on the surface of most proteins makes it difficult to generate a site-specific protein conjugation, which is required for certain applications.[29] Genetic modification of proteins with reactive tags (His-tag and ybbR-tags, for example) and the use of fusion domains (such as streptavidin, intein, SNAP, and HALO) are alternative approaches to achieve site-specific protein-oligo conjugation with very high efficiency.[29] In addition to covalent coupling approaches, noncovalent binding between proteins and specific ligands such as biotin-streptavidin interaction and can also be used for assembling protein nanoarrays.[30] It should be possible to achieve more precise control over the orientation of biomolecules by combining site-specific

conjugation strategies with 3D DNA nanostructures that have specifically tailored cavities or cages to constrain the guest molecule through steric interactions.

1.4. Organization of Multienzyme Reaction Pathways

The metabolism of living systems involves complex synthetic pathways with numerous multistep reactions that possess extraordinary yields and specificities. Many of the enzyme systems carrying out these reaction pathways are highly organized complexes with precisely controlled enzyme positions and orientations, facilitating efficient diffusion of substrates between the enzymes.[1] Artificial synthesis of these multienzyme systems is generally achieved by genetic fusion,[31] chemical cross-linking, and co-immobilization;[32] however, precise control over spatial organization of components is lacking for these methods.

With DNA nanostructures as assembly scaffolds, it has become feasible to organize multiple enzymes with controlled spacing in linear as well as 2D or 3D geometric patterns, which enables the study of cascade activity.[33] One of the first demonstrations was the assembly of a bioenzymatic NAD(P)H:FMN oxidoreductase and luciferase cascade on a double-stranded DNA scaffold with an observed ~3-fold increase in activity compared with the unassembled enzyme pair.[34] This strategy was later applied to probing the distance-dependent activity of multidomain complexes of cytochrome P450 BM3 by varying the length of spacing scaffolds between the BMR reductase domain and the BMP porphyrin domain.[35] 2D DNA nanostructures provide an even greater opportunity to organize multienzyme systems into more complicated geometric patterns. There was a report in 2009 of the self-assembly of a glucose oxidase (GOx) and horseradish peroxidase (HRP) enzyme cascade on 2D hexagonal DNA strips, with the

distance between the two enzymes controlled by the underlying nanostructure.[36] A greater than 10-fold activity enhancement was observed compared with the corresponding unstructured enzymes.

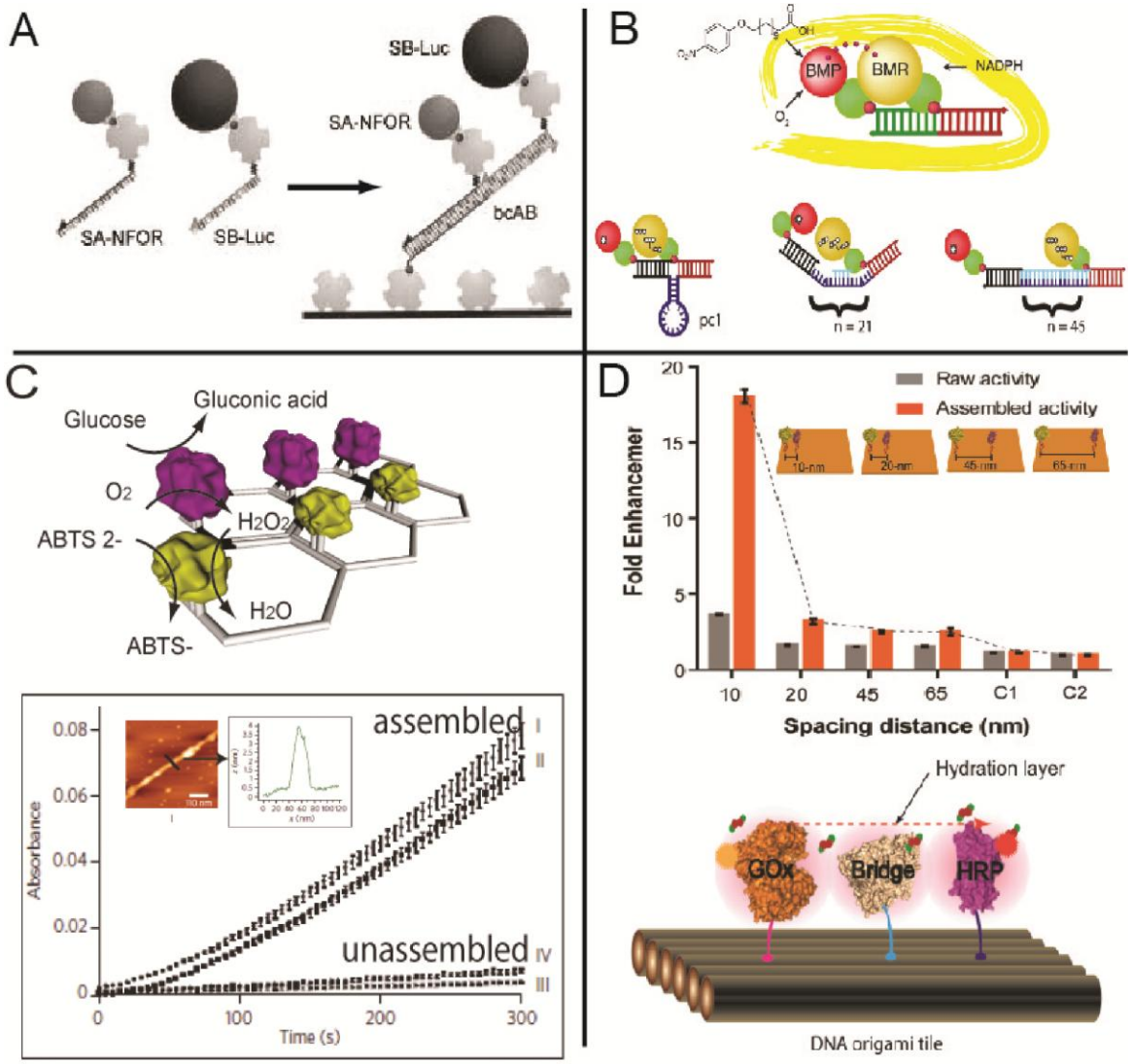

Figure 1.6. DNA nanostructures for engineering multienzyme systems. A linear double-stranded DNA scaffold for the assembly of (A) an enzyme cascade, NAD(P)H:FMN(NFOR) oxidoreductase and luciferase (Luc),[34] and (B) evaluating the distance-dependent activity of cytochrome P450 BM3 by varying the spacing between the BMR reductase domain and the BMP porphyrin domain.[35] (C) 2D DNA strip for

organizing GOx/HRP cascades.[36] (D) Organization of a GOx/HRP cascade on DNA origami tiles with controlled spatial positions, and a protein bridge for facilitating surface-limiting intermediate diffusion between enzymes.[37]

Recently, a GOx/HRP cascade was organized on DNA origami tiles with precisely controlled spatial positions, which was applied to investigating the distance dependent interenzyme substrate diffusion.[37] The study revealed that substrate transfer between enzymes might occur at the connected hydration shells for closely paced enzymes and demonstrated this idea by constructing a protein bridge to facilitate the intermediate transfer across protein surfaces. This work is described in chapter 3.

1.5. Responsive Nanodevice

It has been a dream for many years to create molecular level robots that mimic functional macromolecules and are capable of traveling through the human body. The enormous potential of DNA nanotechnology is bringing us closer to this dream. Autonomous DNA walkers are early demonstrations of functional nanorobots, where the motion of the legs is coordinated and driven by either strand displacement[38] or deoxyribozyme (DNAzyme) substrate binding and cleavage.[39] Recent advances in DNA origami make it possible to construct integrated nanosystems that combine walkers, cargo, tracks, and drive mechanisms to achieve complex motions on 2D or 3D surfaces. There was a report of an integrated system that executed cargo loading, transportation, and destination control functions.[40]

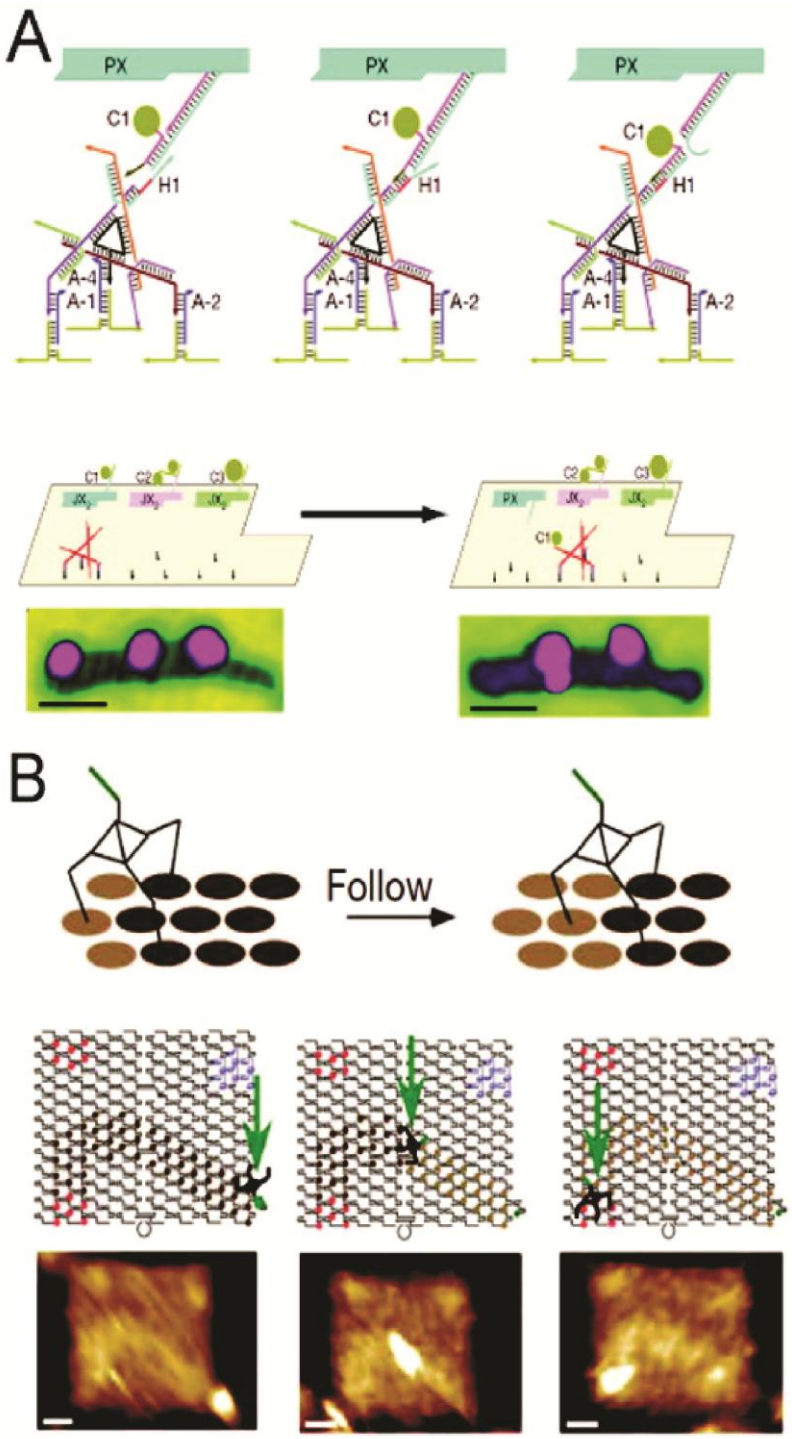

Figure 1.7. Responsive DNA nanowalkers: (A) a cargo transportation system consisting of an assembly template, cargo loading apparatus, and DNA walker,[40] and (B) walker movement along a 2D deoxyribonucleotide substrate surface.[41]

In Figure 1.7A, the hands of the DNA walker bound to specific nanoparticle cargo when the cassette was switched from an "OFF" to "ON" state. Fuel strands were employed to initiate the walker's stepwise movement, with a 120° rotation for each step. The cargo-transportation system was programmed to reach eight different destinations by controlling the states of the three loading cassettes and the movement along the tracks. In parallel, a spider-like molecular walker was developed with the ability to travel along a 2D oligonucleotide substrate track assembled on a DNA origami tile.[41] The walker was composed of an inert streptavidin protein body with three catalytic DNAzyme legs and a single capture leg for loading the molecular spider on the surface of the origami (Figure 1.7B). For movement along a predetermined path, the molecular walker was first loaded at the START position via hybridization of the capture leg to a partially complementary probe extended from the DNA origami surface. The walker was subsequently released by the addition of a 27-nt single-stranded DNA trigger that was fully complementary to the START probe, displacing the capture leg and allowing the walker to move to the substrate track. The catalytic action of the DNAzyme legs, binding to and cleaving the underlying DNA substrate track, drove the spider toward uncleaved substrate until it reached a STOP site, where further movement was inhibited by strong binding between a noncleavable probe and the DNAzyme legs.

In addition to walkers, other responsive DNA nanodevices such as tweezers,[42, 43] I-motif switches,[44] and hybridization-chain-reaction systems[45] have been developed. These devices are capable of sensing the presence of specific DNA or non-covalent interactions, changes in pH, and mRNA expression. An example of DNA tweezer based enzyme nanoreactor is described in chapter 4.

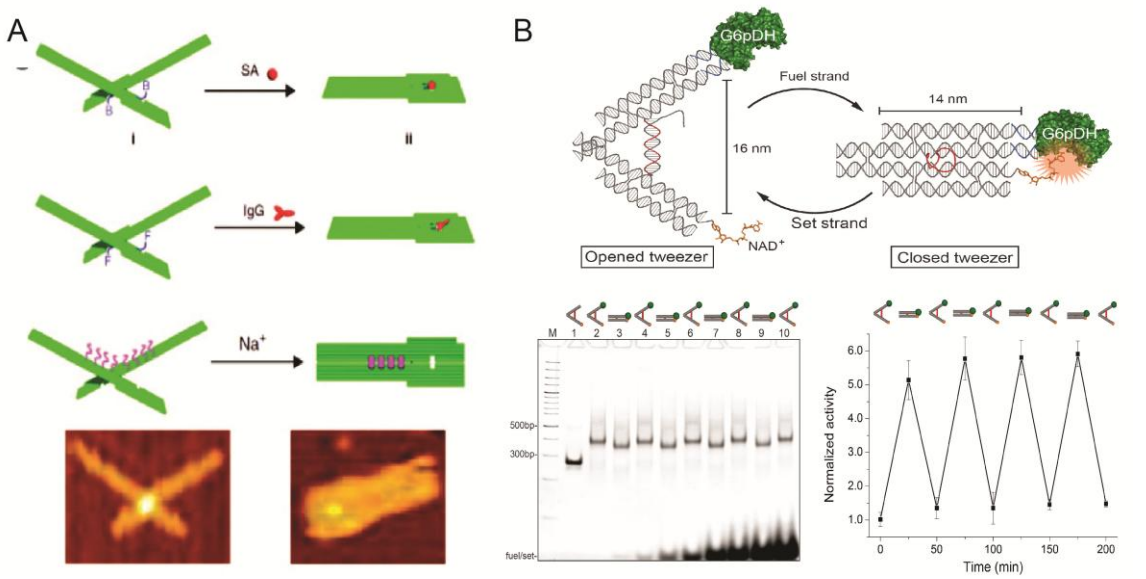

Figure 1.8. DNA tweezer-like nanodevices: (A) DNA origami based tweezers that are regulated by metal ion-nucleotide, biotin-streptavidin and antigen-antibody binding interactions. [42] (B) Functionalized DNA nanoreactors that can reversibly regulate enzyme activities by DNA fuel/set strands. [43]

1.6. Projects

1.6.1. DNA Directed Self Assembly of Virus Capsids with Nanoscale Precision. In this project, we reported a strategy of using DNA origami as a scaffold to arrange spherical virus capsids into one-dimensional arrays with precise nanoscale positioning. To do this, we first modified the interior surface of bacteriophage MS2 capsids with fluorescent dyes as a model cargo. An unnatural amino acid on the external surface was then coupled to DNA strands that were complementary to those extending from origami tiles. Two different geometries of DNA tiles (rectangular and triangular) were used. The capsids associated with tiles of both geometries with virtually 100% efficiency under mild annealing conditions, and the location of capsid immobilization on the tile could be controlled by the position of the probe strands. The rectangular tiles and

capsids could then be arranged into one-dimensional arrays by adding DNA strands linking the corners of the tiles. The resulting structures consisted of multiple capsids with even spacing (~100 nm). We also used a second set of tiles that had probe strands at both ends, resulting in a one-dimensional array of alternating capsids and tiles. This hierarchical self-assembly allows us to position the virus particles with unprecedented control and allows the future construction of integrated multicomponent systems from biological scaffolds using the power of rationally engineered DNA nanostructures.

1.6.2. Organization of GOx/HRP Cascade Using DNA Origami and the Study of Interenzyme Substrate Diffusion. In this project we organized discrete glucose oxidase (GOx)/ horseradish peroxidase (HRP) enzyme pairs on DNA origami tiles with controlled interenzyme spacing and position. The distance between enzymes was systematically varied from 10 to 65 nm, and the corresponding activities were evaluated. The study revealed two different distance-dependent kinetic processes associated with the assembled enzyme pairs. Strongly enhanced activity was observed for those assemblies in which the enzymes were closely spaced, while the activity dropped dramatically for enzymes as little as 20 nm apart. Increasing the spacing further resulted in a much weaker activity dependence on distance. Combined with diffusion modeling, the results suggest that Brownian diffusion of intermediates in solution governed the variations in activity for more distant enzyme pairs, while dimensionally limited diffusion of intermediates across connected protein surfaces contributed to the enhancement in activity for closely spaced GOx/HRP assemblies. To further test the role of limited dimensional diffusion along protein surfaces, a noncatalytic protein bridge was inserted between GOx and HRP

to connect their hydration shells. This resulted in substantially enhanced activity of the enzyme pair.

1.6.3. A DNA Tweezer-like Responsive Enzyme Nanoreactor. In this project, a tweezer-like DNA nanodevice was designed and constructed to actuate the activity of an enzyme/cofactor pair. A dehydrogenase and the corresponding NAD^+ cofactor were attached to different arms of the DNA tweezer structure and actuation of enzymatic function was achieved by switching the tweezers between open and closed states. The enzyme/cofactor pair is spatially separated in the open state which leads to inhibition of enzyme function, while in the closed state the activity of the enzyme is enhanced by the close proximity of the two molecules. The conformational state of the DNA tweezers is controlled by the addition of specific oligonucleotides that served as the thermodynamic driver (fuel) to trigger the change. Using this approach, several cycles of externally controlled enzyme inhibition and activation were successfully demonstrated. This principle of responsive enzyme nanodevices may be used to regulate other types of enzymes and to introduce feedback or feed-forward control loops.

1.7. References

(1) Savage, D. F.; Afonso, B.; Chen, A. H.; Silver, P. A. *Science* **2010**, *327*, 1258-1261.

(2) Cogdell, R. J.; Gall, A.; Köhler, J. *Q. Rev. Biophys*. **2006**, *39*, 227–324.

(3) Stupp, S. I. *Nano Lett*. **2010**, *10*, 4783–4786.

(4) Lin, C.; Liu, Y.; Yan, H. *Biochemistry* **2009**, *48*, 1663-1674.

(5) Watson, J. D.; Crick, F. H. C. *Nature*. **1953**, *171*, 737-738.

(6) Seeman, N. C. *J. Theor. Biol*. **1982**, *99*, 237–247.

(7) Fu, T. J.; Seeman, N. C. *Biochemistry* **1993**, *32*, 3211-3220.

(8) Winfree, E.; Liu, F.; Wenzler, L. A.; Seeman, N. C. *Nature* **1998**, *394*, 539-544.

(9) Park, S. H.; Barish, R.; Li, H.; Reif, J. H.; Finkelstein, G.; Yan, H.; LaBean, T. H. *Nano Lett*. **2005**, *5*, 693-696

(10) Mao, C.; Sun, W.; Seeman, N. C. *J. Am. Chem. Soc*. **1999**, *121*, 5437-5443.

(11) Chen, J.; Seeman, N. C. *Nature* **1991**, *350*, 631-633.

(12) Goodman, R. P.; Schaap, I. A. T.; Tardin, C. F.; Erben, C. M.; Berry, R. M.; Schmidt, C. F.; Turberfield, A. J. *Science* **2005**, *310*, 1661-1665.

(13) He, Y.; Ye, T.; Su,M.; Zhang, C.; Ribbe, A. E.; Jiang,W.;Mao, C. *Nature* **2008**, *452*, 198-201.

(14) Rothemund, P.W. K. Nature **2006**, *440*, 297-302.

(15) Andersen, E. S.; Dong, M.; Nielsen, M. M.; Jahn, K.; Subramani, R.; Mamdouh, W.; Golas, M.M.; Sander, B.; Stark, H.; Oliveira, C. L. P.; Pedersen, J. S.; Birkedal, V.; Besenbacher, F.; Gothelf, K. V.; Kjems, J. *Nature* **2009**, *459*, 73-76.

(16) Douglas, S. M.; Dietz, H.; Liedl, T.; Hogberg, B.; Graf, F.; Shih,W. M. *Nature* **2009**, *459*, 414-418.

(17) Ke, Y.; Douglas, S. M.; Liu, M.; Sharma, J.; Cheng, A.; Leung, A.; Liu, Y.; Shih, W. M.; Yan, H. *J. Am. Chem. Soc*. **2009**, *131*, 15903-15908.

(18) Ke, Y.; Voigt, N. V.; Gothelf, K. V.; Shih,W.M. *J. Am. Chem. Soc*. **2011**, *134*, 1770-1774.

(19) Dietz, H.; Douglas, S. M.; Shih, W. M. *Science* **2009**, *325*, 725-730.

(20) Han, D.; Pal, S.; Nangreave, J.; Deng, Z.; Liu, Y.; Yan, H. *Science* **2011**, *332*, 342–346.

(21) Chhabra, R.; Sharma, J.; Ke, Y.; Liu, Y.; Rinker, S.; Lindsay, S.; Yan, H. *J. Am. Chem. Soc.* **2007**, *129*, 10304-10305.

(22) Williams, B. A. R.; Lund, K.; Liu, Y.; Yan, H.; Chaput, J. C. *Angew. Chem., Int. Ed*. **2007**, *46*, 3051–3054.

(23) Kuzyk, A.; Laitinen, K. T.; Törmä, P. *Nanotechnology* **2009**, *20*, 235305.

(24) Stephanopoulos, N.; Liu, M.; Tong, G. J.; Li, Z.; Liu, Y.; Yan, H.; Francis, M. B. *Nano Lett.* **2010**, *10*, 2714-2720.

(25) Sacc à, B.; Meyer, R.; Erkelenz, M.; Kiko, K.; Arndt, A.; Schroeder, H.; Rabe, K. S. *Angew. Chem., Int. Ed*. **2010**, *49*, 9378-9383.

(26) Goodchild, J. *Bioconjugate Chem*. **1990**, *1*, 165-187.

(27) Williams, B. A. R.; Diehnelt, C. W.; Belcher, P.; Greving, M.; Woodbury, N. W.; Johnston, S. A.; Chaput, J. C. *J. Am. Chem. Soc*. **2009**, *131*, 17233-17241.

(28) Thermo Scientific Pierce Protein Biology Products instruction http://www.piercenet.com/instructions/2160279.pdf

(29) Niemeyer, C. M. *Angew. Chem., Int. Ed*. **2010**, *49*, 1200–1216.

(30) Yan, H.; Park, S. H.; Finkelstein, G.; Reif, J. H.; LaBean, T. H. *Science* **2003**, *301*, 1882-1884.

(31) Dueber, J. E.; Wu, G. C.; Malmirchegini, G. R.; Moon, T. S.; Petzold, C. J.; Ullal, A. V.;Prather, K. L. J.; Keasling, J. D. *Nat. Biotechnol*. **2009**, *27*, 753-759.

(32) Sheldon, R. A. *Adv. Synth. Catal*. **2007**, *349*, 1289-1307.

(33) Teller, C.; Willner, I. *Trends Biotechnol*. **2010**, *28*, 619-628.

(34) Niemeyer, C. M.; Koehler, J.; Wuerdemann, C. *ChemBioChem*. **2002**, *3*, 242-245.

(35) Erkelenz, M.; Kuo, C. H.; Niemeyer, C. M. *J. Am. Chem. Soc*. **2011**, *133*, 16111-16118.

(36) Wilner, O. I.; Weizmann, Y.; Gill, R.; Lioubashevski, O.; Freeman, R.; Willner, I. *Nat. Nanotechnol*. **2009**, *4*, 249-254.

(37) Fu, J.; Liu, M.; Liu, Y.; Woodbury, N. W.; Yan, H. *J. Am. Chem. Soc*. **2012**, *134*, 5516-5519.

(38) Omabegho, T.; Sha, R.; Seeman, N. C. *Science* **2009**, *324*, 67-71.

(39) He, Y.; Liu, D. R. *Nat. Nanotechnol*. **2010**, *5*, 778-782.

(40) Gu, H.; Chao, J.; Xiao, S. J.; Seeman, N. C. *Nature* **2010**, *465*, 202–205

(41) Lund, K.; Manzo, A. J.; Dabby, N.; Michelotti, N.; Johnson-Buck, A.; Nangreave, J.; Taylor, S.; Pei, R.; Stojanovic,M. N.;Walter, N. G.;Winfree, E.; Yan, H. *Nature* **2010**, *465*, 206-210.

(42) Kuzuya, A.; Sakai, Y.; Yamazaki, T.; Xu, Y.; Komiyama, M. *Nat. Commun*. **2011**, *2*, 449.

(43) Liu, M .; Fu, J.; Hejesen, C.; Yang, Y.; Woodbury, N.W.; Gothelf, K.; Liu, Y.; Yan, H. Submitted to *Nature Communication*.

(44) Modi, S.; Swetha, M. G.; Goswami, D.; Gupta, G. D.; Mayor, S.; Krishnan, Y. *Nat. Nanotechnol*. **2009**, *4*, 325-330.

(45) Choi, H. M. T.; Chang, J. Y.; Trinh, L. A.; Padilla, J. E.; Fraser, S. E.; Pierce, N. A. *Nat. Biotechnol*. **2010**, *28*, 1208-1212.

Chapter 2

DNA-Directed Self Assembly: Immobilization and 1D Arrangement of Virus Capsids with Nanoscale Precision Using DNA Origami

Adapted with permission from Stephanopoulos, N.; Liu, M.; Tong, G.; Li, Z.; Liu, Y.; Yan, H.; Francis, M. B. Immobilization and One-Dimensional Arrangement of Virus Capsids with Nanoscale Precision Using DNA Origami. *Nano Lett.* **2010**, *10*, 2714-2720. ; and from Li, Z.; Liu, M.; Wang, L.; Nangreave, J.; Yan, H.; Liu, Y. Molecular Behavior of DNA Origami in Higher Order Self-assembly. *J. Am. Chem. Soc*. **2010**, *138*, 13545-13552.

2.1. Abstract

In this chapter, we report a strategy of using DNA origami as a scaffold to arrange spherical virus capsids into one-dimensional arrays with precise nanoscale positioning. To do this, we first modified the interior surface of bacteriophage MS2 capsids with fluorescent dyes as a model cargo. An unnatural amino acid on the external surface was then coupled to DNA strands that were complementary to those extending from origami tiles. Two different geometries of DNA tiles (rectangular and triangular) were used. The capsids associated with tiles of both geometries with virtually 100% efficiency under mild annealing conditions, and the location of capsid immobilization on the tile could be controlled by the position of the probe strands. The rectangular tiles and capsids could then be arranged into one-dimensional arrays by adding DNA strands linking the corners of the tiles. The resulting structures consisted of multiple capsids with even spacing (~100 nm). We also used a second set of tiles that had probe strands at both ends,

resulting in a one-dimensional array of alternating capsids and tiles. This hierarchical self-assembly allows us to position the virus particles with unprecedented control and allows the future construction of integrated multicomponent systems from biological scaffolds using the power of rationally engineered DNA nanostructures.

2.2. Introduction

Self-assembly has proven to be one of the most effective ways to arrange matter at the nanometer level. Biology, in particular, makes extensive use of self-assembly to position molecules over several length scales with a high degree of spatial control over structure. In recent years, one promising approach that takes advantage of biological self-assembly in order to build synthetic materials employs virus capsids, the protein shells that encapsulate the genetic material of viruses.[1, 2] Capsids are composed of multiple protein subunits that can assemble (either spontaneously or under an external stimulus) into a monodisperse structure with different geometries depending on the virus. By appropriately functionalizing the proteins that comprise the capsid, multiple copies of a molecule or other entity can be positioned with a predictable arrangement. A wide variety of components have been attached to and arranged by virus capsids, including chromophores,[3-8] catalysts,[9, 10] nanoparticles and quantum dots,[11-15] polymers,[16-18] drug molecules,[19-22] and imaging agents.[23-25]

Integrating virus capsid-based materials into higher-order structures, however, remains a challenge and a limitation to their use in many materials applications. A number of groups have investigated various techniques for patterning capsids on larger length scales, including cysteine conjugation to gold surfaces to create a monolayer of capsids,[26] DNA-based aggregation of functionalized capsids,[27] and dip-pen

nanolithography[28] or nanografting[29] to introduce patterns of reactive handles on surfaces for virus immobilization. It is difficult to use these methods, however, to control the inter-capsid spacing and position individual capsids with nanoscale precision.

2.3. Experimental Design

In order to achieve nanoscale precise control, we sought a scaffold that could selectively and efficiently immobilize virus capsids and order them into hierarchical structures, and we chose DNA origami[30] for this purpose. In this method, a long single-stranded piece of DNA (usually the bacteriophage M13 genome) is folded into an arbitrary two-dimensional shape using a large number of short "staple" strands. The predictable and programmable properties of DNA hybridization allow for a high degree of control and the design of virtually any geometry desired. Furthermore, it is possible to synthesize staple strands that contain an extra single-stranded "probe" sequence that extends from the origami structure. The addition of components functionalized with DNA complementary to the probes allows for their immobilization on the origami tile with a high degree of spatial control. It should also be possible to create higher order structures by adding linker strands to connect the origami tiles together. As a final consideration, the size scale of DNA origami (~100 nm) is compatible with that of many virus capsids, facilitating the integration of the two components, unlike other DNA-based scaffolds that are too small to effectively order such large objects.

DNA origami has been used effectively to direct the self-assembly of nanoscale objects such as gold[31, 32] and silver[33]nanoparticles, RNA molecules,[34] or carbon nanotubes[35] with exquisite precision. In addition, several groups have immobilized small proteins on origami tiles using a variety of approaches, including aptamer binding,[36,37]

His_6 tags,[38] or biotin-streptavidin.[39] Our work represents the first attempt, to our knowledge, to attach a large, multiprotein entity like a virus onto an origami tile. For the capsid, we chose bacteriophage MS2, an icosahedral E. coli virus comprised of 180 identical protein subunits that spontaneously assemble into spherical particles 27 nm in diameter.[40-42] The coat protein can be expressed recombinantly, allowing for site-directed mutagenesis, and is purified as a fully assembled capsid devoid of genetic material. Access to the interior is afforded by 32 holes with 2 nm in diameter allowing for orthogonal functionalization of the interior and exterior surfaces by modifying the appropriate amino acid residues. [43, 9] As a result, these capsids are attractive targets as molecular containers or scaffolds for multiple copies of different components.

People have reported a method to modify the inside of the capsid with maleimide reagents (at a mutagenically introduced cysteine) and the exterior of the capsid with single-stranded DNA using an oxidative coupling reaction that targets an unnatural amino acid introduced via amber codon suppression (Figure 2.1.A).[43,44] By functionalizing the exterior of the capsid with DNA complementary to single-stranded probes extending from the DNA origami construct, the capsids should be able to bind the origami tile via Watson-Crick base pairing. For this work, we modified the interior of MS2 with a fluorescent dye (Oregon Green maleimide, as previously reported[9]) to approximately 100% modification, installing 180 copies of the molecule. In these experiments, the dye serves as a model cargo; in principle, however, any maleimide reagent that can fit through the 2 nm holes can be introduced. We next modified the exterior of the capsids with a 20-nt poly-T sequence to ~11% modification, installing approximately 20 copies per capsid. The capsids remained intact, hollow, and 27 nm in diameter after both interior

and exterior modification (see APPENDIX A for characterization of the dual-surface modified MS2 conjugate).

For the DNA origami tile, to improve the one-dimensional array, we utilized a new design for the rectangular-shaped DNA origami that was intended to relieve the deformation present in Rothemund's original design (see APPENDIX A for design of the zigzag DNA origami). Here we explored two different geometries: (1) rectangles, 90 nm in length by 60 nm in width, and (2) equilateral triangles, 120 nm on a side with a 40 nm triangular hole in the center. For the rectangles, we placed probes on either the edge (E) or middle (M) of the tile in order to demonstrate control over the exact location of the immobilized capsid on the tile. Similarly, for the triangles, we added probes either to one side (Tri1) or to all three sides (Tri3). The probes consisted of a 40-nt poly-A sequence, allowing the capsids with the 20-nt poly-T sequence to bind via cDNA pairing. We selected a 40-nt sequence in order to also provide a spacer between the negatively charged tile and the negatively charged capsid-DNA conjugate in order to reduce electrostatic and steric repulsion as much as possible. The multiple probe strands on each tile (3 for E tiles, 5 for Tri1 tiles, 6 for M tiles, and 15 for Tri3 tiles; see APPENDIX A for tile designs and probe locations), and the multiple complementary strands on the capsids allow for multivalent binding and thus stronger association of the two components.

2.4. Materials and Methods

See APPENDIX A

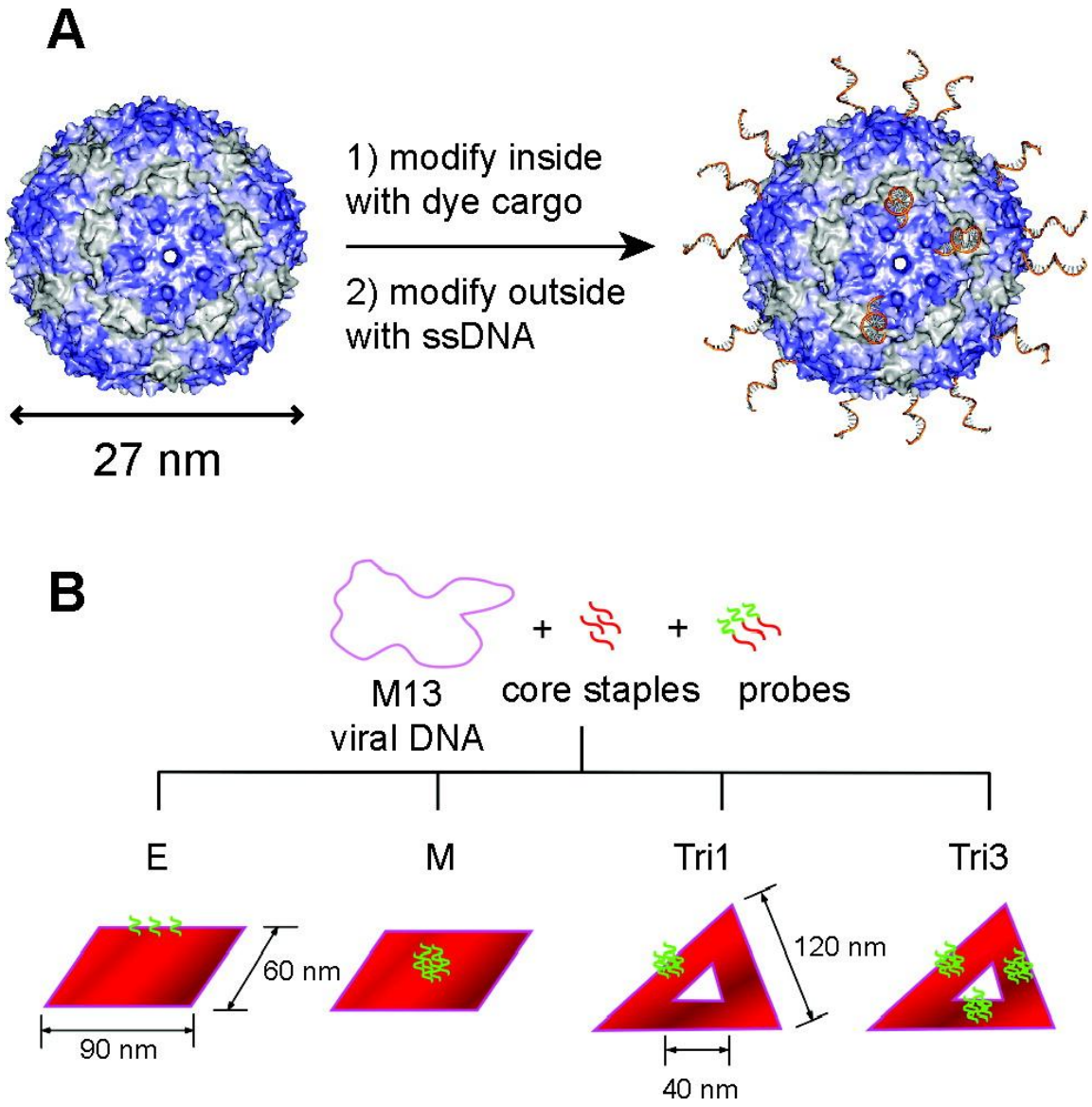

Figure 2.1. Summary of the components integrated in this work. (A) Bacteriophage MS2 capsids were modified on the interior with fluorescent dyes and on the exterior surface with single-stranded DNA (ssDNA). (B) Several different DNA origami tiles were constructed with different geometries and probe locations. The ssDNA probes were complementary to the DNA strands on the capsids, directing the association of the two components.

2.5. Results and Discussion

2.5.1. Association of Single Origami Tiles with MS2 Capsids Using DNA Based Hybridization. In order to attach the capsids to the tiles, we mixed the components in a 2:1 ratio and annealed the mixture from 37 to 4 ℃ at a rate of 1 ℃/min to help facilitate binding. The DNA origami templated viral capsid structures were verified by atomic force microscopy (AFM), allowing us to distinguish the tile shape from the much taller spherical capsid. To determine the efficiency of tile association with capsids, a large number of AFM images were inspected to determine the fraction of tiles with capsids bound to them.

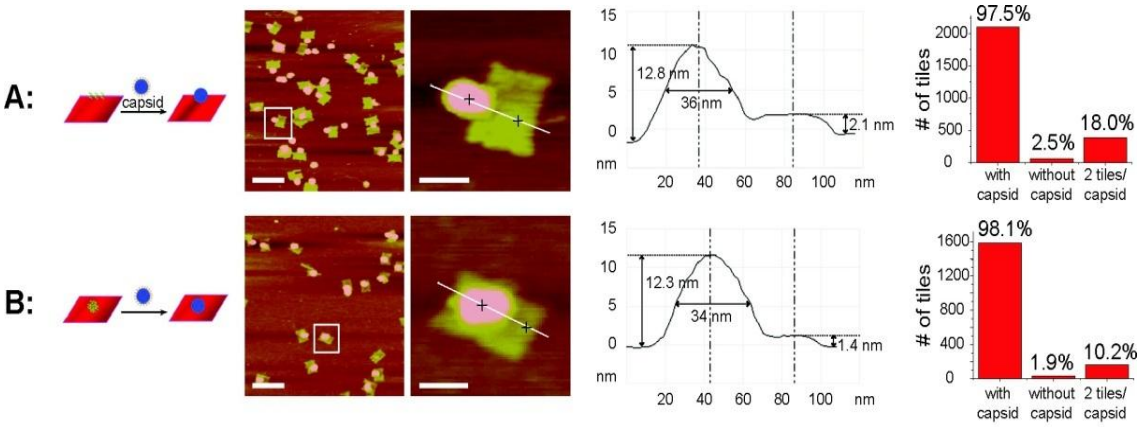

Figure 2.2. Single rectangular tiles with MS2 attached. (A) E tiles + MS2 (left to right): zoom-out AFM image, zoom-in AFM image, height profile of zoom-in image, and characterization of association efficiency. (B) M tiles + MS2 (left to right): zoom-out AFM image, zoom-in AFM image, height profile of zoom-in image, and characterization of association efficiency. Zoom-out scale bars, 200nm. Zoom-in scale bars, 50nm.

Figure 2.2 demonstrates that after annealing, the rectangular tiles showed virtually complete association of tiles with capsids, with 97.5% of E tiles and 98.1% of M tiles bearing an MS2 capsid. For the E tiles, the capsids were clearly attached to the edge of

the tile, where the probes were located. Similarly, for the M tiles the capsids were located in the middle of the tile, demonstrating the DNA-specific association and the ability to position the capsids precisely. Analyzing the height profile of a capsid on a tile demonstrated a spherical object around 35 nm in diameter (slightly larger than the 27 nm diameter of the capsid, due to lateral broadening by the AFM tip) attached on the origami tile 1.5-2 nm in height, as expected for the width of the DNA double helix. The height of the capsids was around 12 nm, resulting from the collapse and concomitant flattening of the hollow structure on the mica surface used for AFM.

Because the capsids display approximately 20 copies of the single-stranded DNA (ssDNA), multiple tiles can, in principle, bind to a single capsid. Roughly 18% of the E tiles were associated with a capsid already bound to a tile, whereas about 10% of the M tiles showed similar aggregation. This disparity between the designs is not surprising given that there is less surface area exposed and thus less electrostatic repulsion when two tiles approach one another from the side, as is the case with the E tiles, compared to face-on, as with the M tiles.

Using only 1 equivalent of MS2 (relative to the tile) resulted in around 89% of E tiles and only 70% of M tiles bearing a capsid. The higher efficiency of association for E tiles is again consistent with a lower amount of charge repulsion involved in an edge-on approach of the tile to the capsid. Because the origami tiles serve as the structural element to arrange the capsids, we wanted complete modification of the tiles with capsids, so we used 2 equivalent of MS2 for all further experiments. Current studies are under way to determine a method to purify MS2 not associated with a tile from the desired tile-capsid conjugates.

Control experiments with capsids without DNA showed no association with the tiles, indicating that the association was not due to some other nonspecific effect (see APPENDIX A). Similarly, mixing tiles bearing DNA that did not complement the sequences on the capsids also showed no significant association of the two components (see APPENDIX A). Furthermore, binding capsids to the tiles and then adding excess 40-nt poly-T ssDNA (which should bind to the 40-nt polyA probe with greater affinity than the 20-nt sequence on the MS2) removed the capsids from the tile (see APPENDIX A). This experiment not only confirmed the specific DNA-based association but also indicates a potential mechanism for releasing the capsids from the tiles if desired.

Figure 2.3 shows that the triangular tiles proved equally efficient at binding capsids as the rectangular tiles. Exposing the Tri1 tiles to 2 equivalent of MS2 and annealing as above resulted in virtually 100% association of capsids to the tiles. The capsids are bound to a single side of the triangular tile, and the hole in the center is clearly visible by AFM. The triangular shape of the tiles allowed facile visualization by transmission electron microscopy (TEM) as well, and the electron micrographs further confirm the association of the capsids to a single side of the triangular tile.

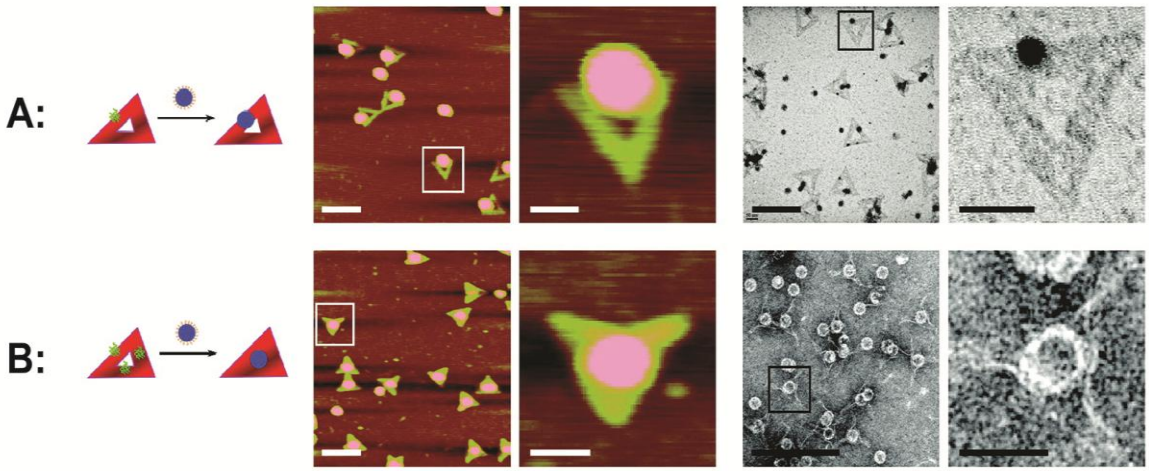

Figure 2.3. Single triangular tiles with MS2 attached. (A) Tri 1 tiles + MS2 (left to right): zoom-out AFM image, zoom-in AFM image, zoom-out TEM image, zoom-in TEM image. (B) Tri 3 tiles + MS2 (left to right): zoom-out AFM image, zoom-out TEM image, zoom-in TEM image. Zoom-out scale bars, 200nm. Zoom-in scale bars, 50nm.

The Tri3 tiles showed a similarly high hybridization efficiency (~100%), but in this design anywhere between one and three capsids can bind to each tile. The majority of samples visualized by AFM and TEM, however, showed a single capsid bound in the central hole of the tile (Figure 2.3B). We believe that once the capsid binds to one side of the triangular tile, the extra DNA strands on its surface quickly hybridize to the probes on the other two sides due to the increased local concentration effect. This hypothesis is supported by the fact that the sides of the Tri3 tiles appear to be contracted toward the center, suggesting that the capsid (which is smaller than the 40 nm hole in which it sits) pulls the sides inward by binding to all three. Some Tri3 tiles were observed bearing one capsid on a single side (instead of in the hole), one capsid on each of two sides, or one capsid on each of three sides (see APPENDIX A), but the majority of the tiles visualized showed a single capsid in the center.

It is important to note that the polyA/T strategy used was necessary for obtaining the high efficiency of capsid association in these results. Similar experiments using a randomly chosen DNA sequence resulted in only around 50% association of capsids with E tiles (see APPENDIX A), and increasing the amount of MS2 added or the annealing time did not result in increased efficiency. We believe that the polyA/T strategy is particularly effective because the strands on the MS2 can bind only one or two bases of the probe initially and then "slide" along the probe to find the thermodynamically

optimum conformation. [45] Furthermore, different strands on the capsid can bind the probe strand with less than 20 base pairs, promoting multivalent binding without requiring complete hybridization. Although it would seem that the polyA/T strategy will only allow for one type of capsid to be immobilized, we believe that any short repeating sequence would allow for a similar "sliding" mechanism and thus efficient binding. This would allow multiple types of capsids, bearing different groups on the interior, for example, to be patterned.

2.5.2. Formation and Distribution of One-Dimensional MS2 Arrays. Having successfully immobilized capsids on origami tiles with high efficiency, we next sought to use the DNA scaffold to organize the capsids on a larger length scale. As a proof of principle, we decided to create a one-dimensional array of capsids by linking the supporting origami tiles together. We designed two sets of strands, each of which partly binds to the M13 genome on opposite corners of the rectangular origami tile. These two sets contain complementary sequences, linking tiles at their corners and arranging them in a step-like array. We hypothesized that we could use this method with the E and M tiles to create a one-dimensional array of capsids with defined nanoscale separation.

Mixing the tiles (E or M), capsids, and linkers together and annealing from 37 to 4 ℃ at a rate of 1 ℃/min resulted in the expected arrays of tiles while retaining the virtually 100% association efficiency of the capsids (Figure 2.4). The AFM images clearly show a one-dimensional arrangement of capsids either on the edge or in the middle of the tiles (for E and M tiles, respectively) separated by approximately 100 nm. About 50% of the tiles formed arrays of at least two tiles, and the percentage of tiles in a given array decreased with increasing length (see APPENDIX A for length distributions).

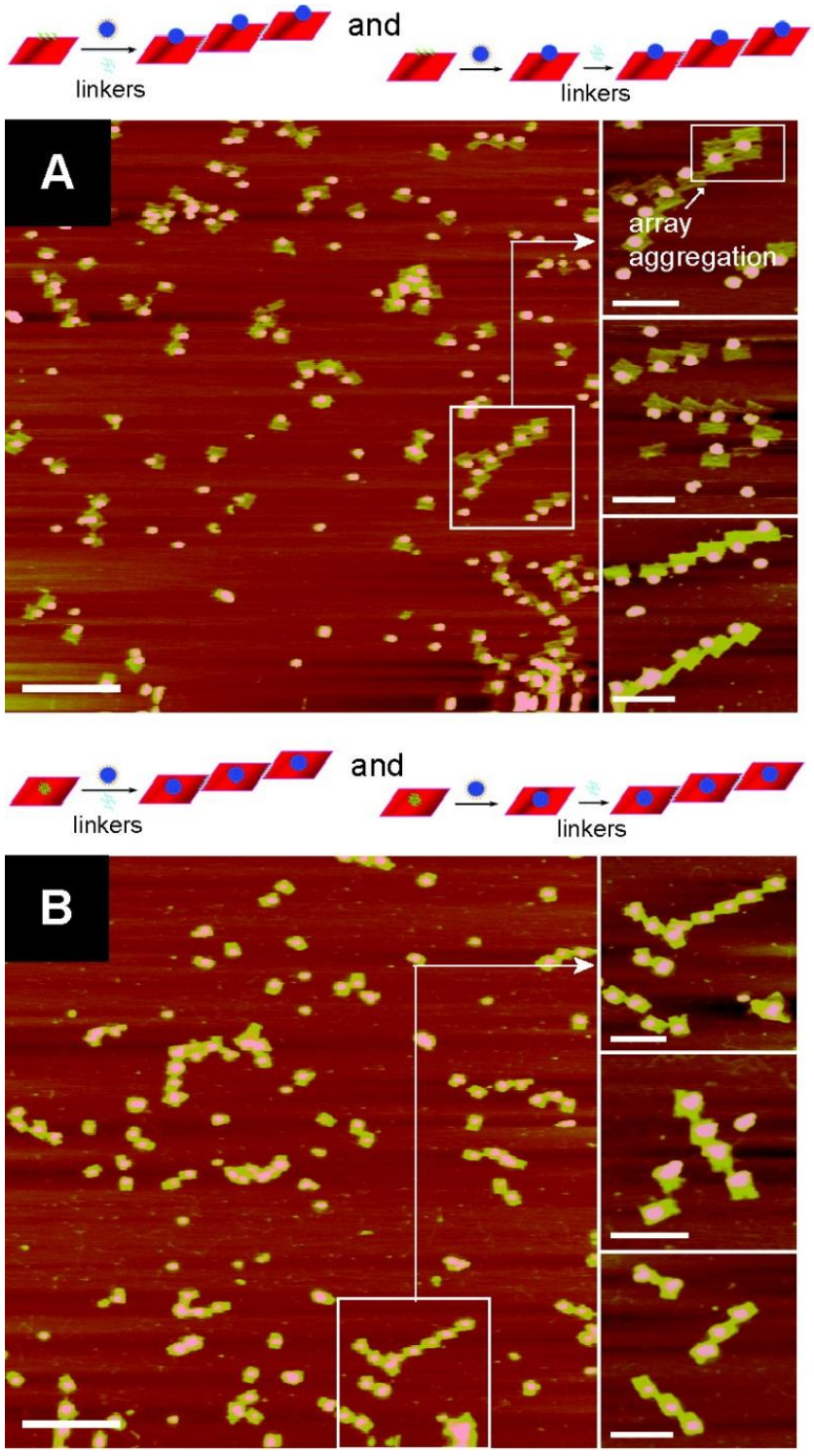

Figure 2.4. AFM images of MS2 arrays formed by origami tiles: one-pot annealing and step-wise annealing. (A) E tiles + MS2 + linkers (one-pot annealing) and E tiles + MS2,

followed by the addition of linkers in a second step. (B) M tiles + MS2 + linkers (one-pot annealing) and M tiles + MS2, followed by the addition of linkers in a second step. The top image of the three zoom-ins corresponds to the indicated area of the zoom-out; the other two zoom-in images come from different areas (see APPENDIX A for additional zoom-out images). Zoom-out scale bars, 500 nm. Zoom-in scale bars, 200 nm.

However, we occasionally observed arrays of five or six tiles, all the while maintaining the spacing between the capsids. Doubling the linker concentration resulted in a higher proportion of tiles in arrays (~60%). It was also possible to create the arrays in a hierarchical, rather than one-pot, procedure by annealing the capsids to the tiles first and then adding the linkers to form arrays in a second annealing step. Once again, arrays formed readily, though slightly fewer tiles (~45%) were in arrays greater than two. This decrease is likely due to the increased steric or electrostatic demands of linking tiles with capsids already bound (see APPENDIX A for summaries of the percentage of tiles in arrays two tiles or greater).

Because the E tiles experience less repulsion when two tiles bind a single capsid compared to the M tiles (Figure 2.2), we saw numerous instances of two E tile arrays that were linked by one set of capsids (see Figure 2.4A, top zoom-in). Also, once a single tile in an E-tile array binds a capsid on another array, the other tiles are perfectly positioned to bind adjacent capsids. The M tile arrays, by comparison, do not suffer as much from these drawbacks and result in structures with markedly less inter-array aggregation.

We also formed arrays of E and M tiles without any MS2 in order to compare the efficiency of the process with and without the capsids present. We found that in both cases a higher proportion of tiles were incorporated into arrays (65-68% compared to

~50% for arrays with MS2) and that the arrays tended to be longer, with a few instances of eight or nine tiles in a row (see APPENDIX A for AFM images of arrays without MS2 and length distributions). We attribute this improvement to the decreased steric and electrostatic repulsion between tiles when capsids were not present.

In light of these results, we sought to first form longer arrays with tiles alone, and then in a second step add capsids to bind to the probes on the arrays. With the E tiles, this strategy resulted in a great degree of inter-array aggregation, as multiple arrays were connected by a single set of capsids. As a result, very few single arrays were observed, and a majority of arrays clumped together into amorphous aggregates (data not shown).

The M tiles, by contrast, proved much more effective for this strategy due to their lower propensity to form aggregates. In Figure 2.5A, long arrays of capsids, occasionally reaching nine or ten capsids in length, were observed. Furthermore, because the linkers were still present in solution during the second annealing step (to attach the capsids to the arrays), the arrays were able to grow yet longer and incorporate even more tiles into arrays of two tiles or longer (~75% as shown in Figure 2.5A bottom). Unlike the one-pot annealing results, however, doubling the concentration of linkers did not result in increased array lengths or an increased percentage of tiles in arrays.

The hierarchical self-assembly in forming the E and M tile arrays is a competition between productive assembly (the capsids associating with the tiles and the tiles forming arrays) and unproductive assembly (multiple tiles binding to a single capsid, resulting in aggregation). Annealing for a longer time (1 ℃/2 min) resulted in a much higher degree of aggregation and significantly fewer well-formed arrays.

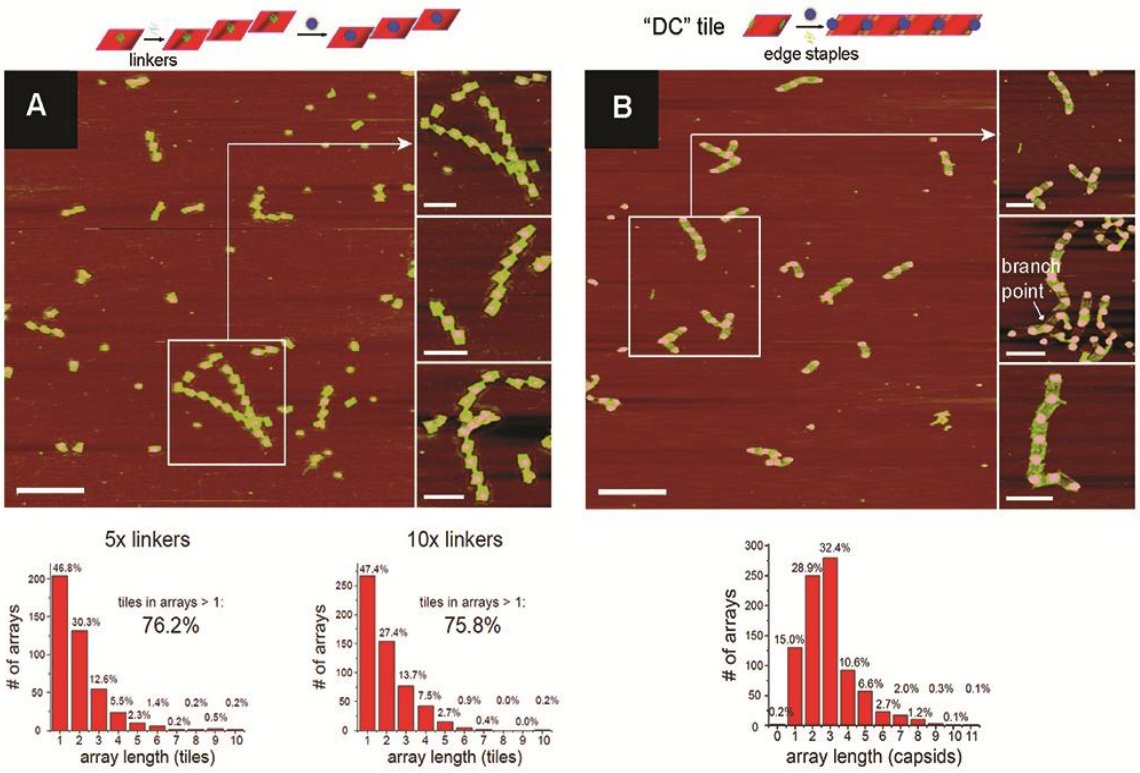

Figure 2.5. AFM images of MS2 arrays and distributions. (A) M tiles + linkers, then addition of MS2 in a second step. (B) DC tiles + MS2 + edge staples (to encourage tile edge stacking). The top image of the three zoom-ins corresponds to the indicated area of the zoom-out; the other two zoom-in images come from different areas (see APPENDIX A for additional zoom-out images). Zoom-out scale bars, 500 nm. Zoom-in scale bars, 200 nm.

Furthermore, although it was possible to create remarkably long arrays by annealing the tiles only (without MS2) for much greater lengths of time (45 to 4 ℃ at a rate of 1 ℃/10 min), the resulting arrays were too flexible, and upon addition of MS2 different sections of the arrays folded back on themselves and bound to a single capsid, again resulting in undesired and intractable aggregates.

The E tiles demonstrated the facility of binding multiple tiles to a single capsid when the probes are located at the edge of the tile. Although this was a liability in the linker based array formation, we decided to capitalize on this property by designing another rectangular tile with a set of five 40-nt poly-A probes on both short ends (see APPENDIX A). We envisioned that this design would allow for two tiles to be linked by a single capsid, creating a "daisy-chain" (DC) array of alternating capsids and tiles. In order to promote association of the tiles further via noncovalent base stacking interactions, we added the staple strands for the short edges of the tiles into the annealing mixture. We hypothesized that this stacking would pre-organize the tiles into short linear arrays, further facilitating the capsids in linking them.

Annealing a mixture of DC tiles, capsids (again, 2 equivalent), and edge staples from 37 to 4 ℃ at a rate of 1 ℃/min resulted in the expected formation of arrays of tiles linked by capsids, with approximately 90-100 nm spacing between capsids (Figure 2.5B). The efficiency was remarkably high, with only a small fraction of tile edges (~6%) that were not associated with a capsid. The length distribution of arrays peaked at three capsids in a row (separated by two tiles) and decreased thereafter, but some arrays of 10 or more capsids were observed (Figure 2.5B bottom). Occasionally, three or four tiles bound to a single capsid resulting in branching arrays; however, only a small fraction of capsids (~5%) served as such branching points, and the vast majority bound only two tiles. The arrays usually formed in a linear fashion (most likely to minimize repulsion between tiles), but because the tiles could bind to any location on the capsid, occasionally the tiles bound the capsids with an angle less than 180°, resulting in kinks in the arrays.

Omitting the edge staples resulted in shorter arrays (data not shown), indicating the usefulness of these staples in promoting array formation.

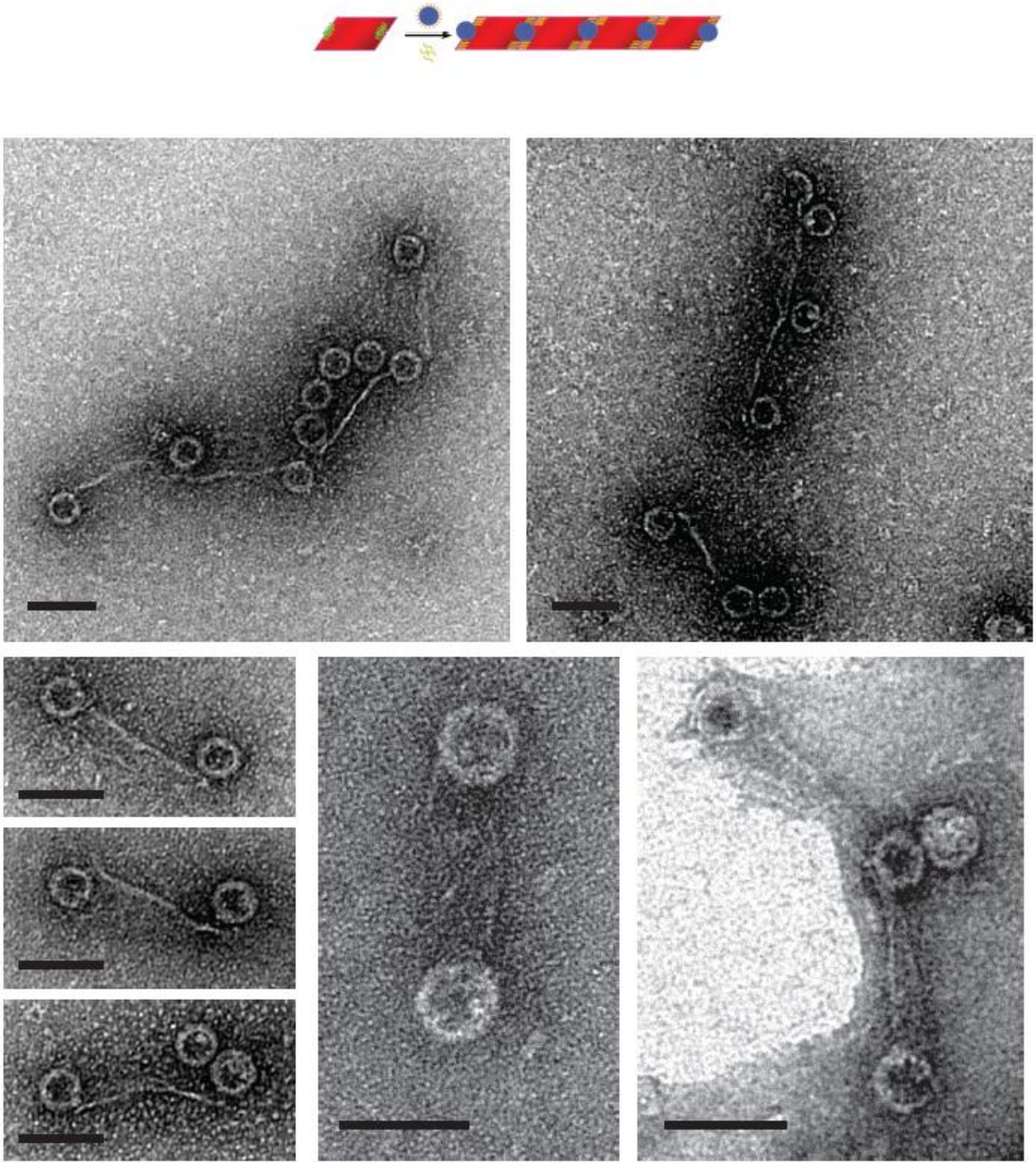

Figure 2.6. TEM images of DC tile arrays formed with MS2. The arrays most likely adsorb to the grid with the tiles sideways, making them appear as lines connecting the

capsids. In addition to illustrating the arrays, these images confirm that the capsids are intact, hollow, and 27 nm in diameter. Scale bars: 50 nm

We note that the DC tile design represents a complementary approach to forming capsid arrays compared to the linker-based approach for the E and M tiles. In the latter case, an external stimulus (i.e., the addition of the linker strands) induces assembly into higher-order structures, whereas in the former case the actual capsid binding event is the stimulus for array growth through a condensation polymerization-like mechanism. Depending on the application at hand, one strategy or the other may prove more useful. (For additional AFM images of all experiments shown in Figure 2.4 and 2.5, see APPENDIX A.)

In order to further characterize the conjugates, we obtained TEM images of both the M and DC tile arrays. Although the rectangular tiles are not easily visualized in TEM, we were able to obtain images that clearly showed the hollow capsids spaced approximately 100 nm apart. The arrays most often adsorbed to the TEM grid edge-on, so the tiles appeared as dark lines connecting the capsids. The tiles were often twisted when deposited on the TEM grid, but these results further confirm that the capsids remained intact during the array formation.

2.6. Conclusion

One of the great advantages of our approach lies in its versatility due to the modular nature of the capsid modification and the high degree of programmability intrinsic to DNA-based nanostructures. By choosing the appropriately designed tile, virtually any geometry is possible, and the capsids can be placed in any location on that tile. Furthermore, the interior of the capsid can be modified with a wide variety of

reagents, allowing for introduction of imaging agents, catalysts, or nucleation sites for nanoparticle growth. The one-dimensional arrays made possible by the origami tiles thus create the possibility of patterning arrays of nanoscale reactors, drug carriers (with programmed release by strand displacement) or metal particles for plasmonic arrays, all with high precision.

Finally, we stress the size and complexity of the components involved in these experiments. The MS2 capsids are 2.5 MDa, spherical objects 27 nm in size, self-assembled from 180 protein monomers, covered in ssDNA, and containing chromophores inside on each monomer at specified locations. The DNA origami tiles are 4.8 MDa objects with dimension around 100 nm, comprised of hundreds of individual DNA strands self-assembled into a well-defined geometry. Yet these two components come together in a predictable manner, with high efficiency and specificity, under mild conditions in only 30 min. Furthermore, the conjugates can then be used to build higher order structures approaching a micrometer in length (for arrays of ten tiles, for example). We believe that the programmability of origami scaffolds and the ability to modify large protein constructs with single-stranded DNA will allow for the construction of increasingly complex and integrated biomolecular systems in the future, and pave the way for a variety of interesting nanotechnology applications.

2.7. References

(1) Douglas, T.; Young, M. *Science* **2006**, *312*, 873-875.

(2) Fischlechner, M.; Donath, E. *Angew. Chem., Int. Ed*. **2007**, *46*, 3184-3193.

(3) Wang, Q.; Lin, T.; Tang, L.; Johnson, J. E.; Finn, M. G. *Angew. Chem., Int. Ed.* **2002**, *41*, 459-462.

(4) Demir, M.; Stowell, M. H. B. *Nanotechnology* **2002**, *13*, 541-544.

(5) Schlick, T. L.; Ding, Z. B.; Kovacs, E. W.; Francis, M. B. *J. Am. Chem. Soc*. **2005**, *127*, 3718-3723.

(6) Miller, R. A.; Presley, A. D.; Francis, M. B. *J. Am. Chem. Soc*. **2007**, *121*, 3104-3109.

(7) Endo, M.; Wang, H.; Fujitsuka, M.; Majima, T. *Chem.-Eur. J.* **2006**, *12*, 3735-3740.

(8) Miller, R. A.; Stephanopoulos, N.; McFarland, J. M.; Rosko, A. S.; Geissler, P. L.; Francis, M. B. *J. Am. Chem. Soc*. **2010**, *132*, 6068-6074.

(9) Stephanopoulos, N.; Carrico, Z. M.; Francis, M. B. *Angew. Chem., Int. Ed*. **2009**, *48*, 9498-9502.

(10) Nam, Y. S.; Magyar, A. P.; Lee, D.; Kim, J.-W.; Yun, D. S.; Park, H.; Pollom, T. S.; Weitz, D. A.; Belcher, A. M. Nat. *Nanotechnol*. **2010**, *5*, 340-344.

(11) Douglas, T.; Young, M. J. *Nature* **1998**, *393*, 152-155.

(12) Douglas, T.; Strable, E.; Willits, D.; Aitouchen, A.; Libera, M.; Young, M. *Adv. Mater*. **2002**, *14*, 415-418.

(13) Loo, L.; Guenther, R. H.; Basnayake, V. R.; Lommel, S. A.; Franzen, S. *J. Am. Chem. Soc*. **2006**, *128*, 4502-4503.

(14) Loo, L.; Guenther, R. H.; Lommel, S. A.; Franzen, S. *J. Am. Chem. Soc*. **2007**, *129*, 11111-11117.

(15) Dixit, S. K.; Goicochea, N. L.; Daniel, M.-C.; Murali, A.; Bronstein, L.; De, M.; Stein, B.; Rotello, V. M.; Kao, C. C.; Dragnea, B. *Nano Lett*. **2006**, *6*, 1993-1999.

(16) Kovacs, E. W.; Hooker, J. M.; Romanini, D. W.; Holder, P. G.; Berry, K. E.; Francis, M. B. *Bioconjugate Chem*. **2007**, *18*, 1140-1147.

(17) Comellas-Aragone`s, M.; Escosura, A.; Dirks, A. J.; van der Ham, A.; Fusté-Cuñé, A.; Cornelissen, J. J. L. M.; Nolte, R. J. M. *Biomacromolecules* **2009**, *10*, 3141-3147.

(18) Abedin, M. J.; Liepold, L.; Suci, P.; Young, M.; Douglas, T. *J. Am. Chem. Soc*. **2009**, *131*, 4346-4354.

(19) Wu, W.; Hsiao, S. C.; Carrico, Z. M.; Francis, M. B. *Angew. Chem., Int. Ed*. **2009**, *48*, 9493-9497.

(20) Manchester, M.; Singh, P. Adv. *Drug Delivery Rev*. **2006**, *58*, 1505-1522.

(21) Suci, P. A.; Varpness, Z.; Gillitzer, E.; Douglas, T.; Young, M. *Langmuir* **2007**, *23*, 12280-12286.

(22) Flenniken, M.; Uchida, M.; Liepold, L.; Kang, S.; Young, M.; Douglas, T. *Viruses Nanotechnol*. **2009**, *327*, 71.

(23) Anderson, E. A.; Isaacman, S.; Peabody, D. S.; Wang, E. Y.; Canary, J. W.; Kirshenbaum, K. *Nano Lett*. **2006**, *6*, 1160-1164.

(24) Hooker, J. M.; Datta, A.; Botta, M.; Raymond, K. N.; Francis, M. B. *Nano Lett.* **2007**, *7*, 2207-2210.

(25) Hooker, J. M.; O'Neil, J. P.; Romanini, D. W.; Taylor, S. E.; Francis, M. B. *Mol. Imaging Biol*. **2008**, *10*, 182-191.

(26) Klem, M. T.; Willits, D.; Young, M.; Douglas, T. *J. Am. Chem. Soc*. **2003**, *125*, 10806-10807.

(27) Strable, E.; Johnson, J. E.; Finn, M. G. *Nano Lett*. **2004**, *4*, 1385-1389.

(28) Smith, J. C.; Lee, K.-B.; Wang, Q.; Finn, M. G.; Johnson, J. E.; Mrksich, M.; Mirkin, C. A. *Nano Lett*. **2003**, *3*, 883-886.

(29) Cheung, C. L.; Camarero, J. A.; Woods, B. W.; Lin, T.; Johnson, J. E.; De Yoreo, J. J. *J. Am. Chem. Soc*. **2003**, *125*, 6848-6849.

(30) Rothemund, P. W. K. *Nature* **2006**, *440*, 297-302.

(31) Ding, B.; Deng, Z.; Yan, H.; Cabrini, S.; Zuckermann, R. N.; Bokor, J. *J. Am. Chem. Soc*. **2010**, *132*, 3248-3249.

(32) Sharma, J.; Chhabra, R.; Andersen, C. S.; Gothelf, K. V.; Yan, H.; Liu, Y. *J. Am. Chem. Soc*. **2008**, *130*, 7820-7821.

(33) Pal, S.; Deng, Z.; Ding, B.; Yan, H.; Liu, Y. *Angew. Chem., Int. Ed*. **2010**, *122*, 2760-2764.

(34) Ke, Y.; Lindsay, S.; Chang, Y.; Liu, Y.; Yan, H. *Science* **2008**, *319*, 180-183.

(35) Maune, H. T.; Han, S.; Barish, R. D.; Bockrath, M.; Goddard III, W. A.; Rothemund, P. W. K.; Winfree, E. *Nat. Nanotechnol*. **2010**, 5, 61-66.

(36) Rinker, S.; Ke, Y.; Liu, Y.; Chhabra, R.; Yan, H. *Nat. Nanotechnol*. **2008**, *3*, 418-422.

(37) Chabra, R.; Sharma, J.; Ke, Y.; Liu, Y.; Rinker, S.; Lindsay, S.; Yan, H. *J. Am. Chem. Soc*. **2007**, *129*, 10304-10305.

(38) Shen, W.; Zhong, H.; Neff, D.; Norton, M. L. *J. Am. Chem. Soc*. **2009**, *131*, 6660-6661.

(39) Kuzuya, A.; Kimura, M.; Numajiri, K.; Koshi, N.; Ohnishi, T.; Okada, F.; Komiyama, K. *ChemBioChem* **2009**, *10*, 1811-1815.

(40) Hooker, J. M.; Kovacs, E. W.; Francis, M. B. *J. Am. Chem. Soc*. **2004**, *126*, 3718-3719.

(41) Valegård, K.; Liljas, L.; Fridborg, K.; Unge, T. *Nature* **1990**, *345*, 36-41.

(42) Mastico, R. A.; Talbot, S. J.; Stockley, P. G. *J. Gen. Virol*. **1993**, *74*, 541-548.

(43) Tong, G. J.; Hsiao, S. C.; Carrico, Z. M.; Francis, M. B. *J. Am. Chem. Soc*. **2009**, *131*, 11174-11178.

(44) Mehl, R. A.; Anderson, J. C.; Santoro, S. W.; Wang, L.; Martin, A. B.; King, D. S.; Horn, D. M.; Schultz, P. G. *J. Am. Chem. Soc*. **2003**, *125*, 935-939.

(45) Le, J. D.; Pinto, Y.; Seeman, N. C.; Musier-Forsyth, K.; Taton, T. A.; Kiehl, R. A. *Nano Lett*. **2004**, *4*, 2343-2347.

Chapter 3

Organization of Multienzyme Reaction Pathways: Interenzyme Substrate Diffusion for an Enzyme Cascade Organized on Spatially Addressable DNA Nanostructures

Adapted with permission from Fu, J.; Liu, M.; Liu, Y.; Woodbury, N. W.; Yan, H. Interenzyme Substrate Diffusion for an Enzyme Cascade Organized on Spatially Addressable DNA Nanostructures. *J. Am. Chem. Soc*. **2012**, *134*, 5516-5519.

3.1. Abstract

Spatially addressable DNA nanostructures facilitate the self-assembly of heterogeneous elements with precisely controlled patterns. In this chapter we organized discrete glucose oxidase (GOx)/ horseradish peroxidase (HRP) enzyme pairs on specific DNA origami tiles with controlled interenzyme spacing and position. The distance between enzymes was systematically varied from 10 to 65 nm, and the corresponding activities were evaluated. The study revealed two different distance-dependent kinetic processes associated with the assembled enzyme pairs. Strongly enhanced activity was observed for those assemblies in which the enzymes were closely spaced, while the activity dropped dramatically for enzymes as little as 20 nm apart. Increasing the spacing further resulted in a much weaker distance dependence. Combined with diffusion modeling, the results suggest that Brownian diffusion of intermediates in solution governed the variations in activity for more distant enzyme pairs, while dimensionally limited diffusion of intermediates across connected protein surfaces contributed to the enhancement in activity for closely spaced GOx/HRP assemblies. To further test the role of limited dimensional diffusion along protein surfaces, a noncatalytic protein bridge was

inserted between GOx and HRP to connect their hydration shells. This resulted in substantially enhanced activity of the enzyme pair.

3.2. Introduction

Cellular activities are directed by complex, multienzyme synthetic pathways that exhibit extraordinary yield and specificity. Many of these enzyme systems are spatially organized to facilitate efficient diffusion of intermediates from one protein to another by substrate channeling[1, 2] and enzyme encapsulation.[3, 4] Understanding the effect of spatial organization on enzymatic activity in multienzyme systems is not only fundamentally interesting, but also important for translating biochemical pathways to noncellular environments. Despite the importance, there are very few methods available to systematically evaluate how spatial factors (e.g., position, orientation, enzyme ratio) influence enzymatic activity in multienzyme systems.

DNA nanotechnology has emerged as a reliable way to organize nanoscale systems because of the programmability of DNA hybridization and versatility of DNA-biomolecule conjugation strategies.[5-7] The *in vitro* and *in vivo* assembly of several enzymatic networks organized on two-dimensional DNA and RNA arrays[8, 9] or simple DNA double helices[10, 11] has led to the enhancement of catalytic activities. Nevertheless, the nucleic acid scaffolds used in these studies are limited in their ability to study spatial parameters in multienzyme systems because of the lack of structural complexity. The development of the DNA origami method[12] provides an addressable platform upon which to display nucleic acids or other ligands, permitting the precise patterning of multiple proteins or other elements.[13] In this chapter we report a study of the distance-dependence

for the activity of glucose oxidase (GOx)/horseradish peroxidase (HRP) cascade by assembling a single GOx/HRP pair on a discrete, rectangular DNA origami tile.

3.3. Materials and Methods

3.3.1. Chemicals. See APPENDIX B

3.3.2. Protein-DNA Conjugation. SPDP was used to crosslink GOx and HRP with DNA strands. GOx was linked to Poly$(T)_{22}$ (5'-HS-TTTTTTTTTTTTTTTTTTTTT-3') and HRP was linked to Poly$(GGT)_6$ (5'-HS-TTGGTGGTGGTGGTGGTGGT-3').

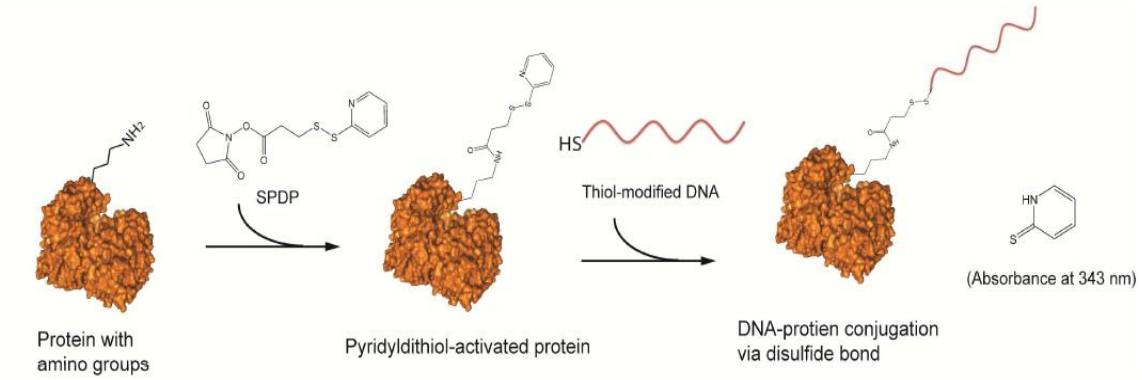

Figure 3.1. Protein-DNA conjugation using a SPDP crosslinker (GOx demonstrated).

As shown in Figure 3.1, 100 µl of 40 µM enzyme solution was first reacted with a 20-fold excess of SPDP in 1×PBS (pH 8) for two hours, allowing amine-reactive N-hydroxysuccinimide (NHS) esters to react with the lysine residues on the protein surface. Excess SPDP was removed by washing, and filtered using Amicon 30 kD cutoff filters. Next, SPDP-modified protein was conjugated to thiolmodified DNA (10-fold excess) through a disulfide bond exchange of the activated pyridyldithiol group. The reaction mixture was incubated in 1×PBS (pH 8) for two hours. The coupling efficiency was

evaluated by monitoring the increase in absorbance at 343 nm due to the release of pyridine-2-thione (extinction coefficient: 8080 M^{-1} cm^{-1}) as shown in Figure 3.2.

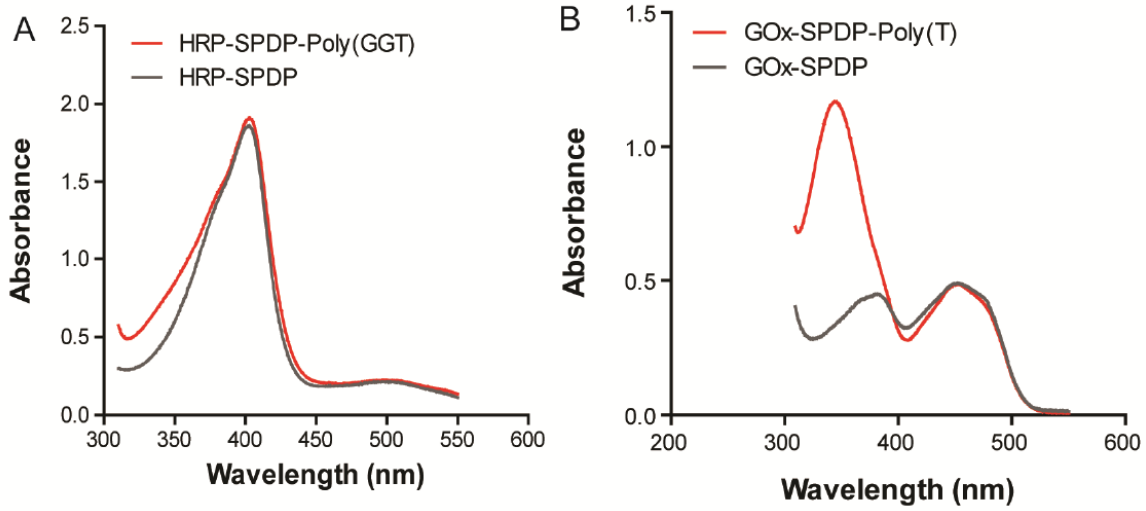

Figure 3.2. Quantification of protein-DNA conjugation efficiency via absorbance spectra. (A) HRP-poly(GGT)6 conjugation: ΔA343 before and after poly$(GGT)_6$ conjugation is ~ 0.266 (extinction coefficient: 8080 M-1 cm-1), corresponding to 33 μM poly$(GGT)_6$ coupled with 19 μM HRP (ε=100000 M^{-1} cm^{-1} at 403 nm for HRP). (B) GOx-poly$(T)_{22}$ conjugation: ΔA343 before and after poly$(T)_{22}$ conjugation is ~ 0.8352, corresponding to 100 μM poly(T)22 coupled with 18 μM GOx (ε=28200 M^{-1} cm^{-1} at 452 nm for GOx). GOx has ~ 30 lysine residues, resulting in a higher ratio of DNA-protein conjugates.

Finally, the excess DNA was removed by washing, and filtered using Amicon 30 kD cutoff filters (see APPENDIX B). The enzymatic activities of DNA-modified GOx and HRP were ~ 75% of the activities of the unmodified enzymes (Figure 3.3).

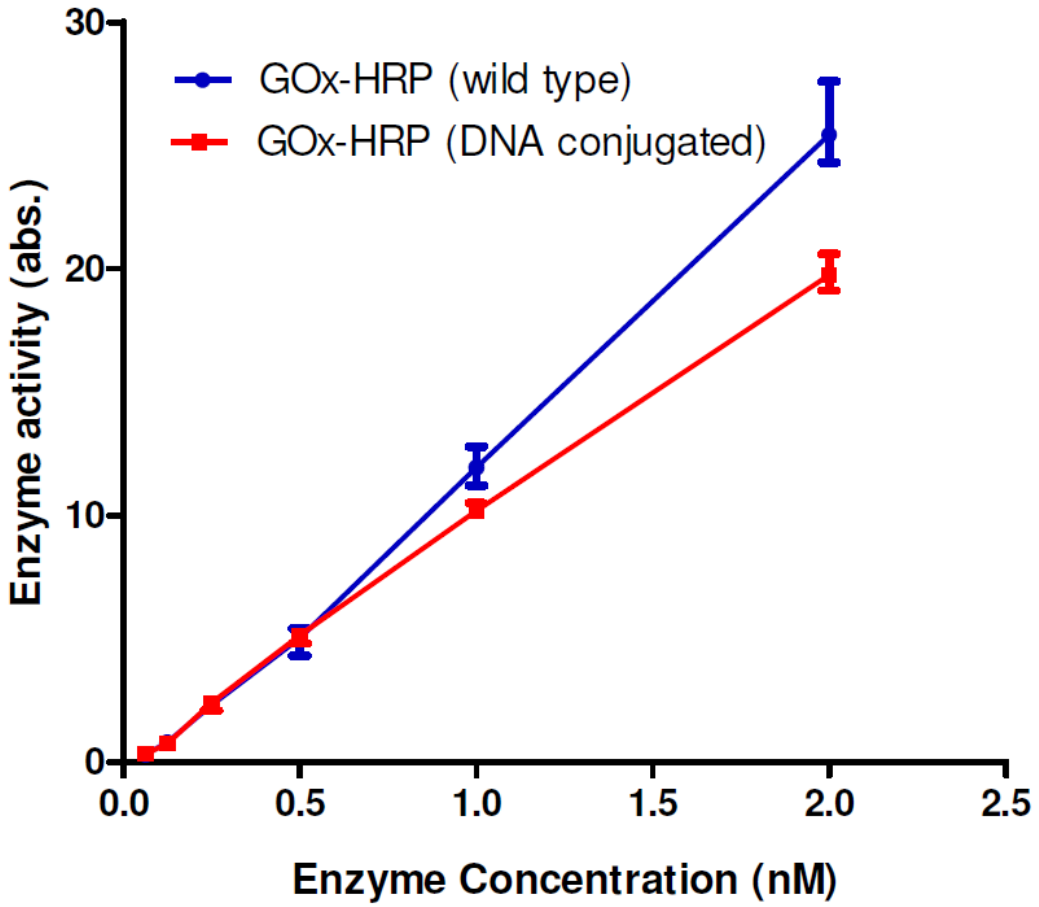

Figure 3.3. Enzyme activity vs. concentration for both DNA-modified GOx/HRP cascades and unmodified enzymes.

3.3.3. DNA Origami Preparation. Rectangular DNA origami tiles were prepared in 1×TAE-Mg^{2+} buffer (40 mM Tris, 20 mM acetic acid, 2 mM EDTA and 12.5 mM magnesium acetate, pH 8.0) using established protocols.[14] For each sample, 20 nM single-stranded M13mp18 DNA (7249 nucleotides) was mixed with a 5-fold molar excess of staple stands and a 10-fold molar excess of probe strands. The mixture was annealed from 95 ℃ to 4 ℃ with the temperature gradient for ~ 10 hours. The excess staple strands were removed by repeated (3 times) washing in 1×TAE-Mg^{2+} buffer (pH 7.5) and filtered using 100 kD 500 μL Amicon filters. The purity of the origami tiles was

analyzed by agarose gel electrophoresis. The concentration of the DNA origami tiles was quantified by absorbance at 260 nm, assuming an extinction coefficient of ~ 109119009 $M^{-1}cm^{-1}$. For detailed sequence design, please see APPENDIX B.

3.3.4. GOx/HRP Co-assembly on DNA Origami Tiles. GOx-poly(T) and HRP-poly(GGT) were mixed with DNA origami tiles in 1×TAE-$Mg2^{+}$ buffer (pH 7.5) with a molar ratio of 3:1. The solution mixture was cooled from 37℃ to 4℃ with the following temperature gradient: 37℃ for 5 min; 36-10℃, 2 min per degree; 4℃ for storing the solution.

3.3.5. Enzyme Assay. 10 nM GOx-HRP origami tiles were diluted to 1 nM for activity assays, which were performed on a SpectraMax M5 96 well plate reader (Molecular Device, Sunnyvale, CA). GOx-HRP cascade activity was measured in 1×TBS (tris buffered saline, pH 7.5) and 1 mM $MgCl_2$ in presence of 1 mM Glucose and 2 mM ABTS by monitoring the increase in absorbance at 410 nm. At least three replicates of each sample were measured.

3.4. Results and Discussion

3.4.1. DNA Origami-directed Coassembly of GOx and HRP enzymes with Control over Interenzyme Distances. The DNA-directed co-assembly of GOx and HRP on DNA origami tiles is illustrated in Figure 3.4A. The DNA-conjugated rectangular DNA origami tiles (~60 × 80 nm) by hybridizing with the corresponding complementary strands displayed on the surface of the origami scaffolds. Four different rectangular origami tiles were prepared with interenzyme probe distances (distance between two protein-binding sites) of 10 nm (S1), 20 nm (S2), 45 nm (S3), and 65 nm (S4). To achieve high coassembly yields of the GOx/HRP pairs, a 3-fold excess of enzymes were

incubated with the DNA tiles. The coassembly of the GOx/HRP cascade was visualized using AFM imaging of DNA nanostructures. The presence of a protein results in a higher region than the surrounding surface of the origami tile (see APPENDIX B for height profiles). Most origami tiles were deposited on the mica surface with the protein decorated side facing up, likely because of the strong interaction (charge or stacking) of the opposite flat side with the mica surface.

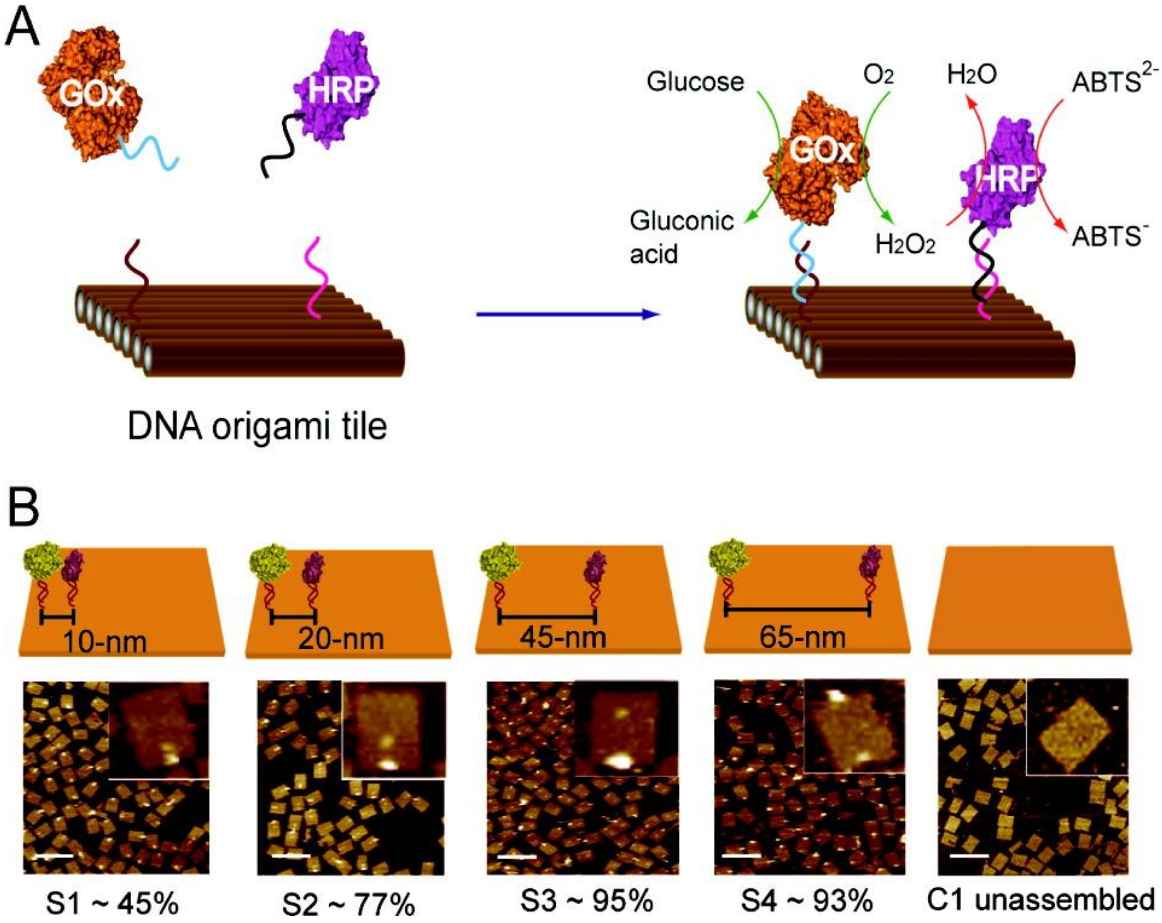

Figure 3.4. DNA nanostructure-directed coassembly of GOx and HRP enzymes with control over interenzyme distances. (A) The assembly strategy and details of the GOx/HRP enzyme cascade. (B) Rectangular DNA origami tiles with assembled

Gox/HRP pairs spacing from 10 to 65 nm. GOx/HRP coassembly yields were determined from AFM images as shown in the bottom panel. Scale bar: 200 nm.

As shown in Figure 3.4B, high coassembly yields of GOx/HRP pairs on DNA origami tiles were achieved for longer interenzyme distances, with ~95% for S3 (45 nm) and ~93% for S4 (65 nm). For shorter distances, the coassembly of GOx/HRP pairs was less efficient because of the steric hindrance between two nearby enzymes, with ~45% for S1 (10 nm) and ~77% for S2 (20 nm). To rule out any nonspecific absorption of the enzymes to the tile surfaces, a control experiment was performed where tiles without any nucleic acid probes (C1) were incubated with DNA modified GOx and HRP, and no binding of the enzymes to the tiles was observed.

3.4.2. Spacing Distance-dependent Effect of Assembled GOx/HRP Pairs. The activities of the enzyme complexes, containing all components of GOx/HRP coassembled on DNA tiles, unbound enzymes and free DNA tiles were measured in the presence of substrates glucose and $ABTS^{2-}$ by monitoring the increase in absorbance at 410 nm (Figure 3.5A). The S1 (10 nm) tile solution exhibited the highest enzyme activity, which was more than 2 times greater than the activity of the S2 (20 nm) tile solution (Figure 3.5B), even though the coassembly yield of GOx/HRP pairs was significantly lower for S1 tiles. Increasing the distance between GOx and HRP from 20 to 65 nm resulted in a small decrease in the raw enzyme activity (~10%). A similar distance-dependent trend in activity was also observed in additional interenzyme distance-dependence studies using a different attachment scheme (see APPENDIX B). All samples containing assembled GOx/HRP tiles exhibited higher activities than unassembled enzyme controls, demonstrating how arranging the enzymes in close proximity results in enhanced activity.

Further, the control solutions (with free enzymes and unbound DNA tiles) had similar activities as free enzymes without any DNA nanostructures, confirming that a DNA-nanostructure environment does not affect enzyme activity under the conditions used.

Both the raw activity (uncorrected for the yield of the completely assembled nanostructures) and yield-corrected activity are shown. The activity correction for assembly yields was performed using equation 1.

$$A_{\text{raw}} = \frac{Y_{\text{assem}}}{3} A_{\text{assem}} + \frac{3 - Y_{\text{assem}}}{3} A_{\text{unassem}} \quad (1)$$

Equation 1 above was used to adjust the activities to account for the differences in yields of coassembled enzymes. In eq 1, the raw activity (A_{raw}) consists of contributions from both assembled GOx/HRP cascades (A_{assem}) and unassembled enzyme (A_{unassem}), where Y_{assem} is the coassembly yield of GOx/HRP pairs on the origami tiles. Because a 3:1 ratio of enzymes to origami tiles was used for the assembly, the percentage of assembled enzymes was $\sim(Y_{\text{assem}}/3)$, while the percentage of unassembled enzymes was $\sim((3 - Y_{\text{assem}})/3)$. The resulting calibrated activities are presented in Figure 3.5B. The largest enhancement in activity was observed for enzymes with 10 nm spacing, which was more than 15 times higher than the corresponding control. A sharp decrease in cascade activity occurred as the interenzyme distance was increased from 10 to 20 nm, followed by a slow and gradual decrease in activity as the distance was further increased to 65 nm.

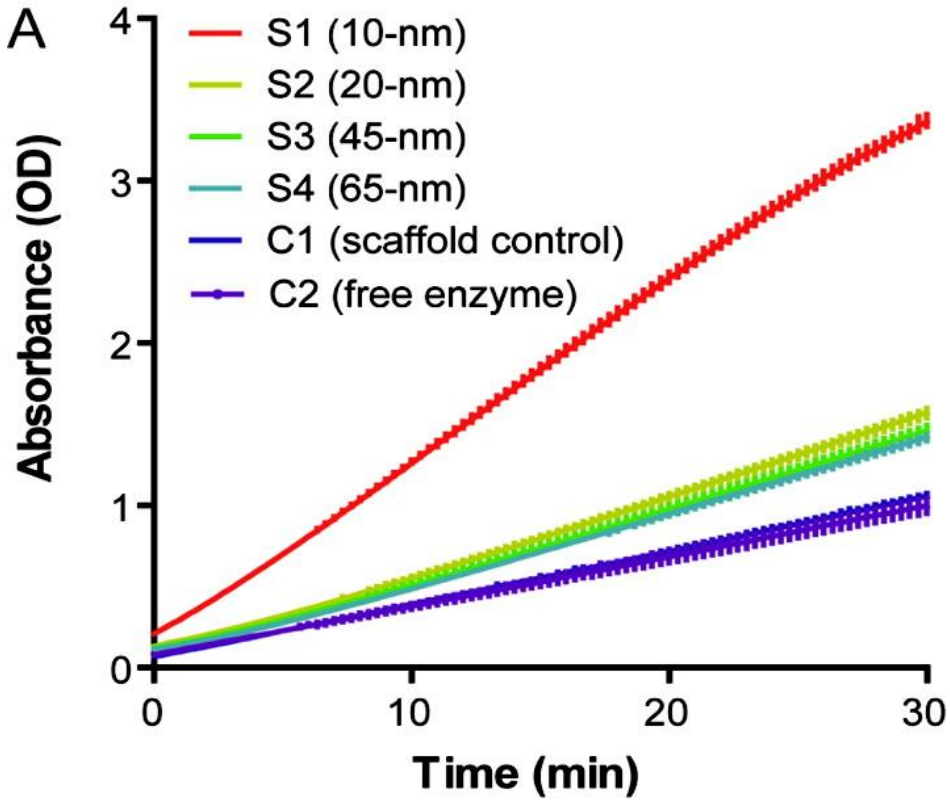
A
S1 (10-nm)
S2 (20-nm)
S3 (45-nm)
S4 (65-nm)
C1 (scaffold control)
C2 (free enzyme)
Absorbance (OD)
0
1
2
3
4
0
10
20
30
Time (min)

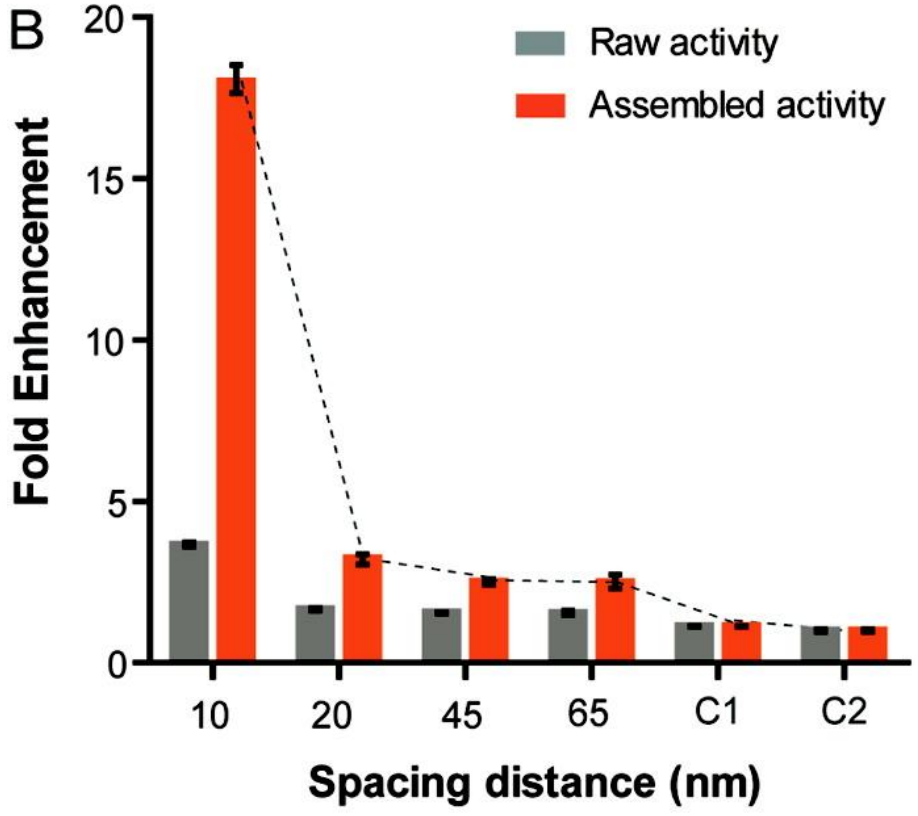
B
Raw activity
Assembled activity
Fold Enhancement
0
5
10
15
20
10
20
45
65
C1
C2
Spacing distance (nm)

Figure 3.5. Spacing distance-dependent effect of assembled GOx/HRP pairs as illustrated by (A) plots of product concentration vs time for various nanostructured and free enzyme samples and (B) enhancement of the activity of the enzyme pairs on DNA nanostructures compared to free enzyme in solution.

3.4.3. Brownian Model of H_2O_2 Diffusion. For a GOx/HRP cascade, effective transfer of the intermediate H_2O_2 between the enzymes is essential to the cascade activity (Figure 3.6A).

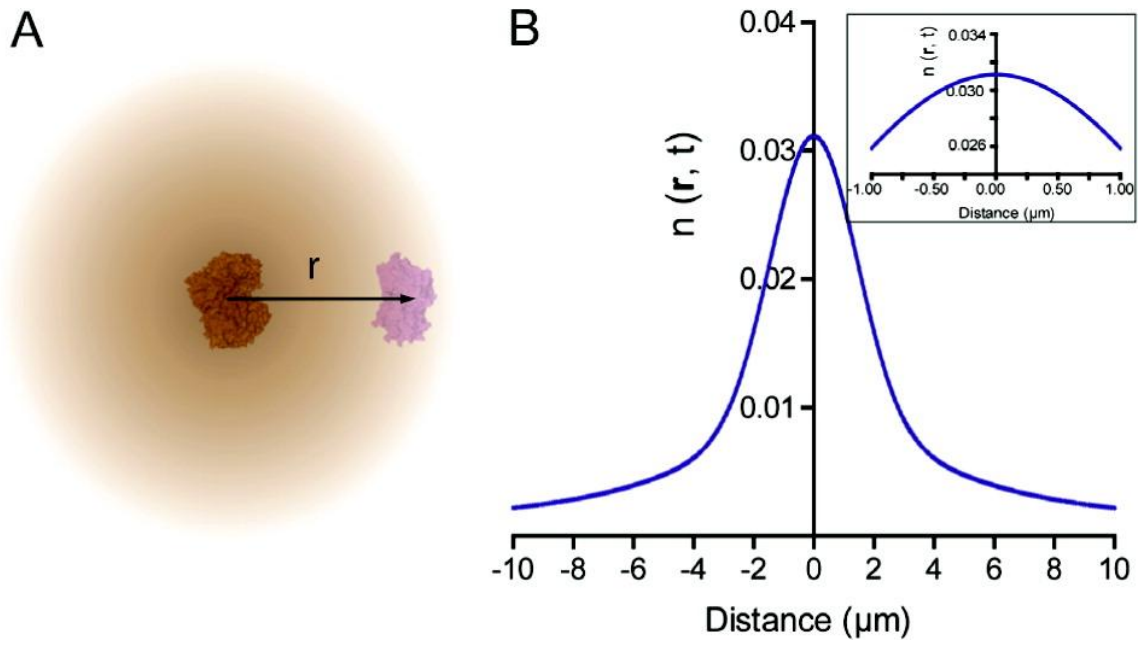

Figure 3.6. Model of H_2O_2 diffusion in a single GOx/HRP pair. (A) Simplified illustration of the distance-dependent (r) H_2O_2 concentration gradient resulting from 3D Brownian diffusion. (B) Simulated H_2O_2 concentration gradient as a function of distance between GOx and HRP using equation 3 with the following parameters: diffusion coefficient ~1000 $\mu m^2/s$; k_{cat} (GOx) ~300 s^{-1}; and the integration time ~1 s. Inset shows the enlarged distance-dependent H_2O_2 concentration gradient within 1 μm.

$$n(\boldsymbol{r},t) = \frac{1}{(4\pi Dt)^{\frac{3}{2}}} * \exp\left(-\frac{r^2}{4Dt}\right) \quad (2)$$

$$n(\boldsymbol{r},t) = \sum_{i=0}^{i=\frac{t}{\tau}-1} \frac{1}{(4\pi D(t-i*\tau))^{\frac{3}{2}}} * \exp\left(-\frac{r^2}{4D(t-i*\tau)}\right) \quad (3)$$

Here, we use Brownian motion to simulate the distance-dependent, three-dimensional (3D) diffusion of H_2O_2 between enzymes as described by equation 2, where $n(r,t)$ is the concentration of H_2O_2 at a distance r from the initial position, D is the diffusion coefficient, and t is the diffusion time.[15] GOx is assumed to generate H_2O_2 at a constant rate, k_{cat}. Equation 3 describes the convolution function of Brownian motion of H_2O_2 with a constant catalytic rate for a GOx/HRP pair in the given time t, where τ is the average time between GOx turnovers ($1/ k_{cat}$). Figure 3.6B shows the simulation result using the following parameters: D = 1000 μm^2/s for H_2O_2,[16,17] k_{cat} = 300 s^{-1} for GOx (Figure 3.7), and t = 1 s.

Because of the rapid diffusion of H_2O_2 in water, the concentration of H_2O_2 drops off only slightly within a few hundred nanometers of GOx. If one assumes that the activity is linear with substrate concentration, this simulation result agrees with the observation that assembled GOx/HRP cascades exhibit only small variations in activity for interenzyme distances between 20 and 65 nm. For a 1 nM solution of unassembled enzymes, the average spacing between proteins is ~1.2 μm, where the H_2O_2 concentration is ~60% of the initial position in the simulation.

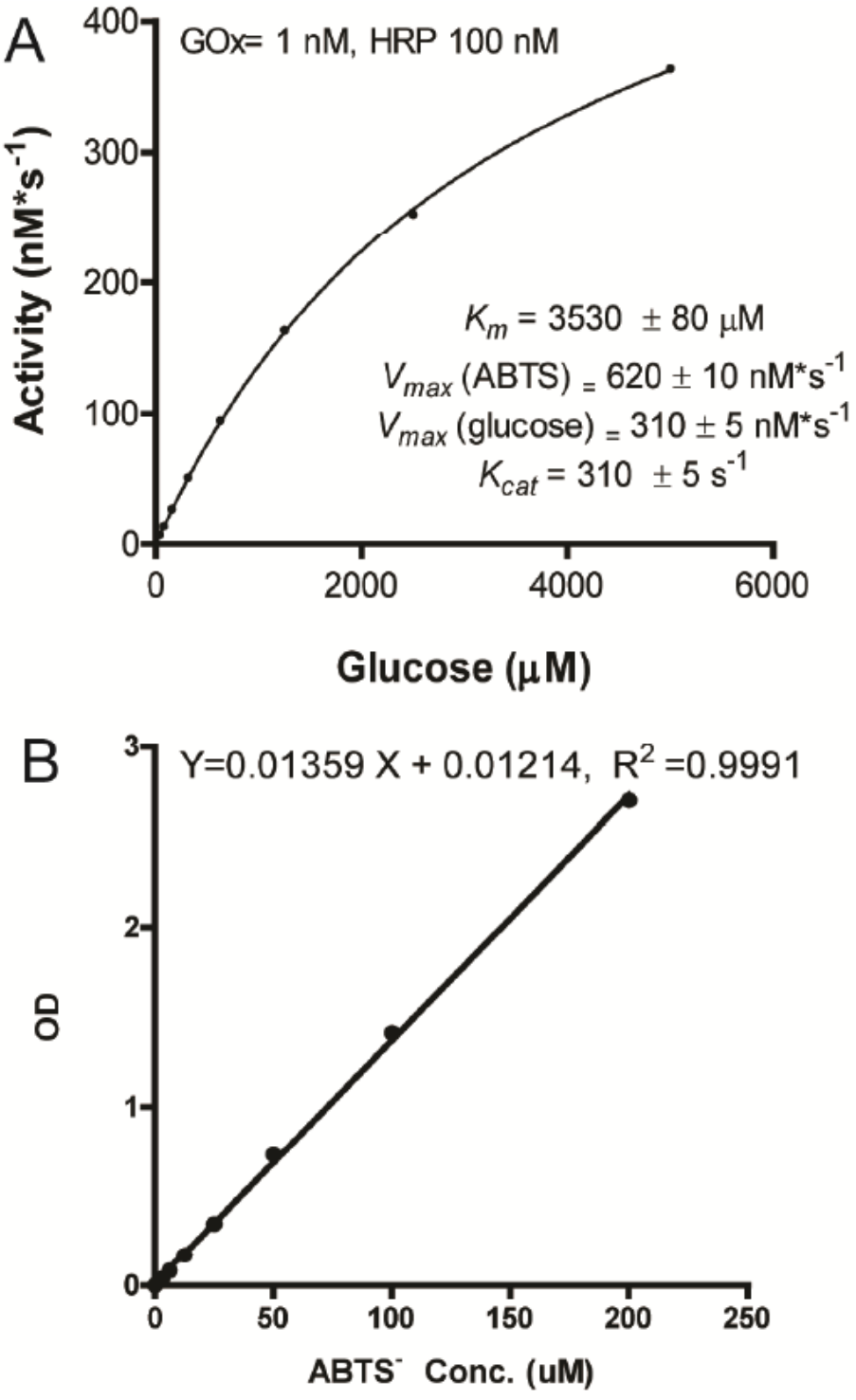

Figure 3.7. Michaelis constants of GOx and standard OD curve for $ABTS^-$ (A) Determining the Michaelis constants of GOx using a cascade detection of 1 nM GOx and

100 nM HRP. Glucose concentration is varied from 40 uM to 5 mM and $ABTS^{2-}$ is kept at 5 mM for the assay. In GOx/HRP cascade detection, one mole of glucose generates one mole of H_2O_2, oxidizing two mole $ABTS^{2-}$ to $ABTS^{-}$.[18] (B) Standard OD curve versus $ABTS^{-}$ concentration.

This result is consistent with the limited activity enhancement (less than 2-fold) for distantly spaced GOx/HRP pairs (e.g., 45 or 65 nm) compared to unassembled enzymes in Figure 3.5. Further, if the intermediate transfer between distantly spaced enzymes is dominated by Brownian motion, diluting the sample will result in a decreased H_2O_2 concentration for free HRP, while the H_2O_2 concentration near HRP in the assembled complexes remains nearly constant. Thus greater activity enhancement will be observed for assembled GOx/HRP pairs relative to the free enzymes under these conditions. This concentration-dependent enhancement was confirmed by performing the assay at a range of GOx/HRP concentrations (Figure 3.8).

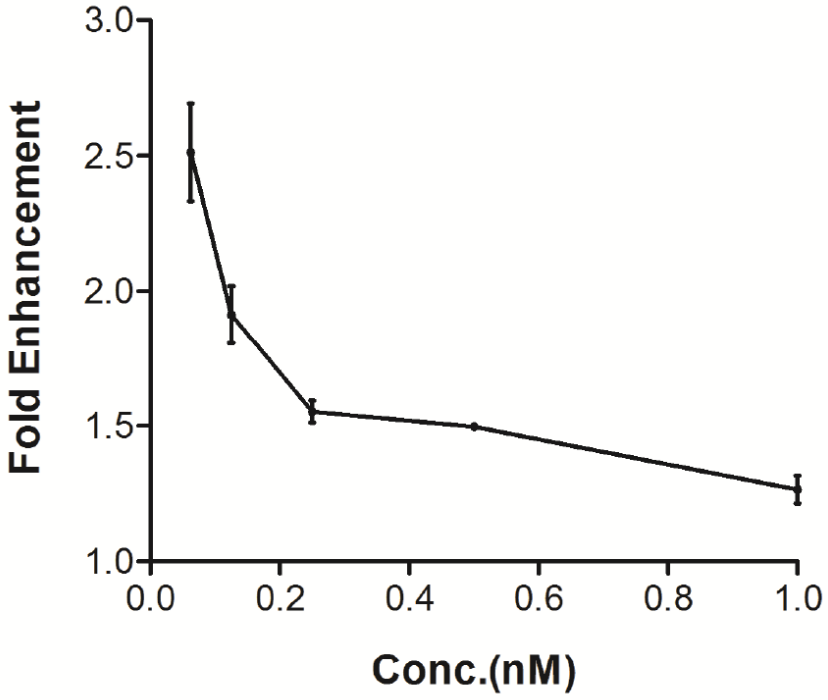

Figure 3.8. Concentration-dependent enhancement in activity for assembled GOx/HRP tiles with 45-nm inter-enzyme distance as compared to unscaffolded enzymes. The expected interenzyme distance in solution for unscaffolded enzymes is noted above with corresponding concentrations. For assembled GOx/HRP tiles, the inter-enzyme is independent of the concentration. The inter-enzyme distance for unassembled enzymes becomes larger as the concentration decreases. Therefore, a greater enhancement in the activity of assembled enzymes is observed at lower enzyme concentrations.

3.4.4. Surface-limited H_2O_2 Diffusion Induced by a Protein Bridge. While the Brownian diffusion model is consistent with the interenzyme distance dependence of the activity at distances greater than 20 nm, the strong activity enhancement for GOx/HRP pairs spaced 10 nm apart cannot be explained by this model. Apparently, the transfer of H_2O_2 between closely spaced enzymes is governed by a different mechanism than that for more distantly spaced enzymes. Since both GOx and HRP are randomly oriented on the DNA origami tiles, it is unlikely that the active sites of GOx and HRP are perfectly aligned to allow the direct transfer of H_2O_2 between active sites. It seems more likely that when GOx and HRP are spaced in very close proximity, the two protein surfaces become essentially connected with one another, as demonstrated by AFM imaging of S1 tiles for 10 nm interenzyme spacing (Figure 3.4B). One possibility is that under these circumstances, H_2O_2 does not generally escape into the bulk solution but instead transfers from GOx to HRP along their mutual, connected protein surface, providing a dimensionally limited diffusion mechanism that dominates over three-dimensional diffusion when the two enzymes are essentially in contact. In support of this concept, it is known that water molecules are translationally and rotationally constrained in the

hydration layer around a protein, relative to bulk solution, because of hydrogen bonding and Coulombic interactions with the protein.[19] Some simulation results have suggested that H_2O_2 also has an affinity for protein surfaces resulting in an even longer residence time in the hydration layer near the protein than water.[20,21] In addition, dimensionally limited diffusion has been observed in a number of biochemical systems, resulting in decreased times for diffusion of a substrate or ligand to its point of action.[1] Examples include linear diffusion of nuclease or transcription factors along DNA[22,23] and the surface-attached "lipoyl swing arm" in the pyruvate dehydrogenase complex.[2]

If the enhancement seen in Figure 3.5 at 10 nm interenzyme distance is in fact due to dimensionally restricted diffusion along protein surfaces, it should be possible to enhance the activity observed at longer interenzyme distances by placing a protein bridge between the enzymes. To test this, we designed a 'bridge-based' cascade in which a noncatalytic protein was inserted between GOx and HRP, in order to connect the protein hydration shells and facilitate the surface-limit diffusion of H_2O_2.

As shown in Figure 3.9A, a GOx/HRP pair was first assembled on a DNA origami tile with a 30 nm interenzyme distance. Next, a noncatalytic protein, either neutravidin (NTV) or streptavidin (STV)-conjugated β-galactosidase (β-Gal), was inserted between the enzymes. As shown in Figure 3.9B, assembled GOx/HRP pairs with a β-Gal bridge exhibited $\sim 42 \pm 4\%$ higher raw activity than control assemblies without the bridge.

STV conjugated β-Gal and NTV in solution did not affect GOx/HRP activities (Figure 3.10).

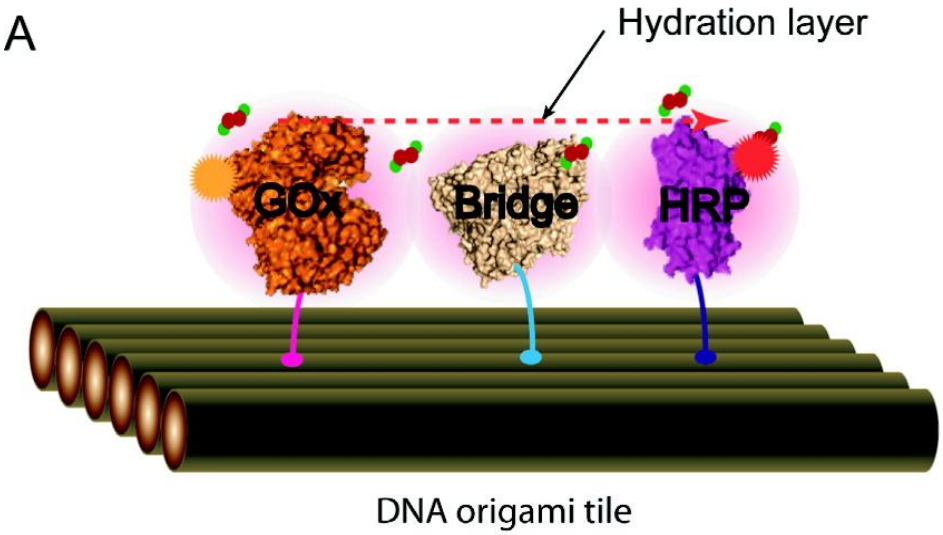

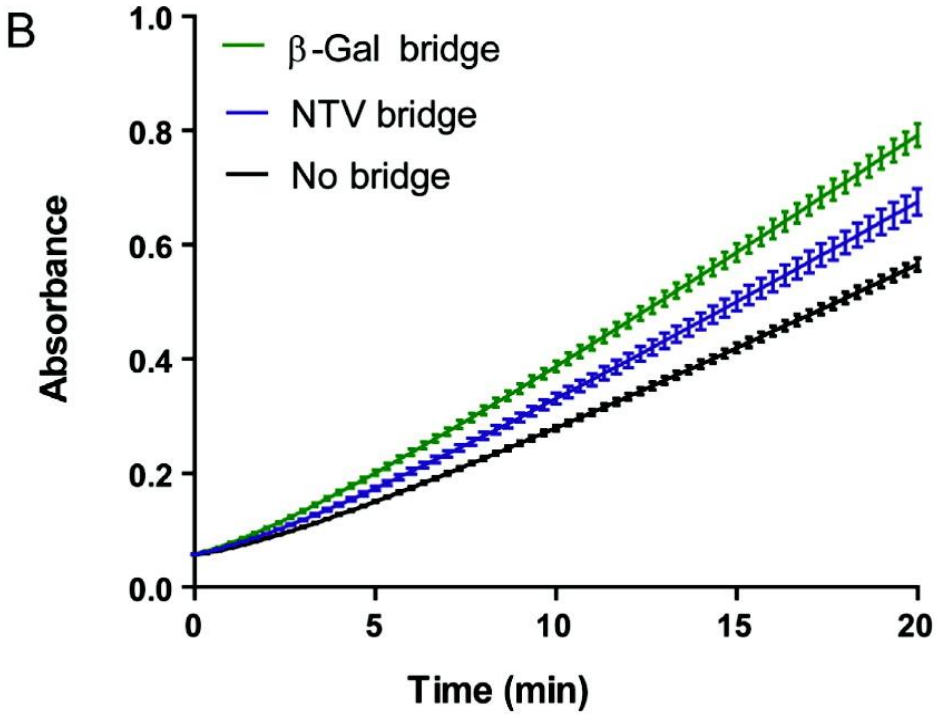

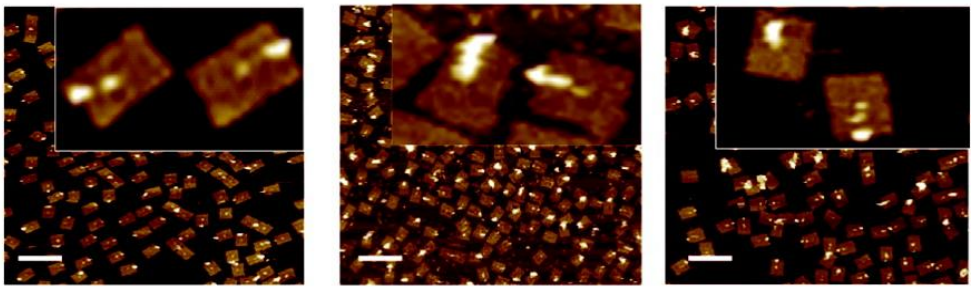

GOx-HRP with 30-nm spacing
~ 85% co-assembly yield

GOx-HRP with β-Gal bridge
~ 38% co-assembly yield

GOx-HRP with NTV bridge
~ 50% co-assembly yield

Figure 3.9. Surface-limited H_2O_2 diffusion induced by a protein bridge. (A) The design of an assembled GOx/HRP pair with a protein bridge used to connect the hydration surfaces of GOx and HRP. (B) Enhancement in the activity of assembled GOx/HRP pairs with β-Gal and NTV bridges compared to unbridged GOx/HRP pairs. AFM images of GOx/HRP pairs with and without protein bridges were used to estimate the coassembly yield. Scale bar: 200 nm.

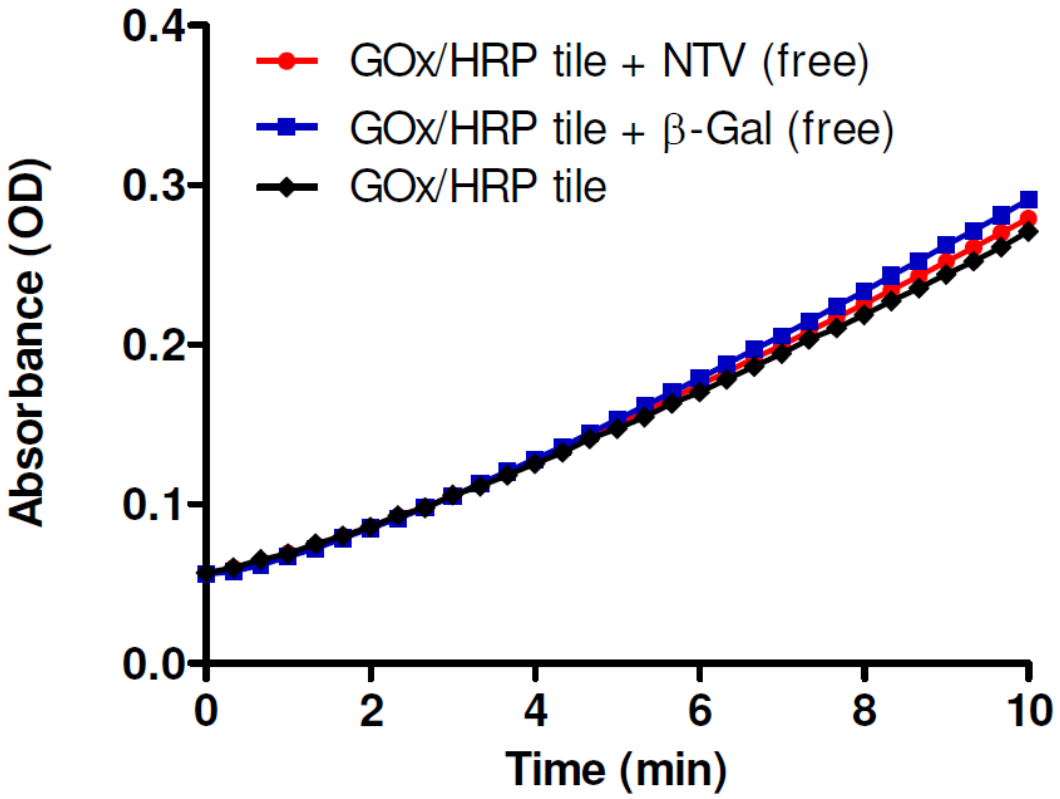

Figure 3.10. Control experiments to evaluate the effect of free NTV and β-Gal on the assembly of GOx/HRP tiles. (black) 1 nM assembled GOx/HRP tiles with 30-nm inter-enzyme distance; (blue) 1 nM assembled GOx/HRP tiles + 3 nM free β-Gal streptavidin conjugate; (red) 1 nM assembled GOx/HRP tiles + 3 nM free NTV. Note, no biotin probe between the assembled GOx and HRP was present for these experiments.

With a larger protein diameter (~16 nm), β-Gal can fill the space between GOx and HRP more completely than NTV (~6 nm diameter), resulting in a more enhanced activity for the β-Gal bridge even with a lower coassembly yield (see APPENDIX B). This result supports the notion that surface-limited diffusion of H_2O_2 between closely spaced enzymes is responsible for the increase in cascade activity beyond what is possible by three-dimensional Brownian diffusion.

3.5. Conclusion

In conclusion, we have systematically studied the activity of a GOx/HRP cascade spatially organized on a DNA nanostructure as a function of interenzyme distance. The intermediate transfer of H_2O_2 between enzymes was found to follow the surface-limited diffusion for closely spaced enzymes, while 3D Brownian diffusion dominated H_2O_2 transfer between enzymes with larger spacing distances. These studies imply that the strong activity enhancement observed for assembled enzyme cascades is not simply achieved by reducing the interenzyme distance to reach high local molecule concentration, but also results from restricting diffusion of intermediates to a two-dimensional surface connecting the enzymes. While it is possible that some coassembled GOx/HRP pairs are aligned in such a way that their active sites are juxtaposed, facilitating H_2O_2 transfer between enzyme pockets, there was no specific attempt to orient the enzymes in this study. In the future, it will be important to study the effect of enzyme orientation on the activity of assembled enzyme complexes as well.[24] With the further development of DNA-protein attachment chemistry through site-specific conjugation or ligand capture,[25,26] it should be possible to start to direct the flow of

substrate molecules between active sites using some of the concepts and tools discussed above.

3.6. References

(1) Miles, E. W.; Rhee, S.; Davies, D. R. *J. Biol. Chem*. **1999**, *274*,12193.

(2) Perham, R. N. *Annu. Rev. Biochem*. **2000**, *69*, 961.

(3) Srere, P. A.; Mosbach, K. *Annu. Rev. Microbiol*. **1974**, *28*, 61.

(4) Yeates, T. O.; Kerfeld, C. A.; Heinhorst, S.; Cannon, G. C.; Shively, J. M. *Nat. Rev. Microbiol*. **2008**, *6*, 681.

(5) Lin, C.; Liu, Y.; Yan, H. *Biochemistry* **2009**, *48*, 1663.

(6) Seeman, N. C. *Annu. Rev. Biochem*. **2010**, *79*, 65.

(7) Voigt, N. V.; Torring, T.; Rotaru, A.; Jacobsen, M. F.; Ravnsbaek, J. B.; Subramani, R.; Mamdouh, W.; Kjems, J.; Mokhir, A.; Besenbacher, F.; Gothelf, K. V. *Nat. Nanotechnol*. **2010**, *5*, 200.

(8) Wilner, O. I.; Weizmann, Y.; Gill, R.; Lioubashevski, O.; Freeman, R.; Willner, I. *Nat. Nanotechnol*. **2009**, *4*, 249.

(9) Delebecque, C. J.; Lindner, A. B.; Silver, P. A.; Aldaye, F. A. *Science* **2011**, *333*, 470.

(10) Niemeyer, C. M.; Koehler, J.; Wuerdemann, C. *ChemBioChem* **2002**, *3*, 242.

(11) Erkelenz, M.; Kuo, C. H.; Niemeyer, C. M. *J. Am. Chem. Soc*. **2011**, *133*, 16111.

(12) Rothemund, P. W. K. *Nature* **2006**, *440*, 297.

(13) Pinheiro, A. V.; Han, D.; Shih, W. M.; Yan, H. *Nat. Nanotechnol*. **2011**, *6*, 763.

(14) Ke, Y.; Lindsay, S.; Chang, Y.; Liu, Y.; Yan, H. *Science* **2008**, *319*, 180.

(15) Pathria, R. K. *Statistical Mechanics*, 2nd ed.; Butterworth- Heinemann: Woburn, MA, **1996**; pp 459−464.

(16) Henzler, T.; Steudle, E. *J. Exp. Bot*. **2000**, *51*, 2053.

(17) Stewart, P. S. *J. Bacteriol*. **2003**, *185*, 1485.

(18) Childs, R. E.; Bardsley, W. G. *Biochem J*. **1975**, *145*, 93.

(19) Bagchi, B. *Chem. Rev*. **2005**, *105*, 3197.

(20) Chung, Y.-H.; Xia, J.; Margulis, C. J. *J. Phys. Chem. B* **2007**, *111*, 13336.

(21) Dom ńguez, L.; Sosa-Peinado, A.; Hansberg, W. *Arch. Biochem. Biophys*. **2010**, *500*, 82.

(22) Gorman, J.; Greene, E. C. *Nat. Struct. Mol. Biol*. **2008**, *15*, 768.

(23) Jeltsch, A.; Pingoud, A. *Biochemistry* **1998**, *37*, 2160.

(24) Mansson, M. O.; Siegbahn, N.; Mosbach, K. *Proc. Natl. Acad. Sci. U. S. A.* **1983**, *80*, 1487.

(25) Niemeyer, C. M. *Angew. Chem., Int. Ed. Engl*. **2010**, *49*, 1200.

(26) Saccà, B.; Meyer, R.; Erkelenz, M.; Kiko, K.; Arndt, A.; Schroeder, H.; Rabe, K. S.; Niemeyer, C. M. *Angew. Chem., Int. Ed. Engl*. **2010**, *49*, 9378.

Chapter 4

Build up Responsive Nanodevice: A DNA Tweezer-actuated Enzyme Nanoreactor

Adapted with permission from Liu, M .; Fu, J.; Hejesen, C.; Yang, Y.; Woodbury, N.W.; Gothelf, K.; Liu, Y.; Yan, H., A DNA Tweezer-actuated Enzyme Nanoreactor. Submitted to *Nature Communication*.

4.1. Abstract

The functions of regulatory enzymes are essential to modulating biochemical cellular pathways. In this chapter, a tweezer-like DNA nanodevice was designed and constructed to actuate the activity of an enzyme/cofactor pair. A dehydrogenase and the corresponding NAD^+ cofactor were attached to different arms of the DNA tweezer structure and actuation of enzymatic function was achieved by switching the tweezers between open and closed states. The enzyme/cofactor pair is spatially separated in the open state which leads to inhibition of enzyme function, while in the closed state the activity of the enzyme is enhanced by the close proximity of the two molecules. The conformational state of the DNA tweezers is controlled by the addition of specific oligonucleotides that served as the thermodynamic driver (fuel) to trigger the change. Using this approach, several cycles of externally controlled enzyme inhibition and activation were successfully demonstrated. This principle of responsive enzyme nanodevices may be used to regulate other types of enzymes and to introduce feedback or feed-forward control loops.

4.2. Introduction

Nature has evolved a myriad of enzymes to catalyze chemical reactions that are vital to the metabolism and reproduction of living systems.[1] The ability to regulate those

enzyme activities in response to cellular environmental conditions (e.g. substrate levels, stimulants, etc.) is critical to many metabolic functions.[2,3] Scientists are currently interested in finding ways to mimic enzyme regulatory circuitry outside of the cell,[4,5] not only to increase our knowledge of cellular metabolism, but also so that we may create man-made nanoreactors that have potential utility in applications ranging from diagnostics to the production of high-value chemicals[6-8] and smart materials.[9] DNA nanostructures are promising scaffolds for use in the organization of molecules on the nanoscale because they can be engineered to site-specifically incorporate functional elements in precise geometries[10-12] and to enable nanomechanical control capabilities. Examples of such structures include autonomous walkers,[13,14] nanotweezers[15-18] and nanocages for controlled encapsulation and payload release.[19,20] New protein-DNA conjugation chemistries make it possible to precisely position proteins and other biomolecules on DNA scaffolds,[21] generating multi-enzyme pathways with the ability to modulate inter-molecular interactions and the local environment.[22-25] Taking advantage of these features, we exploited a DNA tweezer nanostructure to actuate the activity of a glucose-6-phosphate dehydrogenase (G6pDH)/NAD^+ enzyme/cofactor pair. Here, the enzyme and cofactor are displayed from different arms and actuation of enzyme function is achieved by switching between open and closed states to spatially separate the enzyme/cofactor pair for inhibition, or bring the pair together for activation, respectively.

4.3. Materials and Methods

4.3.1. Chemicals. (see APPENDIX C).

4.3.2. Bioconjugation. The conjugation chemistry used to link the protein enzyme to single-stranded oligonucleotides is described in a previous study[22] illustrated in Figure 4.1A.

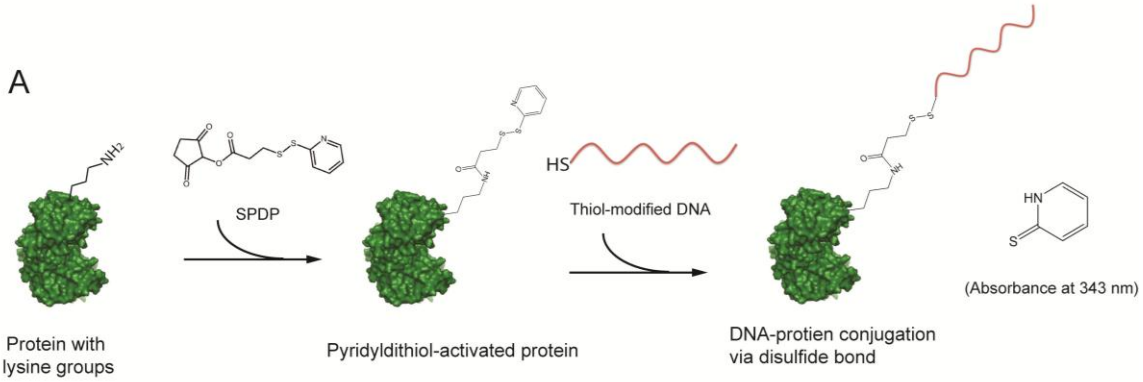

B

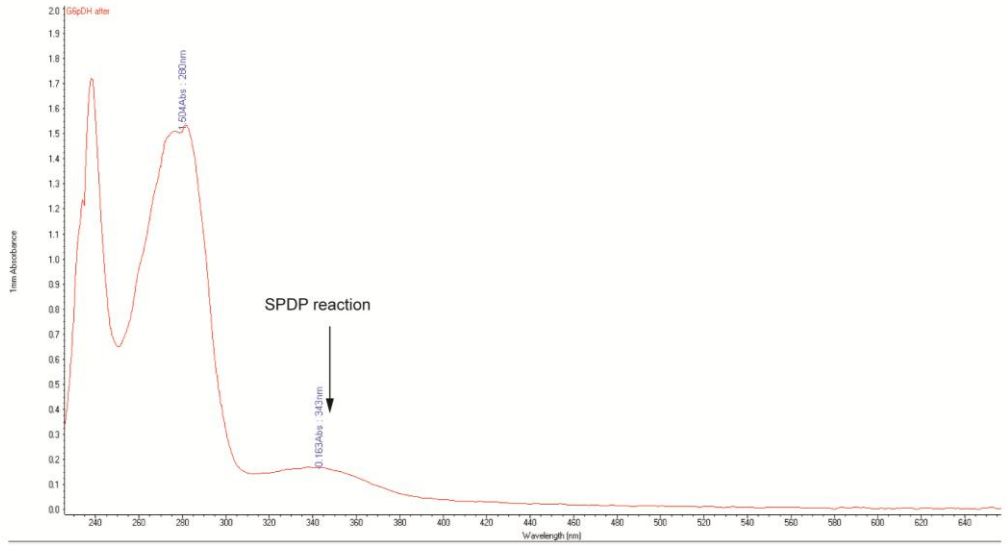

C

Name	A260/A280	A260	A280	Ratio (oligo/protein)	Protein conc. (μM)	A260/A280 (oligo)	Extinc.(260)	Extinc.(280)	A260/A280 (G6pDH)	Extinc.(260)	Extinc.(280)
G6pDH-oligo	0.84	0.81	0.97	0.86	5.1	1.34	115200	85970	0.52	61594	118450

Figure 4.1. Protein-DNA conjugation using a SPDP cross linker. (A) A schematic illustration of the conjugation chemistry; (B) Quantification of protein-SPDP modification via absorbance spectra. G6pDH-SPDP conjugation: ΔA343 before and after

SPDP conjugation is ~ 0.16 (extinction coefficient: 8080 M^{-1} cm^{-1}), corresponding to 20 μM SPDP coupled with 13 μM G6pDH (ε=115200 M^{-1} cm^{-1} at 280 nm for G6pDH). (C) Calculation of DNA ratio to purified G6pDH-TTTTTCCCTCCCTCC: an A260/A80 ratio of 0.84 corresponds to ~ 0.86 DNA per protein, with a protein-DNA concentration of ~ 5.1 μM.

Briefly, SPDP was used to crosslink G6pDH with a 5'thiol-modified oligo (5' HS-TTTTTCCCTCCCTCC). 100 μL of 40 μM enzyme solution was first reacted with a 2-fold excess of SPDP in 10 mM sodium HEPES (pH 8-8.5) for one hour, allowing amine-reactive N-hydroxysuccinimide (NHS) esters to react with the lysine residues on the protein surface. Excess SPDP was removed by washing, and purified using Amicon, 30 kD cutoff filters. Next, SPDP-modified protein was conjugated to a thiol-modified oligo (10-fold excess) through a disulfide bond exchange of the activated pyridyldithiol group. The reaction mixture was incubated in 1 × PBS (pH 8-8.5) for one hour. The coupling efficiency was evaluated by monitoring the increase in absorbance at 343 nm due to the release of pyridine-2-thione (extinction coefficient: 8080 M^{-1} cm^{-1}) as shown in Figure 4.1B. Finally, the excess oligo was removed by washing with 1 M NaCl and 1 × PBS and filtered with Amicon 30 kD cutoff filters. The filtered protein-oligo solution was quantified by absorbance at 260 and 280 nm (Figure 4.1C). Figure 4.2 shows that the enzymatic activity of oligo-labeled G6pDH (label ratio ~ 1) was ~ 50% of the activity of the unmodified enzymes.

Figure 4.3 shows the conjugation of 6AE-NAD^+ to single-stranded oligonucleotide. 200 μL of 100 μM 5'amine-modified oligo was first immobilized onto 200 μL anion-exchange DEAE-Sepharose resin by charge absorption.

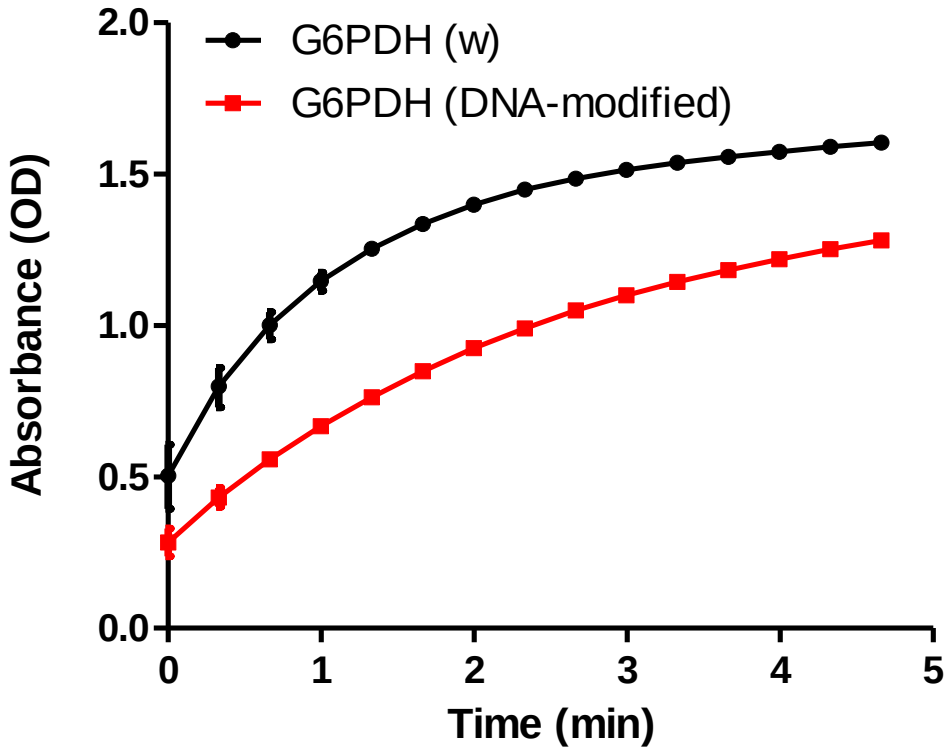

Figure 4.2. Enzyme activity for both G6pDH-DNA and unmodified enzymes.

The unbound oligo and water was removed by washing and filtering the resin with DMF in a Sigma Prep Spin column (7-30 µm). 200 µL of 150 mM DSS was prepared in DMF with 2 %(v/v) DIPEA. The oligo-bound resin was incubated with DSS for one hour. Excess DSS crosslinker was removed by washing the resin with DMF. To couple NAD^+ to an oligo, a 10- fold excess of 6AE-NAD^+ was incubated with oligo-bound resin in 1 M HEPES, pH8 for one hour. After the reaction, the oligo-bound resin was spun down at 3000 rpm to remove any unreacted 6AE-NAD^+. The purification of 6AE-NAD+ was performed using HPLC and characterized by MALDI-TOF Mass Spectrometry (see APPENDIX C). The thermal stability of the NAD^+-coupled oligo was measured as shown in Figure 4.4. NAD^+ could maintain most of its activity after

incubation at temperatures less than 75˚C, while NAD^+ activity quickly decreased after incubation at temperatures higher than 85˚C.

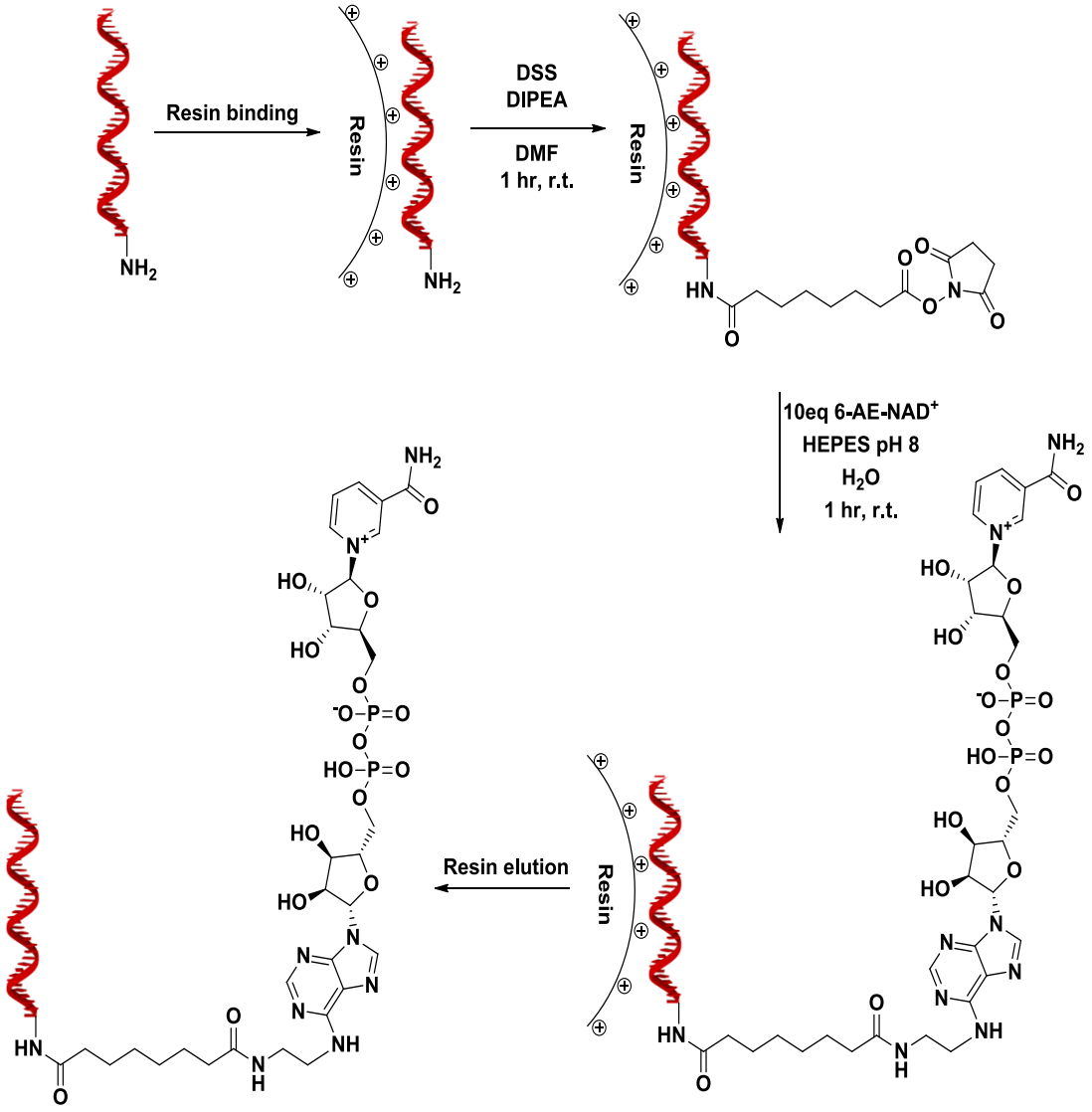

Figure 4.3. Conjugation of an aminoethyl NAD to the 3' end of DNA using resin-based DSS crosslinking chemistry.

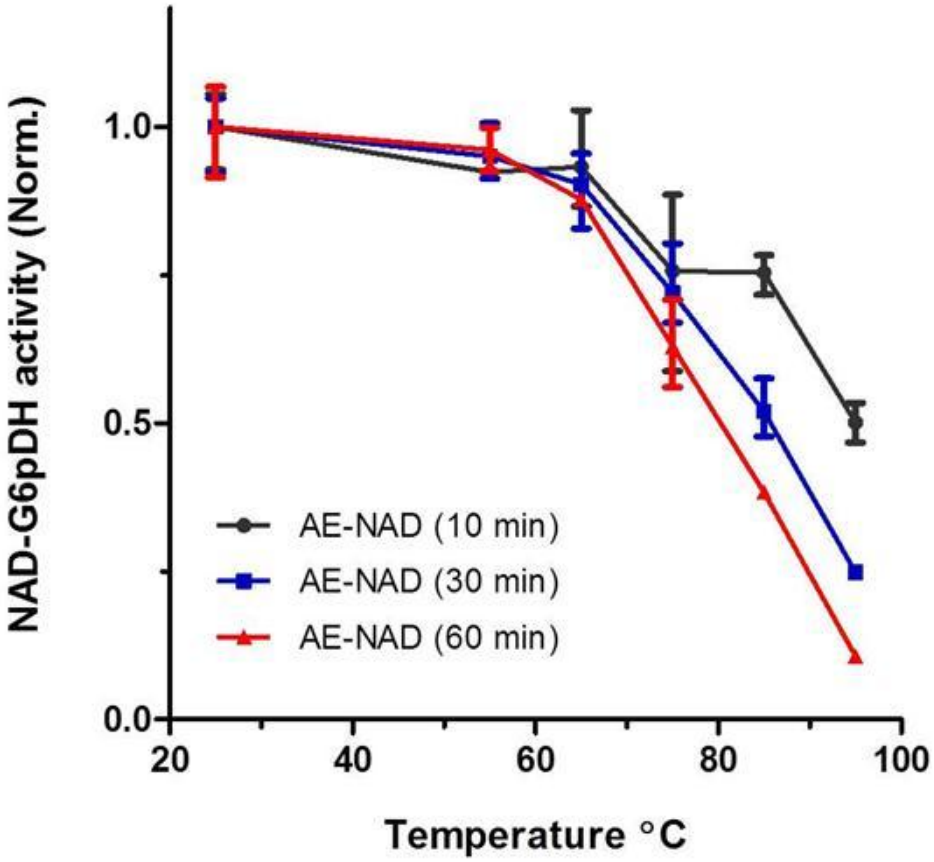

Figure 4.4. Evaluation of the thermal stability of NAD^+. Amino-modified NAD^+ (AE-NAD^+) was incubated at a series of temperatures ranging from 25 to 95 ˚C for 10 min (black), 30 min (blue) and 60 min (red), respectively. NAD^+ activity was evaluated from the reduction of NAD^+ to NADH by G6pDH, followed by a coupled PMA-catalyzed resazurin reaction as described in Figure 4.9. Assay condition: 50 nM G6pDH, 50 μM AE-NAD^+, 1 mM glucose-6 phosphate, 200 μM PMS and 400 μM resazurin in 1×TBS with 1 mM $MgCl_2$ at pH 7.5, room temperature. All the thermal activities were normalized to the sample incubated at 25 ˚C. The results show that after 10 minutes, AE-NAD^+ function is significantly reduced for temperatures higher than 70 ˚C. This indicates

that thermal annealing programs with very short incubation time at high temperature are required.

4.3.3. DNA Tweezer Preparation. Oligonucleotides were purchased from IDT (Integrated DNA Technology, Inc) and purified using denaturing polyacrylamide gel electrophoresis or HPLC. The concentration of each strand was determined by measuring the OD260. Detailed sequences and locations of fluorescent labels are shown in Figure 4.5.

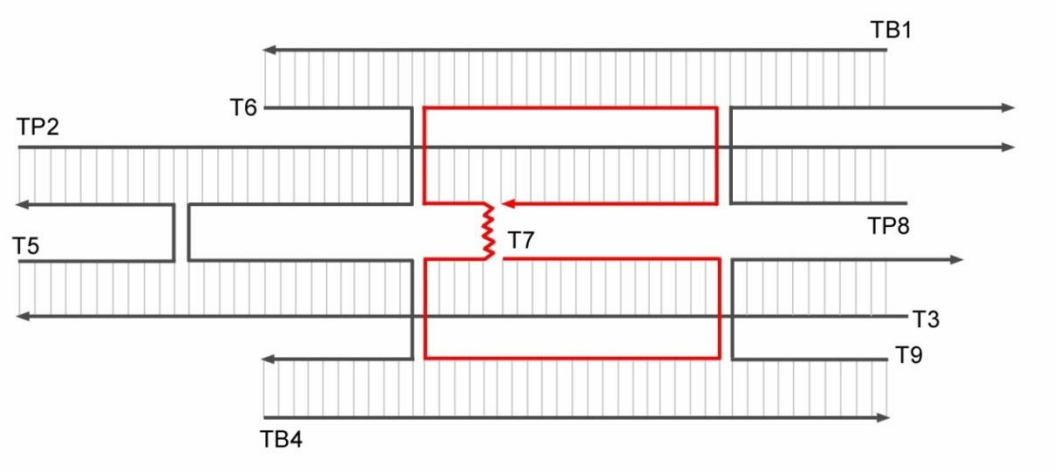

Name	Sequence
TB1	TTTTCGACCGAGCGTGAATTAGTGATCCGGAACTCGCGCAATGAACCTTTT/3BioTEG/
TP2	TTTTTCAGCTGGCCTATCTAAGACTGAACTCGCACCGCCGGCATAAGCTATGCGCTCTGCCGCTTTG GAGGGAGGG
T3	TTTTTTAGGAGATGGCACGTTAATGAATAGTCTCCACTTGCATCCGAGATCCGAACTGCTGCCTTTT
TB4	/5BioTEG/TTTTCGAGAGAAGGCTTGCCAGGTTACGTTCGTACATCGTCTGAGTTTTTT
T5	TTTTGGCAGCAGTTCAGGCCAGCTGATTTT
T6	TTTTGGTTCATTGCGGAGTTCAGTCTTAGATGGATCTCGGATGCAAGGCCTTCTCTCGTTTT
T7	GGTGCCGAGTTCCGGATCACTAATTCCATAGCTTATGCCGGCTTTGCGTAAGACCCACAATCGCTTT ACTATTCATTAACGTGTGTACGAACGTAACCTGGCAATGGAG
TP8	TTTTGCGGCAGAGCGACGCTCGGTCGTTTGGAGGGAGGG
Set	CGTGTGGTTGAAAGCGATTGTGGGTCTTACGCAAA
Fuel	TTTGCGTAAGACCCACAATCGCTTTCAACCACACG
TP8-Cy5	Cy5-TTTTGCGGCAGAGCGACGCTCGGTCGTTTGGAGGGAGGG
T3-Cy3	Cy3-TTTTTAGGAGATGGCACGTTAATGAATAGTCTCCACTTGCATCCGAGATCCGAACTGCTGCC
T9-0T	AACTCAGACGACCATCTCCTAA/3AmMO/
T9-3T	AACTCAGACGACCATCTCCTAATTT/3AmMO/
T9-13T	AACTCAGACGACCATCTCCTAATTTTTTTTTTTTT/3AmMO/
T9-20T	AACTCAGACGACCATCTCCTAATTTTTTTTTTTTTTTTTTT/3AmMO/
T9-30T	AACTCAGACGACCATCTCCTAATTTTTTTTTTTTTTTTTTTTTTTTTTTTT/3AmMO/
T9-40T	AACTCAGACGACCATCTCCTAATTTTTTTTTTTTTTTTTTTTTTTTTTTTTTTTTTTT/3AmMO/

Figure 4.5. Design and sequences of DNA tweezers. The 3' or 5' ends of strands are modified with 4T nucleotides to reduce stacking effects. Strands TB1 and TB4 are labeled with biotin. The probe sequence for G6pDH attachment is incorporated into the 3' ends of strands TP8 and TP2. The 3' end of strand T9 is bound to the NAD^+ molecule via 0 T to 40 T nt linkers. The T7 strand (shown in red) is used to regulate the opening and closing of the tweezers, which initially folds into a hairpin with a "GCG" stem loop. To open the tweezers, a 2-fold excess of set strands are incubated with the tweezers. To switch to a closed state, a 2-fold excess of fuel strands are added to displace the set strands and release the double helical regulatory strand complex.

Core strands for the open state tweezers were mixed in 1×TAE/Mg^{2+} buffer (40 mM Tris, 20 mM acetic acid, 2 mM EDTA and 12.5 mM magnesium acetate, pH 8.0) to reach a final concentration of 0.5 μM, except for the set and NAD^+ conjugated strands which were prepared at 0.75 μM. All samples were annealed in an Eppendorf Mastercycler. The temperature steps in the annealing protocol are shown in APPENDIX C with gradually decrease from 90 ˚C to 72 ˚C over 10 min, decrease from 68 ˚C to 24 ˚C over 60 min then hold at 4 ˚C.

Name	Extinction coefficient ($M^{-1}cm^{-1}$)
0T-open	4002998.8
3T-open	4026906.7
13T-open	4106599.8
20T-open	4162384.9
30T-open	4242077.9
40T-open	4321771.0

Table 4.1. Estimated extinction coefficient at 260nm of the tweezers linked to NAD^+. The extinction coefficient of each tweezer structure was estimated by inputting sequences

into IDT Biophysics analyzer (http://biophysics.idtdna.com/UVSpectrum.html). These values can be used to roughly estimate tile concentration after biotin purification.

3-fold molar excess of oligo-conjugated G6pDH was added to the pre-annealed tweezer structures and mixed well. Proteins were assembled by using a 1 hour annealing program: the temperature was decreased from 37 ˚C to 10 ˚C and held at 4 ˚C using an established protocol.[22] Excess G6pDH-WN1 was removed using monomeric avidin resin (Pierce) and biotin-labeled tweezers; the protein was eluted out with 2mM biotin and the recovery yield was ~30%. Purified assembled enzyme nanoreactor sample was characterized using Native PAGE gel shown in Figure 4.6. The estimated extinction coefficient of the open tweezers at 260nm is shown in Table 4.1.

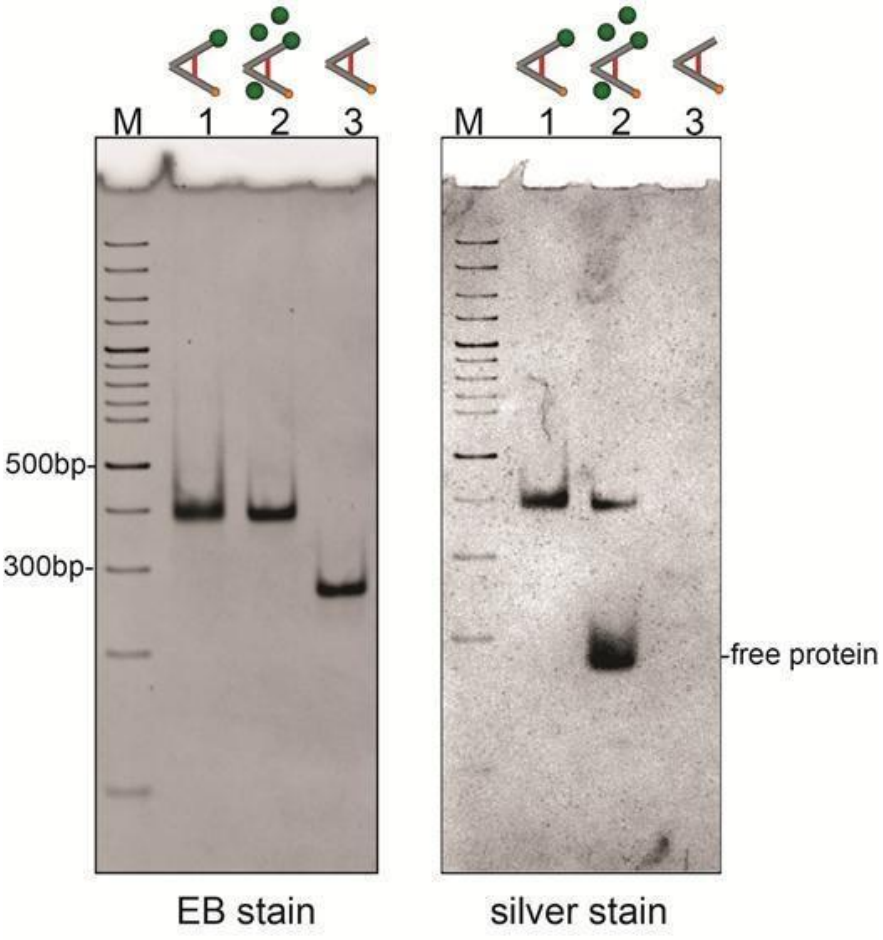

Figure 4.6. Removal of free proteins using biotin-affinity resin purification. The native polyacrylamide gel shown here was first stained with EB (left) to detect the DNA tweezer structure and then rinsed with pure water; the same gel was later stained with silver stain (right) to detect the proteins. Lane 1 is G6pDH-assembled tweezers after purification; no free proteins are observed in the silver stained image. Lane 2 is G6pDH-assembled tweezers before purification; a large quantity of free proteins is visible in the silver stained image. Lane 3 is the tweezers without proteins. Note that the integrity of the tweezers structures is maintained before (Lane 2) and after purification (Lane 3).

4.3.4. Enzyme Assay. 100 nM G6pDH/NAD^+-assembled DNA tweezers were prepared with 100 μL of substrate for the activity assay, which was performed on a SpectraMax M5 96 well plate reader (Molecular Device, Sunnyvale, CA). G6pDH/NAD^+ activity was measured using a coupled assay of PMS (phenazine methosulfate) and resazurin in which PMS first oxidizes NADH to NAD^+, then reduces resazurin to resorufin with the appearance of a fluorescent signal (excitation maxi. ~ 544 nm, emission maxi. ~ 590 nm) as shown in Figure 4.7.

For a typical reaction, 100 nM G6pDH nanotweezers were incubated with 1 mM G6p, 1 mM PMS and 500 μM resazurin. Each addition of fuel or set strands utilized a 50% to 100% excess compared to the previously added amount. Activity was continuously measured for 15 min after 15 min incubation time for each addition of fuel or set strands. Mg^{2+} was removed from the sample solution to avoid the formation of double-stranded DNA/Mg^{2+} complexes that quench resorufin fluorescence (see APPENDIX C).[26]

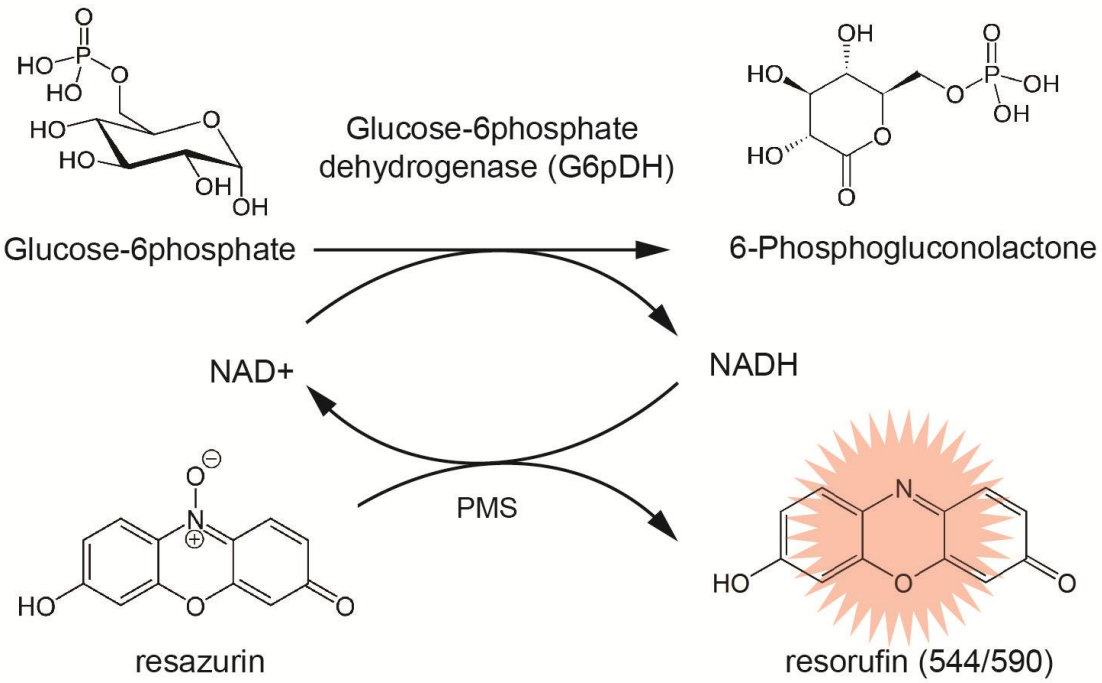

Figure 4.7. Detection of enzymatic activity in the G6pDH/NAD^+-assembled tweezers using a PMS/resazurin coupled assay: NAD^+ is first reduced to NADH by G6pDH. Next, PMS catalyzes electron transfer from NADH to resazurin producing a strongly fluorescent resorufin with an emission maximum ~ 590 nm.

4.3.5. Real-time FRET Experiment. The Cy3 and Cy5 labeled actuator structure is illustrated in Figure 4.8. FRET experiments of fully assembled structures were carried out in a Nanolog fluorometer (Horiba Jobin Yvon) with a 1 cm path length quartz cell (Hellma) at room temperature. DNA tweezer concentration was ~ 60 nM. Excitation wavelength was set at 514nm. The donor (Cy3) and acceptor (Cy5) emission was collected at ~ 570 nm and ~ 670 nm, respectively. The excitation slit was 1 nm and emission slit was 6 nm. The interval time for each data point is 1s after the addition of fuel strands and 3s after the addition of set strands due to the longer observation period.

The addition of fuel or set strands had exactly the same excess percentage as for the enzyme activity measurement.

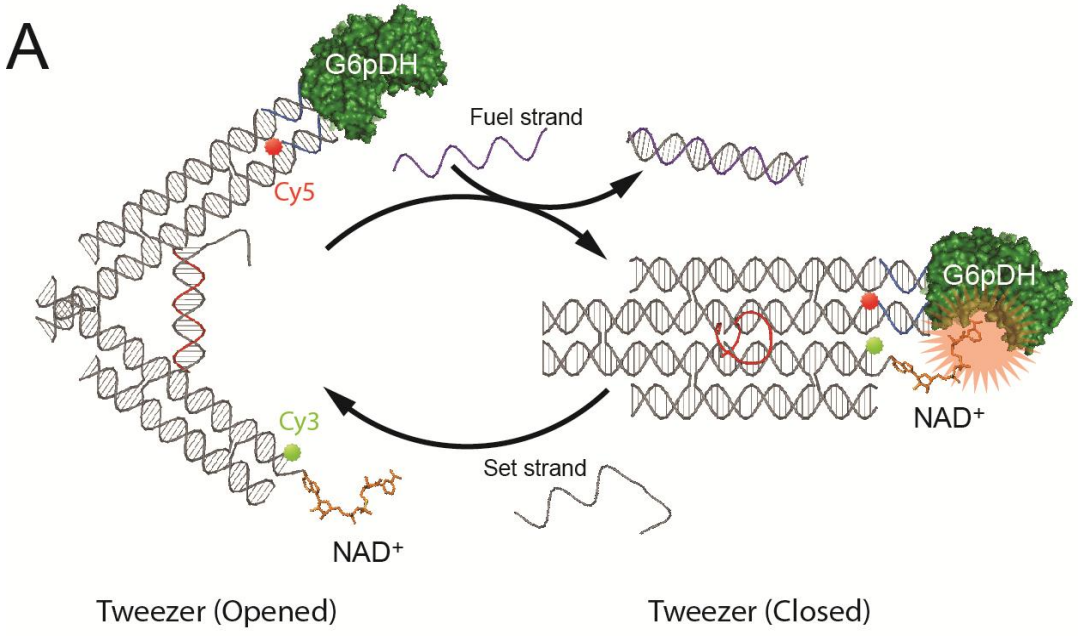

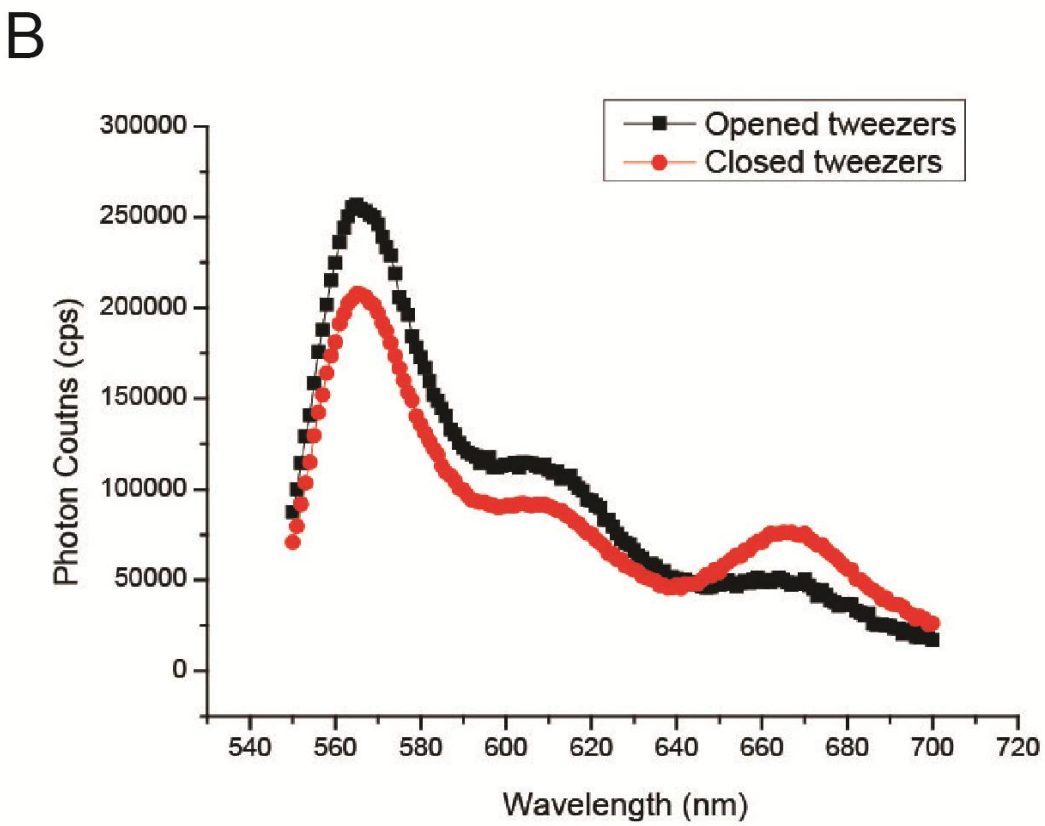

Figure 4.8. FRET analysis of DNA tweezers. (A) Schematic illustration of FRET analysis of G6pDH/NAD^+ tweezers. Two fluorophores, Cy3 and Cy5, are labeled at the end of the two arms, respectively (5' modification of strands TP8 and T3). (B) FRET signal from the Cy3/Cy5 pair in the open and closed state tweezers. For the open tweezers, the distance between the ends of the arms is estimated as ~16 nm, according to the length of the fully hybridized regulatory oligomer. For the closed tweezers the FRET efficiency is ~ 19% which corresponds to ~ 6.9 nm between the Cy3 and Cy5 dyes, as estimated by the equation of '$E = \frac{1}{1+(\frac{r}{R_0})^6}$', given a Förster distance ~ 5.4 nm.[27]

4.3.6. Gel Preparation and Characterization. See APPENDIX C.

4.4. Results and Discussion

4.4.1. Design and Characterization of Enzyme Nanoreactor. The mechanics of the DNA tweezer-regulated enzyme nanoreactor are shown in Figure 4.9A. The design and construction of the nanotweezers, with ~14 nm long arms, are based on a previous report.[15] A 25 nucleotide (nt) single stranded DNA (ssDNA) oligomer (5'-TTTGCGTAAGACCCACAATCGCTTT-3') connects the ends of the tweezer arms and serves as a structural regulatory element to control the state of the tweezers. In the initial closed state the regulatory oligomer is designed to adopt a 'GCG' stem-loop hairpin structure that holds the two arms of the tweezers close together. The average distance between the arms in the closed state is ~ 6.9 nm, according to fluorescence energy transfer measurements (FRET)[28,29] (Figure 4.8). The open state is achieved by disrupting the hairpin via hybridization of a complementary set strand to it, thereby generating a rigid ~16 nm long double helical domain between the ends of the tweezer arms. To switch back to the closed state a fuel strand that is fully complementary to the set strand

is introduced to the system, releasing the regulatory oligomer to a hairpin by a strand displacement mechanism.[30]

Next, G6pDH was conjugated to a ssDNA (5'-TTTTTCCCTCCCTCC-3') using well developed chemical methods.[22] The complementary anchor strand was displayed from one of the tweezer arms to capture the DNA-modified G6pDH via sequence specific hybridization. The other arm of the DNA tweezers was functionalized with an amino-modified NAD^+ molecule.[31]

The G6pDH/NAD^+-assembled tweezer complex was characterized by native polyacrylamide electrophoresis (PAGE) as shown in Figure 4.9B. The protein-bound (~ 100 kD for G6pDH)[32] DNA tweezers exhibited reduced mobility in the PAGE gel due to the relatively higher molecular weight. In addition, the closed state tweezers migrated slightly faster than the open state tweezers due to their more compact conformation. The identity of each band in the gel was verified by ethidium bromide (EB)[33] and silver staining[34], where EB preferentially bound to the DNA and the metallic silver solution of the protein. The expected band shifts were confirmed by both staining methods. A high yield of enzyme-bound tweezers is visible in the gel images, with evidence of successful switching between open and closed states. As shown in Figure 4.9C we also characterized the conformational state of the fully assembled tweezers using FRET between Cy3/Cy5 dye pairs. Here, the end of one of the tweezer arms was labeled with Cy3 and the other with Cy5. The closed tweezers exhibited a lower Cy3 signal and a higher Cy5 signal due to relatively efficient energy transfer between the fluorophores.

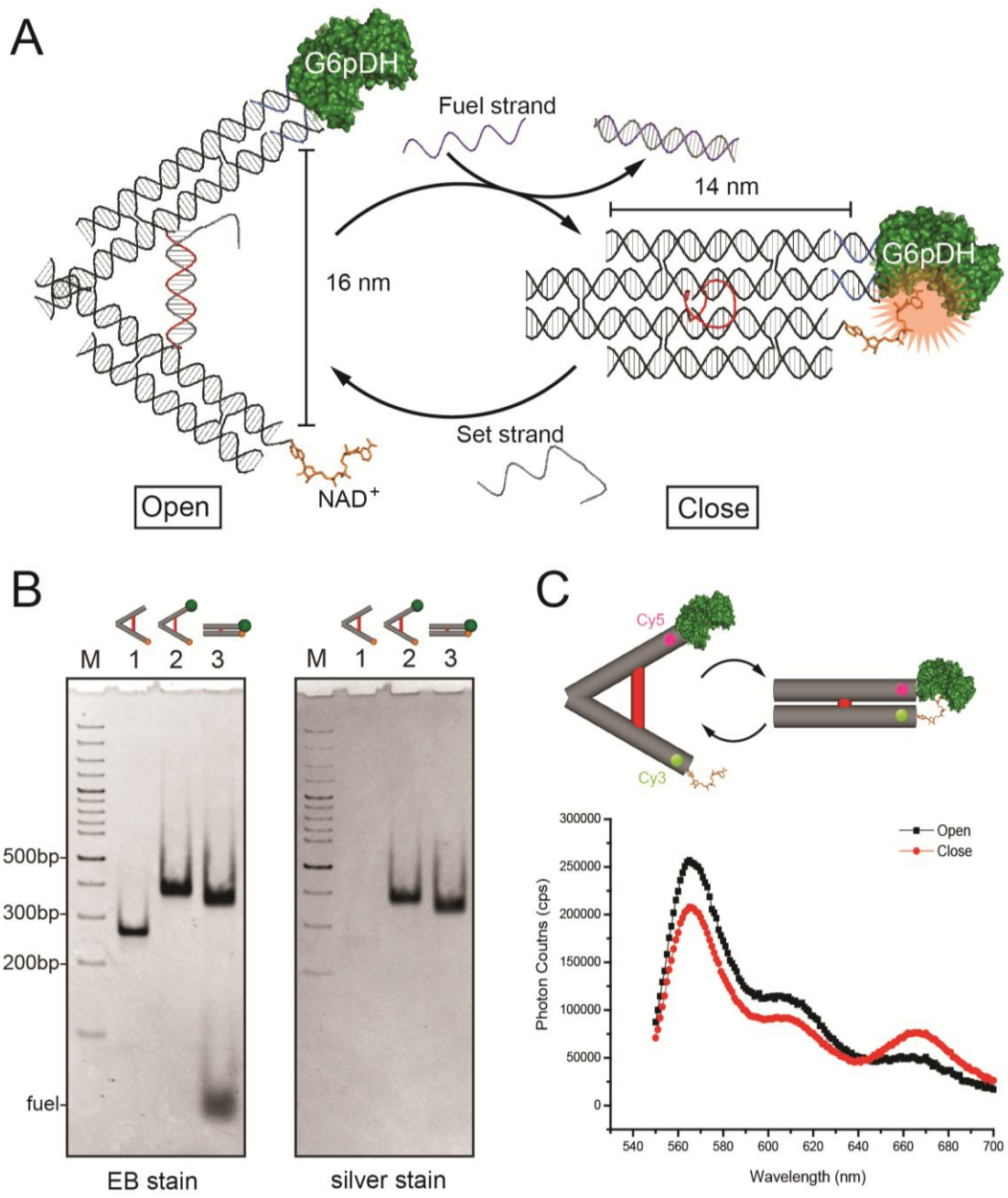

Figure 4.9. Design and characterization of G6pDH/NAD^+ - assembled DNA tweezers. (A) Schematic illustration of the mechanics of the DNA tweezer-regulated enzyme nanoreactor: a regulatory oligomer (shown in red) is designed to adopt a 'GCG' stem-loop hairpin structure that holds the two arms of the tweezers close together. The addition

of a set strand (complementary to the regulatory loop shown in red) to the tweezer structure results in the formation of a DNA double helix between the tweezer arms that separates the G6pDH and NAD^+ enzyme/cofactor pair (open state). Displacement of the set strands from the regulatory loop by fuel strands leads to the active state (closed) in which G6pDH and the cofactor NAD^+ are in close proximity. (B) Characterization of the fully assembled tweezers structures: left – EB stained PAGE gel for detecting DNA; right – the same gel visualized by silver stain for detecting proteins. Lane 1: open tweezers with NAD^+ attached by a poly$(T)_{20}$ linker; lane 2: open tweezers assembled with G6pDH; lane 3: closed tweezers assembled with G6pDH. All structures were purified using biotin-avidin affinity resins. (C) FRET experiment (Cy3/Cy5 dyes) to characterize the open and closed states of the tweezers.

As shown in Figure 4.7, a resazurin-coupled assay was used to evaluate the activity of the tweezer bound G6pDH/NAD^+ pair. The assay involves the phenazine methosulfate (PMS) catalyzed reduction of resazurin to resorufin by NADH, as evidenced by the production of a strong fluorescence signal (ex. ~544nm/em. ~590nm). To remove any unassembled enzymes and minimize the background signal all tweezer constructs were purified by biotin-affinity resin treatment.

4.4.2. Optimization of NAD^+ Linker Length. In an effort to optimize the activity of the G6pDH/NAD^+-assembled tweezers, the NAD^+ cofactor was attached to the tweezers by a single-stranded poly thymidine (T) linker. As shown in Figure 4.10A and B, we investigated the dependence of the length of the poly (T) linker on the activity of the G6pDH/NAD^+-assembled tweezers. Most tweezers were correctly assembled and able to open and close as characterized by native PAGE in Figure 4.10C. A small amount

of aggregation (< 10 %) of the tweezer constructs was observed due to DNA-DNA stacking. The activities of both the open and closed tweezers improved as the length of the linker was increased from 0 to 20 nts (~ 30 nm in linear length), presumably due to the enhanced flexibility of the longer linkers. Further increasing the linker length from 20 nts to 40 nts (~ 60 nm in linear length) did not improve the enzyme activity, but rather resulted in slight decrease.

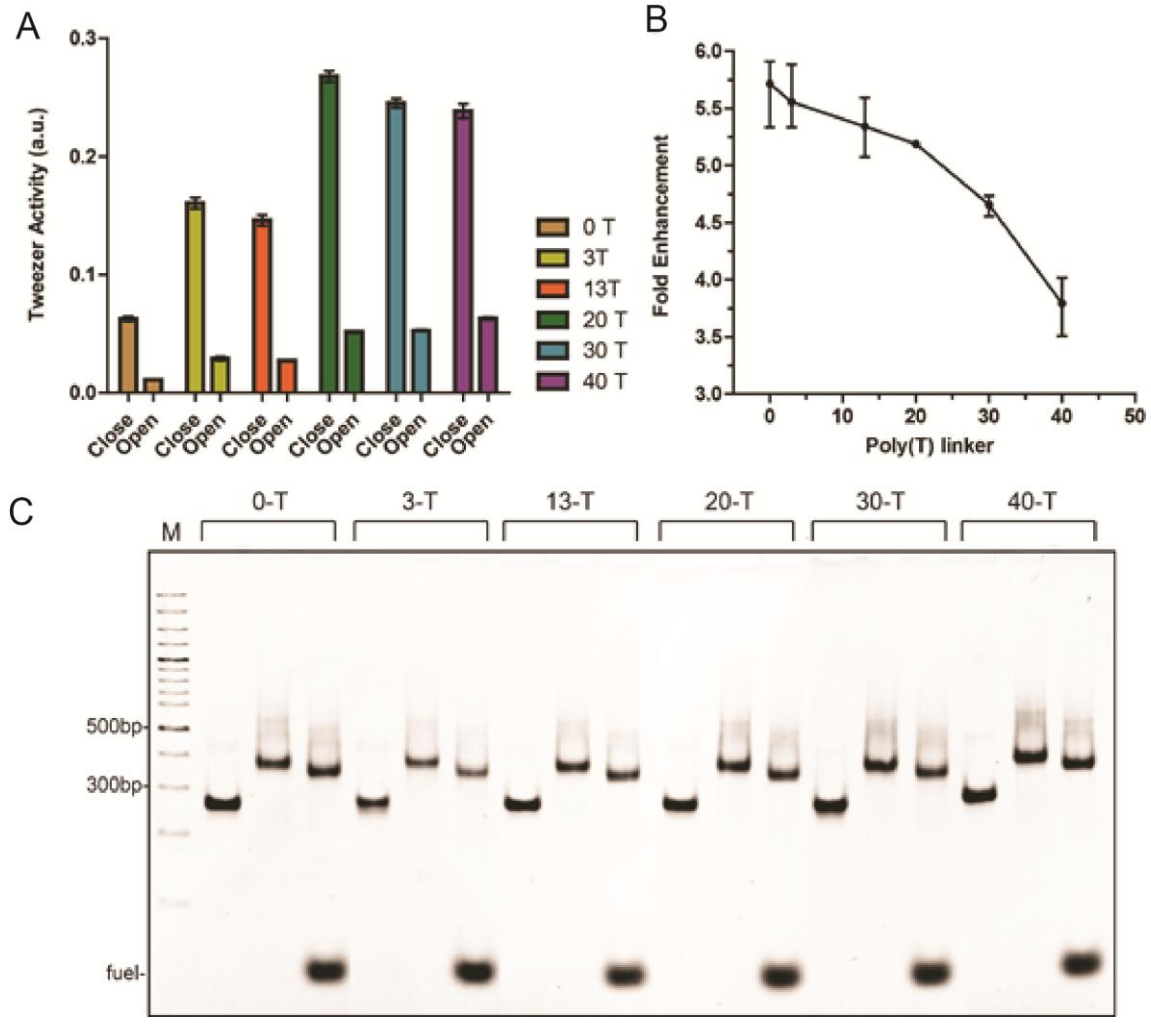

Figure 4.10. Optimization of the NAD^+ linker length for tweezer activity and actuation. (A) The activities of open and closed tweezers as a function of poly(T) linker length. (B) Enhancement of closed tweezers compared to opened tweezers as a function of poly(T)

linker length. (C) Native PAGE characterization of all DNA tweezers with different poly(T) linker length. Slight aggregations of tweezers were observed due to DNA-DNA stacking.

We also evaluated the ability of the tweezers to modulate enzymatic activity by determining the relative level of enhancement of the closed state compared to the open state. As shown in Figure 4.10B, greater than 5.5-fold activity enhancement was observed for closed tweezers with no linker, or with a short poly $(T)_3$ linker. As the length of the linker increased the enhancement in the activity of the closed tweezers compared to the open tweezers gradually decreased. Tweezers with a relatively long poly $(T)_{40}$ linker exhibited less than 4-fold activity enhancement. This is likely because longer linkers increase the accessibility of NAD^+ to G6pDH even in the open state, thereby reducing the ability of the tweezers structure to modulate enzyme activity. We selected a poly $(T)_{20}$ linker for attachment of the NAD^+ cofactor to the tweezers, which yielded more than 3-fold higher enzymatic activity than tweezers with no linker, and maintained greater than 5-fold activity enhancement of closed tweezers compared to open ones. In this way were able to sustain adequate enzyme activity while also preserving the regulatory capacity of the tweezers.

4.4.3. Regulatory Cycling of the G6pDH/NAD^+-assembled Tweezers. We further examined the ability of the G6pDH/NAD^+ tweezers to withstand several cycles of ON/OFF enzyme activity.

To characterize the regulatory cycling of switching, in Figure 4.11A we present a native PAGE gel that demonstrates the ability of the assembled tweezers to switch between open and closed states nine times while maintaining their structural integrity.

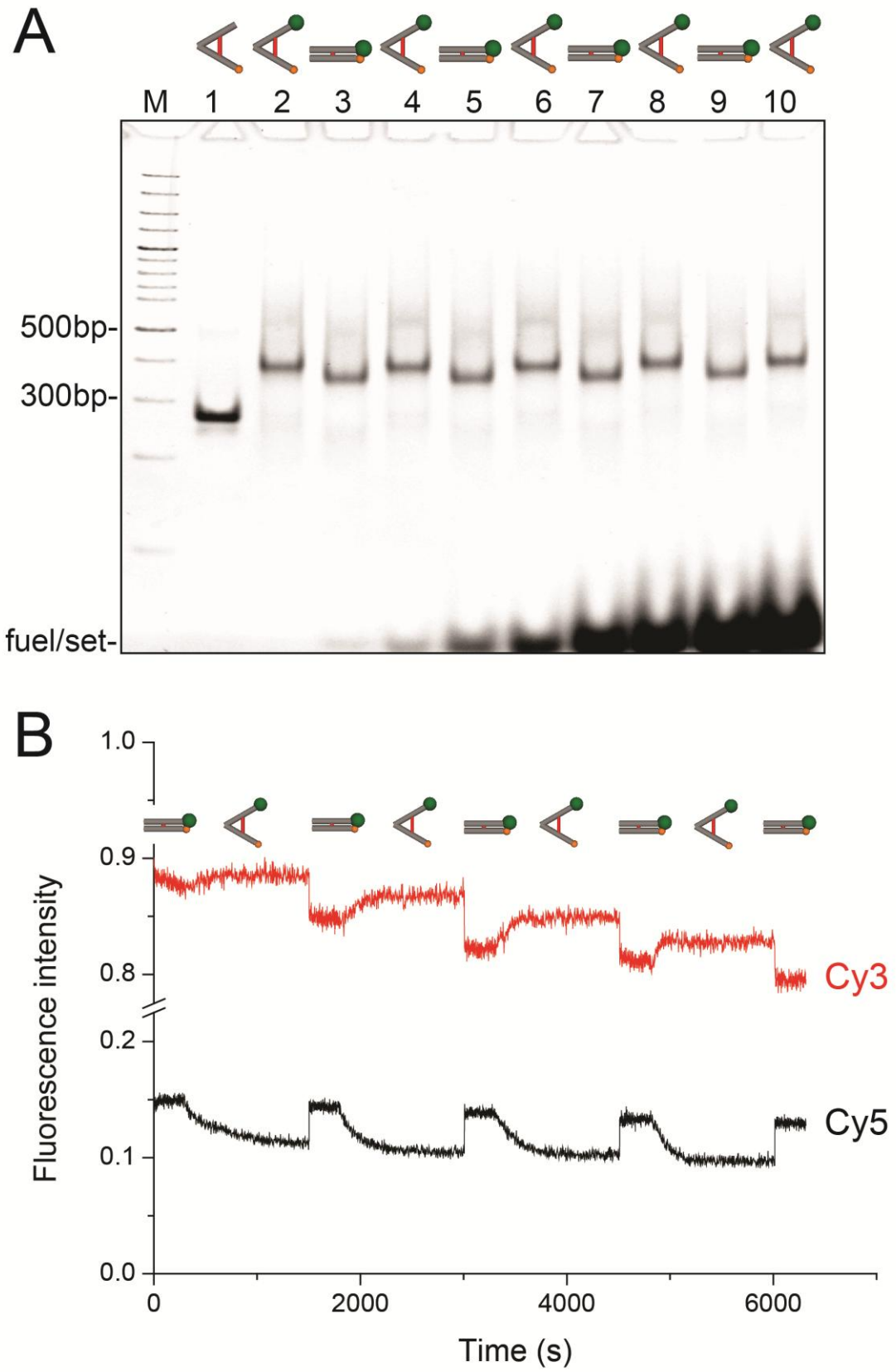
A
M
1
2
3
4
5
6
7
8
9
10
500bp-
300bp-
fuel/set-
B
1.0
0.9
0.8
0.2
0.1
0.0
Fluorescence intensity
Cy3
Cy5
0
2000
4000
6000
Time (s)

Figure 4.11. Characterization of regulatory cycling of the G6pDH/NAD^+-assembled tweezers. Four cycles of conformational and functional transition were measured and analyzed using (A) native PAGE and (B) real-time FRET. Cycles were initiated in the open state, and for each conformational change 50% excess fuel or set strands were added.

Additional cycles are limited by the accumulation of large amounts of set and fuel strands. We also monitored the real-time opening and closing of the tweezers by labeling the tweezer arms with Cy3 and Cy5 FRET dyes, respectively. As shown in Figure 4.11B, Cy3 emitted less fluorescence in the closed state due to energy transfer to Cy5, while Cy5 exhibited higher emission under the same conditions. The gradual decrease in the intensity of Cy3 fluorescence over time that was observed can be attributed to photo bleaching. Real time kinetic analysis revealed that the tweezers switch from open to closed states very quickly, with all tweezers transformed within a few seconds (too fast to measure the kinetic constant accurately).

However, the kinetics of switching from the closed to open state is much slower, with a first-order kinetic constant of ~ 0.0025 ± 0.0003 s^{-1}. The rate constants corresponding to switching from the closed to open state gradually increased as the cycle number increased: ~ 0.0051 s^{-1} for the second cycle; ~ 0.0054 s^{-1} for the third cycle; and 0.0071 s^{-1} for the fourth cycle (Figure 4.12). It is likely that the relatively sluggish process of tweezer opening is due to the slow hybridization of the set strand to the self-folded hairpin structure connecting the tweezer arms and the subsequent disruption of the rather stable hairpin structure.

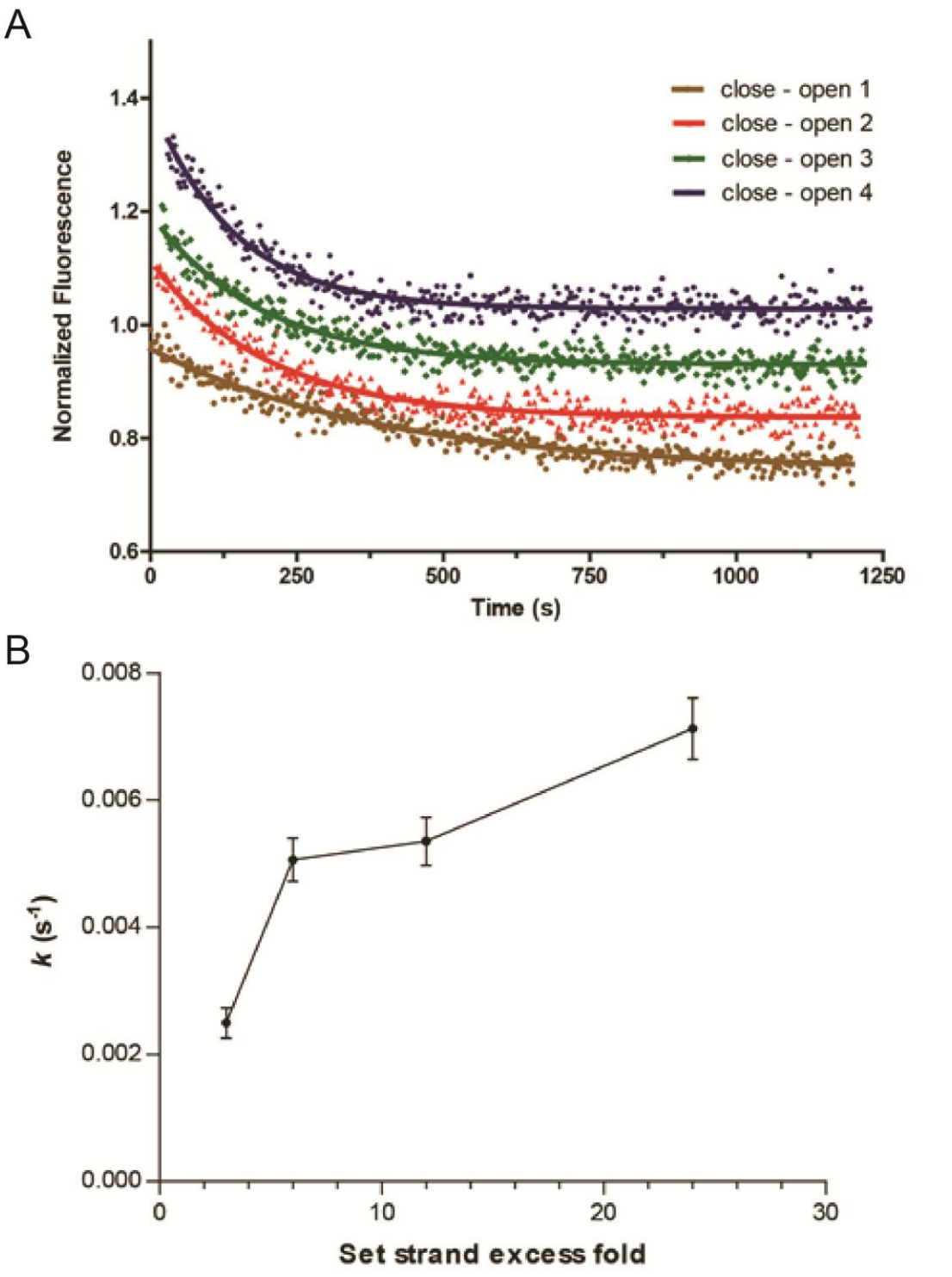

Figure 4.12. (A) Fitting of the first-order rate constants for the opening kinetics of the tweezers, using the fluorescence signal decrease of Cy5. The equation used for first-order

kinetics is described as $Y = (Y_0 - A) * e^{-k*t} + A$, where Y is real-time Cy5 signal, Y_0 is Cy5 signal at fully closed tweezers state, A is Cy5 signal at fully opened tweezers state, k is the first-order rate constant. As the accumulation of extra set strands over cycles, the opening kinetics became faster. (B) The rate constants for tweezer-open kinetics *vs.* excess fold of set strands.

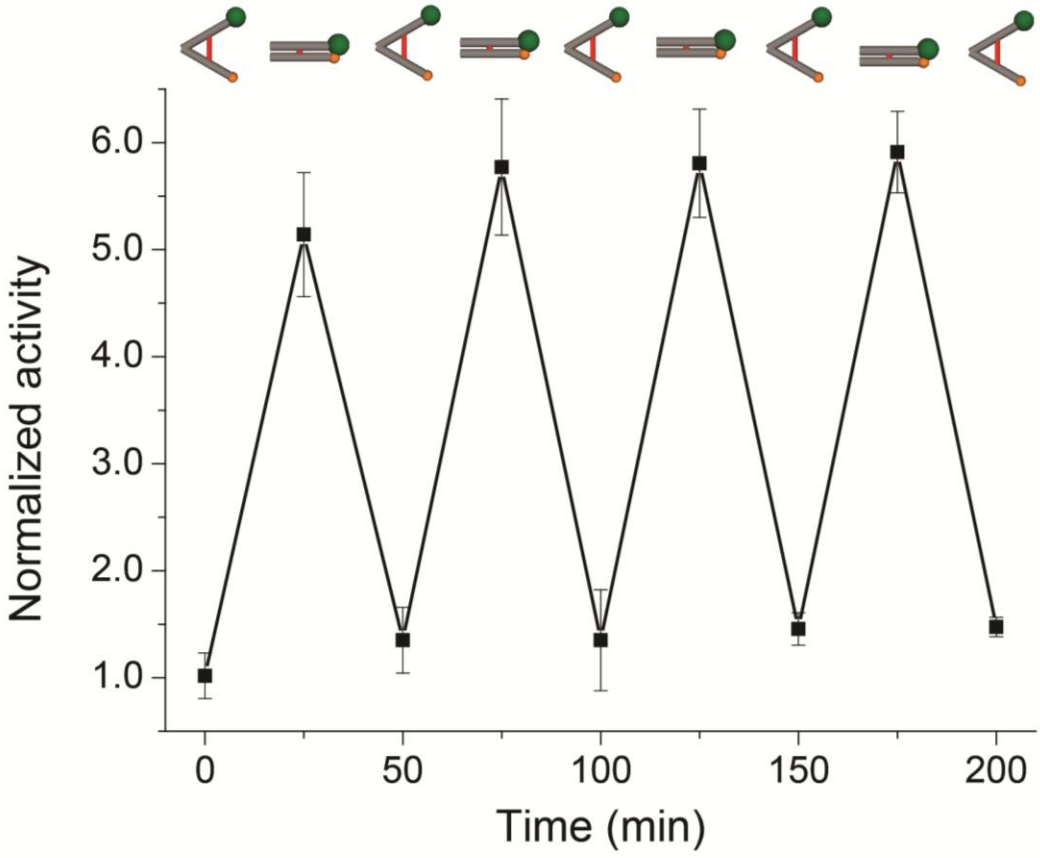

Figure 4.13. Enzymatic assay. Cycles were initiated in the open state, and for each conformational change 50% excess fuel or set strands were added. All the enzyme activities were normalized to the activity of initial open tweezers.

Figure 4.13 demonstrates the ability of the DNA tweezer structure to regulate G6pDH activity by switching between open and closed states. The tweezers were able to

actuate the ON/OFF enzyme activity 8 times in 200 minutes, with the closed state producing 5-fold higher enzymatic activity on average than the open state.

4.5. Conclusion

In conclusion, we have designed and constructed a DNA tweezer-like nanostructured enzyme system with the ability to turn on and off the activity of a G6pDH/NAD^+ enzyme/cofactor pair by means of nano-mechanical control. In the open state the tweezer conformation inhibits the activity of the G6pDH/NAD^+ enzyme/cofactor pair by holding the molecules apart, while in the closed state the close proximity of the pair results in greatly enhanced activity. We successfully demonstrated several cycles of enzyme inhibition and activation in response to external stimuli (regulatory DNA strands). With additional developments in DNA-protein/cofactor attachment chemistry it should be possible to regulate other types of enzymes and to introduce feedback or feed-forward control loops. In the future it may be feasible to develop responsive enzyme nanodevices as highly specific chemical amplifiers in diagnostic applications or as biocatalysts in the production of high value chemicals and smart materials.

4.6. References

(1) Bairoch, A. *Nucleic Acids Res*. **2000**, *28*, 304-305.

(2) Hammes, G. G., Wu, C.W. *Science* **1971**, *172*, 1205-1211.

(3) Drews, J. *Science* **2000**, *287*, 1960-1964.

(4) Ostermeier, M. *Curr. Opin. Struct. Biol*. **2009**, *19*, 442-448.

(5) Khosla, C.; Harbury, P. B. *Nature* **2001**, *409*, 247-252.

(6) Sheldon, Roger A. *Adv. Synth. Catal*. **2007**, *349*, 1289-1307.

(7) Vriezema, Dennis M. et al. *Angew. Chem. Int. Ed*. **2007**, *46*, 7378-7382.

(8) Palomo, J. M. *Curr. Org. Synth*. **2009**, *6*, 1-14.

(9) Bogue, R. *Assembly Autom.* **2012**, *21*, 3-7 (2012).

(10) Fu, J.; Liu, M.; Liu, Y.; Yan, H. *Acc. Chem. Res*. **2012**, *45*, 1215-1226.

(11) Pinheiro, A. V.; Han, D.; Shih, W. M.; Yan, H. *Nature Nanotech*. **2011**, *6*, 763-772.

(12) Seeman, N. C. *Annu. Rev. Biochem*. **2010**, *79*, 65-87.

(13) Lund, K.; Manzo, A. J.; Dabby, N.; Michelotti, N.; Johnson-Buck, A.; Nangreave, J.; Taylor, S.; Pei, R.; Stojanovic,M. N.;Walter, N. G.;Winfree, E.; Yan, H. *Nature* **2010**, *465*, 206-210.

(14) Gu, H.; Chao, J.; Xiao, S.J.; Seeman, N. C. *Nature* **2010**, *465*, 202-205.

(15) Zhou, C.; Yang, Z.; Liu, D. *J. Am. Chem. Soc*. **2012**, *134*, 1416-1418.

(16) Liedl, T.; Hogberg, B.; Tytell, J.; Ingber, D. E.; Shih, W. M. *Nature Nanotech.* **2010**, *5*, 520-524.

(17) Modi, S.; Swetha, M. G.; Goswami, D.; Gupta, G. D.; Mayor, S.; Krishnan, Y. *Nature Nanotech*. **2009**, *4*, 325-330.

(18) Chhabra, R.; Sharma, J.; Liu, Y.; Yan, H. *Nano Lett*. **2006**, *6*, 978-983.

(19) Andersen, E. S.; Dong, M.; Nielsen, M. M.; Jahn, K.; Subramani, R.; Mamdouh, W.; Golas, M.M.; Sander, B.; Stark, H.; Oliveira, C. L. P.; Pedersen, J. S.; Birkedal, V.; Besenbacher, F.; Gothelf, K. V.; Kjems, J. *Nature* **2009**, *459*, 73-76.

(20) Douglas, S. M.; Bachelet, I.; Church, G. M. *Science* **2012**, *335*, 831-834.

(21) Niemeyer, C. M. *Angew. Chem. Int. Ed*. **2010**, *49*, 1200-1216.

(22) Fu, J.; Liu, M.; Liu, Y.; Woodbury, N. W.; Yan, H. *J. Am. Chem. Soc*. **2012**, *134*, 5516-5519.

(23) Wilner, O. I.; Weizmann, Y.; Gill, R.; Lioubashevski, O.; Freeman, R.; Willner, I. *Nature Nanotech*. **2009**, *4*, 249-254.

(24) Delebecque, C. J.; Lindner, A. B.; Silver, P. A.; Aldaye, F. A. *Science* **2011**, *333*, 470-474.

(25) Fu, Y. et. al. *J. Am. Chem. Soc*. **2012**, *135*, 696-702.

(26) Rupcich, N.; Chiuman, W.; Nutiu, R.; Mei, S.; Flora, K. K.; Li, Y.; Brennan, J. D. *J. Am. Chem. Soc*. **2005**, *128*, 780-790.

(27) Lee, S.; Lee, J.; Hohng, S. *PLoS ONE* **2010**, *5*, e12270.

(28) Foerster, T. *Ann. Phys.* **1948**, *2*, 55.

(29) Bowen, M. E.; Weninger, K.; Ernst, J.; Chu, S.; Brunger, A. T. *Biophys. J.* **2005**, *89*, 690-702.

(30) Yurke, B.; Turberfield, A. J.; Mills, A. P.; Simmel, F. C.; Neumann, J. L. *Nature* **2000**, *406*, 605-608.

(31) Schmidt, H.-L.; Grenner, G. *Eur. J. Biochem*. **1976**, *67*, 295-302.

(32) Rowland, P.; Basak, A. K.; Gover, S.; Levy, H. R.; Adams, M. J. *Structure* **1994**, *2*, 1073-1087.

(33) Moore, S. P., Sutherland, B. M. *Anal. Biochem*. **1985**, *144*, 15-19.

(34) Wray, W., Boulikas, T., Wray, V. P., Hancock, R. *Anal. Biochem*. **1981**, *118*, 197-203.

Chapter 5

Summary and Outlook

5.1. Conclusions

It has been 30 years since Nadrian Seeman first proposed the idea of using DNA as a building block to precisely organize and arrange other biomolecules with nanoscale dimensions. The field of DNA nanotechnology has become one of the most successful 'bottom-up' nanofabrication techniques along with the study of lipid vesicles, nanowires and quantum dots. People have constructed various DNA nanostructures from one to three dimensions, and from a few nanometers to a few micrometers scale that were 'glued' using DNA-DNA hybridization and sticky ends. The reliability of base recognition, self-assembling behavior, and attractive structural properties of DNA are unparalleled value in systems of this size. DNA nanostructures have been demonstrated great scaffolds to direct the self-assembly of functional biomolecules. Supermolecular networks that are organized by DNA nanostructures exhibit precisely-controlled intercomponent distances and positions.

In this thesis, we have successfully demonstrated the great ability of DNA directed self-assembly of protein networks or enzyme cascades and explained a few challenging questions in enzymatic field of study. As described in chapter 2,[1] we reported a strategy of using DNA origami as a scaffold to arrange spherical virus capsids into one-dimensional arrays with precise nanoscale positioning. In chapter 3,[2] we organized

discrete glucose oxidase (GOx)/ horseradish peroxidase (HRP) enzyme pairs on specific DNA origami tiles with controlled interenzyme spacing and position. Then we studied the distance-dependent intermediate diffusion and tested the role of limited dimensional diffusion along protein surfaces. In chapter 4,[3] we designed and constructed a tweezer-like DNA nanostructure to actuate the activity of an enzyme/cofactor pair with reversible regulations.

5.2. Future Perspective

Self-assembled DNA nanostructures can now be used to organize a variety of heterogeneous elements into precise patterns on rationally designed 2D and 3D nanoarchitectures. Future challenges include identifying how to harness this power to construct functional, spatially interactive biomolecule complexes. Here, we identify several potential applications of DNA nanotechnology in constructing artificial bionanosystems.

5.2.1. Bottom-up Engineering of Multicomponent Complexes. Translating biochemical reaction pathways to noncellular environments is of great scientific interest. Exerting control over these pathways beyond nature's repertoire would enable enzyme-catalyzed production of novel molecules and energy conversion optimized for ambient and extreme environments. Engineering functional multienzyme complexes requires a method to reliably organize the individual protein components with control over the relative position, orientation, and quantity of the participating molecules. The combination of self-assembled DNA nanostructures and common bioconjugation strategies make it possible to rationally design and organize multiprotein pathways, as well as modulate the local environment and influence the corresponding chemical

reactions. For example, the direct transfer of a substrate from one enzyme to a proximal enzyme (substrate channeling), is one of the primary ways that natural systems facilitate highly efficient enzyme activity.[4] Similar channeling effects can be replicated in a DNA nanostructure system by optimizing the relative position and orientation of the catalytic components. Directed diffusion over longer distances can be achieved by modifying the environment between two enzymes with specific properties (polarity or hydrophobicity) that encourage substrate diffusion. It is also possible to constrain the diffusion between two enzymes by constructing DNA cavities or nanotubes. Further, enzyme pathway feedback mechanisms may be realized by constructing branched reaction pathways, where the catalytic activities are regulated by activation or deactivation of a specific pathway.

5.2.2. *In Vivo* Delivery and Regulation. Nanotechnology has been applied to target-specific drug delivery, *in vivo* regulation, visualization, and sensing. Structural DNA nanotechnology may be used to construct more effective drug delivery vehicles through the implementation of complex control mechanisms to sense specific targets, respond to environmental conditions, release molecular payloads, and trigger additional responses to regulate biological functions that impede disease progression. DNA-based nanocontainers, such as DNA boxes with switchable lids that open and close[5] and nanocages with the ability to encapsulate or release nanoparticles,[6] have demonstrated potential as drug-delivery vehicles. An autonomous DNA nanorobot controlled by an aptamer-encoded logic gate was recently reported to transport molecular payloads to cells, sense cell surface inputs for triggered activation, and transform its structure for payload delivery.[7]

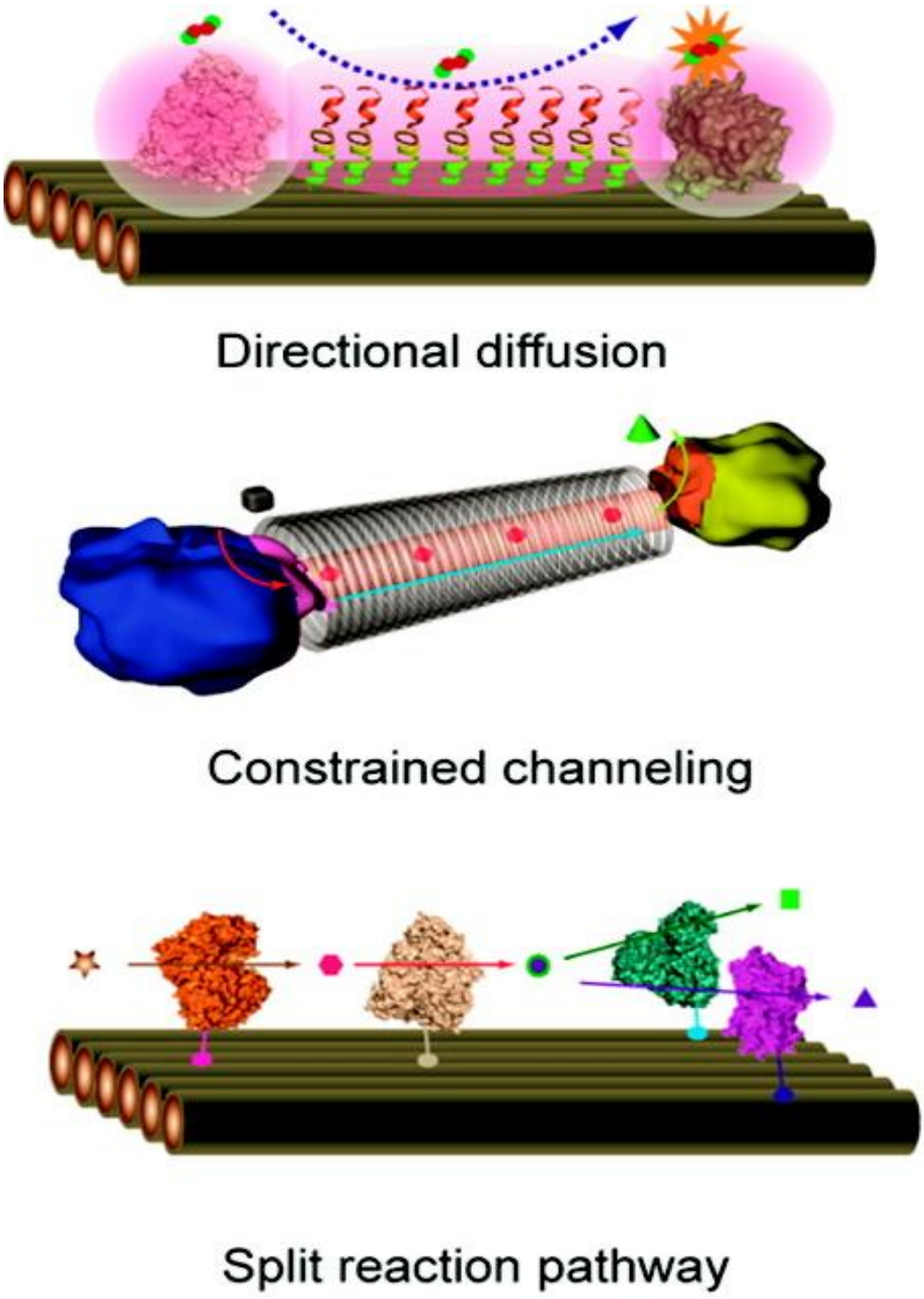

Figure 5.1. Engineering enzyme pathways to achieve directional substrate diffusion (top), constrained substrate tunneling (middle), and split enzyme pathways as feedback mechanisms (bottom).

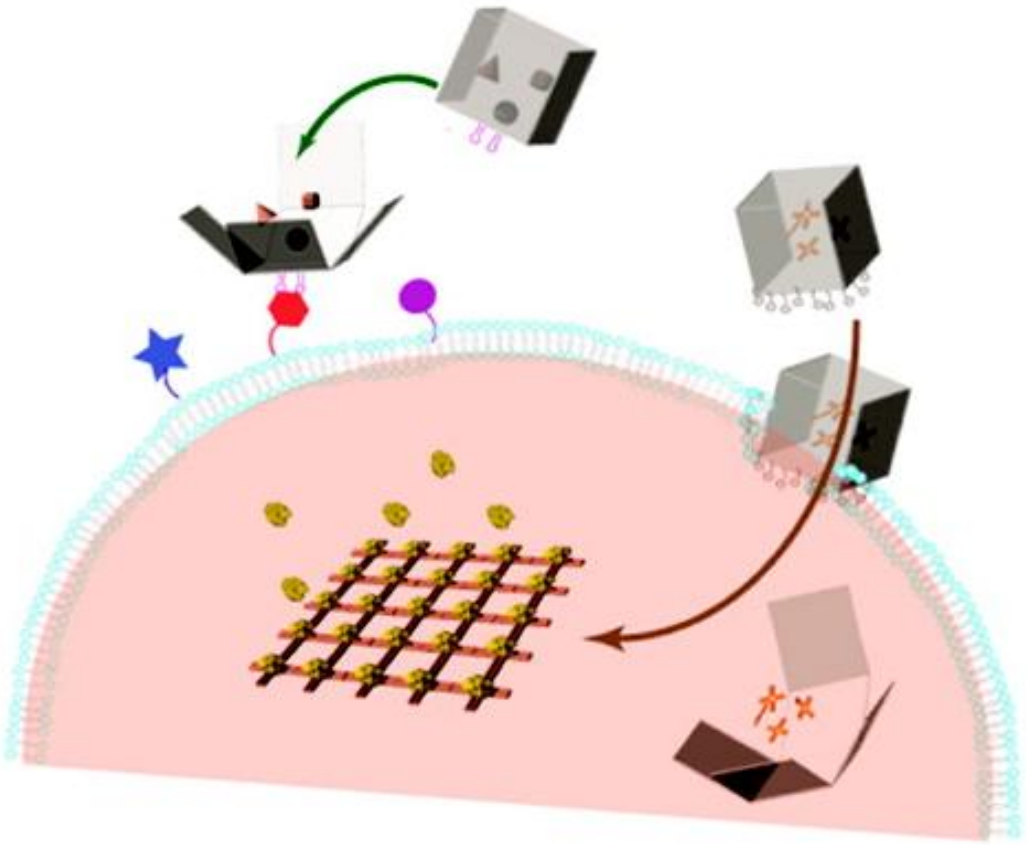

Figure 5.2. Proposed DNA nanocontainer for target-specific drug delivery and in vivo regulation.

In order to realize this nanocontainer application, the resistance of DNA nanostructures to the components of serum and cell lysate must be increased so that they may withstand *in vivo* delivery conditions. A study two years ago showed that certain DNA origami structures maintain their structural integrity after incubation with cell lysate for up to 12 h, a significant increase in stability compared with natural single- and double-stranded DNA.[8] In addition, it is a challenge to transfer DNA nanostructures across cell membranes. Some recent studies have shown that DNA nanostructures modified with CPG[9] or aptamers[10] can be taken up by cells. The display of certain ligands (amphiphilic molecules, for example) from the surface of a DNA nanostructure may

facilitate tissue penetration and cellular uptake of DNA nanodevices. Combining DNA nanotechnology with molecular biology may result in the development of novel ways to regulate cellular response. It may be feasible to construct artificial intracellular or extracellular nanomatrices that are designed to influence gene expression or modulate biological pathways.

5.3. References

(1) Stephanopoulos, N.; Liu, M.; Tong, G. J.; Li, Z.; Liu, Y.; Yan, H.; Francis, M. B. *Nano Lett.* **2010**, *10*, 2714-2720.

(2) Fu, J.; Liu, M.; Liu, Y.; Woodbury, N. W.; Yan, H. *J. Am. Chem. Soc*. **2012**, *134*, 5516-5519.

(3) Liu, M .; Fu, J.; Hejesen, C.; Yang, Y.; Woodbury, N.W.; Gothelf, K.; Liu, Y.; Yan, H. Submitted to *Nature Communication*.

(4) Miles, E. W.; Rhee, S.; Davies, D. R. *J. Biol. Chem*. 1999, 274, 12193-12196.

(5) Andersen, E. S.; Dong, M.; Nielsen, M. M.; Jahn, K.; Subramani, R.; Mamdouh, W.; Golas, M.M.; Sander, B.; Stark, H.; Oliveira, C. L. P.; Pedersen, J. S.; Birkedal, V.; Besenbacher, F.; Gothelf, K. V.; Kjems, J. *Nature* **2009**, *459*, 73-76.

(6) Zhao, Z.; Jacovetty, E. L.; Liu, Y.; Yan, H. *Angew. Chem., Int. Ed*. **2011**, *50*, 2041-2044.

(7) Douglas, S. M.; Bachelet, I.; Church, G. M. *Science* **2012**, *335*, 831-834.

(8) Mei, Q.; Wei, X; Su, F.; Liu, Y.; Youngbull, C.; Johnson, R.; Lindsay, S.; Yan, H.; Meldrum, D. *Nano Lett*. **2011**, *11*, 1477-1482.

(9) Schüller, V. J.; Heidegger, S.; Sandholzer, N.; Nickels, P. C.; Suhartha, N. A.; Endres, S.; Bourquin, C.; Liedl, T. *ACS Nano* **2011**, *5*, 9696-9702.

(10) Chang, M.; Yang, C.-S.; Huang, D.-M. *ACS Nano* **2011**, *5*, 6156-6163.

Bibliography

Chapter 1 References

(1) Savage, D. F.; Afonso, B.; Chen, A. H.; Silver, P. A. *Science* **2010**, *327*, 1258-1261.

(2) Cogdell, R. J.; Gall, A.; Köhler, J. *Q. Rev. Biophys*. **2006**, *39*, 227–324.

(3) Stupp, S. I. *Nano Lett*. **2010**, *10*, 4783–4786.

(4) Lin, C.; Liu, Y.; Yan, H. *Biochemistry* **2009**, *48*, 1663-1674.

(5) Watson, J. D.; Crick, F. H. C. *Nature*. **1953**, *171*, 737-738.

(6) Seeman, N. C. *J. Theor. Biol*. **1982**, *99*, 237–247.

(7) Fu, T. J.; Seeman, N. C. *Biochemistry* **1993**, *32*, 3211-3220.

(8) Winfree, E.; Liu, F.; Wenzler, L. A.; Seeman, N. C. *Nature* **1998**, *394*, 539-544.

(9) Park, S. H.; Barish, R.; Li, H.; Reif, J. H.; Finkelstein, G.; Yan, H.; LaBean, T. H. *Nano Lett*. **2005**, *5*, 693-696

(10) Mao, C.; Sun, W.; Seeman, N. C. *J. Am. Chem. Soc*. **1999**, *121*, 5437-5443.

(11) Chen, J.; Seeman, N. C. *Nature* **1991**, *350*, 631-633.

(12) Goodman, R. P.; Schaap, I. A. T.; Tardin, C. F.; Erben, C. M.; Berry, R. M.; Schmidt, C. F.; Turberfield, A. J. *Science* **2005**, *310*, 1661-1665.

(13) He, Y.; Ye, T.; Su,M.; Zhang, C.; Ribbe, A. E.; Jiang,W.;Mao, C. *Nature* **2008**, *452*, 198-201.

(14) Rothemund, P.W. K. Nature **2006**, *440*, 297-302.

(15) Andersen, E. S.; Dong, M.; Nielsen, M. M.; Jahn, K.; Subramani, R.; Mamdouh, W.; Golas, M.M.; Sander, B.; Stark, H.; Oliveira, C. L. P.; Pedersen, J. S.; Birkedal, V.; Besenbacher, F.; Gothelf, K. V.; Kjems, J. *Nature* **2009**, *459*, 73-76.

(16) Douglas, S. M.; Dietz, H.; Liedl, T.; Hogberg, B.; Graf, F.; Shih,W. M. *Nature* **2009**, *459*, 414-418.

(17) Ke, Y.; Douglas, S. M.; Liu, M.; Sharma, J.; Cheng, A.; Leung, A.; Liu, Y.; Shih, W. M.; Yan, H. *J. Am. Chem. Soc*. **2009**, *131*, 15903-15908.

(18) Ke, Y.; Voigt, N. V.; Gothelf, K. V.; Shih,W.M. *J. Am. Chem. Soc*. **2011**, *134*, 1770-1774.

(19) Dietz, H.; Douglas, S. M.; Shih, W. M. *Science* **2009**, *325*, 725-730.

(20) Han, D.; Pal, S.; Nangreave, J.; Deng, Z.; Liu, Y.; Yan, H. *Science* **2011**, *332*, 342–346.

(21) Chhabra, R.; Sharma, J.; Ke, Y.; Liu, Y.; Rinker, S.; Lindsay, S.; Yan, H. *J. Am. Chem. Soc*. **2007**, *129*, 10304-10305.

(22) Williams, B. A. R.; Lund, K.; Liu, Y.; Yan, H.; Chaput, J. C. *Angew. Chem., Int. Ed*. **2007**, *46*, 3051–3054.

(23) Kuzyk, A.; Laitinen, K. T.; Törmä, P. *Nanotechnology* **2009**, *20*, 235305.

(24) Stephanopoulos, N.; Liu, M.; Tong, G. J.; Li, Z.; Liu, Y.; Yan, H.; Francis, M. B. *Nano Lett.* **2010**, *10*, 2714-2720.

(25) Saccà, B.; Meyer, R.; Erkelenz, M.; Kiko, K.; Arndt, A.; Schroeder, H.; Rabe, K. S. *Angew. Chem., Int. Ed*. **2010**, *49*, 9378-9383.

(26) Goodchild, J. *Bioconjugate Chem*. **1990**, *1*, 165-187.

(27) Williams, B. A. R.; Diehnelt, C. W.; Belcher, P.; Greving, M.; Woodbury, N. W.; Johnston, S. A.; Chaput, J. C. *J. Am. Chem. Soc*. **2009**, *131*, 17233-17241.

(28) Thermo Scientific Pierce Protein Biology Products instruction http://www.piercenet.com/instructions/2160279.pdf

(29) Niemeyer, C. M. *Angew. Chem., Int. Ed*. **2010**, *49*, 1200–1216.

(30) Yan, H.; Park, S. H.; Finkelstein, G.; Reif, J. H.; LaBean, T. H. *Science* **2003**, *301*, 1882-1884.

(31) Dueber, J. E.; Wu, G. C.; Malmirchegini, G. R.; Moon, T. S.; Petzold, C. J.; Ullal, A. V.;Prather, K. L. J.; Keasling, J. D. *Nat. Biotechnol*. **2009**, *27*, 753-759.

(32) Sheldon, R. A. *Adv. Synth. Catal*. **2007**, *349*, 1289-1307.

(33) Teller, C.; Willner, I. *Trends Biotechnol*. **2010**, *28*, 619-628.

(34) Niemeyer, C. M.; Koehler, J.; Wuerdemann, C. *ChemBioChem*. **2002**, *3*, 242-245.

(35) Erkelenz, M.; Kuo, C. H.; Niemeyer, C. M. *J. Am. Chem. Soc*. **2011**, *133*, 16111-16118.

(36) Wilner, O. I.; Weizmann, Y.; Gill, R.; Lioubashevski, O.; Freeman, R.; Willner, I. *Nat. Nanotechnol*. **2009**, *4*, 249-254.

(37) Fu, J.; Liu, M.; Liu, Y.; Woodbury, N. W.; Yan, H. *J. Am. Chem. Soc*. **2012**, *134*, 5516-5519.

(38) Omabegho, T.; Sha, R.; Seeman, N. C. *Science* **2009**, *324*, 67-71.

(39) He, Y.; Liu, D. R. *Nat. Nanotechnol*. **2010**, *5*, 778-782.

(40) Lund, K.; Manzo, A. J.; Dabby, N.; Michelotti, N.; Johnson-Buck, A.; Nangreave, J.; Taylor, S.; Pei, R.; Stojanovic,M. N.;Walter, N. G.;Winfree, E.; Yan, H. *Nature* **2010**, *465*, 206-210.

(41) Chhabra, R.; Sharma, J.; Liu, Y.; Yan, H. *Nano Lett*. **2006**, *6*, 978-983.

(42) Kuzuya, A.; Sakai, Y.; Yamazaki, T.; Xu, Y.; Komiyama, M. *Nat. Commun*. **2011**, *2*, 449.

(43) Liu, M .; Fu, J.; Hejesen, C.; Yang, Y.; Woodbury, N.W.; Gothelf, K.; Liu, Y.; Yan, H. Submitted to *Nature Chemistry*.

(44) Modi, S.; Swetha, M. G.; Goswami, D.; Gupta, G. D.; Mayor, S.; Krishnan, Y. *Nat. Nanotechnol*. **2009**, *4*, 325-330.

(45) Choi, H. M. T.; Chang, J. Y.; Trinh, L. A.; Padilla, J. E.; Fraser, S. E.; Pierce, N. A. *Nat. Biotechnol*. **2010**, *28*, 1208-1212.

Chapter 2 References

(1) Douglas, T.; Young, M. *Science* **2006**, *312*, 873-875.

(2) Fischlechner, M.; Donath, E. *Angew. Chem., Int. Ed*. **2007**, *46*, 3184-3193.

(3) Wang, Q.; Lin, T.; Tang, L.; Johnson, J. E.; Finn, M. G. *Angew. Chem., Int. Ed.* **2002**, *41*, 459-462.

(4) Demir, M.; Stowell, M. H. B. *Nanotechnology* **2002**, *13*, 541-544.

(5) Schlick, T. L.; Ding, Z. B.; Kovacs, E. W.; Francis, M. B. *J. Am. Chem. Soc*. **2005**, *127*, 3718-3723.

(6) Miller, R. A.; Presley, A. D.; Francis, M. B. *J. Am. Chem. Soc*. **2007**, *121*, 3104-3109.

(7) Endo, M.; Wang, H.; Fujitsuka, M.; Majima, T. *Chem.-Eur. J.* **2006**, *12*, 3735-3740.

(8) Miller, R. A.; Stephanopoulos, N.; McFarland, J. M.; Rosko, A. S.; Geissler, P. L.; Francis, M. B. *J. Am. Chem. Soc*. **2010**, *132*, 6068-6074.

(9) Stephanopoulos, N.; Carrico, Z. M.; Francis, M. B. *Angew. Chem., Int. Ed*. **2009**, *48*, 9498-9502.

(10) Nam, Y. S.; Magyar, A. P.; Lee, D.; Kim, J.-W.; Yun, D. S.; Park, H.; Pollom, T. S.; Weitz, D. A.; Belcher, A. M. Nat. *Nanotechnol*. **2010**, *5*, 340-344.

(11) Douglas, T.; Young, M. J. *Nature* **1998**, *393*, 152-155.

(12) Douglas, T.; Strable, E.; Willits, D.; Aitouchen, A.; Libera, M.; Young, M. *Adv. Mater*. **2002**, *14*, 415-418.

(13) Loo, L.; Guenther, R. H.; Basnayake, V. R.; Lommel, S. A.; Franzen, S. *J. Am. Chem. Soc*. **2006**, *128*, 4502-4503.

(14) Loo, L.; Guenther, R. H.; Lommel, S. A.; Franzen, S. *J. Am. Chem. Soc*. **2007**, *129*, 11111-11117.

(15) Dixit, S. K.; Goicochea, N. L.; Daniel, M.-C.; Murali, A.; Bronstein, L.; De, M.; Stein, B.; Rotello, V. M.; Kao, C. C.; Dragnea, B. *Nano Lett*. **2006**, *6*, 1993-1999.

(16) Kovacs, E. W.; Hooker, J. M.; Romanini, D. W.; Holder, P. G.; Berry, K. E.; Francis, M. B. *Bioconjugate Chem*. **2007**, *18*, 1140-1147.

(17) Comellas-Aragone`s, M.; Escosura, A.; Dirks, A. J.; van der Ham, A.; Fusté-Cuñé, A.; Cornelissen, J. J. L. M.; Nolte, R. J. M. *Biomacromolecules* **2009**, *10*, 3141-3147.

(18) Abedin, M. J.; Liepold, L.; Suci, P.; Young, M.; Douglas, T. *J. Am. Chem. Soc*. **2009**, *131*, 4346-4354.

(19) Wu, W.; Hsiao, S. C.; Carrico, Z. M.; Francis, M. B. *Angew. Chem., Int. Ed*. **2009**, *48*, 9493-9497.

(20) Manchester, M.; Singh, P. Adv. *Drug Delivery Rev*. **2006**, *58*, 1505-1522.

(21) Suci, P. A.; Varpness, Z.; Gillitzer, E.; Douglas, T.; Young, M. *Langmuir* **2007**, *23*, 12280-12286.

(22) Flenniken, M.; Uchida, M.; Liepold, L.; Kang, S.; Young, M.; Douglas, T. *Viruses Nanotechnol*. **2009**, *327*, 71.

(23) Anderson, E. A.; Isaacman, S.; Peabody, D. S.; Wang, E. Y.; Canary, J. W.; Kirshenbaum, K. *Nano Lett*. **2006**, *6*, 1160-1164.

(24) Hooker, J. M.; Datta, A.; Botta, M.; Raymond, K. N.; Francis, M. B. *Nano Lett.* **2007**, *7*, 2207-2210.

(25) Hooker, J. M.; O'Neil, J. P.; Romanini, D. W.; Taylor, S. E.; Francis, M. B. *Mol. Imaging Biol*. **2008**, *10*, 182-191.

(26) Klem, M. T.; Willits, D.; Young, M.; Douglas, T. *J. Am. Chem. Soc*. **2003**, *125*, 10806-10807.

(27) Strable, E.; Johnson, J. E.; Finn, M. G. *Nano Lett*. **2004**, *4*, 1385-1389.

(28) Smith, J. C.; Lee, K.-B.; Wang, Q.; Finn, M. G.; Johnson, J. E.; Mrksich, M.; Mirkin, C. A. *Nano Lett*. **2003**, *3*, 883-886.

(29) Cheung, C. L.; Camarero, J. A.; Woods, B. W.; Lin, T.; Johnson, J. E.; De Yoreo, J. J. *J. Am. Chem. Soc*. **2003**, *125*, 6848-6849.

(30) Rothemund, P. W. K. *Nature* **2006**, *440*, 297-302.

(31) Ding, B.; Deng, Z.; Yan, H.; Cabrini, S.; Zuckermann, R. N.; Bokor, J. *J. Am. Chem. Soc*. **2010**, *132*, 3248-3249.

(32) Sharma, J.; Chhabra, R.; Andersen, C. S.; Gothelf, K. V.; Yan, H.; Liu, Y. *J. Am. Chem. Soc*. **2008**, *130*, 7820-7821.

(33) Pal, S.; Deng, Z.; Ding, B.; Yan, H.; Liu, Y. *Angew. Chem., Int. Ed*. **2010**, *122*, 2760-2764.

(34) Ke, Y.; Lindsay, S.; Chang, Y.; Liu, Y.; Yan, H. *Science* **2008**, *319*, 180-183.

(35) Maune, H. T.; Han, S.; Barish, R. D.; Bockrath, M.; Goddard III, W. A.; Rothemund, P. W. K.; Winfree, E. *Nat. Nanotechnol*. **2010**, 5, 61-66.

(36) Rinker, S.; Ke, Y.; Liu, Y.; Chhabra, R.; Yan, H. *Nat. Nanotechnol*. **2008**, *3*, 418-422.

(37) Chabra, R.; Sharma, J.; Ke, Y.; Liu, Y.; Rinker, S.; Lindsay, S.; Yan, H. *J. Am. Chem. Soc*. **2007**, *129*, 10304-10305.

(38) Shen, W.; Zhong, H.; Neff, D.; Norton, M. L. *J. Am. Chem. Soc*. **2009**, *131*, 6660-6661.

(39) Kuzuya, A.; Kimura, M.; Numajiri, K.; Koshi, N.; Ohnishi, T.; Okada, F.; Komiyama, K. *ChemBioChem* **2009**, *10*, 1811-1815.

(40) Hooker, J. M.; Kovacs, E. W.; Francis, M. B. *J. Am. Chem. Soc*. **2004**, *126*, 3718-3719.

(41) Valegård, K.; Liljas, L.; Fridborg, K.; Unge, T. *Nature* **1990**, *345*, 36-41.

(42) Mastico, R. A.; Talbot, S. J.; Stockley, P. G. *J. Gen. Virol*. **1993**, *74*, 541-548.

(43) Tong, G. J.; Hsiao, S. C.; Carrico, Z. M.; Francis, M. B. *J. Am. Chem. Soc*. **2009**, *131*, 11174-11178.

(44) Mehl, R. A.; Anderson, J. C.; Santoro, S. W.; Wang, L.; Martin, A. B.; King, D. S.; Horn, D. M.; Schultz, P. G. *J. Am. Chem. Soc*. **2003**, *125*, 935-939.

(45) Le, J. D.; Pinto, Y.; Seeman, N. C.; Musier-Forsyth, K.; Taton, T. A.; Kiehl, R. A. *Nano Lett*. **2004**, *4*, 2343-2347.

Chapter 3 References

(1) Miles, E. W.; Rhee, S.; Davies, D. R. *J. Biol. Chem*. **1999**, *274*,12193.

(2) Perham, R. N. *Annu. Rev. Biochem*. **2000**, *69*, 961.

(3) Srere, P. A.; Mosbach, K. *Annu. Rev. Microbiol*. **1974**, *28*, 61.

(4) Yeates, T. O.; Kerfeld, C. A.; Heinhorst, S.; Cannon, G. C.; Shively, J. M. *Nat. Rev. Microbiol*. **2008**, *6*, 681.

(5) Lin, C.; Liu, Y.; Yan, H. *Biochemistry* **2009**, *48*, 1663.

(6) Seeman, N. C. *Annu. Rev. Biochem*. **2010**, *79*, 65.

(7) Voigt, N. V.; Torring, T.; Rotaru, A.; Jacobsen, M. F.; Ravnsbaek, J. B.; Subramani, R.; Mamdouh, W.; Kjems, J.; Mokhir, A.; Besenbacher, F.; Gothelf, K. V. *Nat. Nanotechnol*. **2010**, *5*, 200.

(8) Wilner, O. I.; Weizmann, Y.; Gill, R.; Lioubashevski, O.; Freeman, R.; Willner, I. *Nat. Nanotechnol*. **2009**, *4*, 249.

(9) Delebecque, C. J.; Lindner, A. B.; Silver, P. A.; Aldaye, F. A. *Science* **2011**, *333*, 470.

(10) Niemeyer, C. M.; Koehler, J.; Wuerdemann, C. *ChemBioChem* **2002**, *3*, 242.

(11) Erkelenz, M.; Kuo, C. H.; Niemeyer, C. M. *J. Am. Chem. Soc*. **2011**, *133*, 16111.

(12) Rothemund, P. W. K. *Nature* **2006**, *440*, 297.

(13) Pinheiro, A. V.; Han, D.; Shih, W. M.; Yan, H. *Nat. Nanotechnol*. **2011**, *6*, 763.

(14) Ke, Y.; Lindsay, S.; Chang, Y.; Liu, Y.; Yan, H. *Science* **2008**, *319*, 180.

(15) Pathria, R. K. *Statistical Mechanics*, 2nd ed.; Butterworth- Heinemann: Woburn, MA, **1996**; pp 459−464.

(16) Henzler, T.; Steudle, E. *J. Exp. Bot*. **2000**, *51*, 2053.

(17) Stewart, P. S. *J. Bacteriol*. **2003**, *185*, 1485.

(18) Childs, R. E.; Bardsley, W. G. *Biochem J*. **1975**, *145*, 93.

(19) Bagchi, B. *Chem. Rev*. **2005**, *105*, 3197.

(20) Chung, Y.-H.; Xia, J.; Margulis, C. J. *J. Phys. Chem. B* **2007**, *111*, 13336.

(21) Dom ńguez, L.; Sosa-Peinado, A.; Hansberg, W. *Arch. Biochem. Biophys*. **2010**, *500*, 82.

(22) Gorman, J.; Greene, E. C. *Nat. Struct. Mol. Biol*. **2008**, *15*, 768.

(23) Jeltsch, A.; Pingoud, A. *Biochemistry* **1998**, *37*, 2160.

(24) Mansson, M. O.; Siegbahn, N.; Mosbach, K. *Proc. Natl. Acad. Sci. U. S. A.* **1983**, *80*, 1487.

(25) Niemeyer, C. M. *Angew. Chem., Int. Ed. Engl*. **2010**, *49*, 1200.

(26) Saccà, B.; Meyer, R.; Erkelenz, M.; Kiko, K.; Arndt, A.; Schroeder, H.; Rabe, K. S.; Niemeyer, C. M. *Angew. Chem., Int. Ed. Engl*. **2010**, *49*, 9378.

Chapter 4 References

(1) Bairoch, A. *Nucleic Acids Res*. **2000**, *28*, 304-305.

(2) Hammes, G. G., Wu, C.W. *Science* **1971**, *172*, 1205-1211.

(3) Drews, J. *Science* **2000**, *287*, 1960-1964.

(4) Ostermeier, M. *Curr. Opin. Struct. Biol*. **2009**, *19*, 442-448.

(5) Khosla, C.; Harbury, P. B. *Nature* **2001**, *409*, 247-252.

(6) Sheldon, Roger A. *Adv. Synth. Catal*. **2007**, *349*, 1289-1307.

(7) Vriezema, Dennis M. et al. *Angew. Chem. Int. Ed*. **2007**, *46*, 7378-7382.

(8) Palomo, J. M. *Curr. Org. Synth*. **2009**, *6*, 1-14.

(9) Bogue, R. *Assembly Autom.* **2012**, *21*, 3-7 (2012).

(10) Fu, J.; Liu, M.; Liu, Y.; Yan, H. *Acc. Chem. Res*. **2012**, *45*, 1215-1226.

(11) Pinheiro, A. V.; Han, D.; Shih, W. M.; Yan, H. *Nature Nanotech*. **2011**, *6*, 763-772.

(12) Seeman, N. C. *Annu. Rev. Biochem*. **2010**, *79*, 65-87.

(13) Lund, K.; Manzo, A. J.; Dabby, N.; Michelotti, N.; Johnson-Buck, A.; Nangreave, J.; Taylor, S.; Pei, R.; Stojanovic,M. N.;Walter, N. G.;Winfree, E.; Yan, H. *Nature* **2010**, *465*, 206-210.

(14) Gu, H.; Chao, J.; Xiao, S.J.; Seeman, N. C. *Nature* **2010**, *465*, 202-205.

(15) Zhou, C.; Yang, Z.; Liu, D. *J. Am. Chem. Soc*. **2012**, *134*, 1416-1418.

(16) Liedl, T.; Hogberg, B.; Tytell, J.; Ingber, D. E.; Shih, W. M. *Nature Nanotech.* **2010**, *5*, 520-524.

(17) Modi, S.; Swetha, M. G.; Goswami, D.; Gupta, G. D.; Mayor, S.; Krishnan, Y. *Nature Nanotech*. **2009**, *4*, 325-330.

(18) Chhabra, R.; Sharma, J.; Liu, Y.; Yan, H. *Nano Lett*. **2006**, *6*, 978-983.

(19) Andersen, E. S.; Dong, M.; Nielsen, M. M.; Jahn, K.; Subramani, R.; Mamdouh, W.; Golas, M.M.; Sander, B.; Stark, H.; Oliveira, C. L. P.; Pedersen, J. S.; Birkedal, V.; Besenbacher, F.; Gothelf, K. V.; Kjems, J. *Nature* **2009**, *459*, 73-76.

(20) Douglas, S. M.; Bachelet, I.; Church, G. M. *Science* **2012**, *335*, 831-834.

(21) Niemeyer, C. M. *Angew. Chem. Int. Ed*. **2010**, *49*, 1200-1216.

(22) Fu, J.; Liu, M.; Liu, Y.; Woodbury, N. W.; Yan, H. *J. Am. Chem. Soc*. **2012**, *134*, 5516-5519.

(23) Wilner, O. I.; Weizmann, Y.; Gill, R.; Lioubashevski, O.; Freeman, R.; Willner, I. *Nature Nanotech*. **2009**, *4*, 249-254.

(24) Delebecque, C. J.; Lindner, A. B.; Silver, P. A.; Aldaye, F. A. *Science* **2011**, *333*, 470-474.

(25) Fu, Y. et. al. *J. Am. Chem. Soc*. **2012**, *135*, 696-702.

(26) Rupcich, N.; Chiuman, W.; Nutiu, R.; Mei, S.; Flora, K. K.; Li, Y.; Brennan, J. D. *J. Am. Chem. Soc*. **2005**, *128*, 780-790.

(27) Lee, S.; Lee, J.; Hohng, S. *PLoS ONE* **2010**, *5*, e12270.

(28) Foerster, T. *Ann. Phys.* **1948**, *2*, 55.

(29) Bowen, M. E.; Weninger, K.; Ernst, J.; Chu, S.; Brunger, A. T. *Biophys. J.* **2005**, *89*, 690-702.

(30) Yurke, B.; Turberfield, A. J.; Mills, A. P.; Simmel, F. C.; Neumann, J. L. *Nature* **2000**, *406*, 605-608.

(31) Schmidt, H.-L.; Grenner, G. *Eur. J. Biochem*. **1976**, *67*, 295-302.

(32) Rowland, P.; Basak, A. K.; Gover, S.; Levy, H. R.; Adams, M. J. *Structure* **1994**, *2*, 1073-1087.

(33) Moore, S. P., Sutherland, B. M. *Anal. Biochem*. **1985**, *144*, 15-19.

(34) Wray, W., Boulikas, T., Wray, V. P., Hancock, R. *Anal. Biochem*. **1981**, *118*, 197-203.

Chapter 5 References

(1) Stephanopoulos, N.; Liu, M.; Tong, G. J.; Li, Z.; Liu, Y.; Yan, H.; Francis, M. B. *Nano Lett.* **2010**, *10*, 2714-2720.

(2) Fu, J.; Liu, M.; Liu, Y.; Woodbury, N. W.; Yan, H. *J. Am. Chem. Soc*. **2012**, *134*, 5516-5519.

(3) Liu, M .; Fu, J.; Hejesen, C.; Yang, Y.; Woodbury, N.W.; Gothelf, K.; Liu, Y.; Yan, H. Submitted to *Nature Chemistry*.

(4) Miles, E. W.; Rhee, S.; Davies, D. R. *J. Biol. Chem*. 1999, 274, 12193-12196.

(5) Andersen, E. S.; Dong, M.; Nielsen, M. M.; Jahn, K.; Subramani, R.; Mamdouh, W.; Golas, M.M.; Sander, B.; Stark, H.; Oliveira, C. L. P.; Pedersen, J. S.; Birkedal, V.; Besenbacher, F.; Gothelf, K. V.; Kjems, J. *Nature* **2009**, *459*, 73-76.

(6) Zhao, Z.; Jacovetty, E. L.; Liu, Y.; Yan, H. *Angew. Chem., Int. Ed*. **2011**, *50*, 2041-2044.

(7) Douglas, S. M.; Bachelet, I.; Church, G. M. *Science* **2012**, *335*, 831-834.

(8) Mei, Q.; Wei, X; Su, F.; Liu, Y.; Youngbull, C.; Johnson, R.; Lindsay, S.; Yan, H.; Meldrum, D. *Nano Lett*. **2011**, *11*, 1477-1482.

(9) Schüller, V. J.; Heidegger, S.; Sandholzer, N.; Nickels, P. C.; Suhartha, N. A.; Endres, S.; Bourquin, C.; Liedl, T. *ACS Nano* **2011**, *5*, 9696-9702.

(10) Chang, M.; Yang, C.-S.; Huang, D.-M. *ACS Nano* **2011**, *5*, 6156-6163.

APPENDIX A

SUPPLEMENTAL INFORMATION FOR CHAPTER 2

Supplemental Information

DNA-Directed Self-Assembly: Immobilization and 1D Arrangement of Virus Capsids with Nanoscale Precision Using DNA Origami

Nicholas Stephanopoulos[‡1], Minghui Liu[‡2], Gary Tong[1], Zhe Li[2], Yan Liu[2], Hao Yan[*2], Matthew B. Francis[*1]

[1]Department of Chemistry, University of California, Berkeley, and Materials Sciences Division, Lawrence Berkeley National Labs, Berkeley, CA 94720-1460

[2]Department of Chemistry and Biochemistry and the Biodesign Institute, Arizona State University, Tempe AZ 85287

Author Contributions: Nicholas Stephanopoulos and Minghui Liu contributed equally to this work.

1. Experimental Methods and Materials

1.1. General

Unless otherwise noted, all chemicals and solvents were of analytical grade and were used as received from commercial sources. Water (ddH2O) used in biological procedures or as reaction solvents was deionized using a NANOpure purification system (Barnstead, USA). The centrifugations required in spin-concentration steps were conducted using a Sorvall Legend Mach 1.6R centrifuge (Thermo Fisher Scientific, USA).

Prior to analysis, biological samples were desalted and separated from small molecule contaminants using NAP-5 or NAP-10 gel filtration columns (Amersham Biosciences, USA). MS2 capsids elute in the void volume of these columns, while small molecules are retained. Additionally, 100,000 Da molecular weight cut-off filters (Millipore, USA) were employed as indicated below.

All oligonucleotides were obtained from Integrated DNA Technologies (www.idtdna.com). The origami staple strands were ordered in the format of 96-well plates that were normalized to 100μM, and were used without further purification. The probe strands were purified by denaturing PAGE. Then concentration of each strand was measured and estimated by measuring the OD260 (Eppendorf, USA). Oligonucleotides for capsid conjugation were purified by reverse-phase HPLC or NAP-5 gel filtration columns (GE Healthcare). Samples were lyophilized using a LAB CONCO Freezone 4.5 (Lab Conco). Lyophilized oligonucleotides were re-suspended in the appropriate buffer and the concentration was determined by measuring the OD260.

1.2. UV-Vis

UV-Vis spectroscopic measurements were conducted on a Cary 50 Scan benchtop spectrophotometer (Varian Inc., USA).

1.3. Protein Gel Analysis

For protein analysis, sodium dodecyl sulfate-polyacrylamide gel electrophoresis (SDS-PAGE) was accomplished on a Mini-Protean apparatus (BioRad, USA), following the general protocol of Laemmli.[1] Commercially-available markers (BioRad, USA) were applied to at least one lane of each gel for calculation of apparent molecular weights. Visualization of protein bands was accomplished by staining with Coomassie Brilliant Blue R-250 (BioRad, USA). Gel imaging was performed on an EpiChem3 Darkroom system (UVP, USA).

1.4. Transmission Electron Microscopy (TEM)

Part of TEM images were prepared for TEM analysis by applying analyte solution to carbon-coated copper grids (400 mesh, Ted Pella, USA) for 3 min, followed by rinsing with ddH_2O. The grids were then exposed to a solution of uranyl acetate (15 mg/mL in ddH_2O) for 90 seconds as a negative stain and rinsed with ddH_2O. TEM images were obtained at the Berkeley Electron Microscope Lab using a FEI Tecnai 12 transmission electron microscope with 120 kV accelerating voltage.

Part of TEM images were prepared by applying the sample solution (2.5 μL) onto carbon-coated grids (400 mesh, Ted Pella, USA). Before depositing the sample, the grids were glow discharged using an Emitech K100X machine. After deposition, the sample was wicked from the grid with a piece of filter paper. The grid was washed with water by touching it quickly with a drop of water and wicking away the excess using filter paper. The origami-capsid complex sample was stained using 0.7% uranyl formate and imaged

using a Philips CM12 transmission electron microscope, operated at 80kV in the bright field mode.

For Tri3 tiles, the capsids were clearly visualized as hollow spherical structures); for Tri1 tiles, however, the capsids did not stain as well, and the walls are not as easily discerned in some cases. The size of these objects (~30 nm) and the fact that in some of them the walls can be distinguished makes us confident that these are indeed the capsids. For arrays formed with rectangular tiles and capsids (either using M or DC tiles), the arrays adsorb to the grid edge-on, so the tile is visualized as a line connecting the capsids. The inter-capsid aggregation on the surface (which is commonly observed with MS2) often prevented distinguishing individual arrays as by AFM, but in numerous cases individual capsids clearly linked by tiles are visible. We note that the tiles are flexible and can curve, as seen in the TEM images, unlike in the AFM images where they adsorb flat on the surface.

1.5. Atomic Force Miscroscopy (AFM)

For imaging in air, after annealing samples, the tile-capsid conjugates were analyzed by tapping-mode AFM. To prepare samples, first 2 μL of 1 mM $NiCl_2$ in ddH_2O was applied to a freshly cleaved mica surface for 2 min. Next, 2 μL of sample was applied for an additional 2 min. The mica was then rinsed by dipping into ddH_2O and dried using a stream of nitrogen. Images were obtained using a Veeco Nanoscope V scanning probe miscroscopy (Veeco, USA) using FM-50 tips with a 75 kHz resonant frequency and a force constant of 2.8 N/m (Nano World, USA).

For imaging in solution, the AFM images were performed under 1x TAE-Mg^{2+} buffer (40 mM Tris, 20 mM acetic acid, 2 mM EDTA, 12.5 mM $Mg(OAc)_2$, pH 8.0) in a

fluid cell in tapping mode, using the tip on the shorter cantilever of the SNL tips (Veeco, USA). The sample (2 μL) was first deposited onto the freshly cleaved mica surface and left to adsorb for 1min. Then, 35 μL of 1x TAE-Mg^{2+} buffer was added onto the surface before obtaining the image.

1.6. Design of DNA Origami Tiles

The position of each probe strand was determined using the software program Tiamat (developed by the Yan Lab and collaborators: http://yanlab.asu.edu/Resources.html). The design of the rectangular origami tiles was as shown in Figure S1.The design of triangular origami was used as previously described by Rothemund. [2]A polyA/T hybridization strategy was chosen over a polyG/C strategy to avoid potential problems due to G-quadruplex formation.

1.7. Formation of Single DNA Origami Tiles

The origami tiles were formed according to the method of Rothemund.2 A molar ratio of 1:5 between the long M13 viral ssDNA and the short unmodified staple strands was used. The probe strands for hybridization with the poly-T strands on the capsid were used in 10:1 ratio to that of the viral DNA. Origami tiles were assembled in 1x TAE-Mg^{2+} buffer (40 mM Tris, 20 mM acetic acid, 2 mM EDTA, 12.5 mM $Mg(OAc)_2$, pH 8.0) by cooling slowly from 90 ℃ to room temperature. The origami tiles and excess staples were then separated by EtBr stained 1.5% agarose gel (running buffer 1x TAE-Mg^{2+} buffer, 10 V/cm), running in an ice-water bath. The band corresponding to the tiles was excised and the probe tiles were extracted from the gel using Freeze N' Squeeze columns (Bio-Rad, USA). After purification, the tiles were then concentrated using 100 kDa Microcon centrifugal filter devices (Millipore, USA). The final concentration of

origami tiles was estimated according to the dsDNA absorbance at 260nm and the calculated extinction coefficient (http://biophysics.idtdna.com/).

1.8. Single Tile Analysis

Purified origami tiles were verified by both EtBr stained 1.5% agarose gel (the same as the purification step) and AFM. Samples (10 μL) were mixed with 1 μL 10x native gel loading dye and then loaded into each well.

1.9. Production of N87C T19paF MS2

The unnatural amino acid p-aminophenylalanine (*p*aF) was incorporated into MS2 as previously described.[3] The N87C/T19*p*aF mutant plasmid was created by site-directed mutagenesis of the pBAD-T19*p*aF MS2 vector using forward primer following the Qiagen protocol:

5'-AGCCGCATGGCGTTCGTACTTATGTATGGAACTAACCATTC-3'

and reverse primer:

5'-GAATGGTTAGTTCCATACATAAGTACGAACGCCATGCGGCT-3'.

The pBAD-N87C/T19*p*aF was subsequently grown and purified as previously described.[3]

1.10. Modification of MS2 with Oregon Green (OG) Maleimide

The modification of capsids with OG maleimide was carried out as previously described.[4] To a solution of N87C T19*p*aF MS2 (80 μM in 10 mM phosphate buffer, pH 7) was added 20 equivalents of Oregon Green maleimide as a 100 mM solution in DMF. The reaction mixture was vortexed briefly, and then incubated at RT for 2 h in the dark. The mixture was then passed through a NAP-5 column equilibrated with 10 mM phosphate buffer, pH 7, to remove excess chromophore. The capsids were further concentrated using a 100,000 Da molecular weight cut-off filter. The conversion of

porphyrin was determined by comparing the absorbance of the Oregon Green absorption maximum (ε = 80,000 $M^{-1}cm^{-1}$) to the A260 of the protein (ε = 172,000 $M^{-1}cm^{-1}$) and assuming negligible dye absorbance at 260 nm. All exctinction coefficients were determined in 10 mM phosphate, pH 7, the buffer in which the MS2 conjugates were stored.

1.11. DNA attachment via oxidative coupling

The $(T)_{20}$ ssDNA sequence was appended to MS2 capsids modified inside with Oregon Green (OG) as previously described.[5] To synthesize the phenylene diamine conjugate necessary for the oxidative coupling, DNA strands containing a primary amine at the 5'-end were reacted with 4-(4-diethylamino-phenylcarbamoyl)-butyric acid (60-120 eq.) in a 1:1 solution of DMF and 50 mM phosphate buffer, pH 8. The reaction mixture was allowed to react at RT for 2 h, then purified by gel filtration to remove excess small molecule. The DNA was then lyophilized and resuspended in the desired buffer. The concentration was determined by measuring the absorbance at 260 nm.

The phenylene diamine-modified DNA strand was next attached to the MS2-OG conjugate via the oxidative coupling reaction as previously described. An Eppendorf tube was charged with MS2-OG (20 μM), the phenylene diamine-modified oligonucleotide (200 μM), and $NaIO_4$ (5 mM). The reaction mixture was vortexed and allowed to react at RT for 1 h. The reaction was quenched by the addition of 1/10 volume of 500 mM TCEP, then purified by NAP-5 filtration and spin-concentration using 100 kDa molecular weight cut-off filters.

1.12. Procedure for Annealing of Capsids to Tiles

For annealing reactions between capsids and tiles, the components were mixed in 2x TAE-Mg^{2+} buffer (80 mM Tris, 40 mM acetic acid, 4 mM EDTA, 25 mM $Mg(OAc)_2$, pH 8.0) and annealed from 37 to 4 ℃ at a rate of 1 ℃/min on a S1000 Thermal Cycler PCR machine (Bio-Rad, USA). Typical final tile concentration was ~2 nM, and the capsid concentration was scaled accordingly (e.g. ~ 4 nM in capsid for the experiments described in the paper). To make the E and M tile arrays, a small aliquot (~1 μL) of a concentrated solution of linker strands was added (either 5 or 10 equivalents) to the mixture prior to annealing. For the DC tile arrays, 5 equivalents of the edge staples (again as a small aliquot of concentrated solution) were added to the mixture prior to annealing. All samples were imaged by AFM immediately following annealing in order to prevent inter-tile or inter-array aggregation with time. A 2x concentration of buffer was used because we found that it gave longer arrays in general, most likely due to the increased electrostatic screening of the higher-salt buffer.

It appears that origami tiles and DNA in general bind to the mica surface with a greater efficiency than the MS2-dye-DNA conjugate or capsids alone. Thus, the two-fold excess of capsids used in most experiments is not obvious from inspecting the AFM images alone. Furthermore, in Figure S19, almost no capsids can be seen in the AFM image despite a two-fold excess relative to tiles. This is likely due to the large excess of $(T)_{40}$ ssDNA added, which preferentially binds the mica and passivates it against capsid binding.

Virtually 100% efficiency of capsid-tile association was also observed upon incubating the components at 4 ℃ overnight (without an annealing step), but we used the annealing procedure due to the efficacy and speed it afforded. We have also observed that

prolonged incubation of capsids and tiles results in lower-quality images for as of yet undetermined reasons, so shorter incubation times were preferred.

The dye modification of the interior of the capsids with OG did not have any effect on the hybridization efficiency. Capsids that did not contain the dye associated just as effectively with the tiles as capsids with the dye.

An "on-surface" association of tiles with capsids was also attempted. In this experiment, we took tile arrays formed without MS2 and deposited them on the surface first. After rinsing and drying the mica surface, a dilute solution of DNA-modified capsids was applied for about 5 minutes. Imaging by AFM showed that while a modest fraction of binding sites on the tiles contained MS2, there was too much non-specific background adsorption of capsids to the surface to make this approach useful. Furthermore, this approach may not be optimal because the arrays could bind to the surface with the probe strands facing downward, preventing access by the ssDNA on the capsids.

1.13. Array Length Distribution Quantification

To determine the distribution of array lengths shown in Figures S20-S22, multiple AFM images were obtained for each sample calculated (not all images were included in the Supporting Information). Manual counting of these images yielded the statistics reported in the distributions. For single tiles, visual inspection determined whether a tile had a capsid or not, and whether more than one tile was bound to a given capsid. Broken or incompletely formed tiles were not counted.

In counting the E and M tile arrays, only arrays that were completely in the field of view of the AFM image were counted. Furthermore, only arrays that were clearly

distinguishable were counted; occasional aggregates that prevented distinguishing individual arrays were disregarded. Array lengths are reported based on the number of tiles in an array; however, the association efficiency of tiles with capsids remained close to 100%, so the tile array length correlates pretty much exactly with the capsid array length.

In counting the DC tile arrays, once again only arrays that were completely in the field of view were counted, and large aggregates were disregarded. Due to the presence of tile edges without capsids bound, array lengths were reported with respect to the number of capsids in a row. The total number of tile edges without capsids was determined, as well as the number of branch points (defined as capsids that had more than two tiles bound to them).

1.14. Control Experiments

Control experiments were first carried out using the three rectangular tiles (E, M, and DC) and capsids modified with the dye but not with DNA (Figures S15-S17). Edge staples were added in the mixture as well for the case of the DC tiles. No significant association of the capsids with the tiles was observed; in addition, the DC tiles show significant edge stacking due to the staples added, indicating that this factor was an important "pre-organization" effect that aided the array. Control experiments were also carried out with E tiles bearing a random 40-nt sequence and capsids modified with the $(T)_{20}$ sequence used in the main experiments (Figure S18). Once again, no significant association of the capsids with the tiles was seen.

In another experiment, MS2-OG-$(T)_{20}$ was mixed with E tiles (bearing the correct $(A)_{40}$ sequence) and annealed, then in a second step a large excess (~1000-fold) of $(T)_{40}$

ssDNA was added and a second annealing carried out. The competing strand binds to the 40-nt probe on the tiles with a greater affinity than the 20-nt strands on the MS2; combined with the large excess added, this effect results in the displacement of the MS2 strands from the tile (Figure S19). Fewer tiles are seen on the surface than in other experiments, likely due to the passivation of the surface to MS2 binding due to the excess $(T)_{40}$ strand. The removal of the MS2 upon addition of the $(T)_{40}$ strand not only confirms the DNA-specific binding of the capsids, but also suggests a possible way to remove the capsids from the tiles if capsid release is required at a later time.

2. DNA Sequences

2.1. E-tile Probe Sequences

Probe-57:

AACAGGGAAGCGCAGAACAAAGTCAGAGGGTAATTGAGCGCTTATTACGCA

GTATGAAAAAAAAAAAAAAAAAAAAAAAAAAAAAAAAAAAAA

Probe-82:

AGTAATTCTGTCCACGAGCCAGTAATAAGAGAATATAAAGTAATCCAATCGC

AAGAAAAAAAAAAAAAAAAAAAAAAAAAAAAAAAAAAAAAA

Probe-107:

TAATGCAGAACGCGATATTTAACAACGCCAACATGTAATTTAATATTTTAGTT

AATAAAAAAAAAAAAAAAAAAAAAAAAAAAAAAAAAAAAAA

2.2. M-tile Probe Sequences

Probe-85:

GAAGGAGCGGAATTGTTTGAGTAACATTATCATTTTGCGGAATGCAACAGTG

CCACAAAAAAAAAAAAAAAAAAAAAAAAAAAAAAAAAAAAA

Probe-87:

GCTGAGAGCCAGCAAGGTGAGGCGGTCAGTATTAACACCGCCCCAGCCATTG

CAACAAAAAAAAAAAAAAAAAAAAAAAAAAAAAAAAAAAAA

Probe-89:

AGGAAAAACGCTCAGCTGGTAATATCCAGAACAATATTACCGCGCGCTTAAT

GCGCAAAAAAAAAAAAAAAAAAAAAAAAAAAAAAAAAAAAA

Probe-110:

GGCAATTCATCAATACTCGTATTAAATCCTTTGCCCGAACGTTAAAGCATCAC

CTTAAAAAAAAAAAAAAAAAAAAAAAAAAAAAAAAAAAAAA

Probe-112:

GCTGAACCTCAAATCATTAAAAATACCGAACGAACCACCAGCTTTTGACGCT

CAATAAAAAAAAAAAAAAAAAAAAAAAAAAAAAAAAAAAAA

Probe-114:

CGTCTGAAATGGATAACATCACTTGCCTGAGTAGAAGAACTCTGACGAGCAC

GTATAAAAAAAAAAAAAAAAAAAAAAAAAAAAAAAAAAAAA

2.3. DC-tile Probe Sequences

Probe-17:

TATCACCGTCACCGCCATCTTTTCATAATCAAAATCACCGGATCAGAGCCGCC

ACCAAAAAAAAAAAAAAAAAAAAAAAAAAAAAAAAAAAAAA

Probe-18:

CTCAGAACCGCCACAGGAGTGTACTGGTAATAAGTTTTAACGTATAAACAGT

TAATAAAAAAAAAAAAAAAAAAAAAAAAAAAAAAAAAAAAA

Probe-19:

GCCCCCTGCCTATTGAACCGCCACCCTCAGAGCCACCACCCTAACCCATGTAC

CGTAAAAAAAAAAAAAAAAAAAAAAAAAAAAAAAAAAAAA

Probe-20:

AACACTGAGTTTCGTCACGTTGAAAATCTCCAAAAAAAAGGCTTATCAGCTT

GCTTAAAAAAAAAAAAAAAAAAAAAAAAAAAAAAAAAAAAA

Probe-21:

TCGAGGTGAATTTCTGAGGAAGTTTCCATTAAACGGGTAAAACTAAAACGAA

AGAGAAAAAAAAAAAAAAAAAAAAAAAAAAAAAAAAAAAAA

Probe-152:

CGCTATTAATTAATAATAAAGAAATTGCGTAGATTTTCAGGTTATCAAAATTA

TTTAAAAAAAAAAAAAAAAAAAAAAAAAAAAAAAAAAAAAA

Probe-160:

GCACGTAAAACAGAGCACTAACAACTAATAGATTAGAGCCGTAGGAAGGTT

ATCTAAAAAAAAAAAAAAAAAAAAAAAAAAAAAAAAAAAAA

Probe-162:

AAATATCTTTAGGAAAAGCGTAAGAATACGTGGCACAGACAACCAACAGAG

ATAGAAAAAAAAAAAAAAAAAAAAAAAAAAAAAAAAAAAAA

Probe-164:

ACCCTTCTGACCTGTTTATAATCAGTGAGGCCACCGAGTAAAACGGTACGCC

AGAAAAAAAAAAAAAAAAAAAAAAAAAAAAAAAAAAAAAAA

Probe-166:

TCCTGAGAAGTGTTCACTAAATCGGAACCCTAAAGGGAGCCCAGTTTTTTGG

GGTCAAAAAAAAAAAAAAAAAAAAAAAAAAAAAAAAAAAAA

2.4. Tri1-tile Probe Sequences

Probe-A37:

AGAGAATAACATAAAAACAGGGAAGCGCATTAAAAAAAAAAAAAAAAAAA

AAAAAAAAAAAAAAAAAAAAA

Probe-A33:

CCTTTTTTCATTTAACAATTTCATAGGATTAGAAAAAAAAAAAAAAAAAAA

AAAAAAAAAAAAAAAAAAAA

Probe-A10:

TGTACTGGAAATCCTCATTAAAGCAGAGCCACAAAAAAAAAAAAAAAAAAA

AAAAAAAAAAAAAAAAAAAA

Probe-A39:

TTATCAAACCGGCTTAGGTTGGGTAAGCCTGTAAAAAAAAAAAAAAAAAAA

AAAAAAAAAAAAAAAAAAAA

Probe-A35:

AGTATAAAATATGCGTTATACAAAGCCATCTTAAAAAAAAAAAAAAAAAAA

AAAAAAAAAAAAAAAAAAAA

2.5. Tri3-tile Probe Sequences

Probe-A37:

AGAGAATAACATAAAAACAGGGAAGCGCATTAAAAAAAAAAAAAAAAAAA

AAAAAAAAAAAAAAAAAAAAA

Probe-A33:

CCTTTTTTCATTTAACAATTTCATAGGATTAGAAAAAAAAAAAAAAAAAAA

AAAAAAAAAAAAAAAAAAAA

Probe-A10:

TGTACTGGAAATCCTCATTAAAGCAGAGCCACAAAAAAAAAAAAAAAAAAA

AAAAAAAAAAAAAAAAAAAA

Probe-A39:

TTATCAAACCGGCTTAGGTTGGGTAAGCCTGTAAAAAAAAAAAAAAAAAAA

AAAAAAAAAAAAAAAAAAAA

Probe-A35:

AGTATAAAATATGCGTTATACAAAGCCATCTTAAAAAAAAAAAAAAAAAAA

AAAAAAAAAAAAAAAAAAAA

Probe-B37:

ACAGGTAGAAAGATTCATCAGTTGAGATTTAGAAAAAAAAAAAAAAAAAAA

AAAAAAAAAAAAAAAAAAAA

Probe-B33:

AGGGATAGCTCAGAGCCACCACCCCATGTCAAAAAAAAAAAAAAAAAAAAA

AAAAAAAAAAAAAAAAAAAA

Probe-B10:

CAATATGACCCTCATATATTTTAAAGCATTAAAAAAAAAAAAAAAAAAAAA

AAAAAAAAAAAAAAAAAAAA

Probe-B39:

ATTTTCTGTCAGCGGAGTGAGAATACCGATATAAAAAAAAAAAAAAAAAAA

AAAAAAAAAAAAAAAAAAAA

Probe-B35:

GCCGCTTTGCTGAGGCTTGCAGGGGAAAAGGTAAAAAAAAAAAAAAAAAAA

AAAAAAAAAAAAAAAAAAAA

Probe-C37:

CGAGAAAGGAAGGGAAGCGTACTATGGTTGCTAAAAAAAAAAAAAAAAAAA

AAAAAAAAAAAAAAAAAAAA

Probe-C33:

CGCGTCTGATAGGAACGCCATCAACTTTTACAAAAAAAAAAAAAAAAAAAA

AAAAAAAAAAAAAAAAAAAA

Probe-C10:

TAATCCTGATTATCATTTTGCGGAGAGGAAGGAAAAAAAAAAAAAAAAAAA

AAAAAAAAAAAAAAAAAAAA

Probe-C39:

CAGTTTGACGCACTCCAGCCAGCTAAACGACGAAAAAAAAAAAAAAAAAAA

AAAAAAAAAAAAAAAAAAAA

Probe-C35:

CTCTAGAGCAAGCTTGCATGCCTGGTCAGTTGAAAAAAAAAAAAAAAAAAA

AAAAAAAAAAAAAAAAAAAA

2.6. E- and M-tile Array Linker Sequences

L1: CACCAACTACGTAATGCCACT TCGGCTGTCTTTCC

L2: GAACCGGCATCAAGAGTAATC AGCCTGTTTAGTAT

L3: ACTAATGGATTTAGGAATACC TTTCCCTTAGAATC

L4: AGTCAGAGGTCTTTACCCTGA AATAAAGAAATTGC

L5: ATTCTGCCCATATAACAGTTG GCACTAACAACTAA

L6: GTAGATTTTCAGGTTATCAAAATTATTTGCACGTAAAACAGA CTATTAT

L7: CTTGAAAACATAGCCTTCTGTAAATCGTCGCTATTAATTAAT ACATTCA

L8: CATATGCGTTATACAAACACCGGAATCATAATTACTAGAAAA TTGACAA

L9: TTATCATTCCAAGATTACGAGCATGTAGAAACCAATCAATAA ACGAAGG

L10: TAGATTAGAGCCGTAGGAAGGTTATCTAAAATATCTTTAGGA ATTCCCA

3. References

(1) Laemmli, U.K. *Nature* **1970**, *227*, 680-685.

(2) Rothemund, P.W.K. *Nature* **2006**, *440*, 297-302.

(3) Carrico, Z.M.; Romanini, D.W.; Mehl, R.A.; Francis, M.B. *Chem. Commun.* **2008**, 1205-1207.

(4) Stephanopoulos, N.; Carrico, Z.M.; Francis, M.B. *Angew. Chem. Int. Ed.* **2009**, *48*, 9498-9502.

(5) Tong, G.J.; Hsiao, S.C.; Carrico, Z.M.; Francis, M.B. *J. Am. Chem. Soc.* **2009**, *131*, 11174-11178.

4. Supplemental Figures

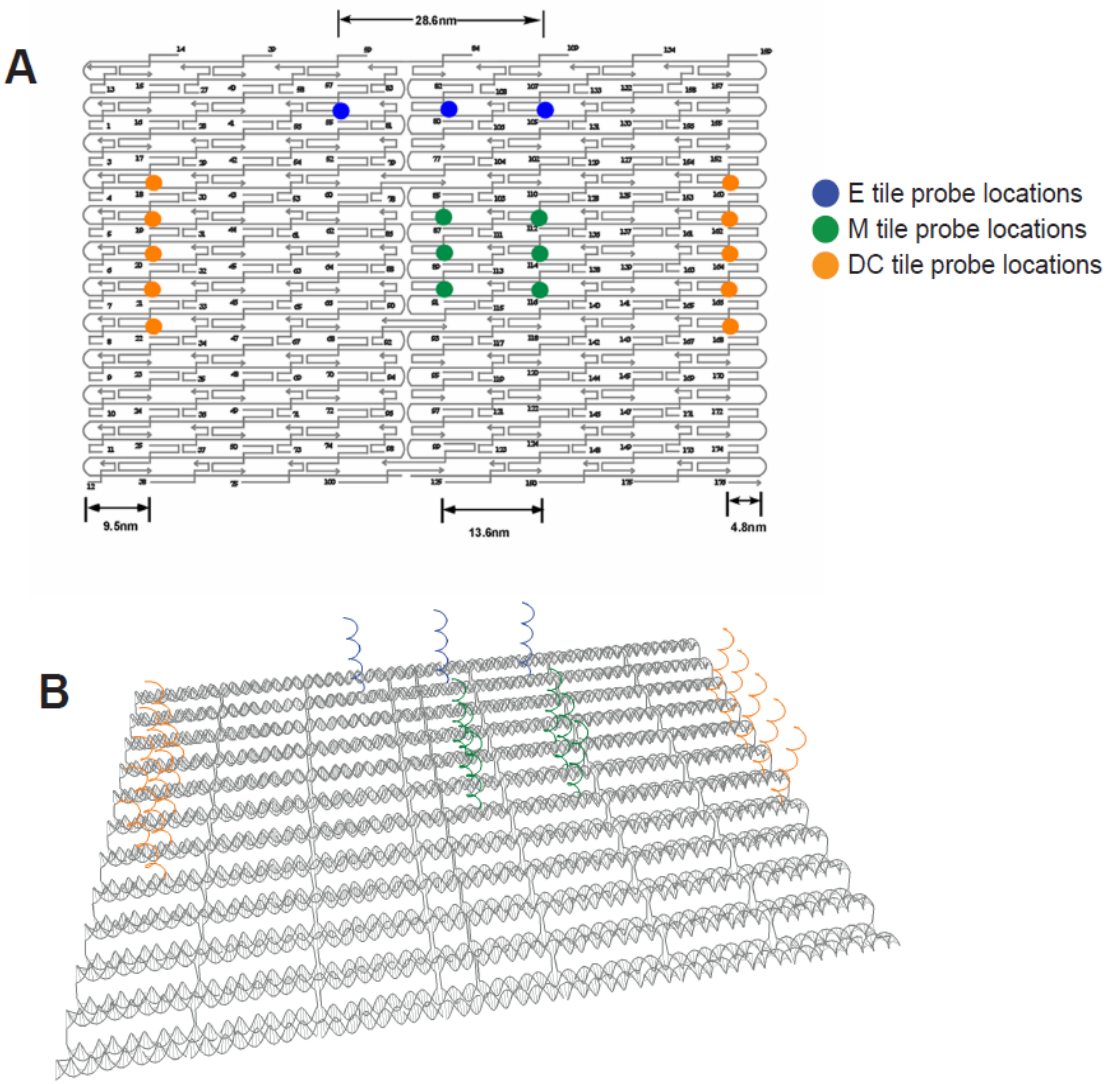

Figure S1. Schematic representation of the rectangular tiles used in this study. (A) Digram showing the location of the probes in the three designs. Numbers refer to the staples holding together the M13 back-bone. (B) Image of rectangular tile showing all the helices as well as the protruding probes for the three designs. The 3' end of each probe is protruding from the tile.

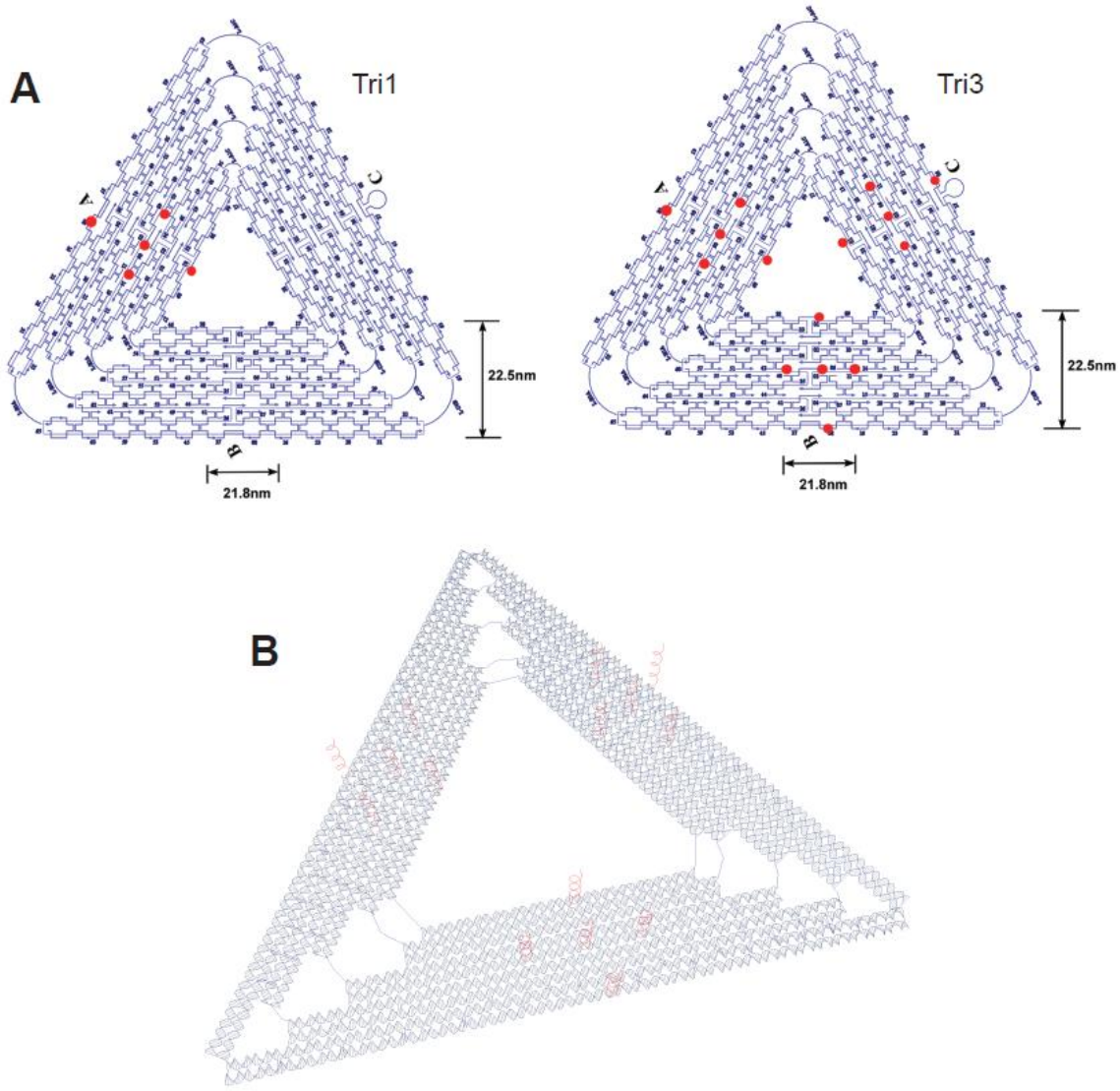

Figure S2. Schematic representation of the triangular tiles used in this study. (A) Diagram showing the location of the probes (red dots) in the two triangle designs. Numbers refer to the staples holding together the M13 backbone. (B) Image of the Tri3 tile showing all the helices as well as the protruding probes. The design of the Tri1 tile was identical, but with only one set of probes. The 3' end of each probe is protruding out from the planar.

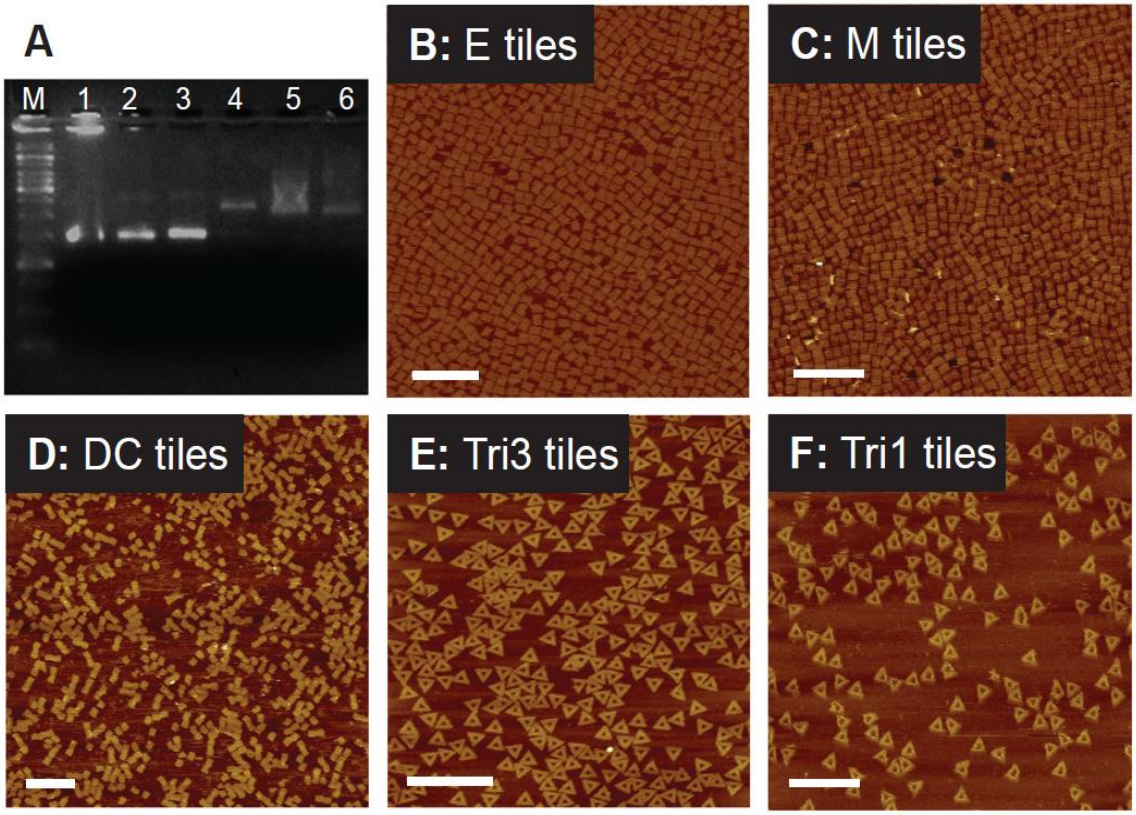

Figure S3. Characterization of the origami tiles. (A) Agarose gel of the tiles used in this paper. Lanes: M: 1 kb ladder, 1: M13 genome, 2: E tiles, 3: M tiles, 4: DC tiles (dimer due to edge stacking), 5: Tri1 tiles, 6: Tri3 tiles. (B-F): AFM images of single tiles after purification. Scale bars: 500 nm.

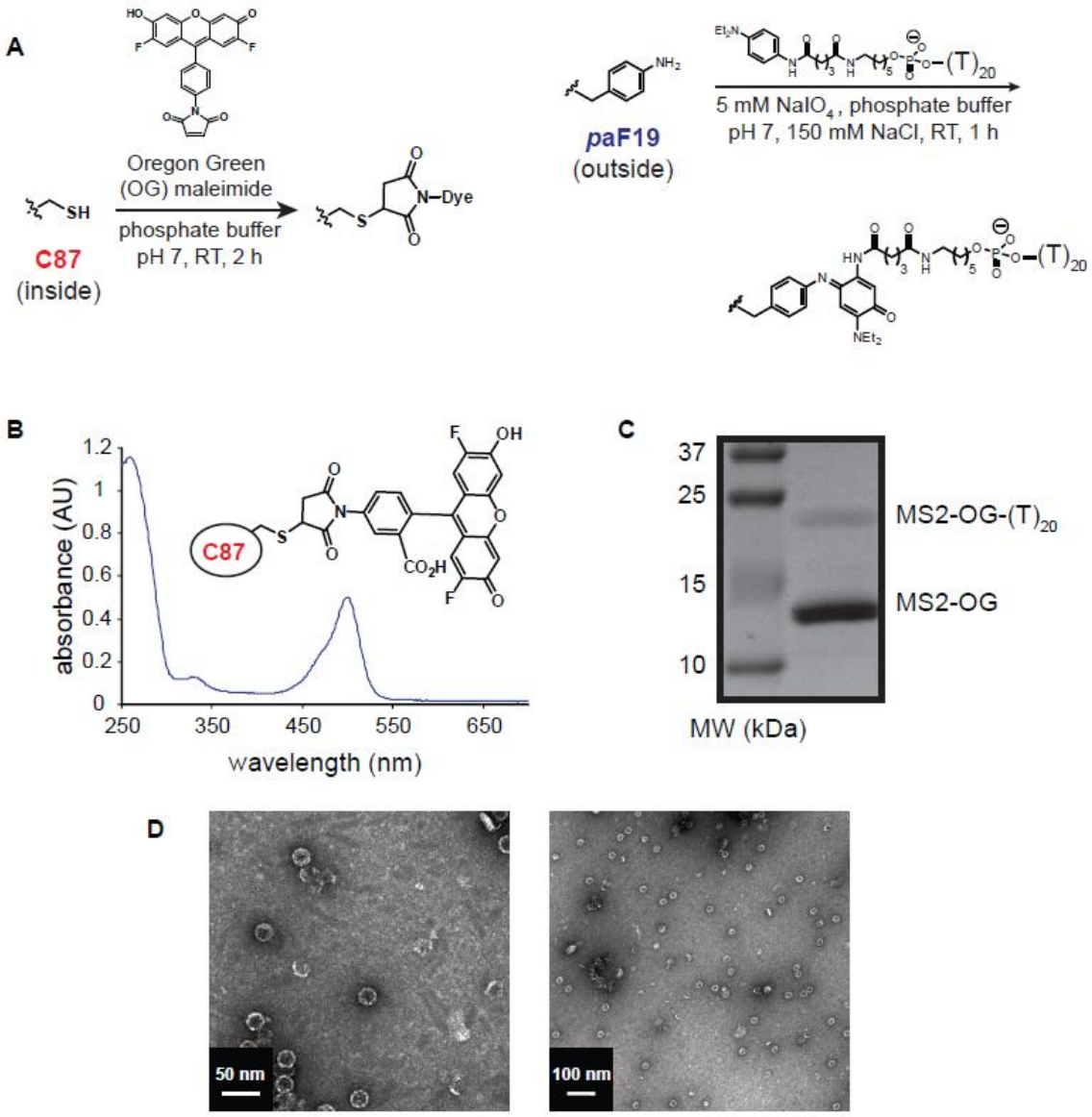

Figure S4. Synthesis and characterization of the MS2 capsids with Oregon Green (OG) inside and ssDNA outside. The 5' end of the ssDNA strand is attached to the capsid. The 5' end of the ssDNA strand is attached to the capsid. (A) Synthetic scheme to modify the interior of the capsid with Oregon Green maleimide at C87 and the exterior of the capsid with (T)20 DNA at the unnatural amino acid *p*aF19 using an oxidative coupling reaction. (B) The UV-Vis spectrum of the MS2-OG conjugate shows the chromophore absorbance at 500 nm. The conversion was estimated to be nearly quantitative by the comparison of

the dye extinction coefficient (ε500 nm = 80,000 $M^{-1}cm^{-1}$) and the protein's extinction coefficent (ε260 nm = 176,000 $M^{-1}cm^{-1}$). (C) SDS-PAGE analysis of the MS2-OG-$(T)_{20}$ conjugate shows a new band at higher molecular weight corresponding to the protein-DNA conjugate. The conversion was estimated to at ~11% by densitometry (corresponding to ~20 copies/capsid). (D) Transmission electron microscopy images of the MS2-OG-$(T)_{20}$ conjugate indicated that the capsids were intact, assembled, and 27 nm in diameter as expected.

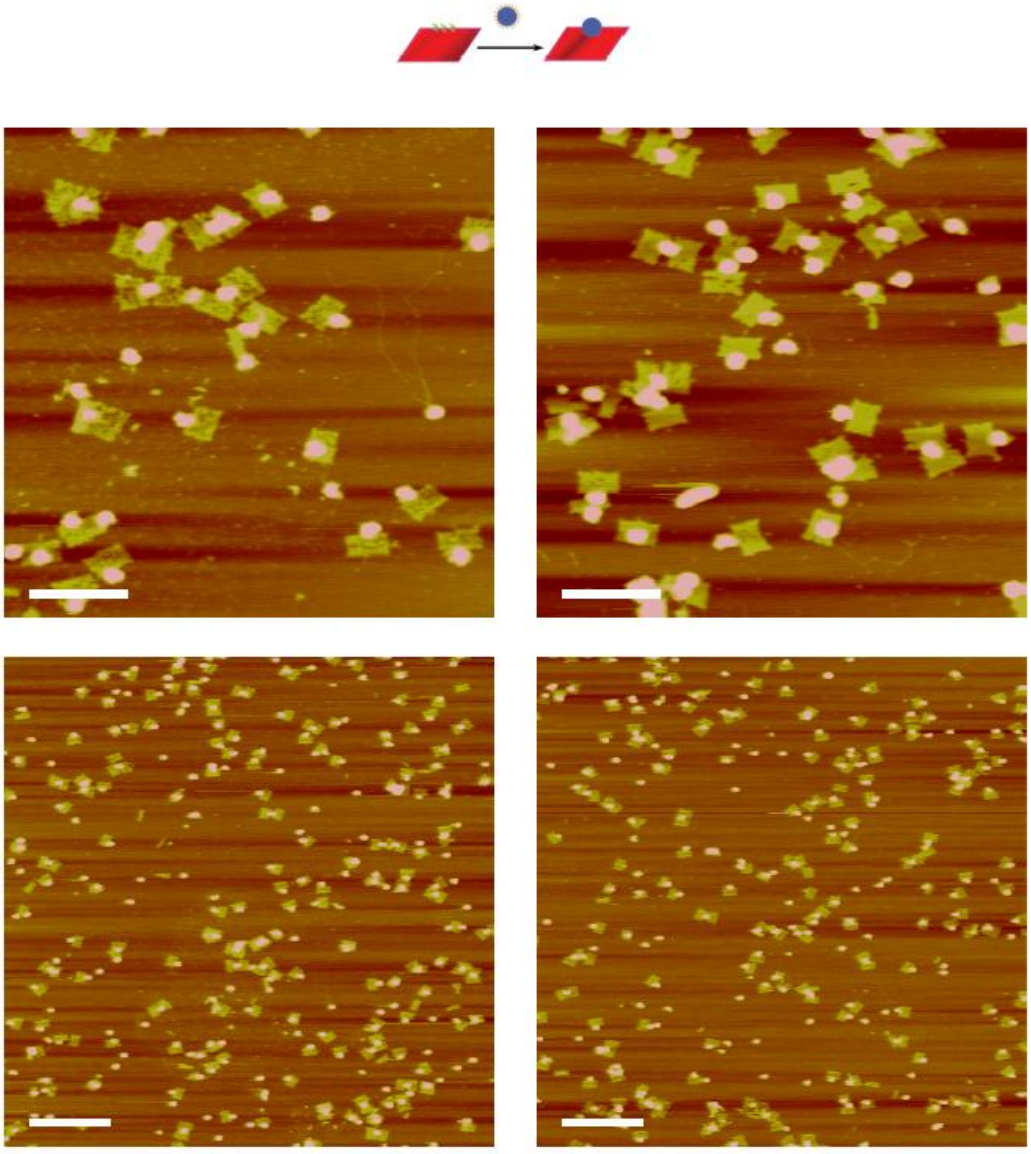

Figure S5. Additional AFM images of E tiles + MS2. Zoom-in scale bars: 200 nm. Zoom-out scale bars: 500 nm.

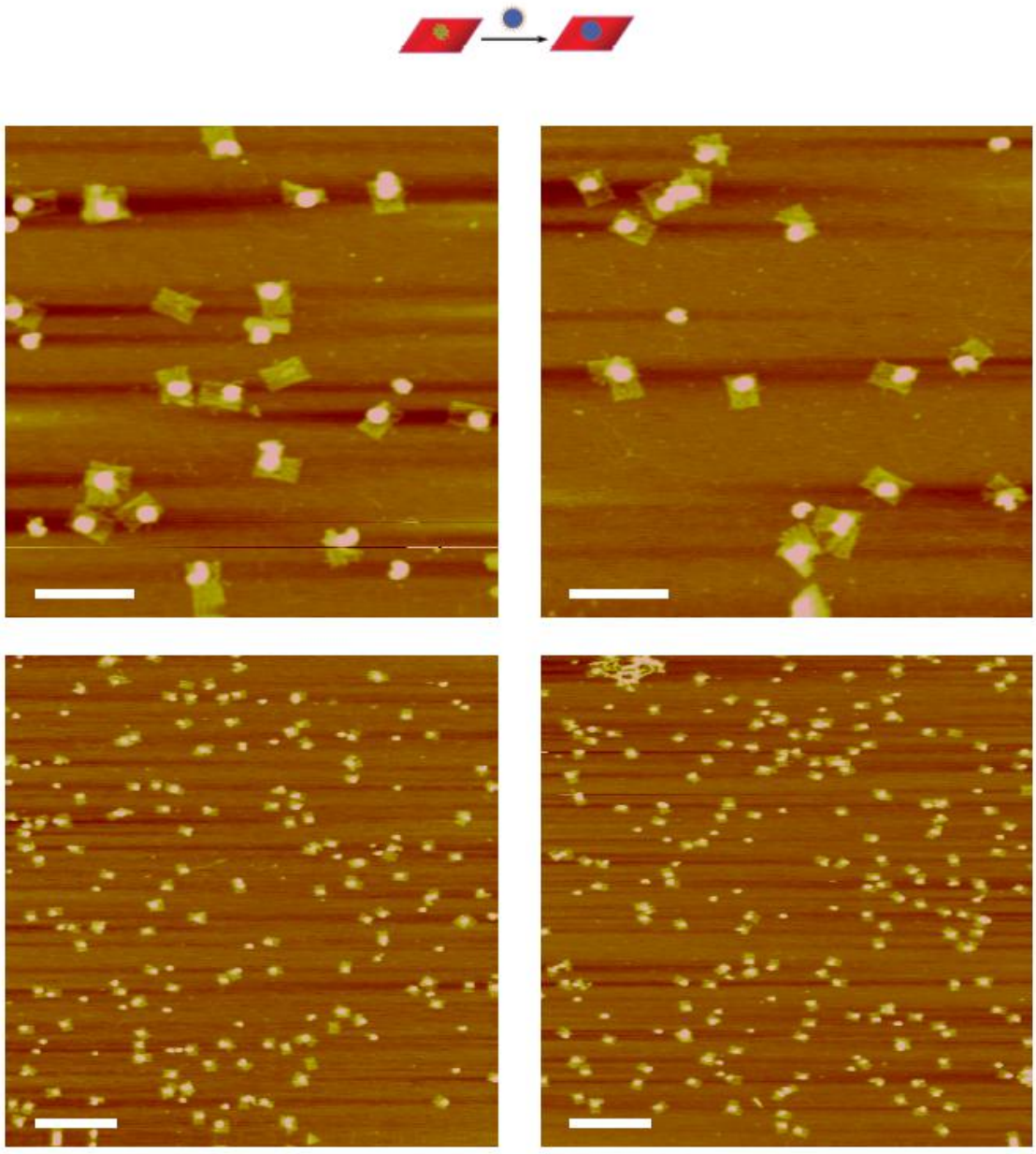

Figure S6. Additional AFM images of M tiles + MS2. Zoom-in scale bars: 200 nm. Zoom-out scale bars: 500 nm.

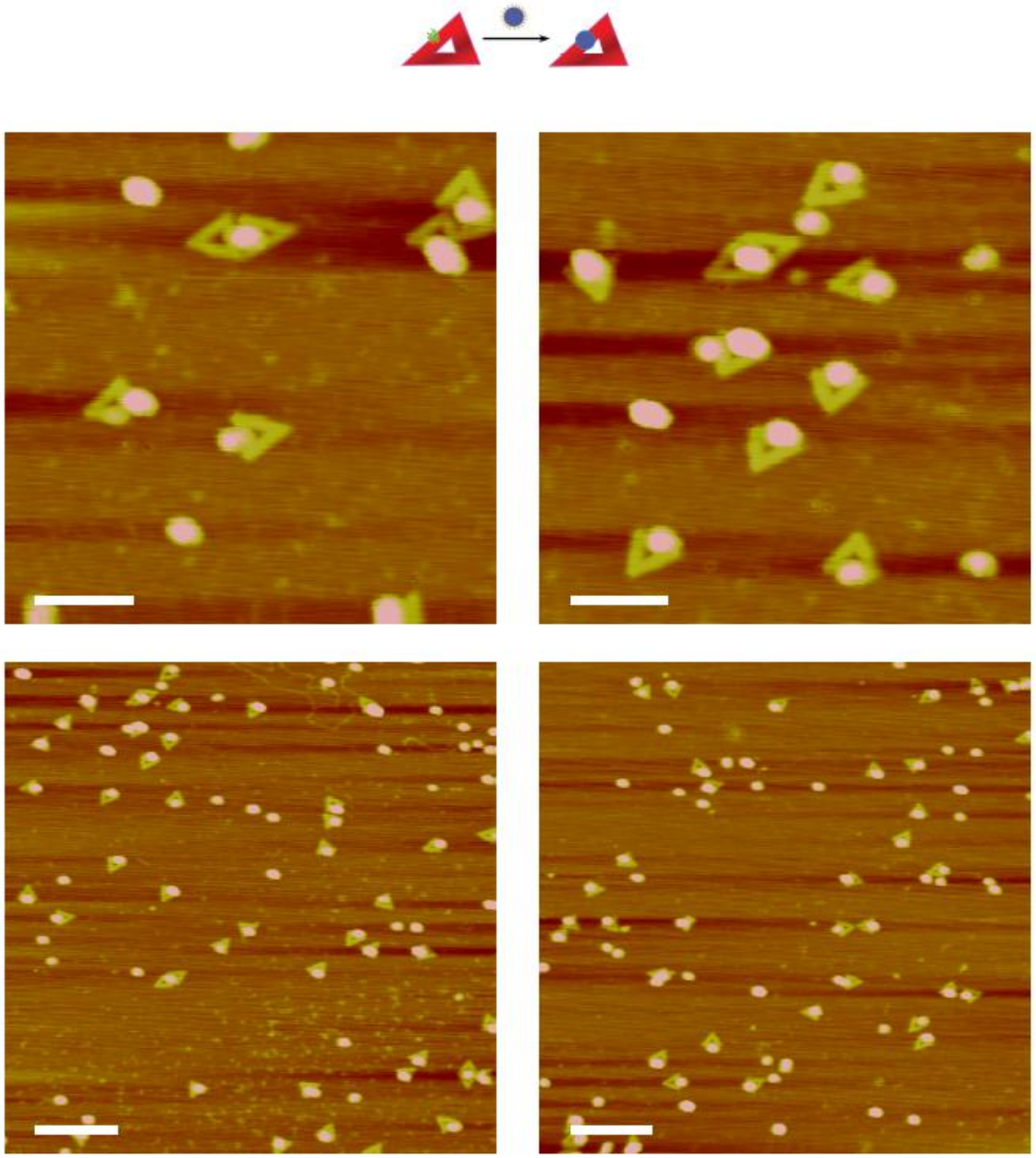

Figure S7. Additional AFM images of Tri1 tiles + MS2. Zoom-in scale bars: 200 nm. Zoom-out scale bars: 500 nm.

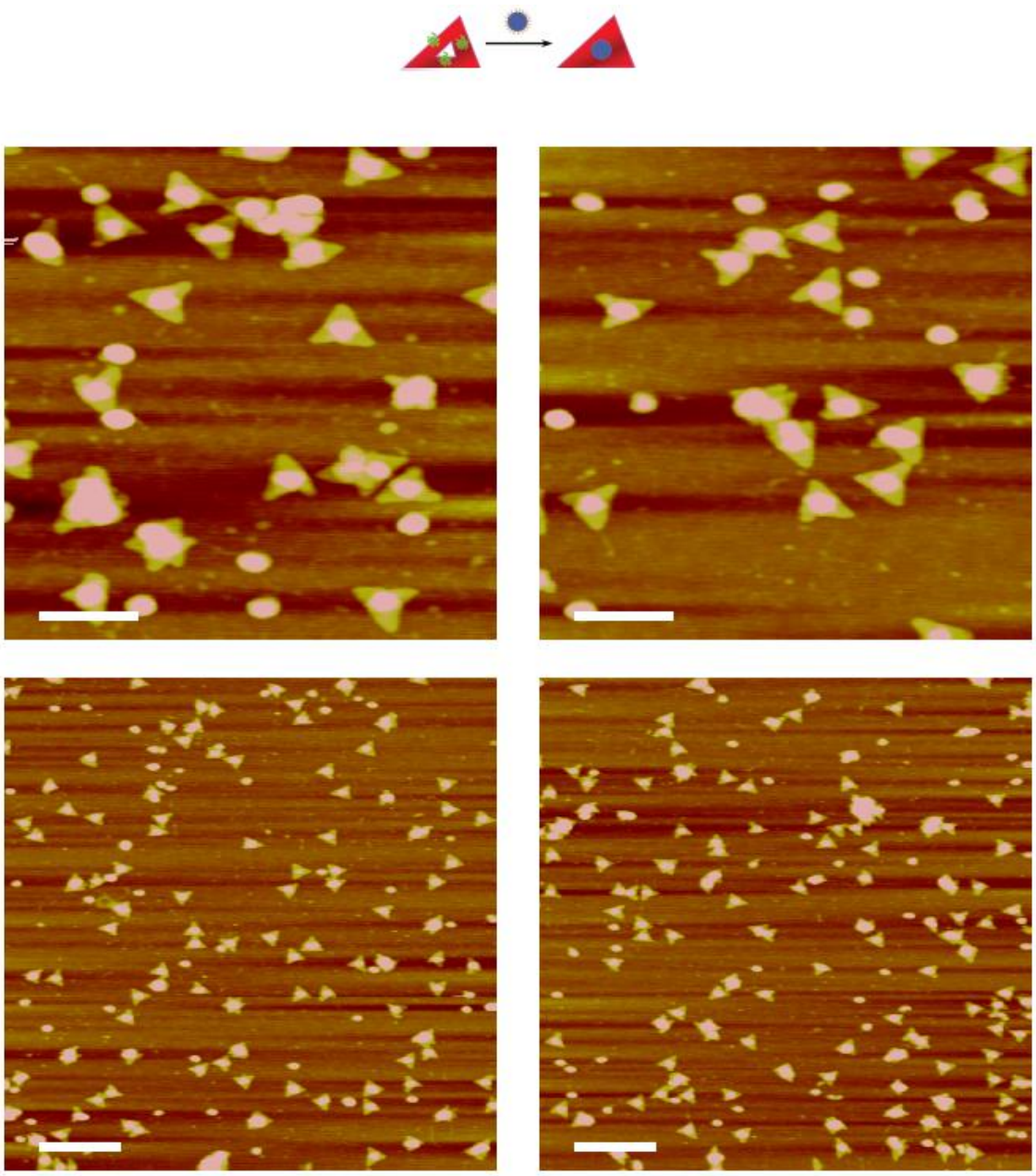

Figure S8. Additional AFM images of Tri3 tiles + MS2. Zoom-in scale bars: 200 nm. Zoom-out scale bars: 500 nm.

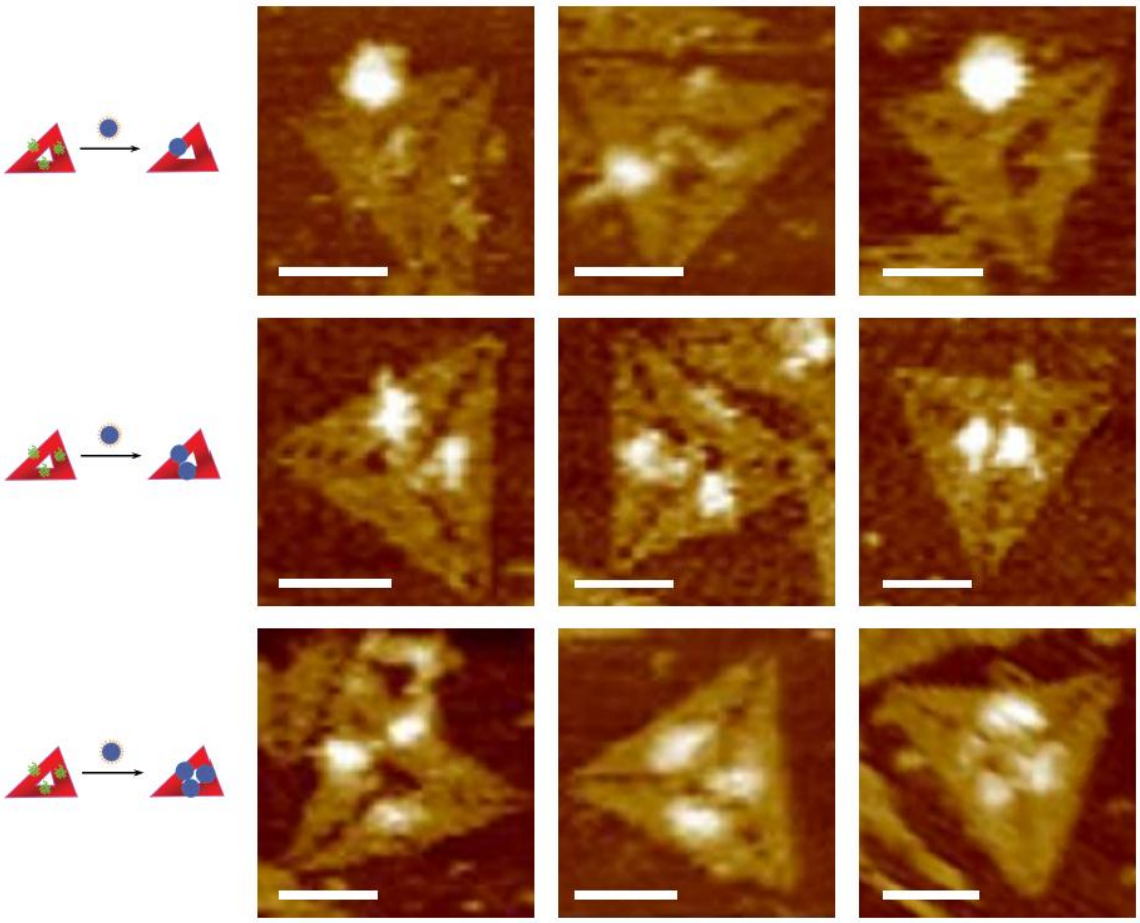

Figure S9. Additional AFM images of Tri3 tiles showing the occasional binding of one capsid to a single edge of the tile (but not sitting in the hole), two capsids binding to two edges of the tile, or three capsids binding to three edges of the tile. Scale bars: 50 nm.

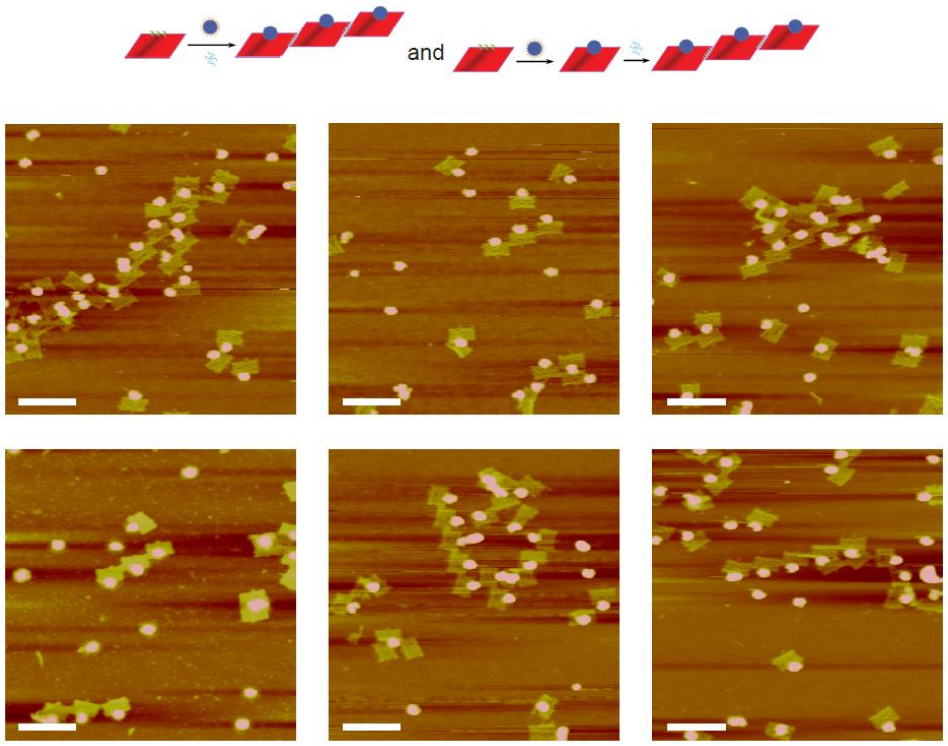

Figure S10. Additional AFM images of E tile arrays with MS2. Note the frequent occurence of array aggregation due to multiple tiles binding a single capsid. Scale bars: 200 nm.

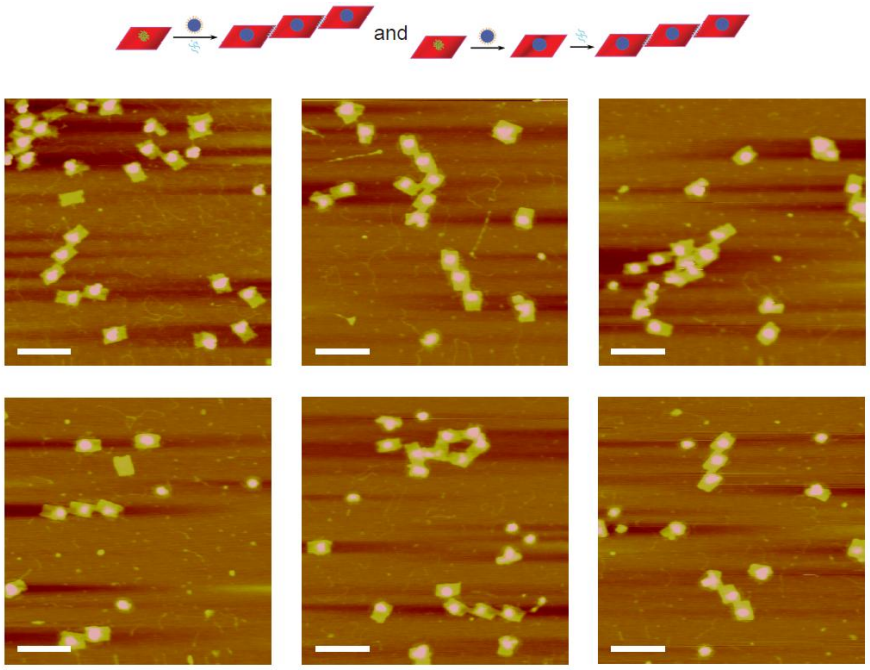

Figure S11. Additional AFM images of M tile arrays with MS2. Scale bars: 200 nm.

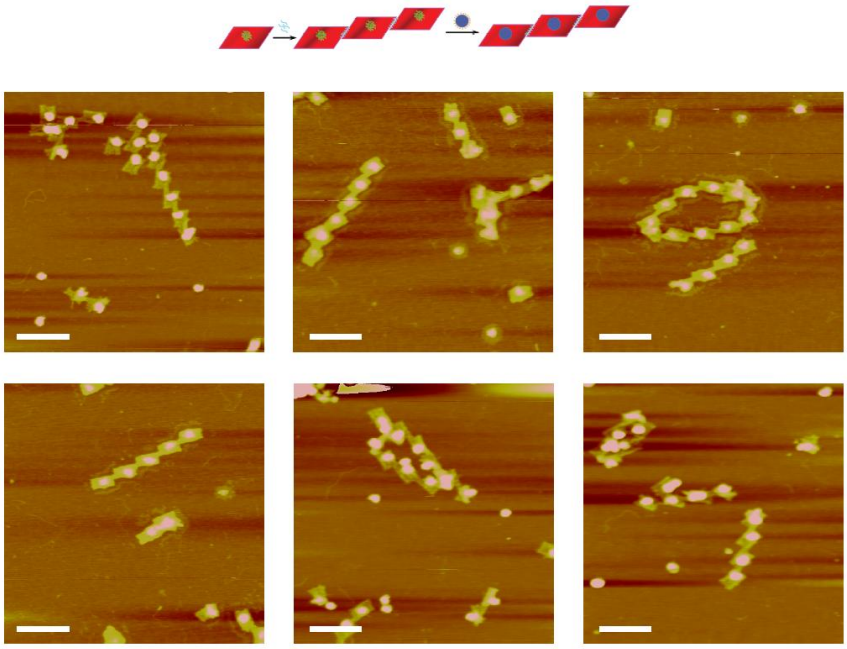

Figure S11 (cont). Additional AFM images of M tile arrays with MS2. Scale bars: 200 nm.

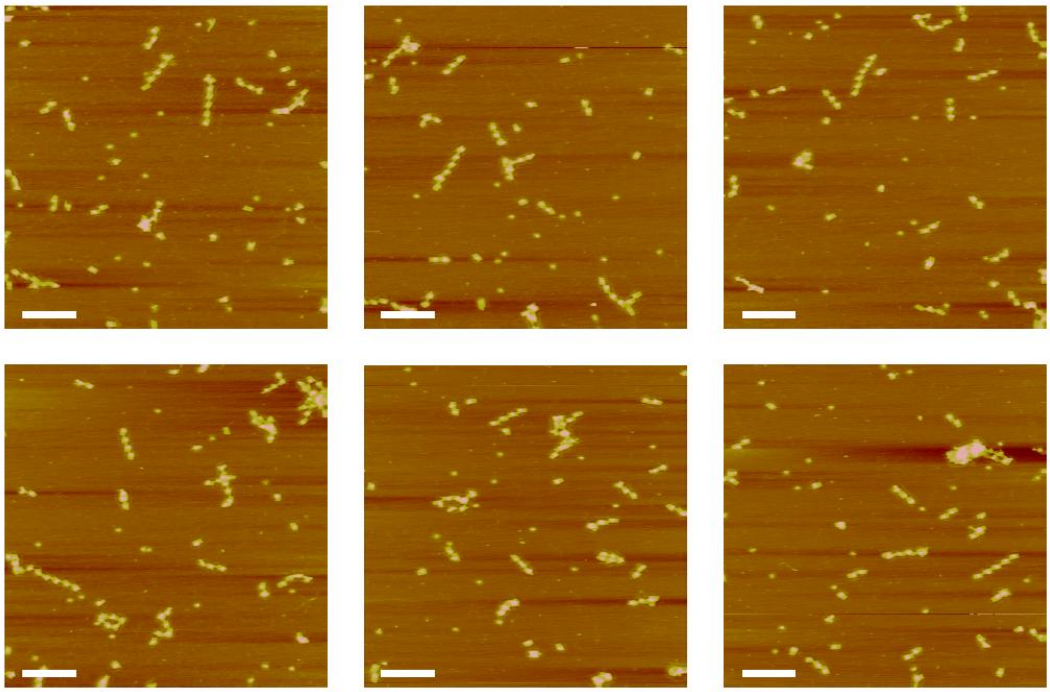

Figure S11 (cont). Additional AFM images of M tile arrays with MS2 . Scale bars: 500 nm.

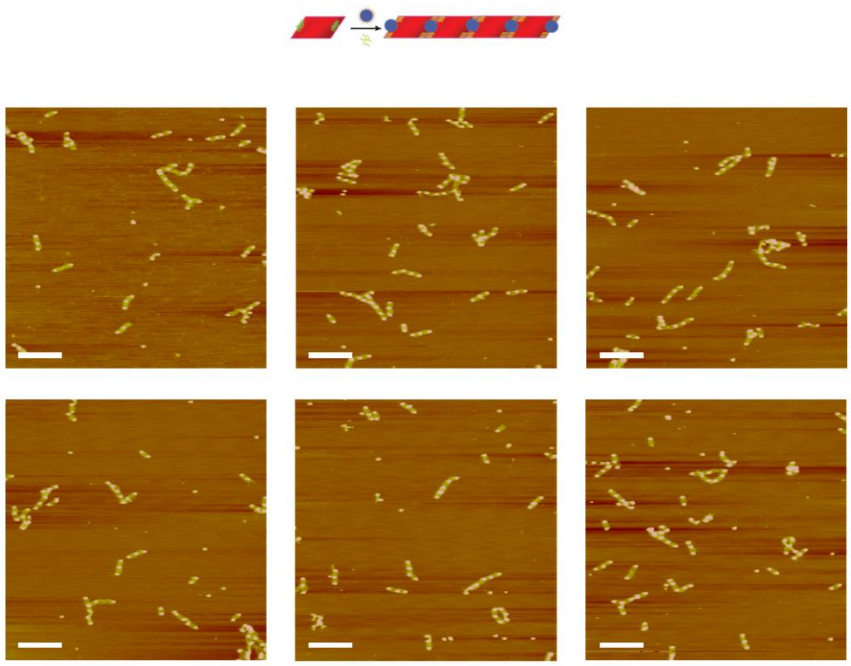

Figure S12. AFM images of additional DC tile arrays formed with MS2. Scale bars: 500 nm.

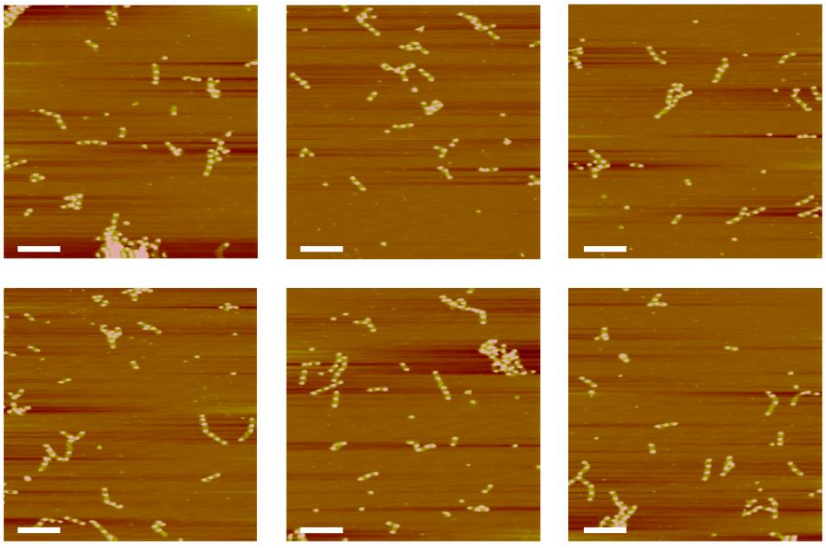

Figure S12 (cont). AFM images of additional DC tile arrays formed with MS2. Scale bars: 500 nm.

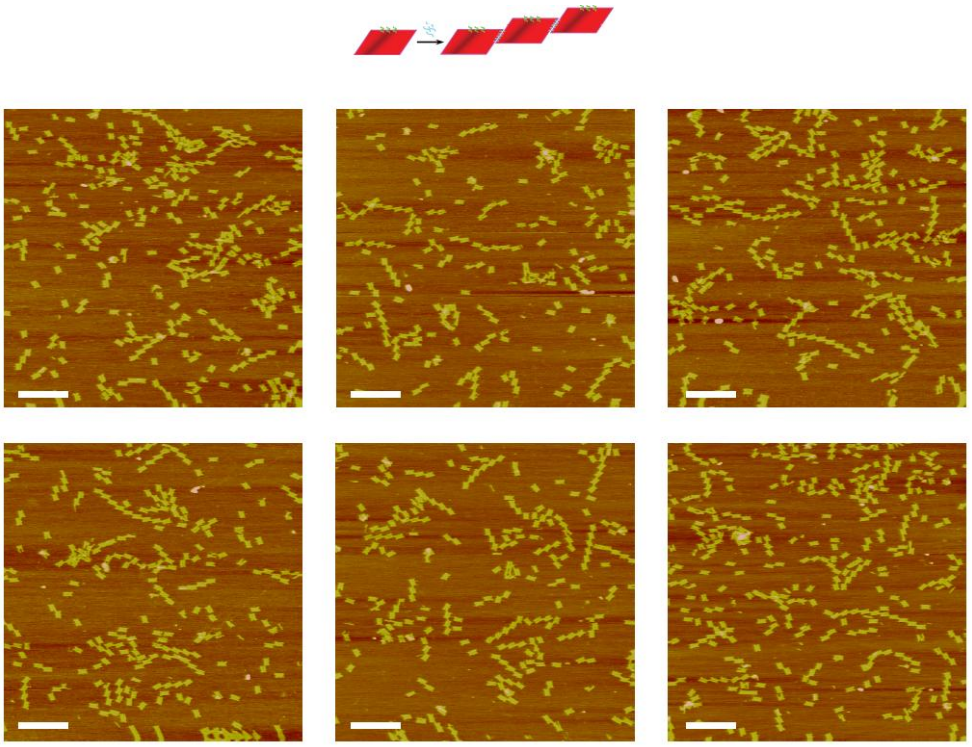

Figure S13. AFM images of E tile arrays formed without MS2. Scale bars: 500 nm.

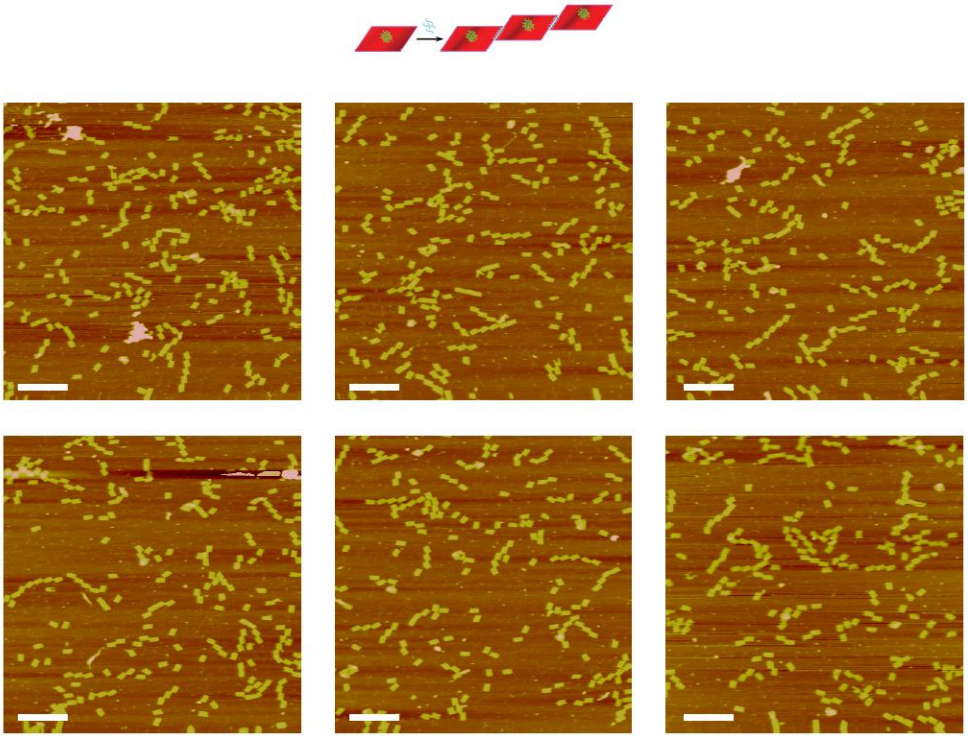

Figure S14. AFM images of M tile arrays formed without MS2. Scale bars: 500 nm.

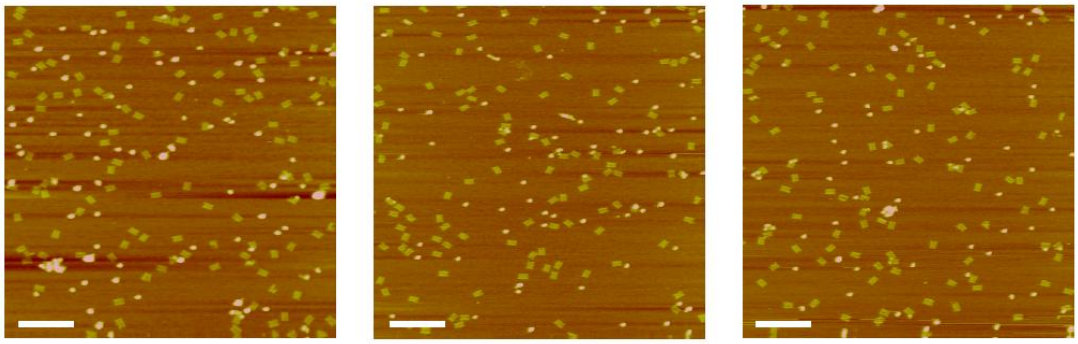

Figure S15. AFM images of control experiment: E tiles with MS2-dye (no DNA). No significant asso-ciation of the capsids with the tiles is visible. Scale bars: 500 nm.

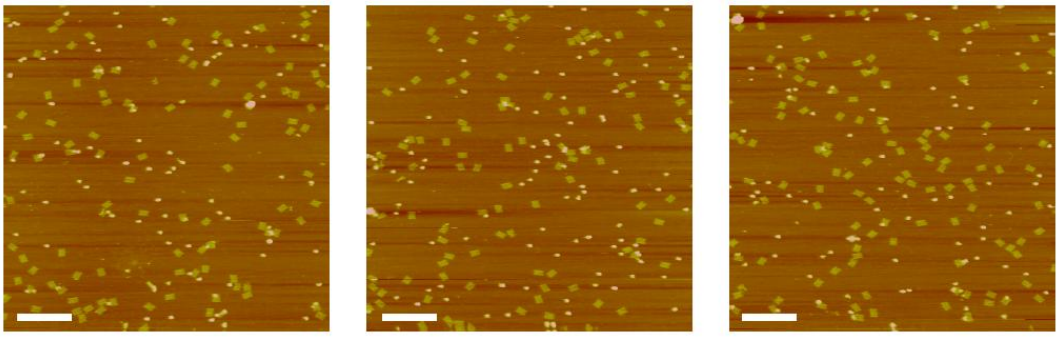

Figure S16. AFM images of control experiment: M tiles with MS2-dye (no DNA). No significant asso-ciation of the capsids with the tiles is visible. Scale bars: 500 nm

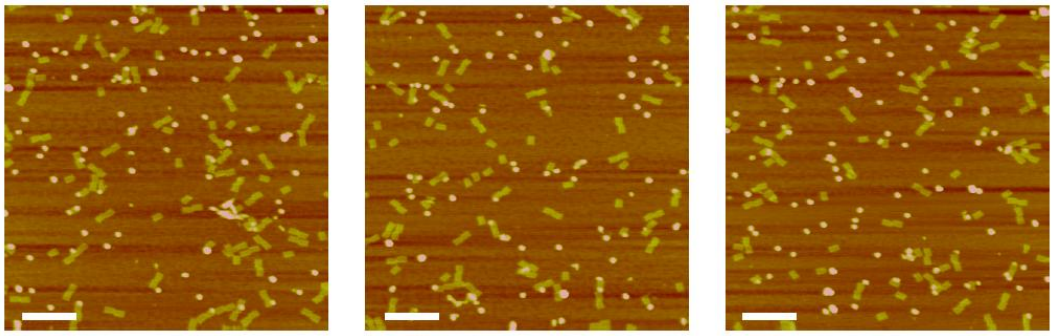

Figure S17. AFM images of control experiment: DC tiles with MS2-dye (no DNA) + edge staples. No significant association of the capsids with the tiles is visible. Note the

prevalent association of the tile short edges due to noncovalent base stacking induced by the edge staples. Scale bars: 500 nm.

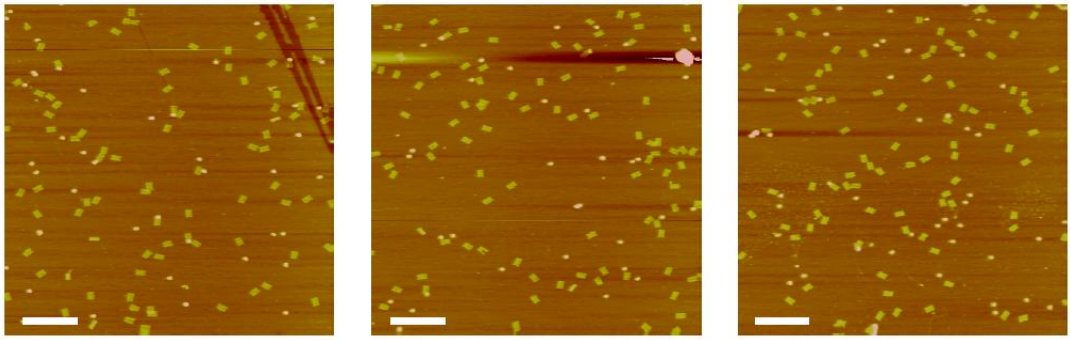

Figure S18. AFM images of control experiment: E tiles with capsids, but with mismatched probes. The capsids contained the 20-bp polyT sequence, but the tiles contained probes with a random 40-bp sequence. No association is seen between the capsids and the tiles, further indicating that specific DNA hybridization is necessary and the association is not a non-specific DNA-based effect. Scale bars: 500 nm.

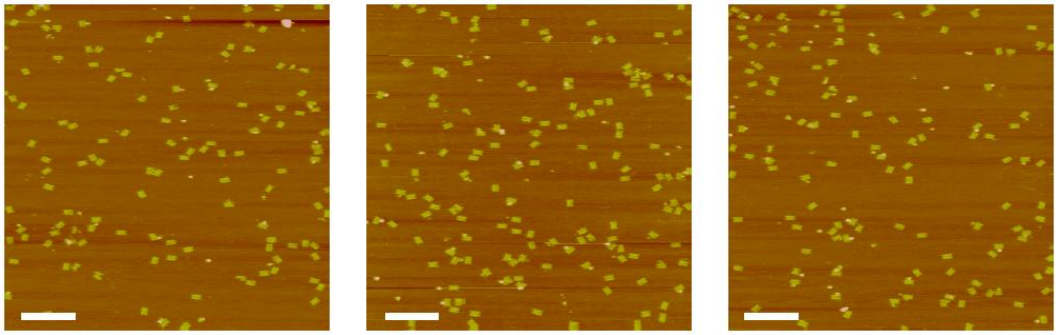

Figure S19. Control experiments: E tiles with capsids with matched probes, then addition of excess $(T)_{40}$ strand. Very few tiles still have capsids bound to them, indicating both the sequence selective nature of the capsid-tile association, as well as suggesting a release mechanism for capsids once bound to the tiles. Fewer capsids are seen on the surface than usual, likely due to passivation of the mica by the excess ssDNA, thus electrostatically occluding the surface to the capsids. Scale bars: 500 nm.

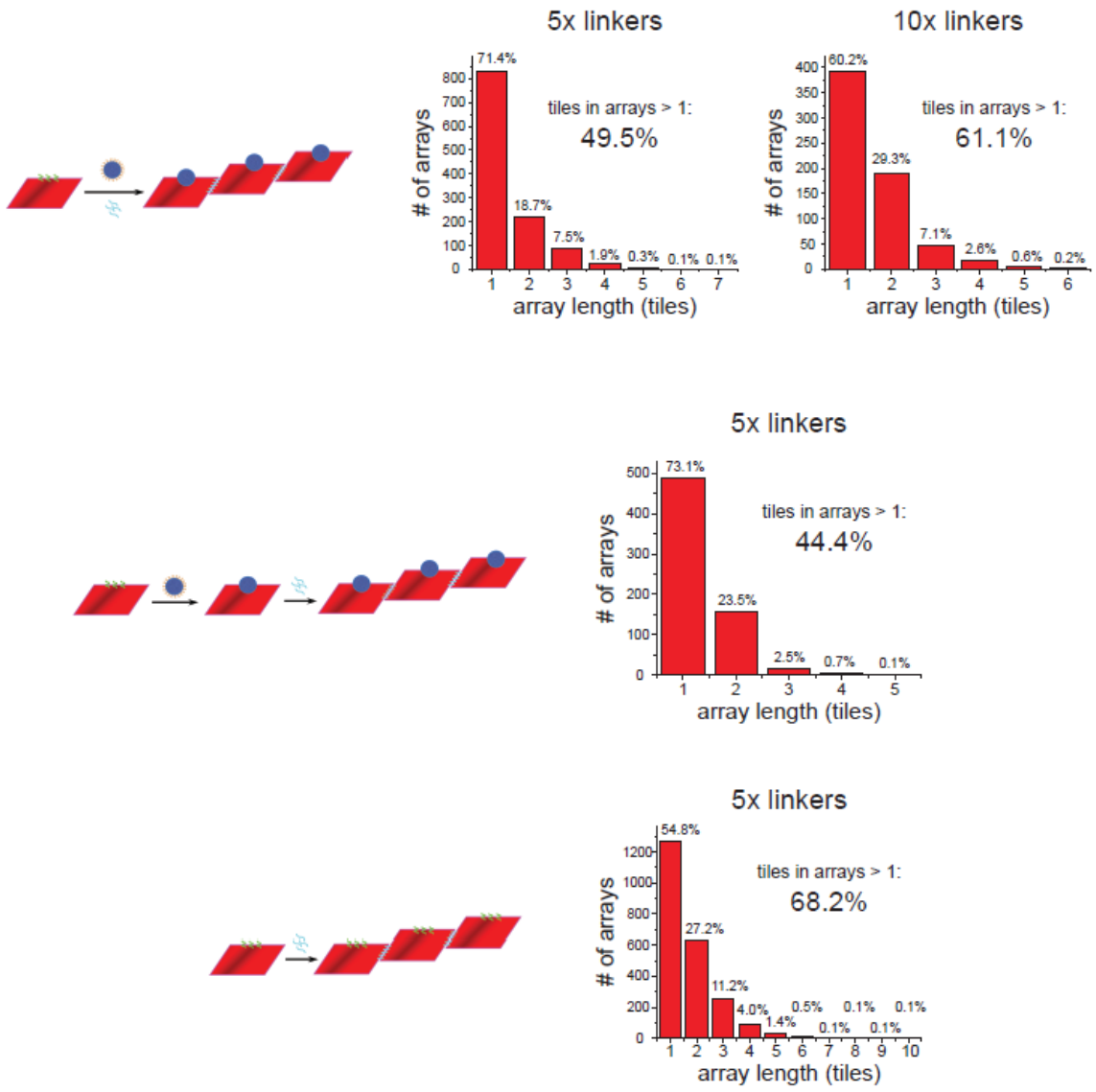

Figure S20. E tile array length distributions. An array length of 1 indicates a single tile not in an array. For the samples that include MS2, virtually complete association of the caspids with tiles was maintained

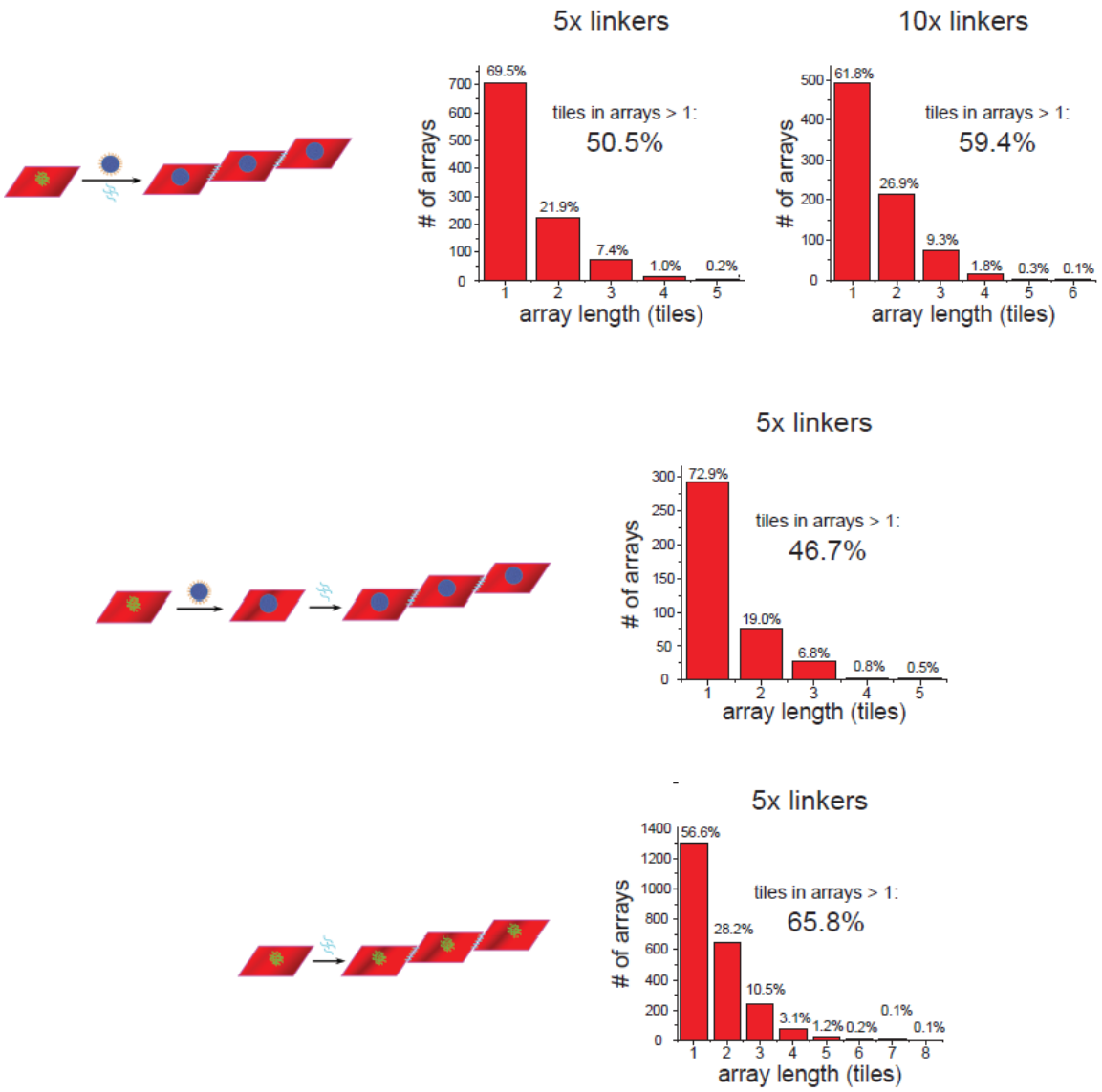

Figure S21. M tile array length distributions. An array length of 1 indicates a single tile not in an array. For the samples that include MS2, virtually complete association of the caspids with tiles was maintained

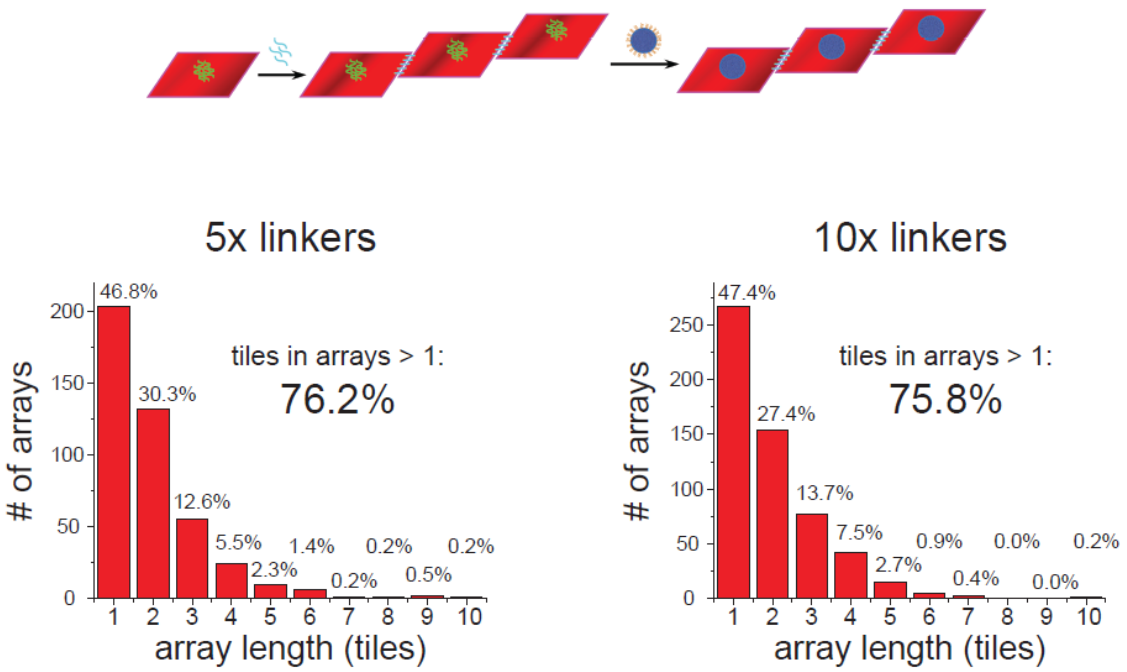

Figure S21 (cont). M tile array length distributions.

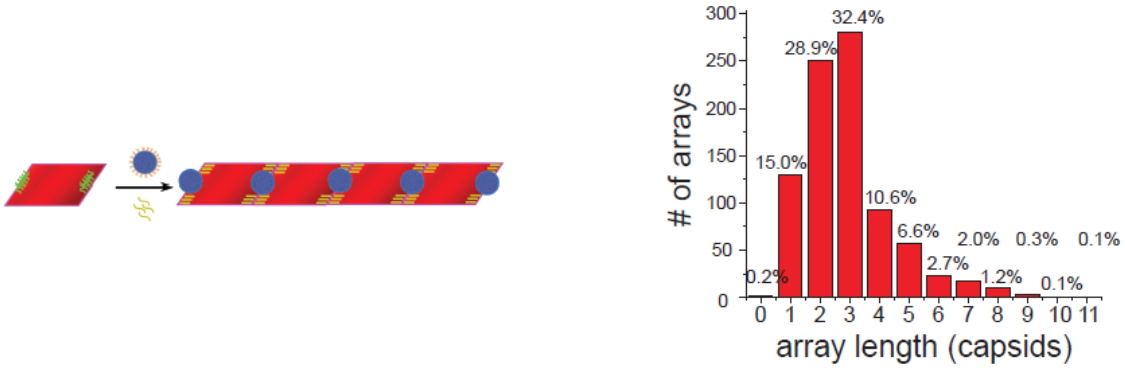

Figure S22. DC tile array length distributions. The arrays are counted in the number of capsids in a row, not tiles (as with the E and M tile arrays). An array length of 0 signifies a tile with no capsids bound.

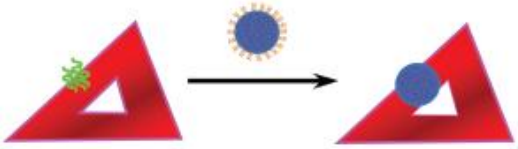

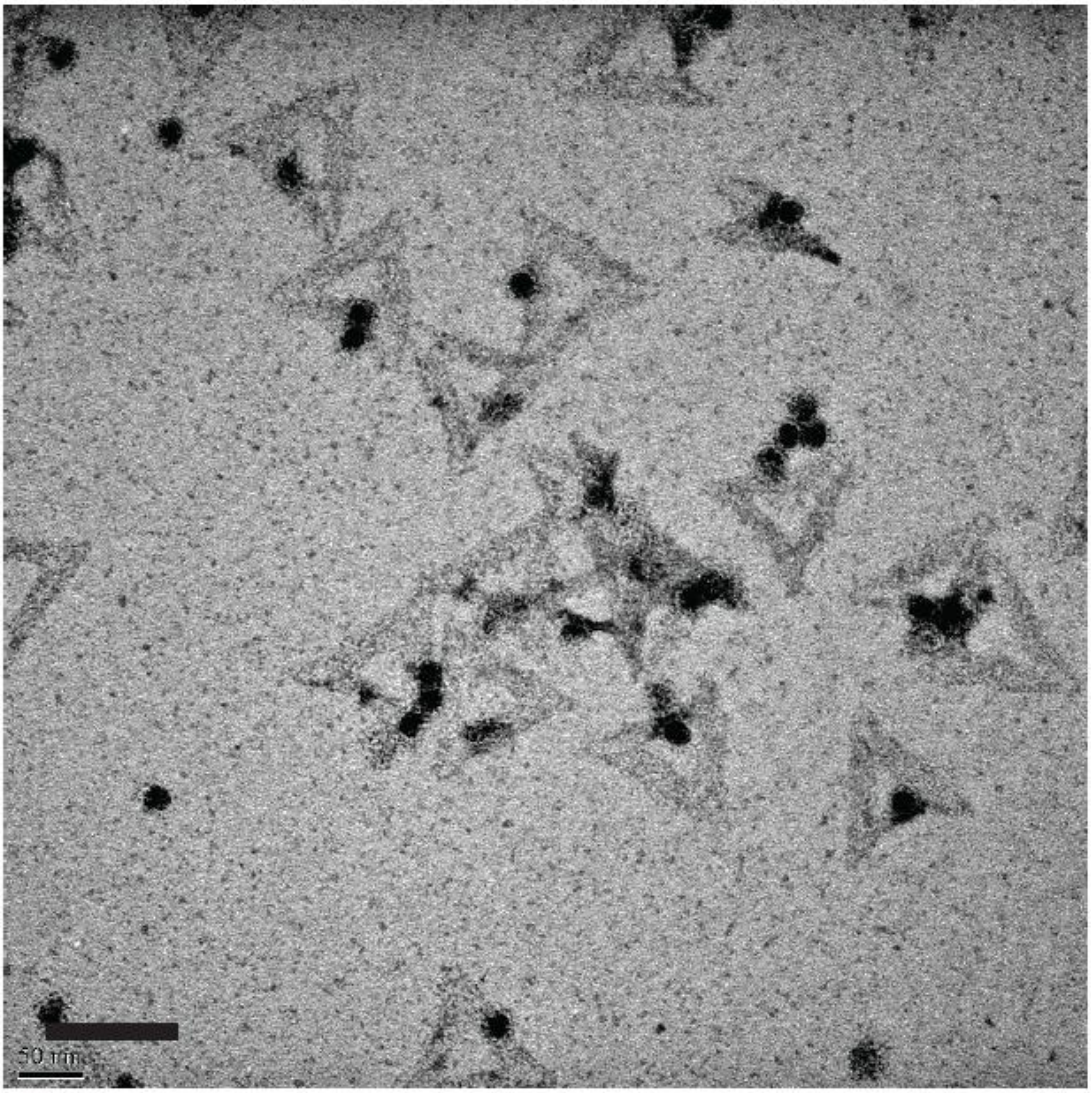

Figure S23. Additional TEM image of Tri1 tiles and MS2. The triangular tiles are clearly visible, as are the caspids adhered to one side. Scale bar: 100 nm.

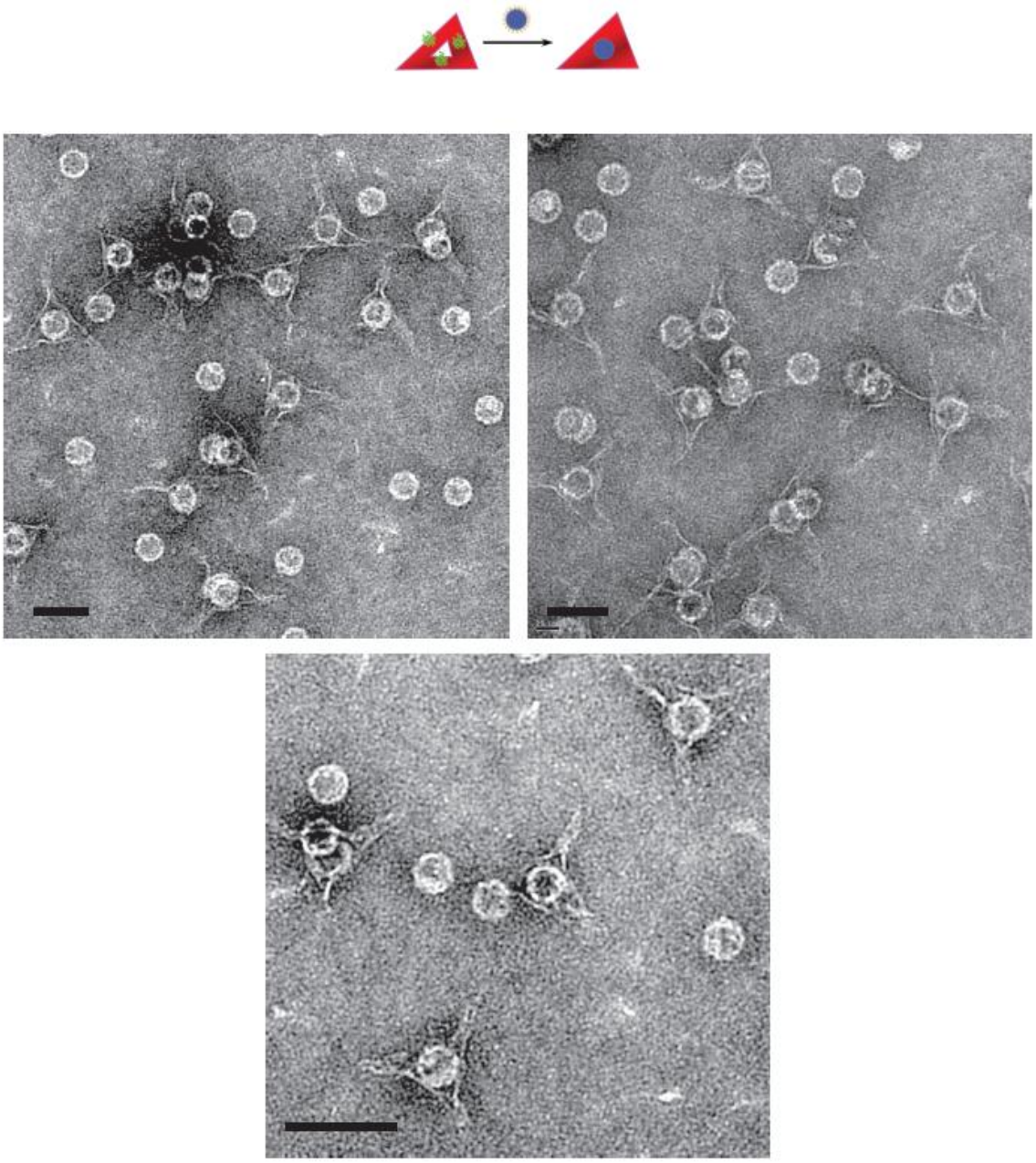

Figure S24. Additional zoom-out TEM images of Tri3 tiles and MS2. The capsids are almost exclusively immobilized in the center of the tiles and pull the three sides inwards towards the center of the tile, distorting them. Scale bars: 50 nm.

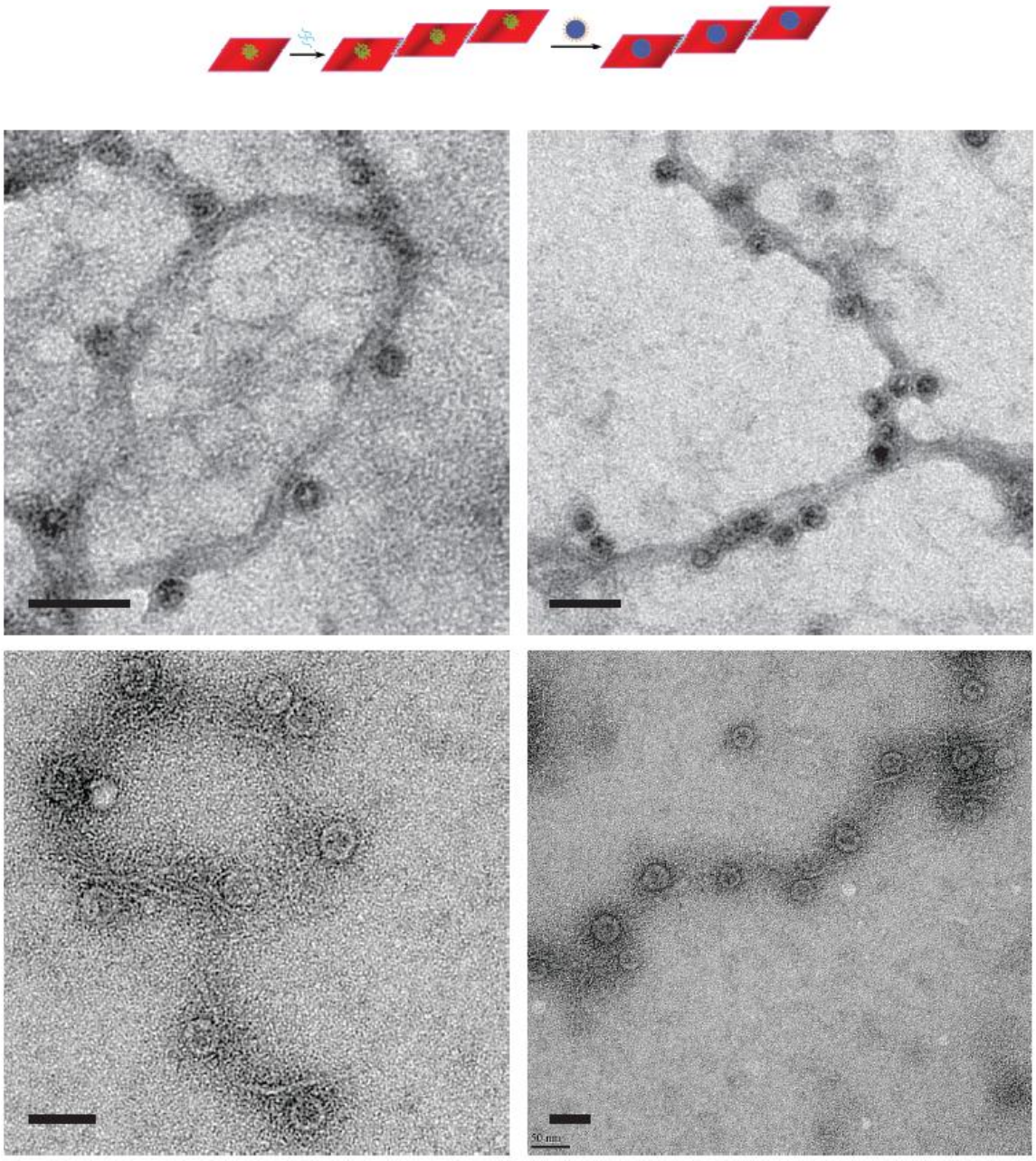

Figure S25. TEM images of M tile arrays with MS2. The tiles do not stain well, and likely shrink due to the uranyl acetate stain, as well as lying sideways on the grid, but the capsids are intact and spaced approximately 100 nm apart. Scale bars: 50 nm.

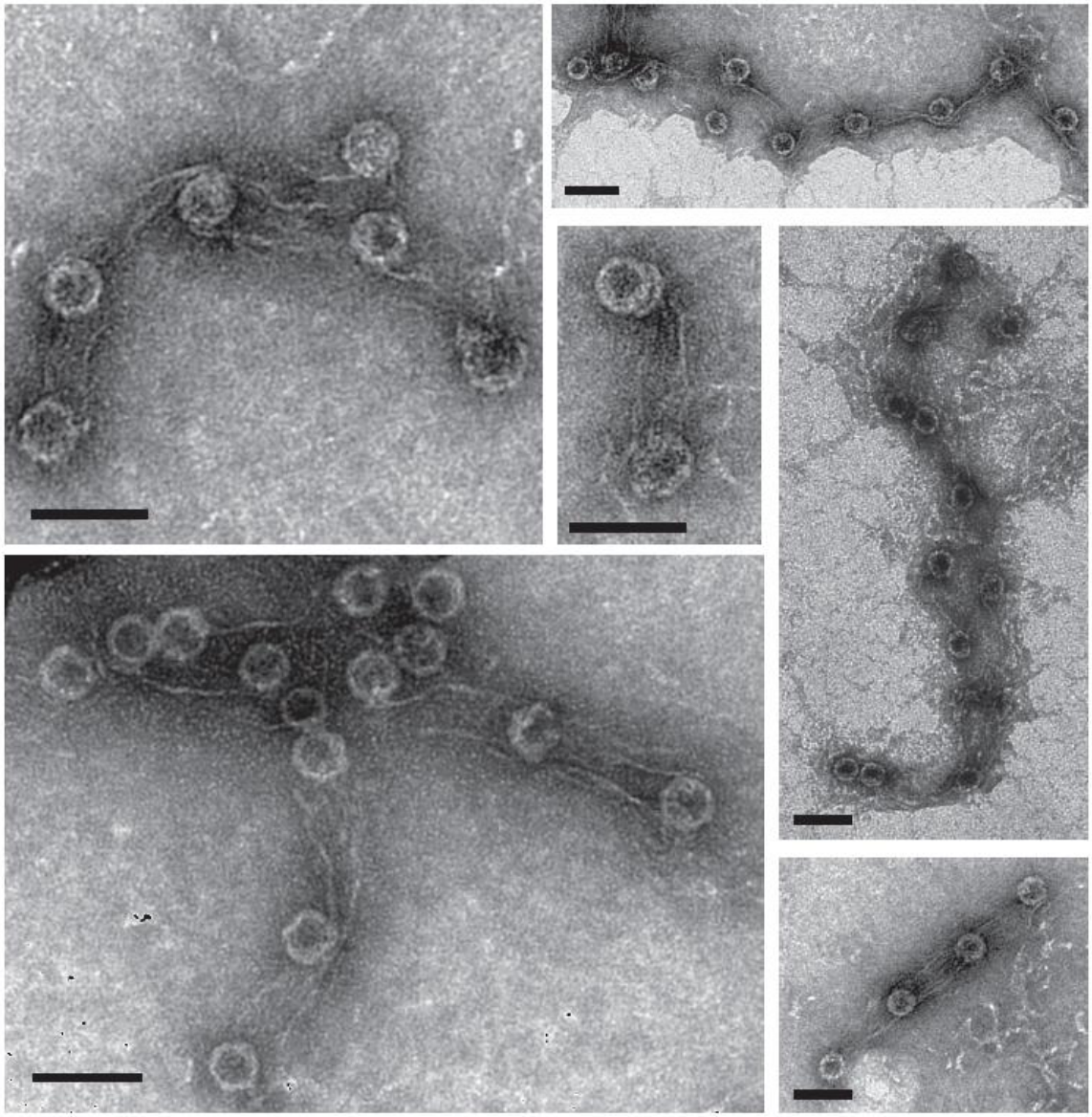

Figure S26. TEM images of DC tile arrays formed with MS2. Scale bars: 50 nm.

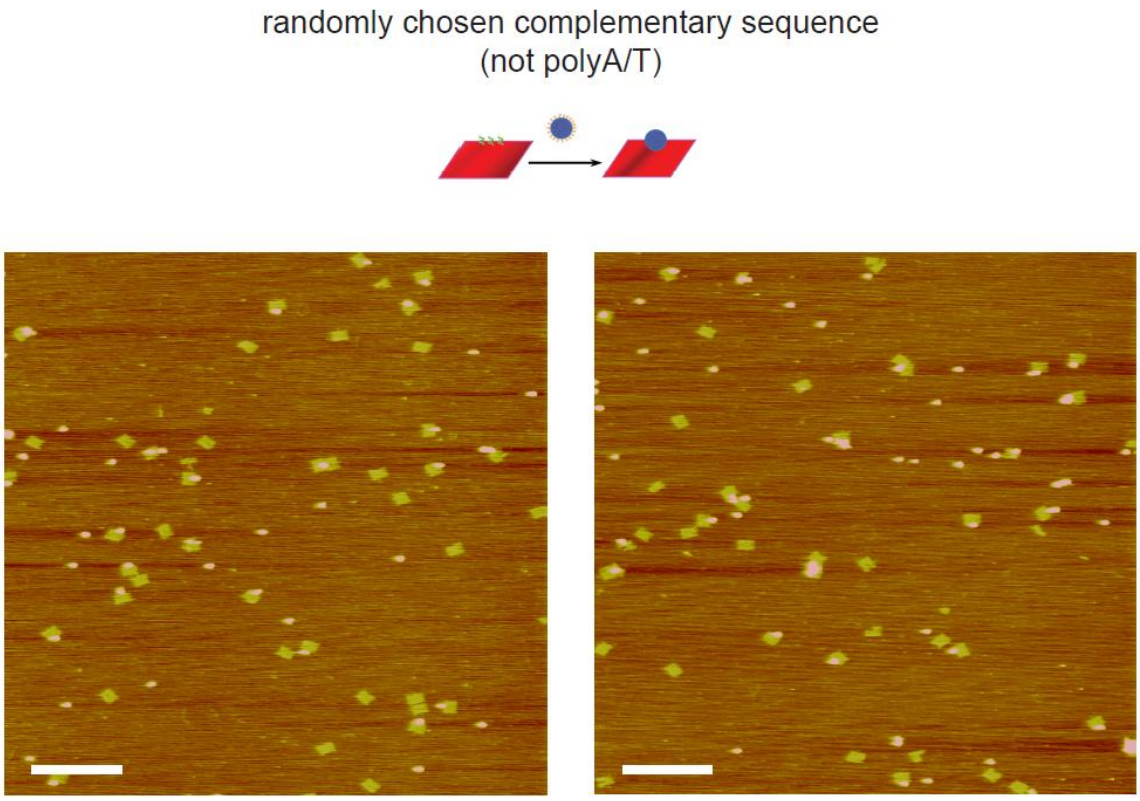

Figure S27. AFM images of capsids and tiles association using a random, complementary sequence (not polyA/T). The probes on the tiles are a random 40-bp sequence and the DNA on the caspids is complemen-tary to the last 20 bp of the probe. The hybridization efficiency does not surpass ~50%.

APPENDIX B

SUPPLEMENTAL INFORMATION FOR CHAPTER 3

Supplemental Information

Organization of Multienzyme Reaction Pathways: Interenzyme Substrate Diffusion for an Enzyme Cascade Organized on Spatially Addressable DNA Nanostructures

Jinglin Fu[1,2], Minghui Liu[1,3], Yan Liu[1,3], Neal W. Woodbury[2,3] *, and Hao Yan[1,3]*

[1]Center for Single Molecule Biophysics, the Biodesign Institute at Arizona State University, 1001 S. McAllister Avenue, Tempe, AZ 85287-5201

[2]Center for Innovations in Medicine, the Biodesign Institute at Arizona State University, 1001 S. McAllister Avenue, Tempe, AZ 85287-5201

[3]Department of Chemistry and Biochemistry, Arizona State University, Tempe, AZ 85287

*To whom correspondence should be addressed:

Hao Yan: (Tel) 480-727-8579; (E-mail) Hao.Yan@asu.edu

Neal W. Woodbury: (Tel) 480-965-3294; (E-mail) nwoodbury@asu.edu

Author Contributions: Jinglin Fu and Minghui Liu contributed equally to this work.

1. Chemicals

Glucose oxidase (Aspergillus niger), horseradish peroxidase, and phosphate buffered saline (PBS) were purchased from Sigma (St.Louis, MO). β-Gal streptavidin conjugates were purchased from Rockland (Gilbertsville, PA). Neutravidin, ABTS (2, 2'-Azinobis [3-ethylbenzothiazoline-6-sulfonic acid] -diammonium salt) and SPDP (N-Succinimidyl 3-(2-pyridyldithio)-propionate) were purchased from Pierce (Rockford, IL). M13 single-stranded DNA was purchased from Affymetrix (Santa Clara, CA). Single-stranded oligonucleotides were purchased from IDT (Coralville, Iowa).

2. AFM Imaging

~ 2 μL sample was deposited onto a freshly cleaved mica surface (Ted Pella, Inc.) and left to adsorb for 1 min. 400 μL of 1 x TAE-Mg^{2+} buffer was added to the liquid cell and the sample was scanned using SNL tips (Veeco, Inc.) in AC acoustic mode using a Pico-Plus AFM (Molecular Imaging, Agilent Technologies), or on a Veeco 8 AFM in peak-force mode.

Assembly Protocol	
Temperature	Gradient
90 °C	30 sec
86-71 °C	1 min/step
70-60 °C	10 min/step
59-30 °C	15 min/step
29-26 °C	10 min/step
25 °C	25 min
4 °C	hold

Table S1. Detailed annealing program for assembling DNA origami tiles.

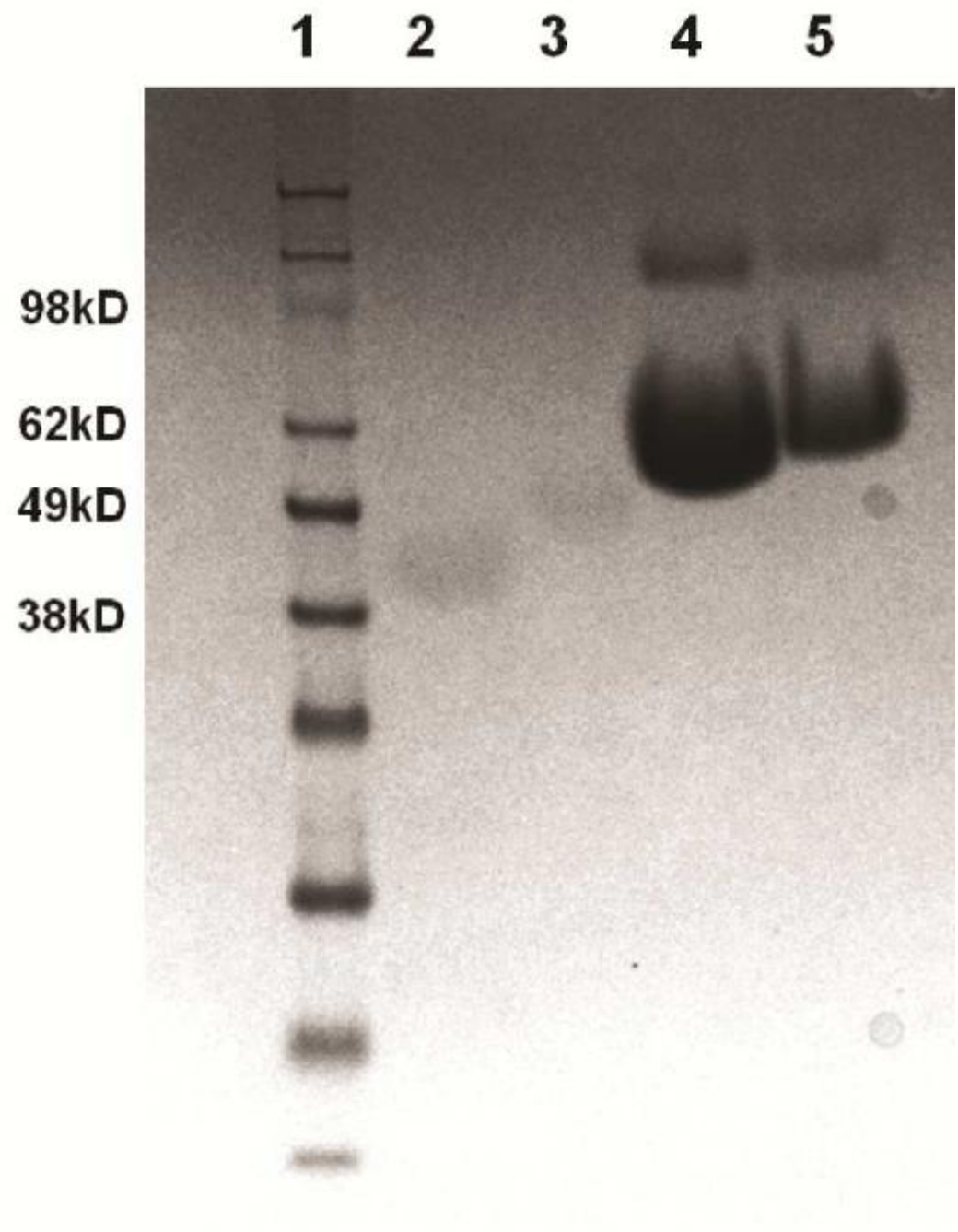

Figure S1. SDS-PAGE electrophoresis of purified protein-DNA conjugates: lane1, ladder; lane 2, wild-type HRP; lane 3, HRP-poly$(GGT)_6$; lane 4, wild-type GOx; lane5, GOx-poly$(T)_{22}$. Conditions: NuPAGE 4%-12% Bis Tris Gel with a constant voltage of 150 V for 50mins.

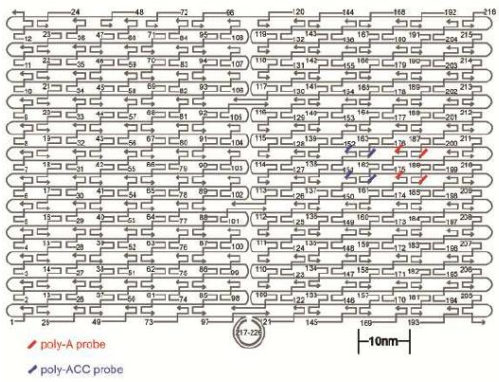

S1 tile (10-nm spacing)

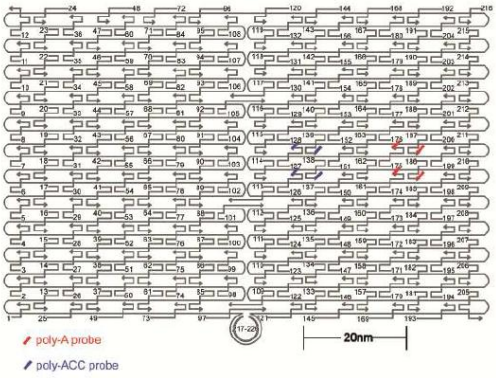

S2 tile (20-nm spacing)

Figure S2. DNA Origami tile schematics.

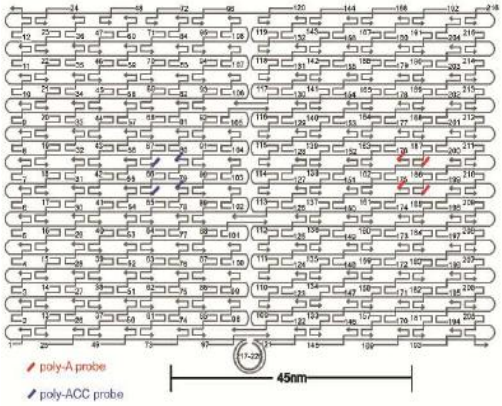

S3 tile (45-nm spacing)

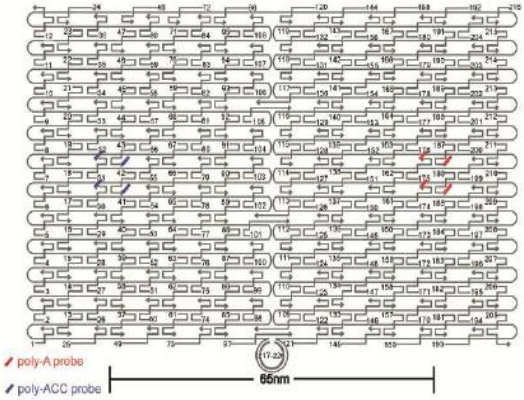

S4 tile (65-nm spacing)

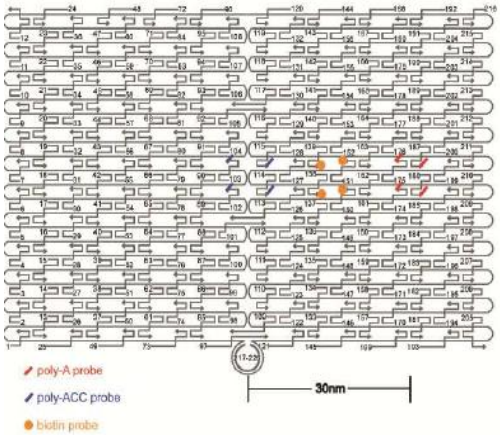

30-nm biotin tile

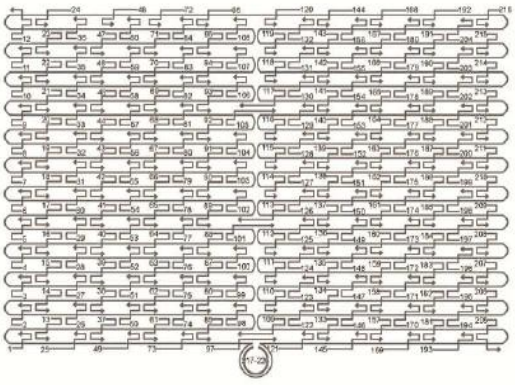

Control tile

Figure S2(cont). DNA Origami tile schematics.

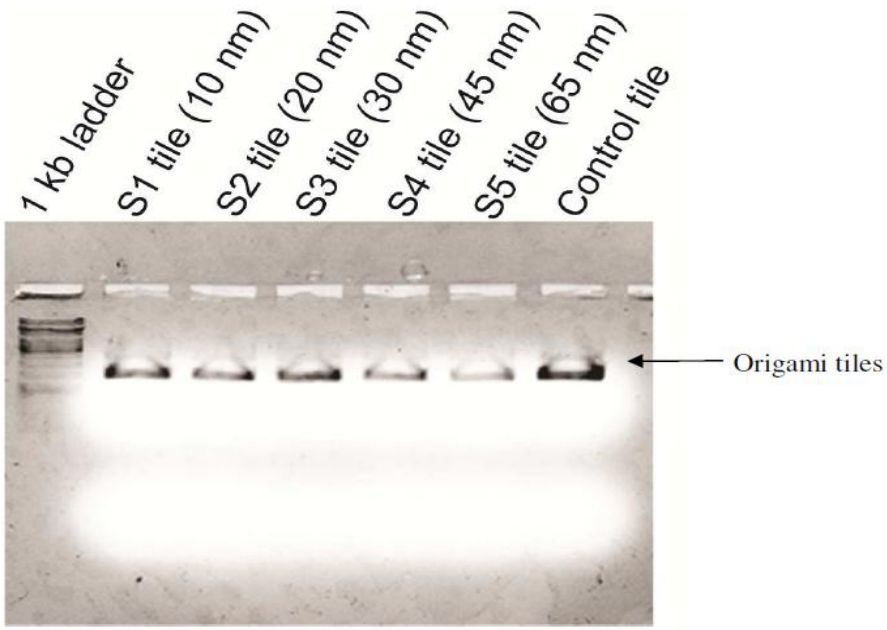

Figure S3. Agarose gel electrophoresis of DNA origami tiles after purification. Condition: 1.0% agarose (1xTAE-Mg^{2+}, 0.5 g/mL ethidium bromide) at 75-80 V for two-three hours; visualized with UV light. The bright background is a result of the loading dye (inverse color).

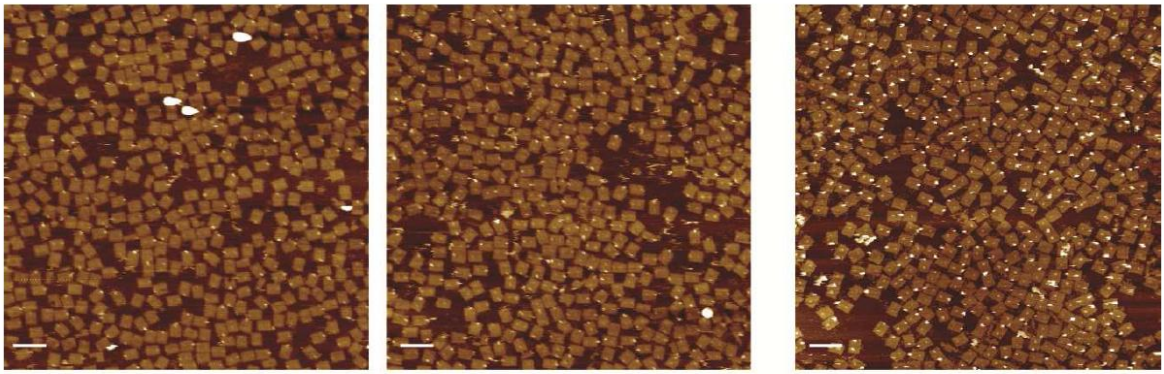

Figure S4. Titration of enzyme-to-origami ratio to achieve efficient co-assembly yields. DNA origami tiles with 45-nm inter-enzyme distance were used for this assay (scale bar ~ 200 nm).

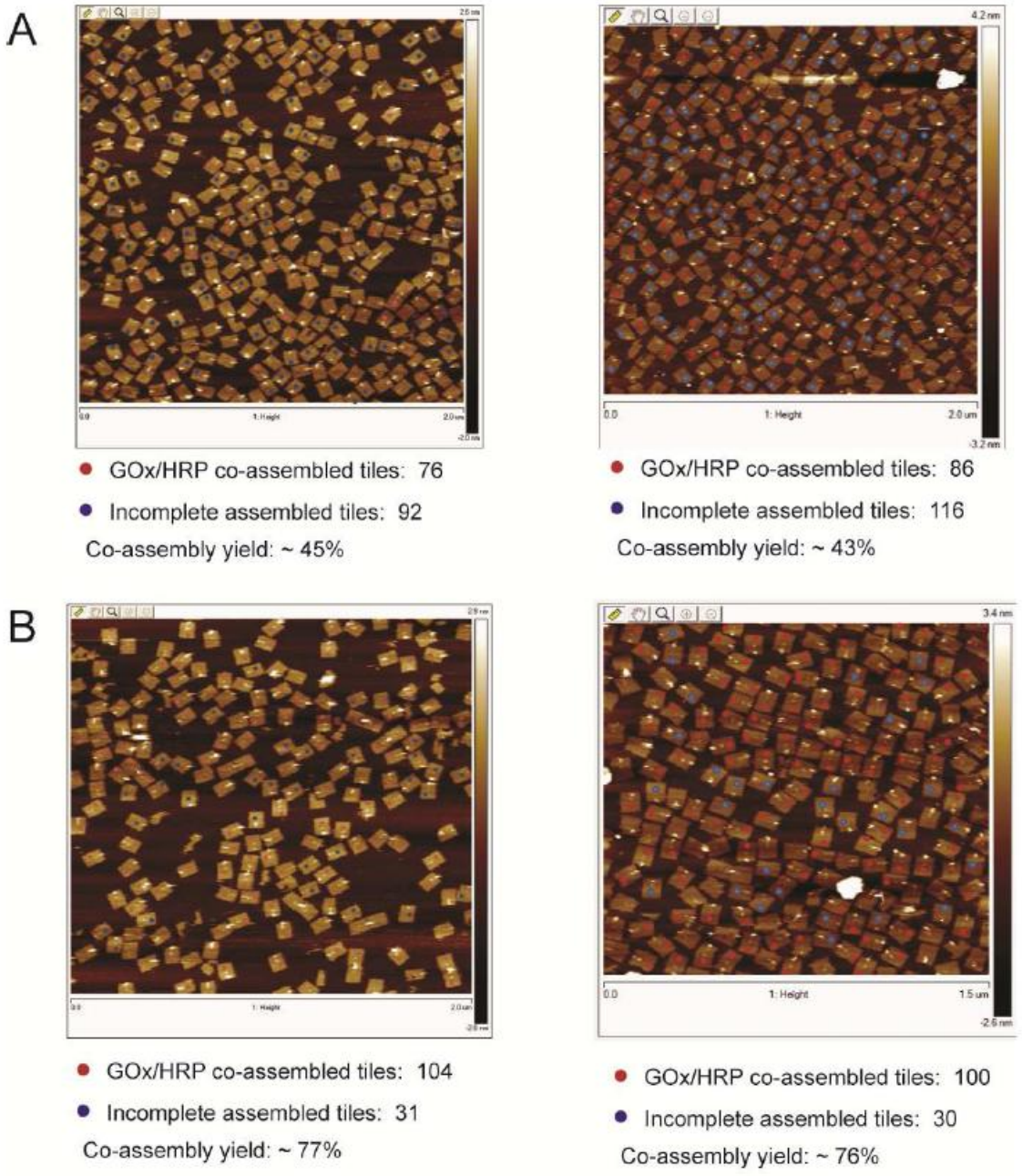

Figure S5. Evaluation of co-assembly yield of GOx and HRP on designed origami tiles. Each AFM image is generated by scanning an area of 2 μm× 2 μm. (A) 10-nm GOx/HRP interenzyme distance with ~ 44% assembly yield; (B) 20-nm GOx/HRP inter-enzyme distance with ~ 77% assembly yield;

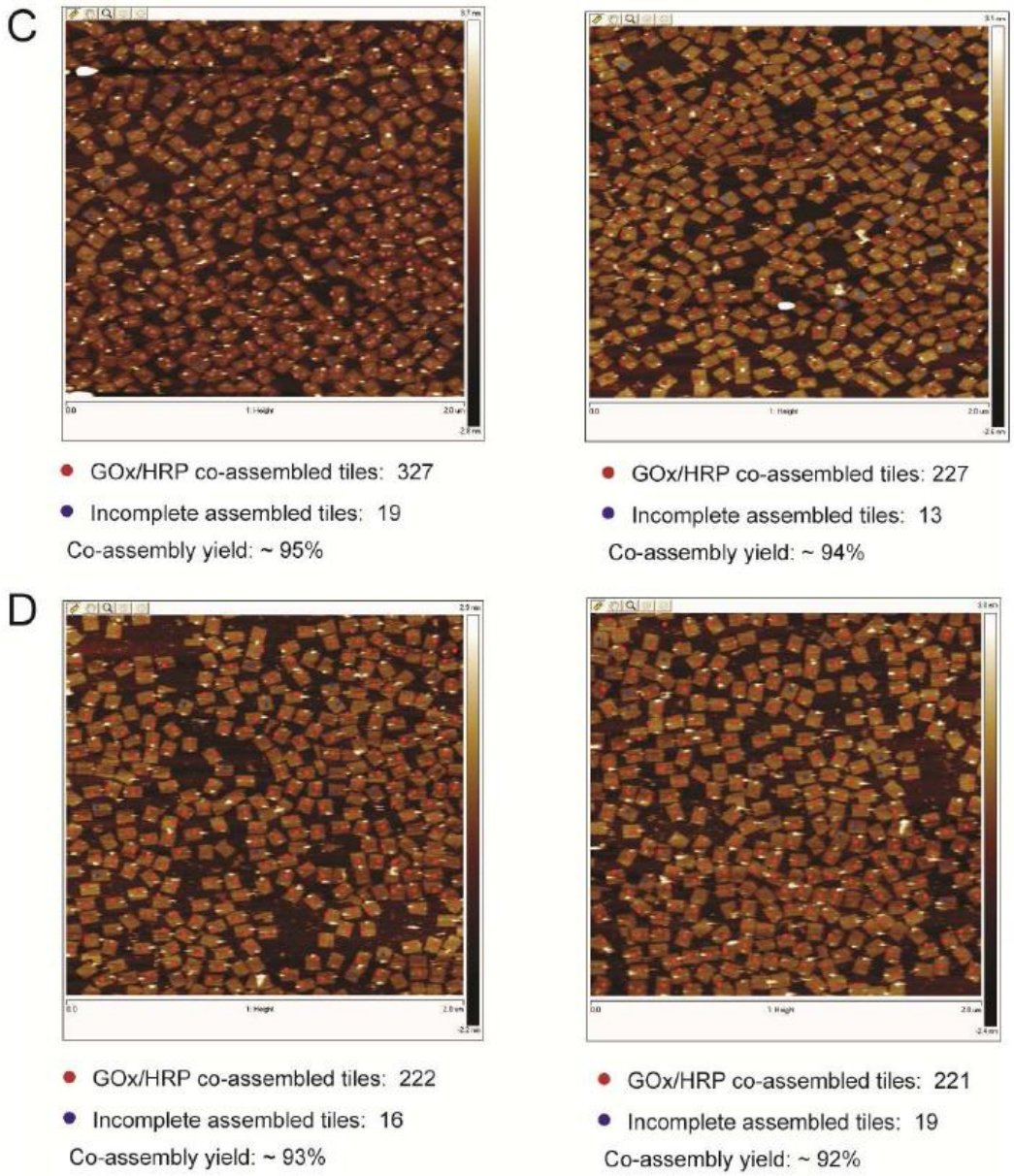

Figure S5 (cont). (C) 45-nm GOx/HRP inter-enzyme distance with ~ 95% assembly yield and (D) 65-nm GOx/HRP inter-enzyme distance with ~ 93% assembly yield. The calculated assembly yield is the average of two AFM images. Unclear origami tiles were not counted.

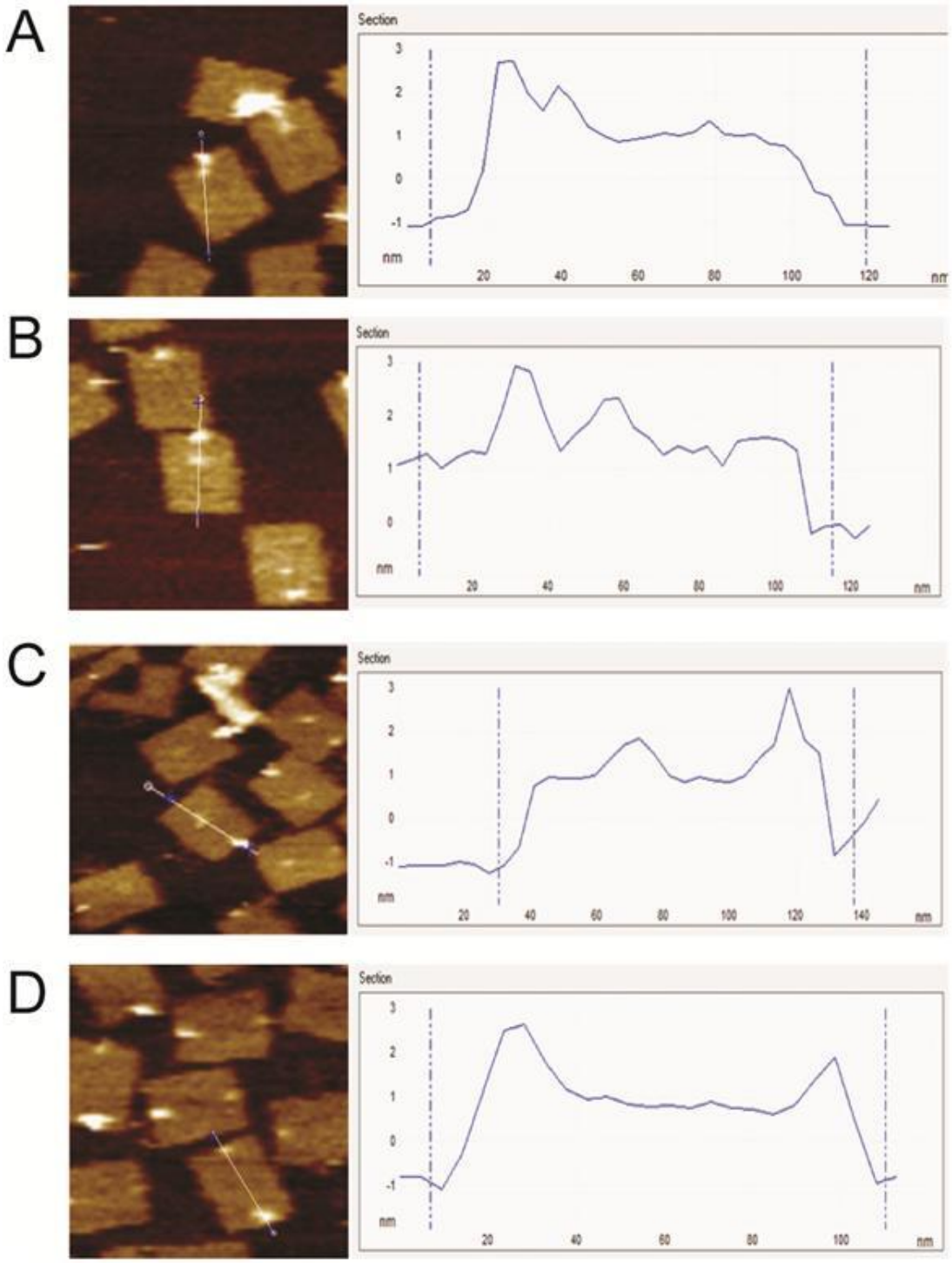

Figure S6. Height profiles of typical GOx/HRP pairs assembled on DNA origami tiles with (a)10-nm inter-enzyme distance, (B) 20-nm inter-enzyme distance, (C) 45-nm inter-enzyme distance and (D) 65-nm inter-enzyme distance.

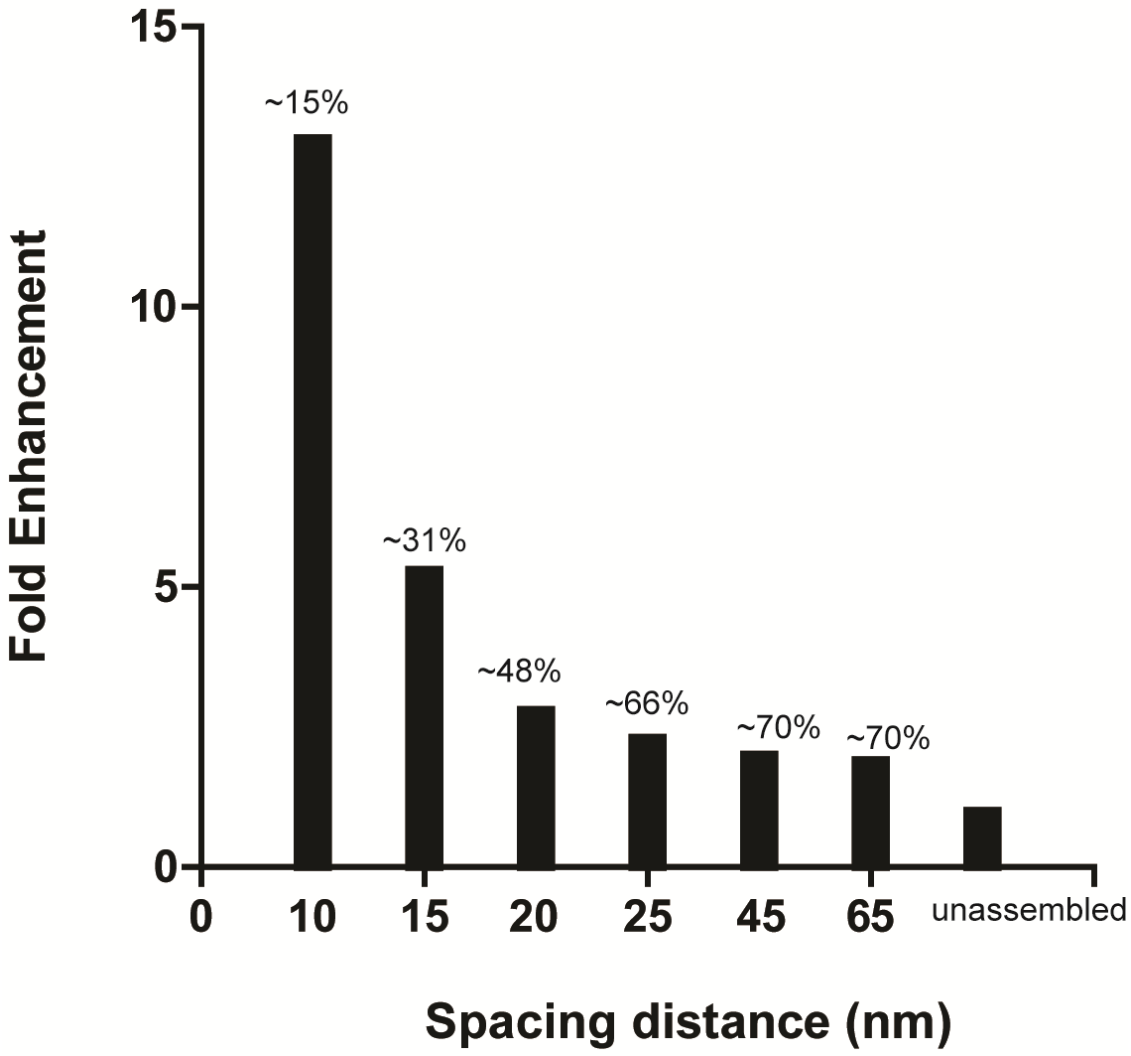

Figure S7. Enhancement in the calibrated enzyme activity of assembled GOx/HRP tiles with six inter-enzyme distances ranging from 10-nm to 65-nm (GOx/HRP co-assembly yields are noted above each bar). Note, only two capture probes were used for these experiments, with relatively low co-assembly yields compared to experiments utilizing four capture probes.

A

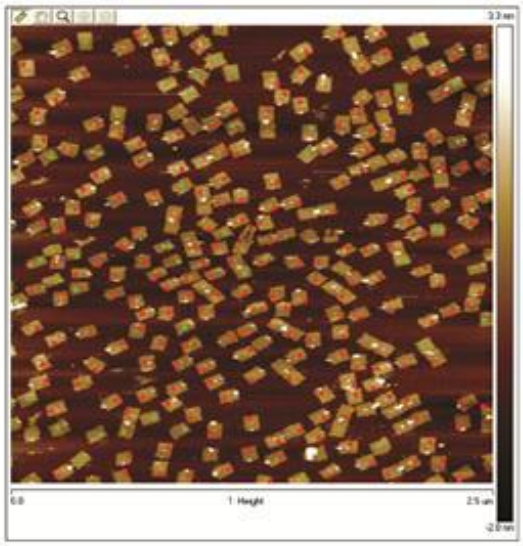

- Assembled tiles 213
- Incomplete tiles 40

Assembly yield: ~ 84%

B

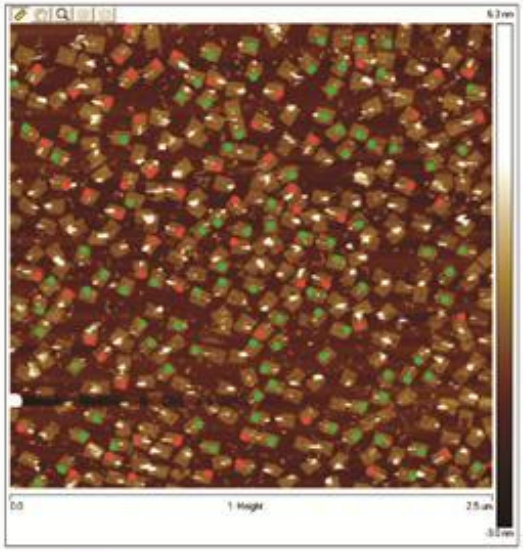

- Assembled tiles 59
- Incomplete tiles 95

Assembly yield: ~ 38%

C

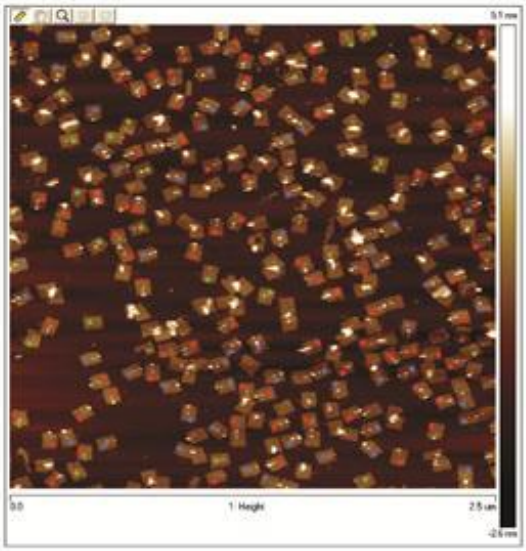

- Assembled tiles 78
- Incomplete tiles 79

Assembly yield: ~ 50%

Figure S8. Evaluation of co-assembly yield of GOx/HRP pairs with a protein bridge on designed origami tiles. Each AFM image is generated by scanning an area of 2.5 μm× 2.5 μm. (A) 30-nm GOx/HRP tile inter-enzyme distance with ~ 84% assembly yield; (B) 30-nm GOx-(β-Gal)-HRP- inter-enzyme distance with ~ 38% assembly yield; (C) 30-nm GOx-(NTV)-HRP inter-enzyme distance with ~ 50% assembly yield.

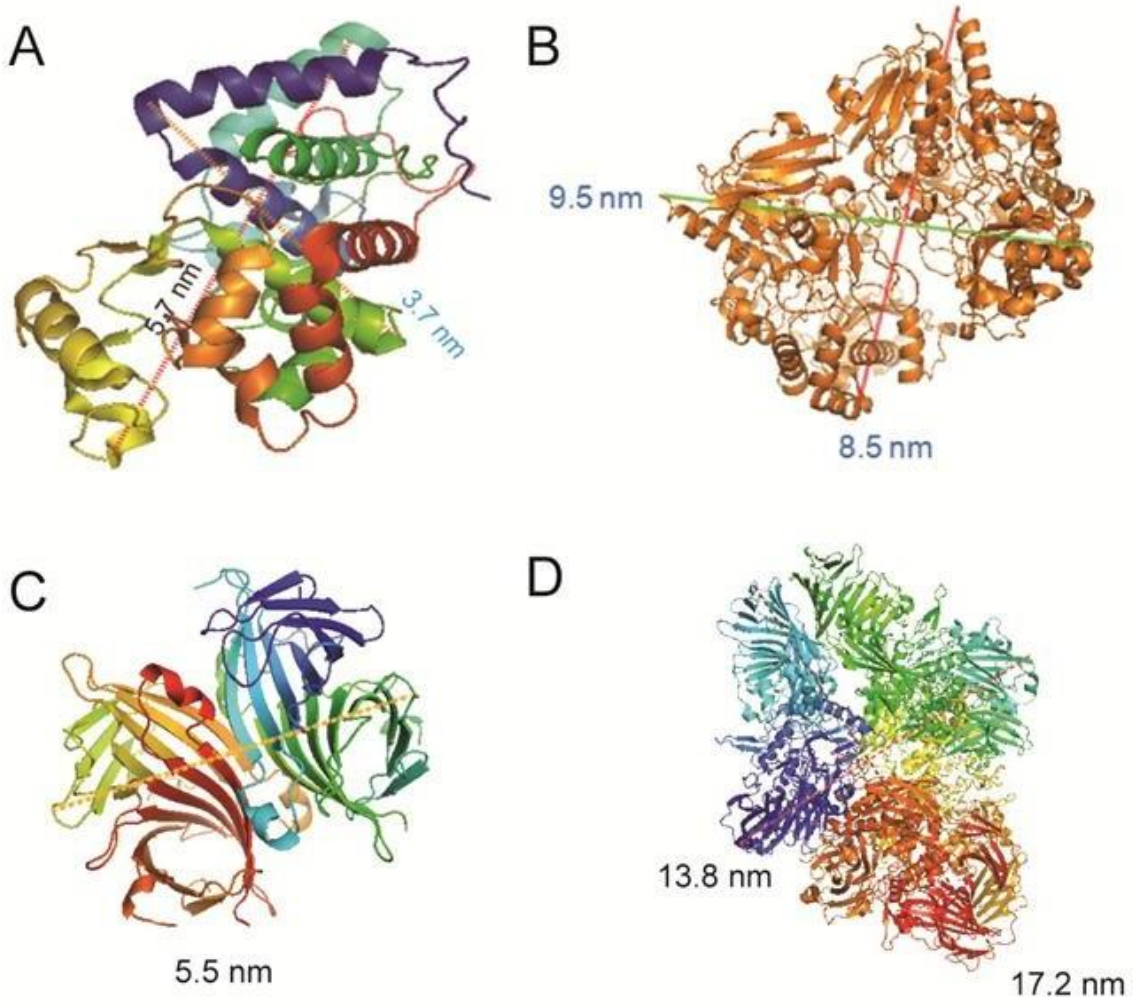

Figure S9. Crystal structures generated by PyMOL program. (A) Horseradish peroxidase (PDB 1ATJ); (B) Glucose oxidase (*Apergillus Niger*, PDB 1CF3); (C) Neutravidin; (D) β-galactosidase

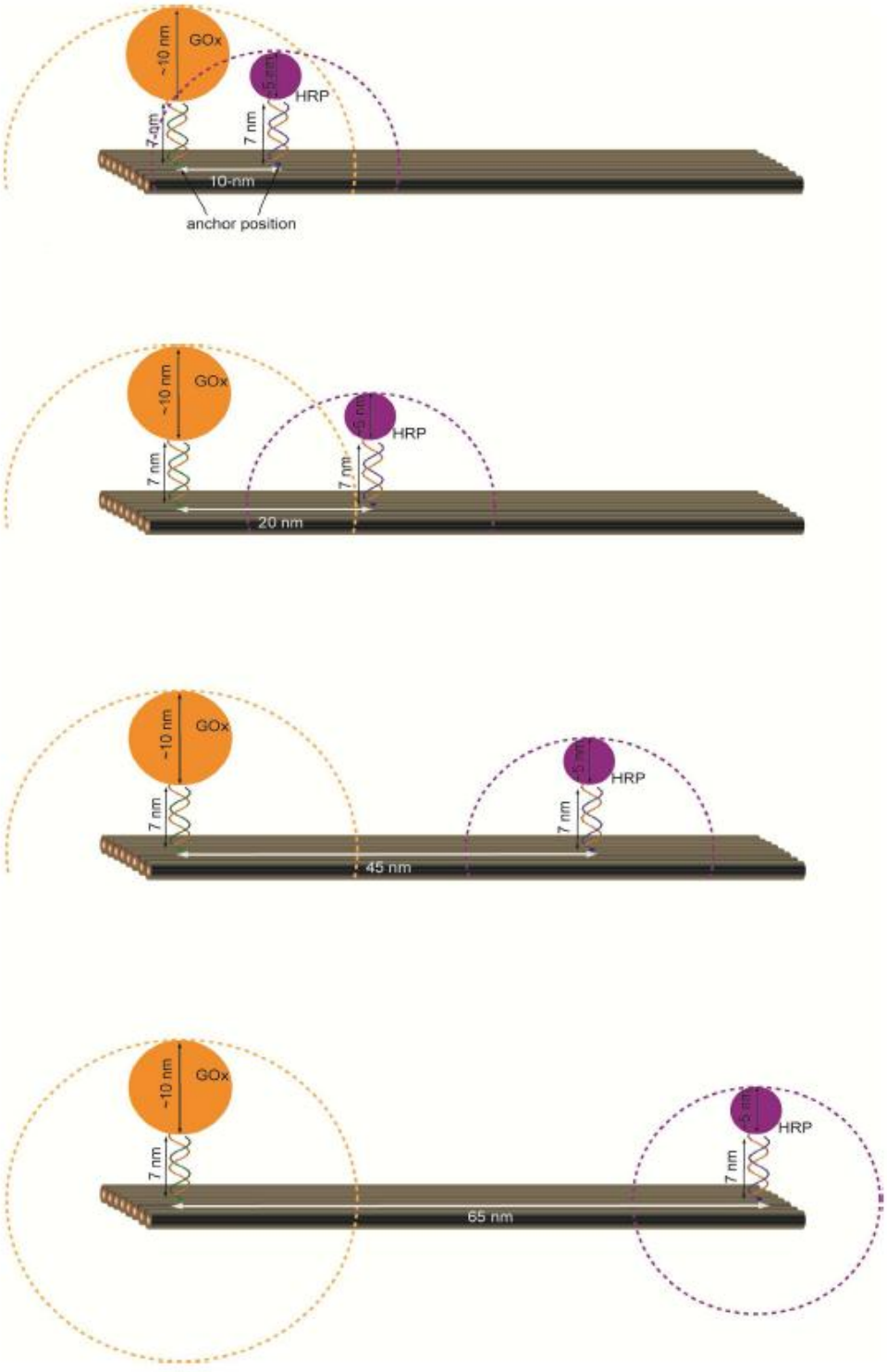
~10 nm
GOx
HRP
7 nm
10-nm
anchor position
20 nm
45 nm
65 nm

Figure S10. 3D model of GOx/HRP cascade assembled on origami tiles with anchor spacing distance ranged from 10-nm to 65-nm. Double-stranded DNA linker for anchoring enzymes is 20- 22-bp with ~ 7 nm in length. GOx (yellow sphere) has a diameter ~ 10 nm from crystal structure, and HRP (purple sphere) has a diameter ~ 5 nm. The yellow dot line indicates the accessible range for GOx, and the purple dot line indicates the accessible range for HRP on the origami tiles. For a GOx/HRP pair spaced with 10-nm, there is a high possibility that two proteins will connect to each other. The crowded space also results in the lower assembly yield for the 10-nm spacing distance.

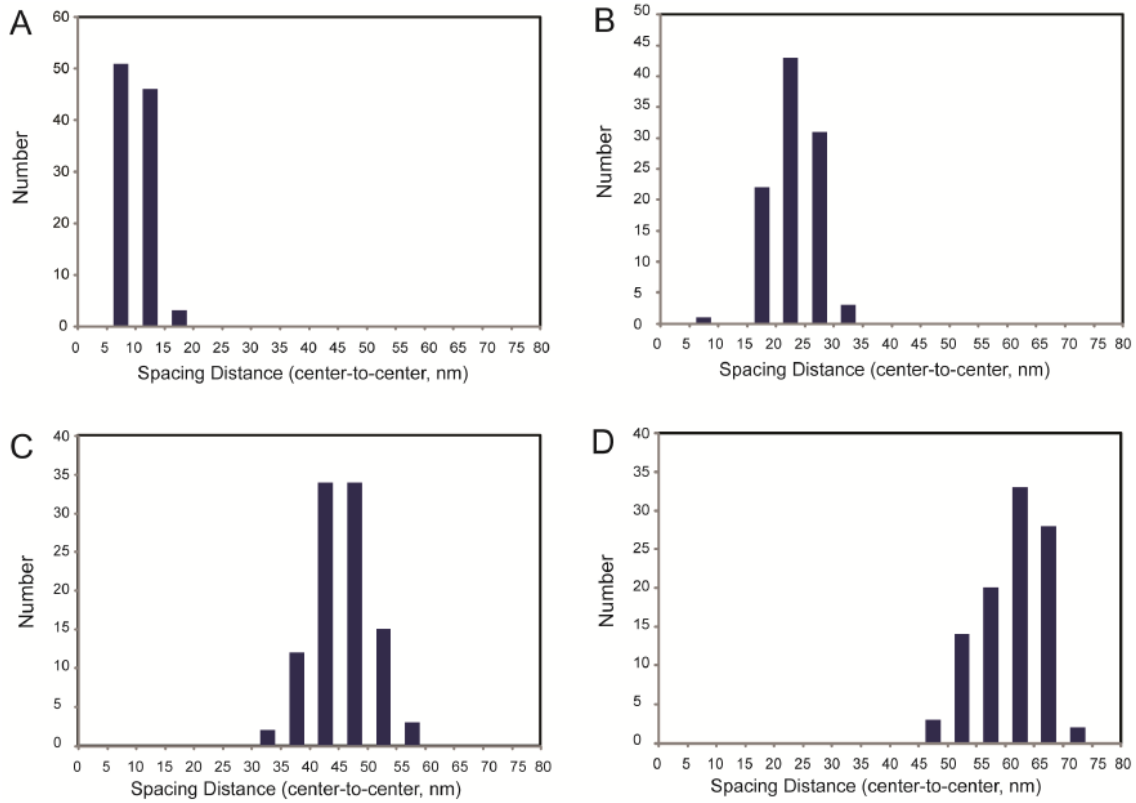

Figure S11. Statistical analysis of the observed inter-enzyme distances (center-to-center) for GOx/HRP assembled origami tiles using the AFM images in Figure S8: (A) 10-nm spaced origami tiles, (B) 20-nm spaced origami tiles; (C) 45-nm spaced origami tiles and

(D) 65-nm spaced origami tiles. 100 GOx/HRP-assembled tiles were statically analyzed for each interenzyme distance. No origami tiles were observed with inter-enzyme distance less than 5 nm due to the overlap of protein volume. Nearly 50% of GOx/HRP pairs on 10-nm spaced origami tiles exhibited an inter-enzyme distance between 5-10 nm, indicating that two enzymes are essentially touched with each other. This connected surface will strongly facilitate the H_2O_2 transfer across the shared hydration shell.

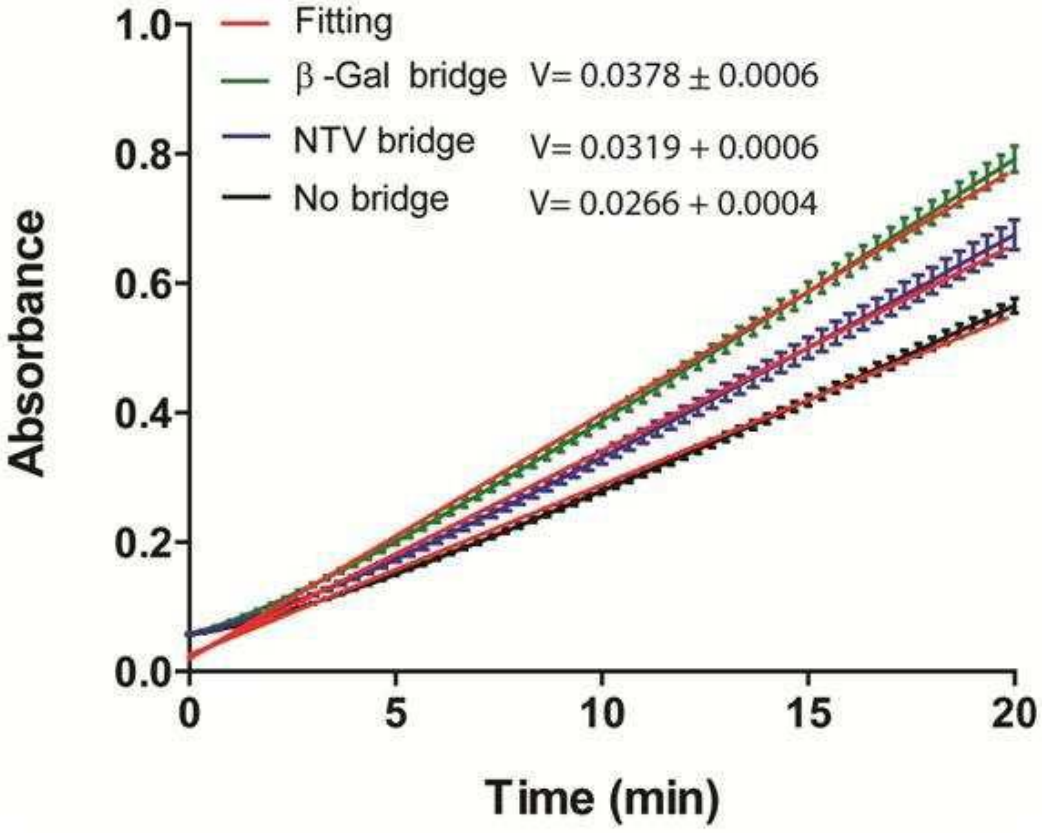

Figure S12. Curve fitting for the activity of assembled GOx/HRP pairs with β-Gal and NTV bridges compared to un-bridged GOx/HRP pairs. The velocity of each GOx/HRP pair is estimated by the fitting the slope of the curve. The β-Gal bridges result in 42 ± 4 % higher activity than un-bridged GOx/HRP pairs, while the HRP bridges result in 20 ± 4 % higher activity than un-bridged GOx/HRP pairs.

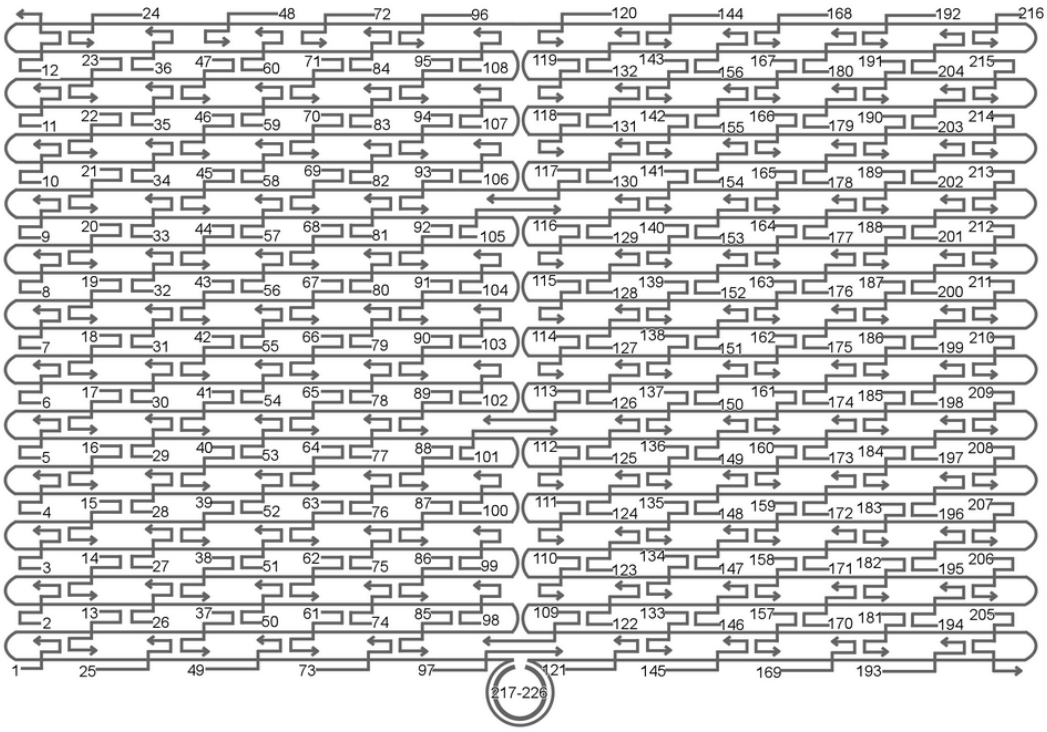

Name	Sequence
13	TGGTTTTTAACGTCAAAGGGCGAAGAACCATC
14	CTTGCATGCATTAATGAATCGGCCCGCCAGGG
15	TAGATGGGGGGTAACGCCAGGGTTGTGCCAAG
16	CATGTCAAGATTCTCCGTGGGAACCGTTGGTG
17	CTGTAATATTGCCTGAGAGTCTGGAAAACTAG
18	TGCAACTAAGCAATAAAGCCTCAGTTATGACC
19	AAACAGTTGATGGCTTAGAGCTTATTTAAATA
20	ACGAACTAGCGTCCAATACTGCGGAATGCTTT
21	CTTTGAAAAGAACTGGCTCATTATTTAATAAA
22	ACGGCTACTTACTTAGCCGGAACGCTGACCAA
23	GAGAATAGCTTTTGCGGGATCGTCGGGTAGCA
24	ACGTTAGTAAATGAATTTTCTGTAAGCGGAGT
25	ACCCAAATCAAGTTTTTTGGGGTCAAAGAACG
26	TGGACTCCCTTTTCACCAGTGAGACCTGTCGT
27	GCCAGCTGCCTGCAGGTCGACTCTGCAAGGCG
28	ATTAAGTTCGCATCGTAACCGTGCGAGTAACA
29	ACCCGTCGTCATATGTACCCCGGTAAAGGCTA
30	TCAGGTCACTTTTGCGGGAGAAGCAGAATTAG
31	CAAAATTAAAGTACGGTGTCTGGAAGAGGTCA
32	TTTTTGCGCAGAAAACGAGAATGAATGTTTAG
33	ACTGGATAACGGAACAACATTATTACCTTATG
34	CGATTTTAGAGGACAGATGAACGGCGCGACCT
35	GCTCCATGAGAGGCTTTGAGGACTAGGGAGTT
36	AAAGGCCGAAAGGAACAACTAAAGCTTTCCAG
37	AGCTGATTACAAGAGTCCACTATTGAGGTGCC
38	CCCGGGTACTTTCCAGTCGGGAAACGGGCAAC
39	GTTTGAGGGAAAGGGGGATGTGCTAGAGGATC
40	AGAAAAGCAACATTAAATGTGAGCATCTGCCA

41	CAACGCAATTTTTGAGAGATCTACTGATAATC
42	TCCATATACATACAGGCAAGGCAACTTTATTT
43	CAAAAATCATTGCTCCTTTTGATAAGTTTCAT
44	AAAGATTCAGGGGGTAATAGTAAACCATAAAT
45	CCAGGCGCTTAATCATTGTGAATTACAGGTAG
46	TTTCATGAAAATTGTGTCGAAATCTGTACAGA
47	AATAATAAGGTCGCTGAGGCTTGCAAAGACTT
48	CGTAACGATCTAAAGTTTTGTCGTGAATTGCG
49	GTAAAGCACTAAATCGGAACCCTAGTTGTTCC
50	AGTTTGGAGCCCTTCACCGCCTGGTTGCGCTC
51	ACTGCCCGCCGAGCTCGAATTCGTTATTACGC
52	CAGCTGGCGGACGACGACAGTATCGTAGCCAG
53	CTTTCATCCCCAAAAACAGGAAGACCGGAGAG
54	GGTAGCTAGGATAAAAATTTTTAGTTAACATC
55	CAATAAATACAGTTGATTCCCAATTTAGAGAG
56	TACCTTTAAGGTCTTTACCCTGACAAAGAAGT
57	TTTGCCAGATCAGTTGAGATTTAGTGGTTTAA
58	TTTCAACTATAGGCTGGCTGACCTTGTATCAT
59	CGCCTGATGGAAGTTTCCATTAAACATAACCG
60	ATATATTCTTTTTTCACGTTGAAAATAGTTAG
61	GAGTTGCACGAGATAGGGTTGAGTAAGGGAGC
62	TCATAGCTACTCACATTAATTGCGCCCTGAGA
63	GAAGATCGGTGCGGGCCTCTTCGCAATCATGG
64	GCAAATATCGCGTCTGGCCTTCCTGGCCTCAG
65	TATATTTTAGCTGATAAATTAATGTTGTATAA
66	CGAGTAGAACTAATAGTAGTAGCAAACCCTCA
67	TCAGAAGCCTCCAACAGGTCAGGATCTGCGAA
68	CATTCAACGCGAGAGGCTTTTGCATATTATAG
69	AGTAATCTTAAATTGGGCTTGAGAGAATACCA
70	ATACGTAAAAGTACAACGGAGATTTCATCAAG
71	AAAAAAGGACAACCATCGCCCACGCGGGTAAA
72	TGTAGCATTCCACAGACAGCCCTCATCTCCAA
73	CCCCGATTTAGAGCTTGACGGGGAAATCAAAA
74	GAATAGCCGCAAGCGGTCCACGCTCCTAATGA
75	GTGAGCTAGTTTCCTGTGTGAAATTTGGGAAG
76	GGCGATCGCACTCCAGCCAGCTTTGCCATCAA
77	AAATAATTTTAAATTGTAAACGTTGATATTCA
78	ACCGTTCTAAATGCAATGCCTGAGAGGTGGCA
79	TCAATTCTTTTAGTTTGACCATTACCAGACCG
80	GAAGCAAAAAAGCGGATTGCATCAGATAAAAA
81	CCAAAATATAATGCAGATACATAAACACCAGA
82	ACGAGTAGTGACAAGAACCGGATATACCAAGC
83	GCGAAACATGCCACTACGAAGGCATGCGCCGA
84	CAATGACACTCCAAAAGGAGCCTTACAACGCC
85	CCAGCAGGGGCAAAATCCCTTATAAAGCCGGC
86	GCTCACAATGTAAAGCCTGGGGTGGGTTTGCC
87	GCTTCTGGTCAGGCTGCGCAACTGTGTTATCC
88	GTTAAAATTTTAACCAATAGGAACCCGGCACC
89	AGGTAAAGAAATCACCATCAATATAATATTTT
90	TCGCAAATGGGGCGCGAGCTGAAATAATGTGT
91	AAGAGGAACGAGCTTCAAAGCGAAGATACATT
92	GGAATTACTCGTTTACCAGACGACAAAAGATT
93	CCAAATCACTTGCCCTGACGAGAACGCCAAAA
94	AAACGAAATGACCCCCAGCGATTATTCATTAC
95	TCGGTTTAGCTTGATACCGATAGTCCAACCTA
96	TGAGTTTCGTCACCAGTACAAACTTAATTGTA
97	GAACGTGGCGAGAAAGGAAGGGAACAAACTAT
98	CCGAAATCCGAAAATCCTGTTTGAAGCCGGAA
99	GCATAAAGTTCCACACAACATACGAAGCGCCA
100	TTCGCCATTGCCGGAAACCAGGCATTAAATCA

101	GCTCATTTTCGCATTAAATTTTTGAGCTTAGA
102	AGACAGTCATTCAAAAGGGTGAGAAGCTATAT
103	TTTCATTTGGTCAATAACCTGTTTATATCGCG
104	TTTTAATTGCCCGAAAGACTTCAAAACACTAT
105	CATAACCCGAGGCATAGTAAGAGCTTTTTAAG
106	GAATAAGGACGTAACAAAGCTGCTCTAAAACA
107	CTCATCTTGAGGCAAAAGAATACAGTGAATTT
108	CTTAAACATCAGCTTGCTTTCGAGCGTAACAC
109	ACGAACCAAAACATCGCCATTAAATGGTGGTT
110	CGACAACTAAGTATTAGACTTTACAATACCGA
111	CTTTTACACAGATGAATATACAGTAAACAATT
112	TTAAGACGTTGAAAACATAGCGATAACAGTAC
113	GCGTTATAGAAAAAGCCTGTTTAGAAGGCCGG

Name	Sequence
114	ATCGGCTGCGAGCATGTAGAAACCTATCATAT
115	CCTAATTTACGCTAACGAGCGTCTAATCAATA
116	AAAAGTAATATCTTACCGAAGCCCTTCCAGAG
117	TTATTCATAGGGAAGGTAAATATTCATTCAGT
118	GAGCCGCCCCACCACCGGAACCGCGACGGAAA
119	AATGCCCCGTAACAGTGCCCGTATCTCCCTCA
120	CAAGCCCAATAGGAACCCATGTACAAACAGTT
121	CGGCCTTGCTGGTAATATCCAGAACGAACTGA
122	TAGCCCTACCAGCAGAAGATAAAAACATTTGA
123	GGATTTAGCGTATTAAATCCTTTGTTTTCAGG
124	TTTAACGTTCGGGAGAAACAATAATTTTCCCT
125	TAGAATCCCTGAGAAGAGTCAATAGGAATCAT
126	AATTACTACAAATTCTTACCAGTAATCCCATC
127	CTAATTTATCTTTCCTTATCATTCATCCTGAA
128	TCTTACCAGCCAGTTACAAAATAAATGAAATA
129	GCAATAGCGCAGATAGCCGAACAATTCAACCG
130	ATTGAGGGTAAAGGTGAATTATCAATCACCGG
131	AACCAGAGACCCTCAGAACCGCCAGGGGTCAG
132	TGCCTTGACTGCCTATTTCGGAACAGGGATAG
133	AGGCGGTCATTAGTCTTTAATGCGCAATATTA
134	TTATTAATGCCGTCAATAGATAATCAGAGGTG
135	CCTGATTGAAAGAAATTGCGTAGACCCGAACG
136	ATCAAAATCGTCGCTATTAATTAACGGATTCG
137	ACGCTCAAAATAAGAATAAACACCGTGAATTT
138	GGTATTAAGAACAAGAAAAATAATTAAAGCCA
139	ATTATTTAACCCAGCTACAATTTTCAAGAACG
140	GAAGGAAAATAAGAGCAAGAAACAACAGCCAT
141	GACTTGAGAGACAAAAGGGCGACAAGTTACCA
142	GCCACCACTCTTTTCATAATCAAACCGTCACC
143	CTGAAACAGGTAATAAGTTTTAACCCCTCAGA
144	CTCAGAGCCACCACCCTCATTTTCCTATTATT
145	CCGCCAGCCATTGCAACAGGAAAAATATTTTT
146	GAATGGCTAGTATTAACACCGCCTCAACTAAT
147	AGATTAGATTTAAAAGTTTGAGTACACGTAAA
148	ACAGAAATCTTTGAATACCAAGTTCCTTGCTT
149	CTGTAAATCATAGGTCTGAGAGACGATAAATA
150	AGGCGTTACAGTAGGGCTTAATTGACAATAGA
151	TAAGTCCTACCAAGTACCGCACTCTTAGTTGC
152	TATTTTGCTCCCAATCCAAATAAGTGAGTTAA
153	GCCCAATACCGAGGAAACGCAATAGGTTTACC
154	AGCGCCAACCATTTGGGAATTAGATTATTAGC
155	GTTTGCCACCTCAGAGCCGCCACCGATACAGG
156	AGTGTACTTGAAAGTATTAAGAGGCCGCCACC

157	GCCACGCTATACGTGGCACAGACAACGCTCAT
158	ATTTTGCGTCTTTAGGAGCACTAAGCAACAGT
159	GCGCAGAGATATCAAAATTATTTGACATTATC
160	TAACCTCCATATGTGAGTGAATAAACAAAATC
161	CATATTTAGAAATACCGACCGTGTTACCTTTT
162	CAAGCAAGACGCGCCTGTTTATCAAGAATCGC
163	TTTTGTTTAAGCCTTAAATCAAGAATCGAGAA
164	ATACCCAAGATAACCCACAAGAATAAACGATT
165	AATCACCAAATAGAAAATTCATATATAACGGA
166	CACCAGAGTTCGGTCATAGCCCCCGCCAGCAA
167	CCTCAAGAATACATGGCTTTTGATAGAACCAC
168	CCCTCAGAACCGCCACCCTCAGAACTGAGACT
169	GGAAATACCTACATTTTGACGCTCACCTGAAA
170	GCGTAAGAGAGAGCCAGCAGCAAAAAGGTTAT
171	CTAAAATAGAACAAAGAAACCACCAGGGTTAG
172	AACCTACCGCGAATTATTCATTTCCAGTACAT
173	AAATCAATGGCTTAGGTTGGGTTACTAAATTT
174	AATGGTTTACAACGCCAACATGTAGTTCAGCT
175	AATGCAGACCGTTTTTATTTTCATCTTGCGGG
176	AGGTTTTGAACGTCAA AAATGAAAGCGCTAAT
177	ATCAGAGAAAGAACTG GCATGATTTTATTTTG
178	TCACAATCGTAGCACCATTACCATCGTTTTCA
179	TCGGCATTCCGCCGCCAGCATTGACGTTCCAG
180	TAAGCGTCGAAGGATT AGGATTAGTACCGCCA
181	CTAAAGCAAGATAGAA CCCTTCTGAATCGTCT
182	CGGAATTATTGAAAGGAATTGAGGTGAAAAAT
183	GAGCAAAAACTTCTGAATAATGGAAGAAGGAG
184	TATGTAAACCTTTTTTAATGGAAAAATTACCT
185	AGAGGCATAATTTCATCTTCTGACTATAACTA
186	TCATTACCCGACAATAAACAACATATTTAGGC
187	CTTTACAGTTAGCGAACCTCCCGACGTAGGAA
188	TTATTACGGTCAGAGG GTAATTGAATAGCAGC
189	CCGGAAACACACCACG GAATAAGTAAGACTCC
190	TGAGGCAGGCGTCAGACTGTAGCGTAGCAAGG
191	TGCTCAGTCAGTCTCTGAATTTACCAGGAGGT
192	TATCACCGTACTCAGGAGGTTTAGCGGGGTTT
193	GAAATGGATTATTTACATTGGCAGACATTCTG
194	GCCAACAGTCACCTTGCTGAACCTGTTGGCAA
195	ATCAACAGTCATCATATTCCTGATTGATTGTT
196	TGGATTATGAAGATGA TGAAACAAAATTTCAT
197	TTGAATTATGCTGATG CAAATCCACAAATATA
198	TTTTAGTTTTTCGAGCCAGTAATAAATTCTGT
199	CCAGACGAGCGCCCAATAGCAAGCAAGAACGC
200	GAGGCGTTAGAGAATAACATAAAAGAACACCC
201	TGAACAAACAGTATGTTAGCAAACTAAAAGAA
202	ACGCAAAGGTCACCAATGAAACCAATCAAGTT
203	TGCCTTTAGTCAGACGATTGGCCTGCCAGAAT
204	GGAAAGCGACCAGGCGGATAAGTGAATAGGTG
217	AACATCACTTGCCTGAGTAGAAGAACT
218	TGTAGCAATACTTCTTTGATTAGTAAT
219	AGTCTGTCCATCACGCAAATTAACCGT
220	ATAATCAGTGAGGCCACCGAGTAAAAG
221	ACGCCAGAATCCTGAGAAGTGTTTTT
222	TTAAAGGGATTTTAGACAGGAACGGT
223	AGAGCGGGAGCTAAACAGGAGGCCGA
224	TATAACGTGCTTTCCTCGTTAGAATC
225	GTACTATGGTTGCTTTGACGAGCACG
226	GCGCTTAATGCGCCGCTACAGGGCGC

Figure S13. Rectangular DNA origami tile (C1 tile) and the corresponding staple strands.

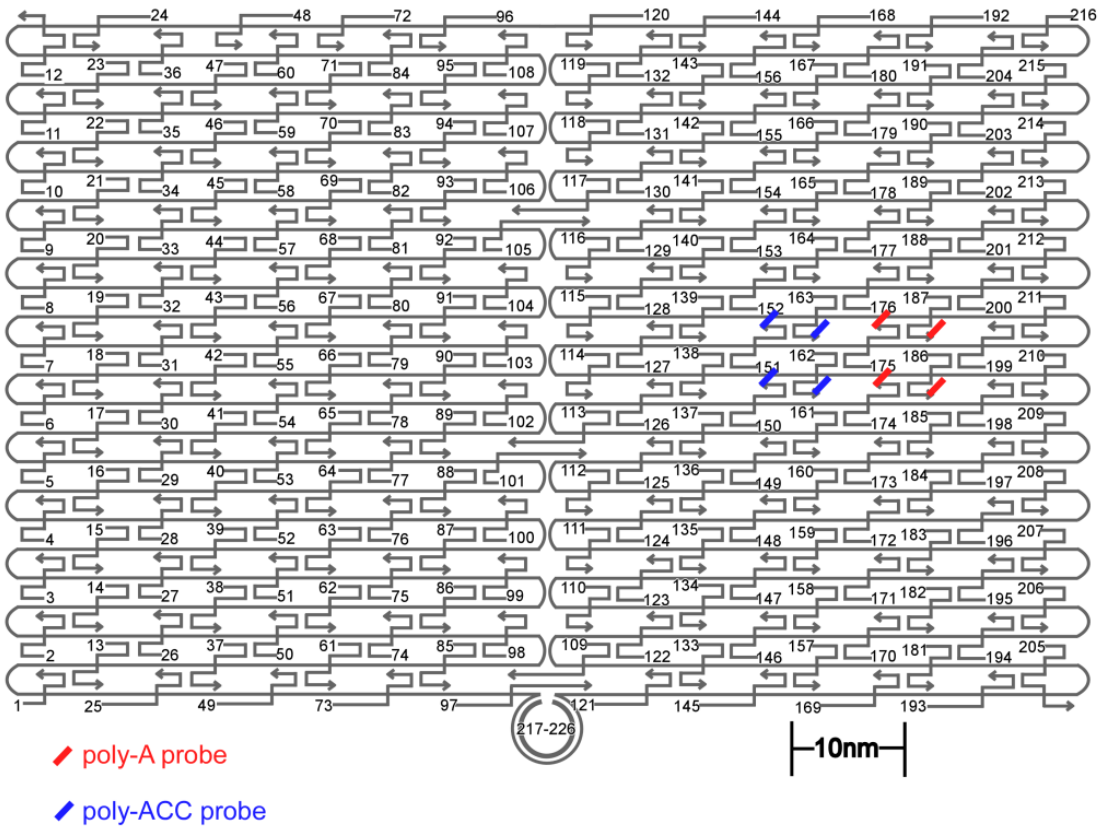

Name	Sequence
A-174	AATGGTTTACAACGCCAACATGTAGTTCAGCTAAAAAAAAAAAAAAAAAAAAAAAAAA
A-175	AATGCAGACCGTTTTTATTTTCATCTTGCGGGAAAAAAAAAAAAAAAAAAAAAAAAAA
A-186	TCATTACCCGACAATAAACAACATATTTAGGCAAAAAAAAAAAAAAAAAAAAAAAAAA
A-187	CTTTACAGTTAGCGAACCTCCCGACGTAGGAAAAAAAAAAAAAAAAAAAAAAAAAAA
ACC10-150	AGGCGTTACAGTAGGGCTTAATTGACAATAGAACCACCACCACCACCACCACCACCACC
ACC10-151	TAAGTCCTACCAAGTACCGCACTCTTAGTTGCACCACCACCACCACCACCACCACCACC
ACC10-162	CAAGCAAGACGCGCCTGTTTATCAAGAATCGCACCACCACCACCACCACCACCACCACC
ACC10-163	TTTTGTTTAAGCCTTAAATCAAGAATCGAGAAACCACCACCACCACCACCACCACCACC

Figure S14. S1 origami tile schematic with 10-nm distance between probes.

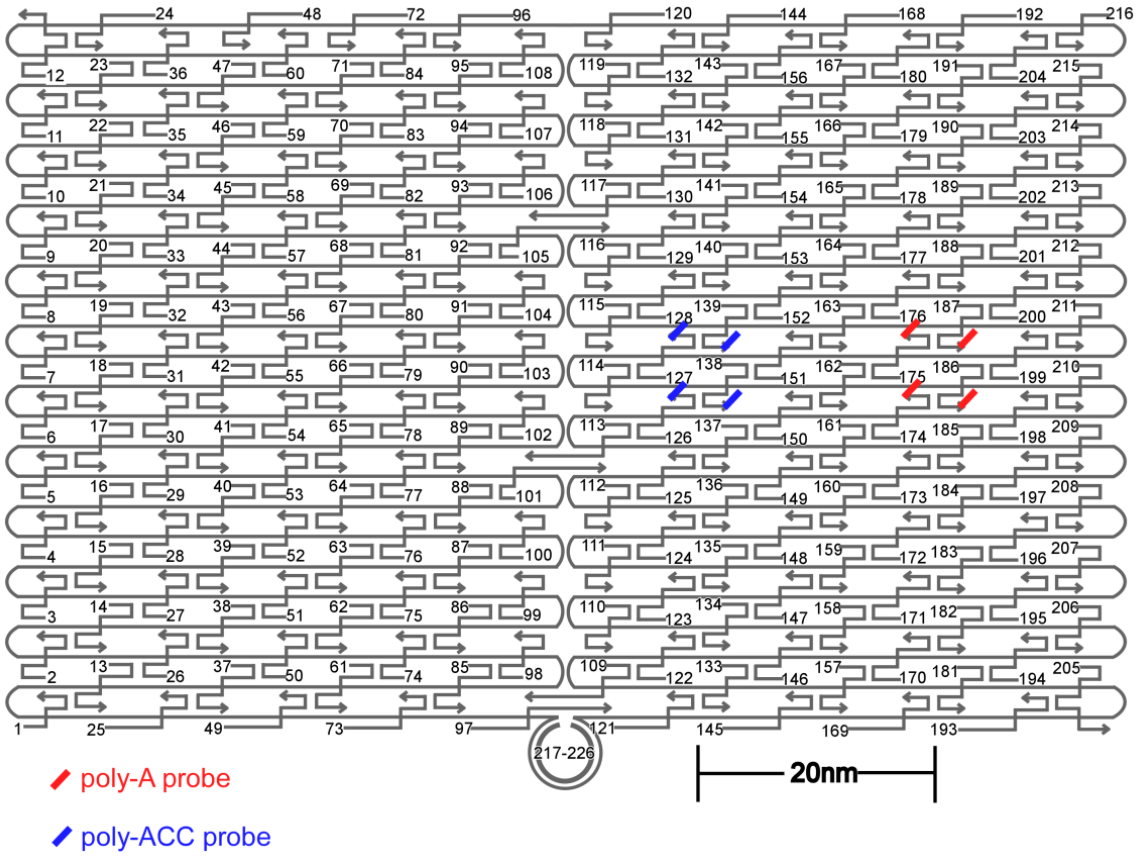

Name	Sequence
A-174	AATGGTTTACAACGCCAACATGTAGTTCAGCTAAAAAAAAAAAAAAAAAAAAAAAAAAAA
A-175	AATGCAGACCGTTTTTATTTTCATCTTGCGGGAAAAAAAAAAAAAAAAAAAAAAAAAAAA
A-186	TCATTACCCGACAATAAACAACATATTTAGGCAAAAAAAAAAAAAAAAAAAAAAAAAAAA
A-187	CTTTACAGTTAGCGAACCTCCCGACGTAGGAAAAAAAAAAAAAAAAAAAAAAAAAAAAA
ACC20-126	AATTACTACAAATTCTTACCAGTAATCCCATCACCACCACCACCACCACCACCACCACC
ACC20-127	CTAATTTATCTTTCCTTATCATTCATCCTGAAACCACCACCACCACCACCACCACCACC
ACC20-138	GGTATTAAGAACAAGAAAAATAATTAAAGCCAACCACCACCACCACCACCACCACCACC
ACC20-139	ATTATTTAACCCAGCTACAATTTTCAAGAACGACCACCACCACCACCACCACCACCACC

Figure S15. S2 origami tile schematic with 20-nm distance between probes.

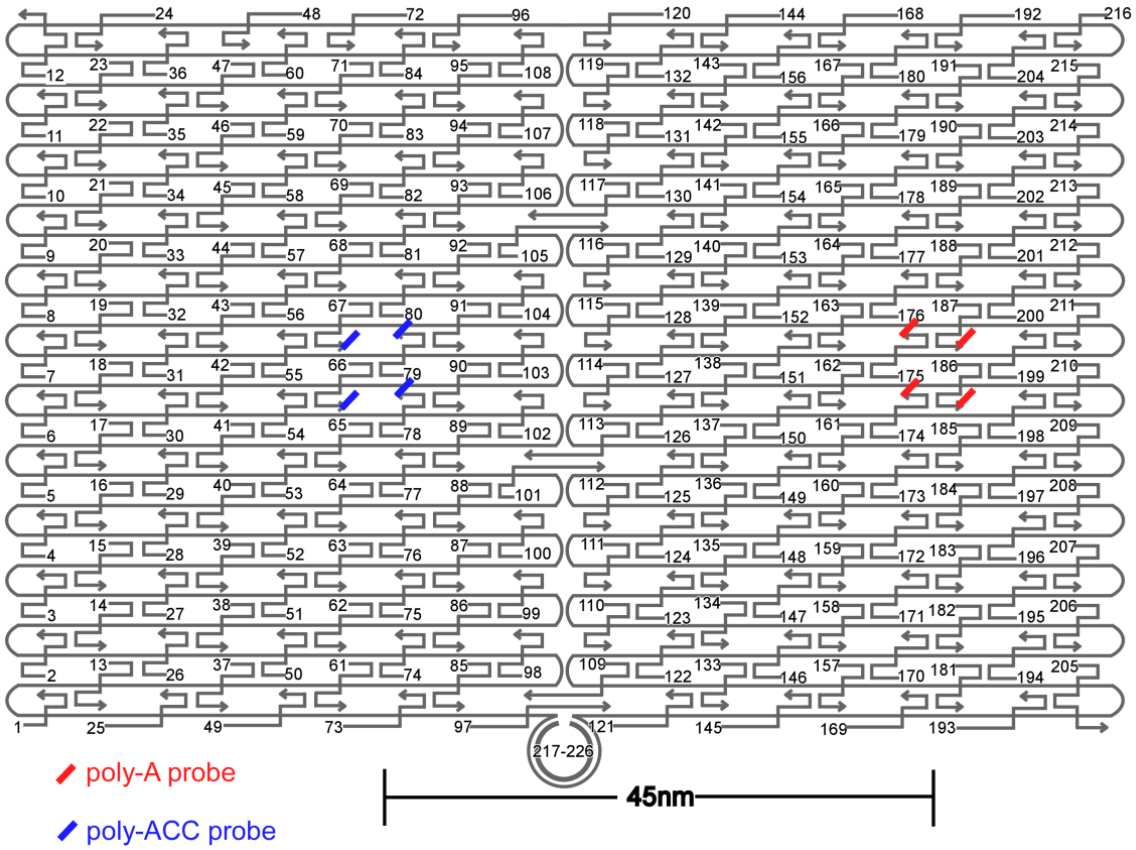

Name	Sequence
A-174	AATGGTTTACAACGCCAACATGTAGTTCAGCTAAAAAAAAAAAAAAAAAAAAAAAAAAA
A-175	AATGCAGACCGTTTTTATTTTCATCTTGCGGGAAAAAAAAAAAAAAAAAAAAAAAAAAA
A-186	TCATTACCCGACAATAAACAACATATTTAGGCAAAAAAAAAAAAAAAAAAAAAAAAAAA
A-187	CTTTACAGTTAGCGAACCTCCCGACGTAGGAAAAAAAAAAAAAAAAAAAAAAAAAAAA
ACC45-66	CGAGTAGAACTAATAGTAGTAGCAAACCCTCAACCACCACCACCACCACCACCACCACC
ACC45-67	TCAGAAGCCTCCAACAGGTCAGGATCTGCGAAACCACCACCACCACCACCACCACCACC
ACC45-78	ACCGTTCTAAATGCAATGCCTGAGAGGTGGCAACCACCACCACCACCACCACCACCACC
ACC45-79	TCAATTCTTTTAGTTTGACCATTACCAGACCGACCACCACCACCACCACCACCACCACC

Figure S16. S3 origami tile schematic with 45-nm distance between probes.

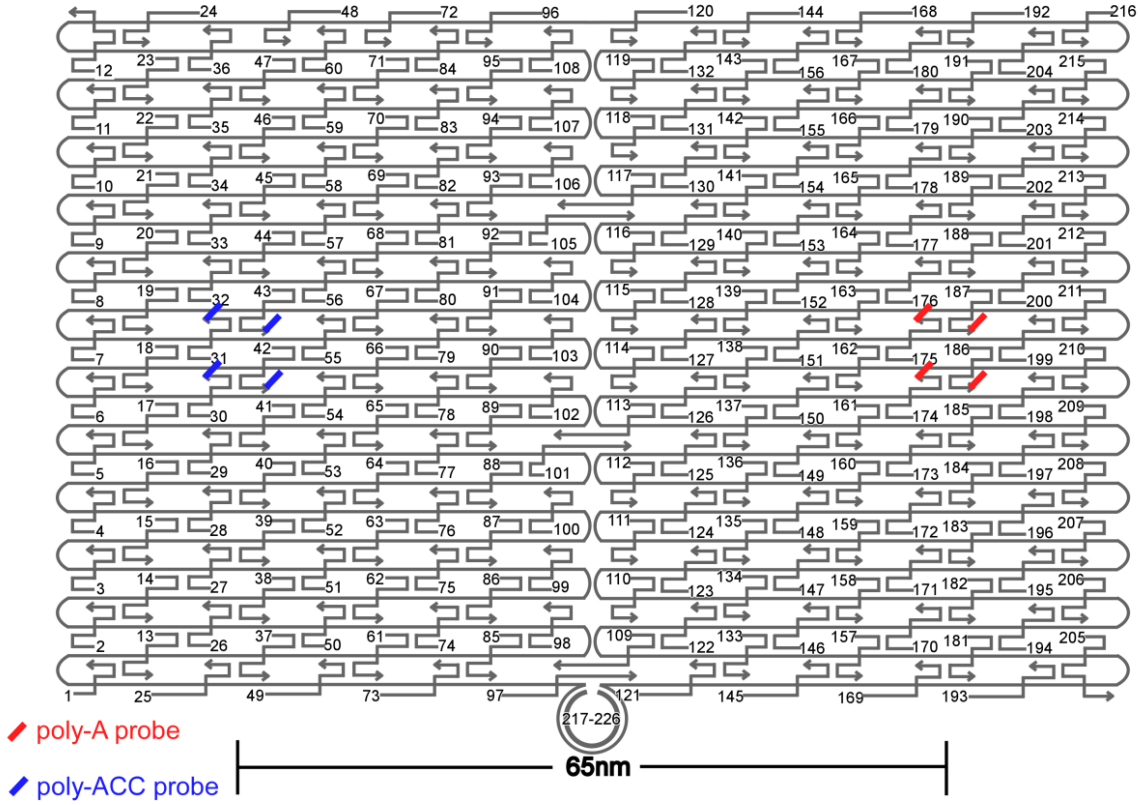

Name	Sequence
A-174	AATGGTTTACAACGCCAACATGTAGTTCAGCTAAAAAAAAAAAAAAAAAAAAAAAAAAAA
A-175	AATGCAGACCGTTTTTATTTTCATCTTGCGGGAAAAAAAAAAAAAAAAAAAAAAAAAAAA
A-186	TCATTACCCGACAATAAACAACATATTTAGGCAAAAAAAAAAAAAAAAAAAAAAAAAAAA
A-187	CTTTACAGTTAGCGAACCTCCCGACGTAGGAAAAAAAAAAAAAAAAAAAAAAAAAAAAA
ACC65-30	TCAGGTCACTTTTGCGGGAGAAGCAGAATTAGACCACCACCACCACCACCACCACCACC
ACC65-31	CAAAATTAAAGTACGGTGTCTGGAAGAGGTCAACCACCACCACCACCACCACCACCACC
ACC65-42	TCCATATACATACAGGCAAGGCAACTTTATTTACCACCACCACCACCACCACCACCACC
ACC65-43	CAAAAATCATTGCTCCTTTTGATAAGTTTCATACCACCACCACCACCACCACCACCACC

Figure S17. S4 origami tile schematic with 65-nm distance between probes.

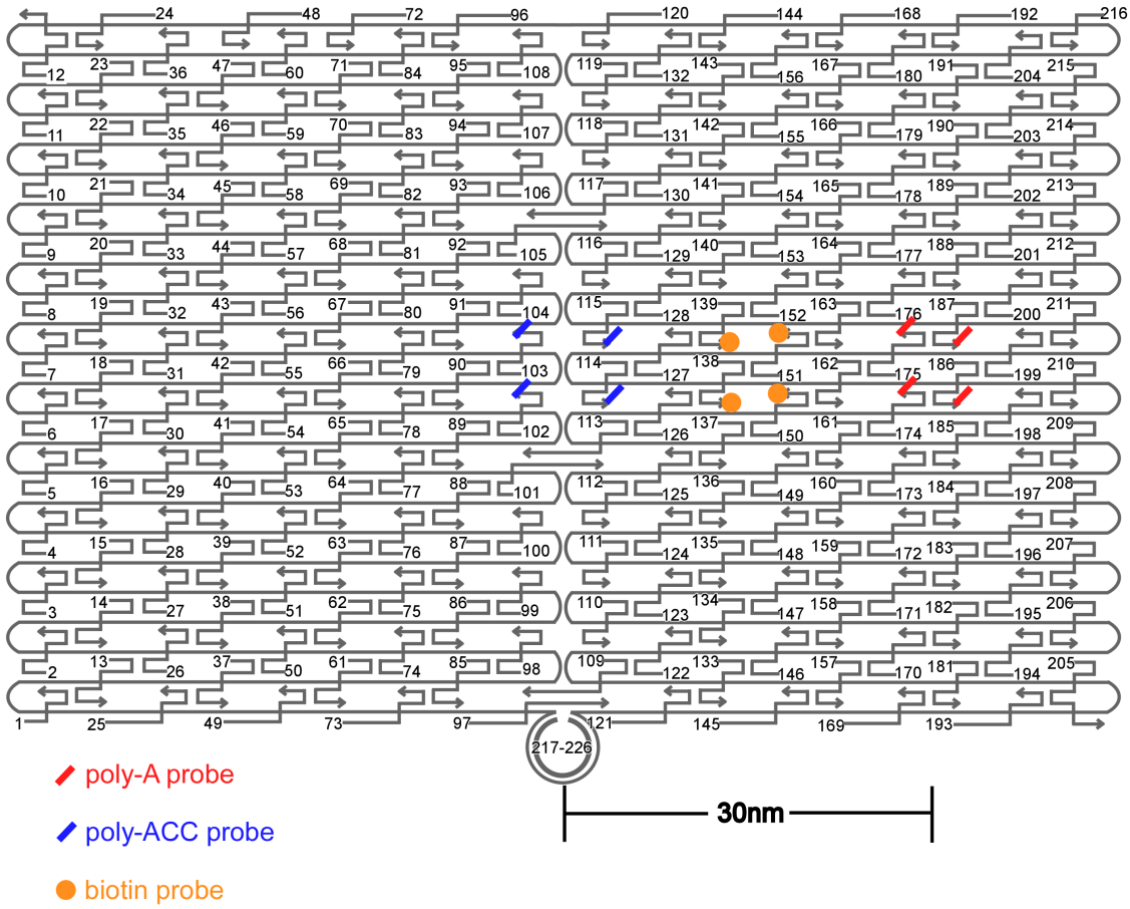

Name	Sequence
A-174	AATGGTTTACAACGCCAACATGTAGTTCAGCTAAAAAAAAAAAAAAAAAAAAAAAAAAAA
A-175	AATGCAGACCGTTTTTATTTTCATCTTGCGGGAAAAAAAAAAAAAAAAAAAAAAAAAAAA
A-186	TCATTACCCGACAATAAACAACATATTTAGGCAAAAAAAAAAAAAAAAAAAAAAAAAAAA
A-187	CTTTACAGTTAGCGAACCTCCCGACGTAGGAAAAAAAAAAAAAAAAAAAAAAAAAAAAA
ACC30-102	AGACAGTCATTCAAAAGGGTGAGAAGCTATATACCACCACCACCACCACCACCACCACC
ACC30-102	TTTCATTTGGTCAATAACCTGTTTATATCGCGACCACCACCACCACCACCACCACCACC
ACC30-114	ATCGGCTGCGAGCATGTAGAAACCTATCATATACCACCACCACCACCACCACCACCACC
ACC30-115	CCTAATTTACGCTAACGAGCGTCTAATCAATAACCACCACCACCACCACCACCACCACC
bio138	GGTATTAAGAACAAGAAAAATAATTAAAGCCATCCAAATCCAATCCAAATCCAA/3BioTEG/
bio139	ATTATTTAACCCAGCTACAATTTTCAAGAACGTCCAAATCCAATCCAAATCCAA/3BioTEG/
bio150	AGGCGTTACAGTAGGGCTTAATTGACAATAGATCCAAATCCAATCCAAATCCAA/3BioTEG/
bio151	TAAGTCCTACCAAGTACCGCACTCTTAGTTGCTCCAAATCCAATCCAAATCCAA/3BioTEG/

Figure S18. Schematic of the origami tile used for capturing NTV or β-Gal protein bridges.

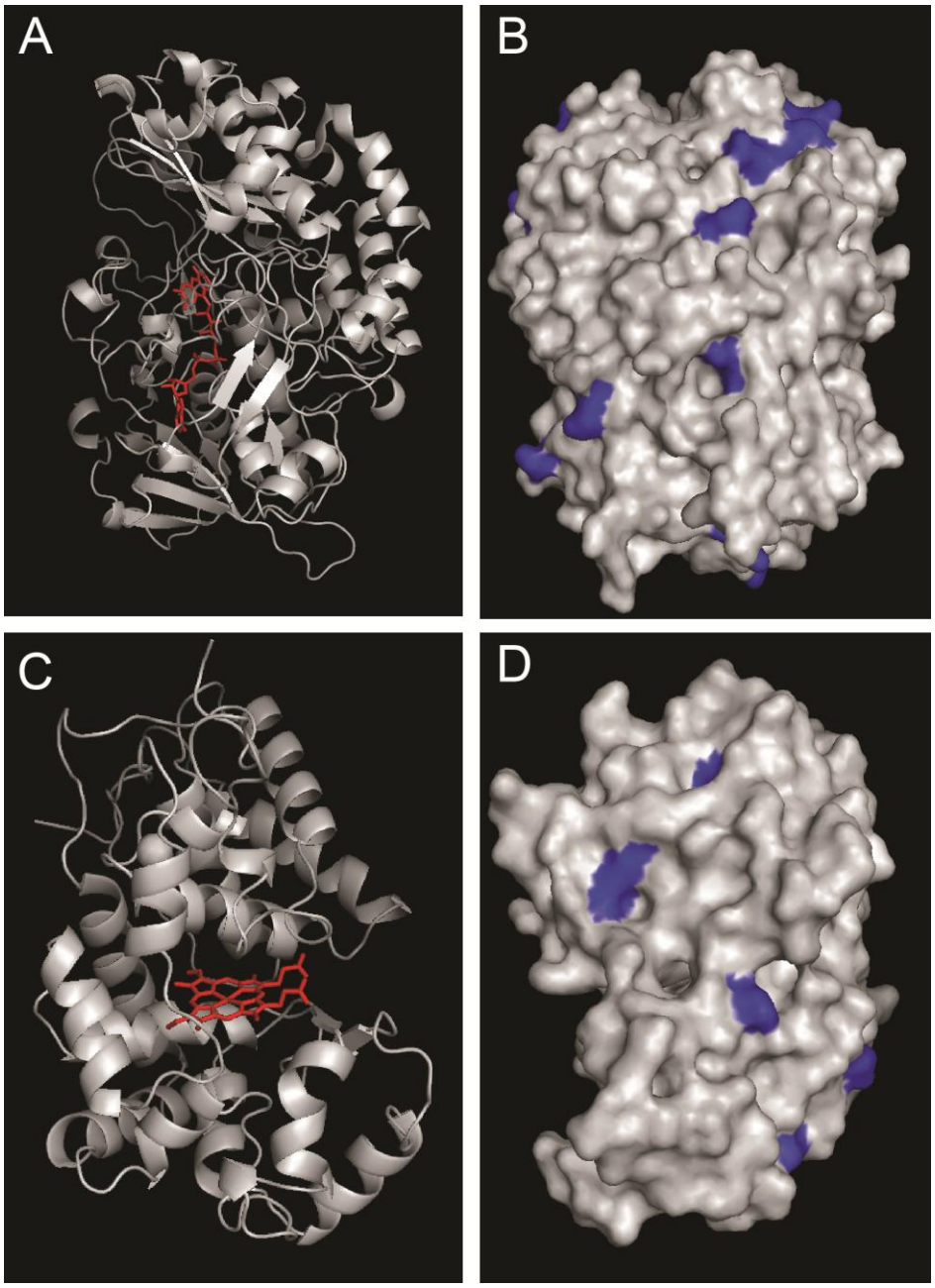

Figure S19. X-ray crystal structures of GOx and HRP with cofactors and potential surface lysines. Figures are generated by PyMOL program. (A) GOx (1CF3) structure with FAD cofactor (red); (B) (blue) potential surface lysines of GOx for DNA conjugation; (C) HRP (1ATJ) structure with heme cofactor (red); (D) (blue) potential surface lysines of HRP for DNA conjugation.

APPENDIX C

SUPPLEMENTAL INFORMATION FOR CHAPTER 4

Supplemental Information

Build up Responsive Nanodevice: A DNA Tweezer-actuated Enzyme Nanoreactor

Minghui Liu,[1,3] Jinglin Fu,[1,2] Christian Hejesen,[4] Yuhe Yang,[1,3] Neal W. Woodbury,[2,3] Kurt Gothelf,[4] Yan Liu[1,3] and Hao Yan[1,3]

[1]Center for Single Molecule Biophysics,

[2]Center for Innovations in Medicine, the Biodesign Institute,

[3]Department of Chemistry and Biochemistry, Arizona State University, Tempe, AZ 85287, USA.

[4]Centre for DNA Nanotechnology, Department of Chemistry and iNANO, Aarhus University, Aarhus C, DK-8000, Denmark.

Corresponding authors: hao.yan@asu.edu; jfu06@asu.edu

Author Contributions: Minghui Liu and Jinglin Fu contributed equally to this work.

1. Chemicals

Glucose-6 phosphate dehydrogenase, G6pDH (*Leuconostoc mesenteroides*), glucose-6 phosphate (G6p), resazurin, phenazine methosulfate (PMS), *N*-Succinimidyl 3-(2-pyridyldithio)-propionate (SPDP), disuccinimidyl suberate (DSS), N,N-Diisopropylethylamine (DIPEA), phosphate buffered saline (PBS), sodium HEPES salt, tris buffered saline (TBS) and DEAE-Sepharose resin were purchased from Sigma (St.Louis, MO). β-Nicotinamide-N6-(2-aminoethyl) adenine dinucleotide (6AE-NAD^+) was ordered from BIOLOG (Bremen, Germany). Single-stranded oligonucleotides were purchased from IDT (Coralville, Iowa).

2. Gel Preparation and Characterization

3% Native PAGE gels were prepared at room temperature and run for 2.5 to 3 hours at constant 200V and subsequently stained with ethidium bromide. To verify the assembled proteins, the same gel was then washed and stained using Pierce Silver Stain Kit (Thermo Fisher Scientific Inc.).

Temperature	Time
90 ℃	1 min
88 ℃	1 min
86 ℃	1 min
84 ℃	1 min
82 ℃	1 min
80 ℃	1 min
78 ℃	1 min
76 ℃	2 min
72 ℃	2 min
68 ℃	5 min
64 ℃	5 min
60 ℃	5 min
56 ℃	5 min
52 ℃	5 min
48 ℃	5 min
44 ℃	5 min
40 ℃	5 min
36 ℃	5 min
32 ℃	5 min
28 ℃	5 min
24 ℃	5 min
4 ℃	hold

Table S1. Thermal annealing program for DNA tweezers.

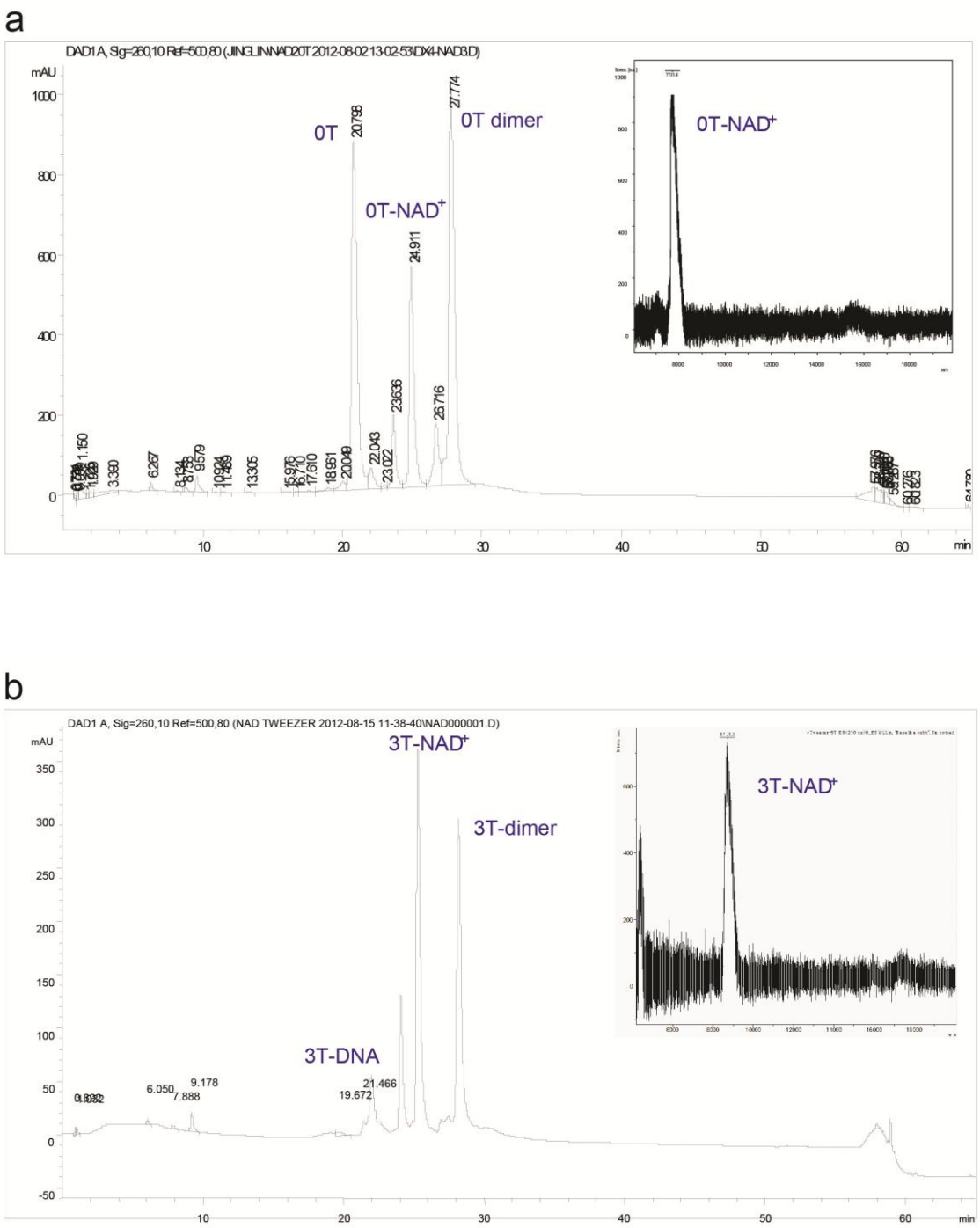

Figure S1. Mass spectrometry characterization of HPLC purified NAD-DNA conjugates: (a) NAD-T9 (0T); (b) NAD-T9 (3T).

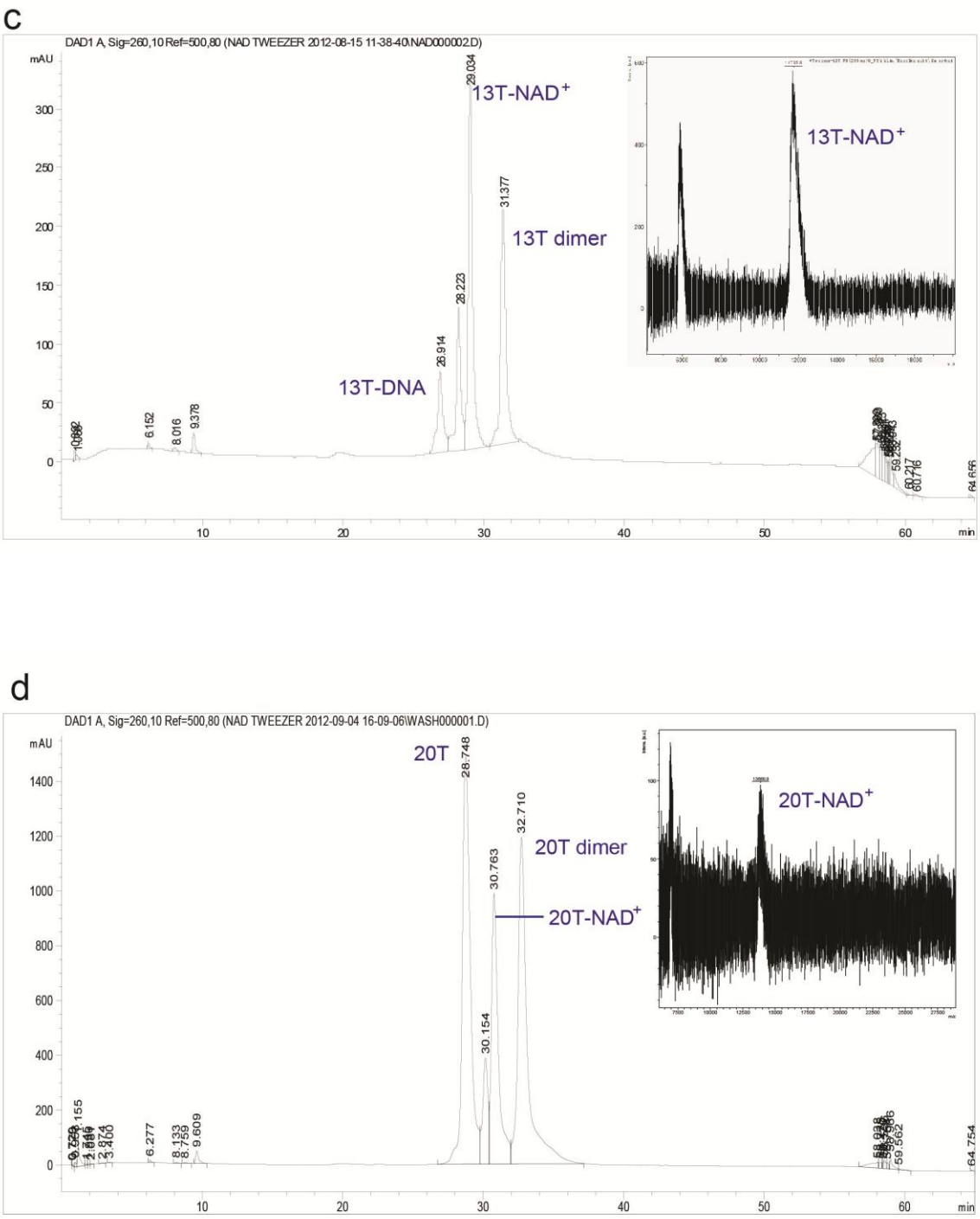

Figure S1 (cont). (c) NAD-T9 (13T); (d) NAD-T9 (20T).

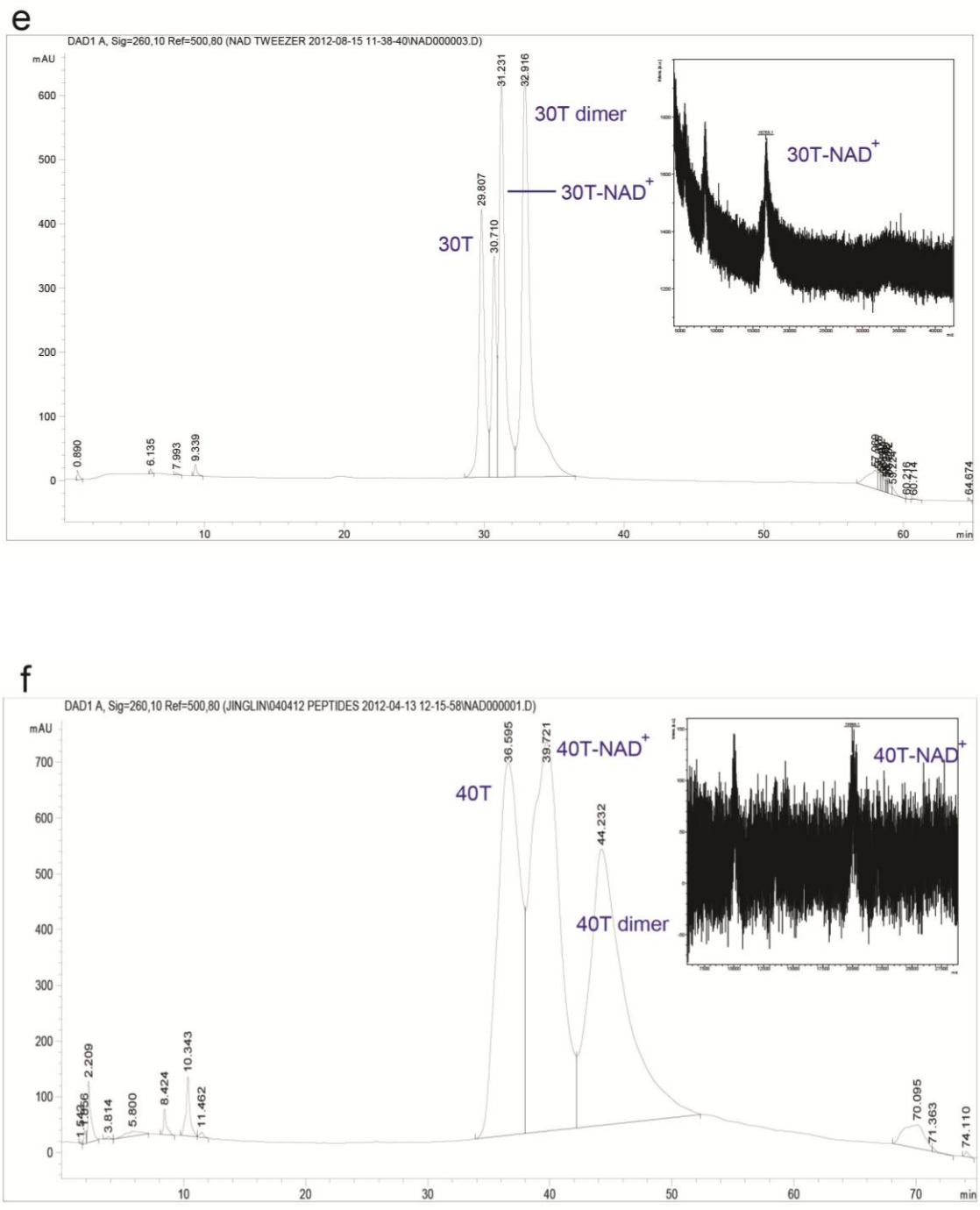

Figure S1 (cont). (e) NAD-T9 (30T); (f) NAD-T9 (40T).

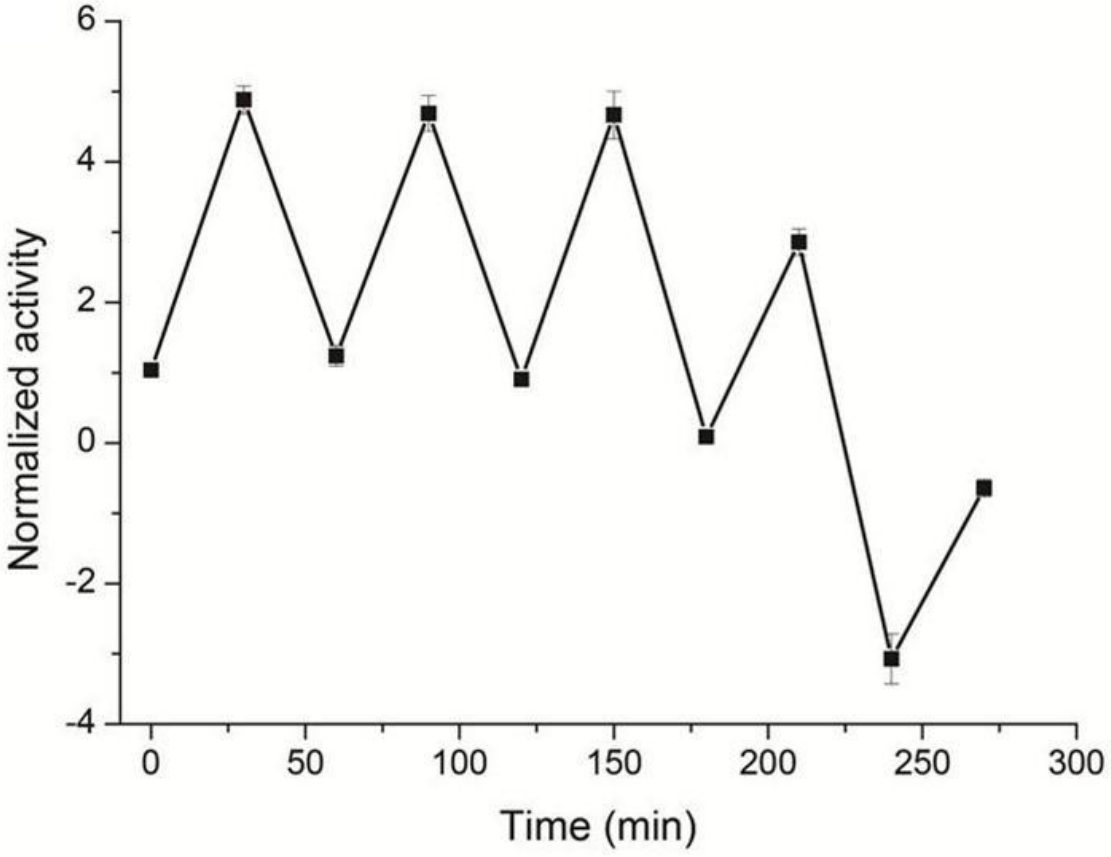

Figure S3. Evaluating the effect of the double-stranded DNA/Mg^{2+} complex in quenching resorufin fluorescence. After 4 cycles of opening and closing the tweezer structures, and in the presence of 1 mM Mg^{2+}, the enzyme activity was reduced due to accumulation of excess fuel and set strands bound to Mg^{2+} and the formation of DNA/Mg^{2+} complexes that quench resorufin fluorescence. By removing Mg^{2+} from the assay solution, no fluorescence quenching was observed, as shown in Figure 4.13.

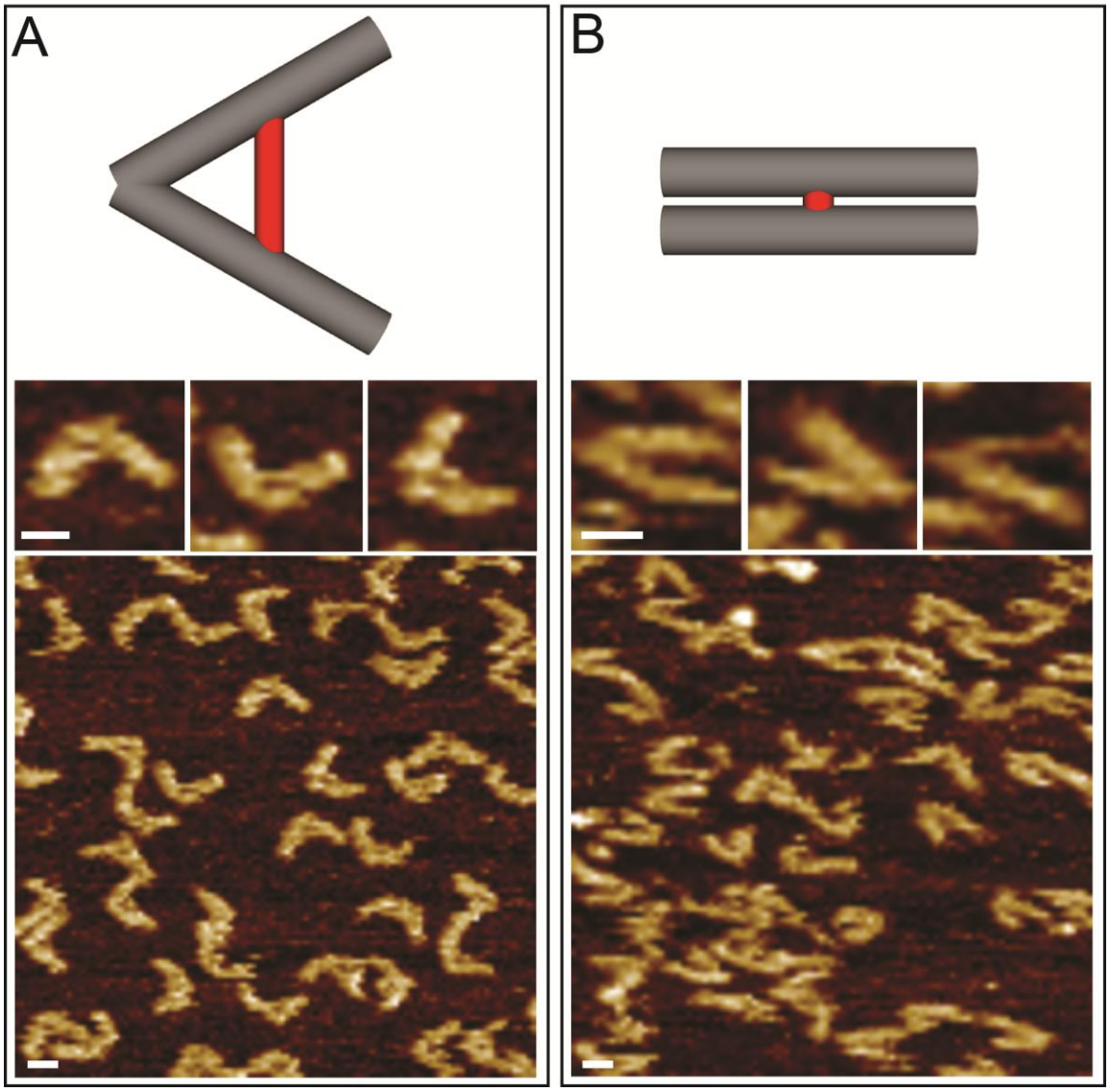

Figure S4. AFM characterization of DNA tweezers. (A) Open tweezers: design (top); zoom-ins (middle); zoom-out image (bottom). A wider distance between two arms was observed (20-25 nm). (B) Close tweezers: design (top); zoom-ins (middle); zoom-out image (bottom). Due to the flexibility of two arms, the actual distance between two arms was observed ~5-7 nm which correlates to FRET measurement.

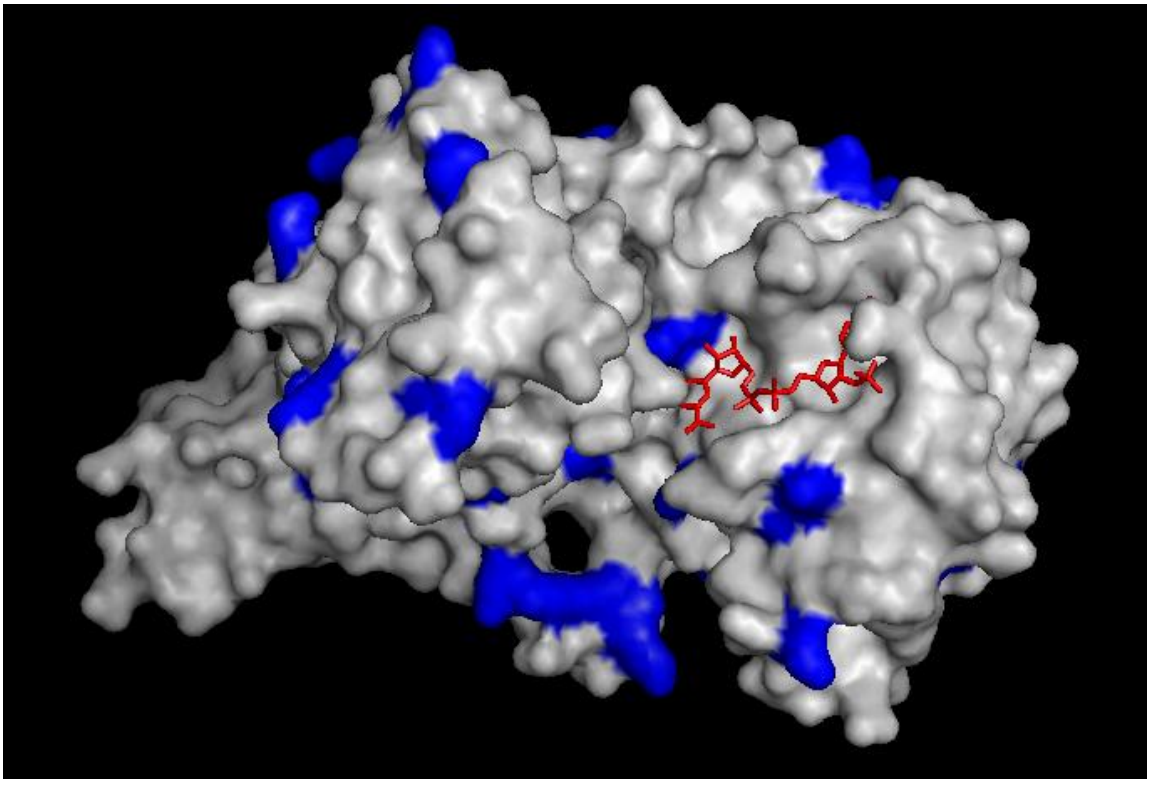

Figure S5. 3D crystal structure of G6pDH (*Leuconostoc Mesenteroides*, PDB 1DPG) generated by PyMOL program with cofactor NADP (red) and potential surface lysines (blue) for DNA conjugation.

APPENDIX D

CO-AUTHOR APPROVAL

I verify that the following co-authors have approved of my use of our publications in my dissertation.

Yan Liu (Arizona State University)

Hao Yan (Arizona State University)

Neal W. Woodbury (Arizona State University)

Jinglin Fu (Arizona State University)

Jeanette Nangreave (Arizona State University)

Zhe Li (Arizona State University[1])

Yuhe Yang (Arizona State University)

Nicholas Stephanopoulos (University of California, Berkeley[1])

Gary Tong (University of California, Berkeley[1])

Matthew B. Francis (University of California, Berkeley)

Christian Hejesen (Aarhus University)

Kurt Gothelf (Aarhus University)

Lei Wang (Shandong University)

[1]Note: The author's address is listed as when the research was performed.